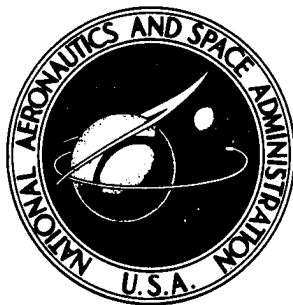


NASA TECHNICAL NOTE



NASA TN D-6946

NASA TN D-6946

LATERAL-DIRECTIONAL AERODYNAMIC
CHARACTERISTICS OF LIGHT, TWIN-ENGINE,
PROPELLER-DRIVEN AIRPLANES

by Chester H. Wolowicz and Roxanah B. Yancey

Flight Research Center
Edwards, Calif. 93523

NATIONAL AERONAUTICS AND SPACE ADMINISTRATION • WASHINGTON, D. C. • OCTOBER 1972

1. Report No. NASA TN D-6946	2. Government Accession No.	3. Recipient's Catalog No.	
4. Title and Subtitle LATERAL-DIRECTIONAL AERODYNAMIC CHARACTERISTICS OF LIGHT, TWIN-ENGINE, PROPELLER-DRIVEN AIRPLANES		5. Report Date October 1972	
		6. Performing Organization Code	
7. Author(s) Chester H. Wolowicz and Roxanah B. Yancey		8. Performing Organization Report No. H-694	
9. Performing Organization Name and Address NASA Flight Research Center P. O. Box 273 Edwards, California 93523		10. Work Unit No. 760-71-03-00-24	
		11. Contract or Grant No.	
		13. Type of Report and Period Covered Technical Note	
12. Sponsoring Agency Name and Address National Aeronautics and Space Administration Washington, D. C. 20546		14. Sponsoring Agency Code	
15. Supplementary Notes			
16. Abstract <p>This report documents representative state-of-the-art analytical procedures and design data for predicting the lateral-directional static and dynamic stability and control characteristics of light, twin-engine, propeller-driven airplanes for propeller-off and power-on conditions. Although the consideration of power effects is limited to twin-engine airplanes, the propeller-off considerations are applicable to single-engine airplanes as well.</p> <p>The procedures are applied to a twin-engine, propeller-driven, semi-low-wing airplane in the clean configuration through the linear lift range. The calculated derivative characteristics are compared with wind-tunnel and flight data. Included in the calculated characteristics are the spiral mode, roll mode, and Dutch roll mode over the speed range of the airplane. All calculations are documented.</p>			
17. Key Words (Suggested by Author(s)) Light airplane Aerodynamic characteristics - prediction		18. Distribution Statement Unclassified - Unlimited	
19. Security Classif. (of this report) Unclassified	20. Security Classif. (of this page) Unclassified	21. No. of Pages 293	22. Price* \$6.00

* For sale by the National Technical Information Service, Springfield, Virginia 22151

CONTENTS

	Page
TABLES RELATED TO THE SUBJECT AIRPLANE	vii
FIGURES COMPARING CALCULATED CHARACTERISTICS WITH WIND-TUNNEL AND FLIGHT DATA	ix
SUMMARY	1
1.0 INTRODUCTION	2
2.0 SCOPE OF THE STUDY	3
3.0 THE AIRPLANE	4
3.1 Center-of-Gravity Positions Used in the Analysis	7
3.2 Pertinent Geometric Parameters	8
3.2.1 Symbols	8
4.0 PREDICTION OF PROPELLER-OFF AERODYNAMIC CHARACTERISTICS	17
4.1 Side-Force Derivative, C_{Y_β}	17
4.1.1 Wing Contribution, $(C_{Y_\beta})_{w_{\Gamma=0}} + (C_{Y_\beta})_\Gamma$	17
4.1.2 Fuselage Contribution to C_{Y_β}	18
4.1.3 Nacelles Contribution to C_{Y_β}	19
4.1.4 Vertical-Tail Contribution to C_{Y_β}	20
4.1.5 C_{Y_β} of the Complete Airplane	23
4.1.6 Symbols	24
4.2 Weathercock Stability, C_{n_β}	41
4.2.1 Wing Contribution to C_{n_β}	41
4.2.2 Fuselage Contribution to C_{n_β}	42
4.2.3 Nacelles Contribution to C_{n_β}	44
4.2.4 Vertical-Tail Contribution to C_{n_β}	44
4.2.5 Weathercock Stability of the Complete Airplane	44
4.2.6 Symbols	45
4.3 Effective Dihedral, C_{l_β}	57
4.3.1 Wing Contribution to C_{l_β}	57
4.3.2 Effect of Fuselage on Wing Contribution to C_{l_β}	59
4.3.3 Vertical-Tail Contribution to C_{l_β}	60
4.3.4 C_{l_β} of the Complete Airplane	61
4.3.5 Symbols	61
4.4 Rolling and Yawing Moments Due to Aileron Deflection	77
4.4.1 Rolling Moment Due to Aileron Deflection, $C_{l_{\delta_a}}$	77

CONTENTS - Continued

	Page
4.4.2 Yawing Moment Due to Aileron Deflection, $C_{n\delta_a}$	79
4.4.3 Symbols	81
4.5 Yawing and Rolling Moments Due to Rudder Deflection.	97
4.5.1 Side Force Due to Rudder Deflection, $C_{Y\delta_r}$	97
4.5.2 Yawing and Rolling Moments Due to Rudder Deflection . . .	98
4.5.3 Symbols	99
5.0 PREDICTION OF POWER-ON STATIC STABILITY AND CONTROL CHARACTERISTICS	108
5.1 Power-On Static Stability Characteristics	109
5.1.1 Power Effects on $C_{Y\beta}$	109
5.1.2 Power Effects on $C_{n\beta}$	112
5.1.3 Power Effects on $C_{l\beta}$	113
5.1.4 Symbols	115
5.2 Power-On Control Characteristics	132
5.2.1 Aileron Parameters	132
5.2.2 Rudder Parameters	132
5.2.3 Symbols	132
5.3 Comparison of Predicted Static Stability and Control Characteristics With Flight Data	136
5.3.1 Flight-Test Conditions and Maneuvers	136
5.3.2 Analysis of the Dutch-Roll Maneuver Flight Data	136
5.3.3 Analysis of the Increasing-Sideslip-Maneuver Flight Data .	140
5.3.4 Comparison of Predicted Stability and Control Characteristics With Flight Data	140
5.3.5 Symbols	142
6.0 DYNAMIC DERIVATIVE CHARACTERISTICS	150
6.1 Damping-in-Roll Derivative, C_{l_p}	151
6.1.1 Wing-Body Contribution to C_{l_p}	151
6.1.2 Horizontal-Tail Contribution to C_{l_p}	152
6.1.3 Vertical-Tail Contribution to C_{l_p}	153
6.1.4 Nacelles Contribution to C_{l_p}	154
6.1.5 Power Contributions to C_{l_p}	155
6.1.6 Summary of Contributions to C_{l_p}	158
6.1.7 Symbols	158
6.2 Damping-in-Yaw Derivative, C_{n_r}	179
6.2.1 Wing Contribution to C_{n_r}	179
6.2.2 Fuselage Contribution to C_{n_r}	181

CONTENTS - Continued

	Page
6.2.3 Vertical-Tail Contribution to C_{n_r}	181
6.2.4 Power Contributions to C_{n_r} and Summary	182
6.2.5 Symbols	183
6.3 Roll-Due-to-Yawing Derivative, C_{l_r}	195
6.3.1 Wing Contribution to C_{l_r}	195
6.3.2 Vertical-Tail Contribution to C_{l_r}	197
6.3.3 Power Contributions to C_{l_r}	197
6.3.4 Summary of Contributions to C_{l_r}	198
6.3.5 Symbols	199
6.4 Yaw-Due-to-Rolling Derivative, C_{n_p}	208
6.4.1 Wing Contribution to C_{n_p}	208
6.4.2 Vertical-Tail Contribution to C_{n_p}	210
6.4.3 Power Contributions to C_{n_p}	210
6.4.4 Summary of Contributions to C_{n_p}	211
6.4.5 Symbols	211
6.5 The Derivatives C_{n_β} and C_{l_β}	224
6.5.1 Symbols	226
6.6 Comparison of Predicted Dynamic Derivatives With Flight Data	229
6.6.1 Analysis of Flight Data	229
6.6.2 Comparison of Predicted and Flight-Determined Dynamic Derivatives	230
6.6.3 Symbols	230
7.0 DYNAMIC STABILITY CHARACTERISTICS	234
7.1 Equations of Motion	235
7.1.1 Symbols	237
7.2 Determination of Roots of Characteristic Equation When Spiral Divergence, Roll Subsidence, and Dutch Roll Modes Exist	241
7.2.1 Spiral Divergence Root	241
7.2.2 Roll Subsidence Root	243
7.2.3 Roots of the Dutch Roll Mode	244
7.2.4 Symbols	247
7.3 Ratio of Roll to Sideslip in the Dutch Roll Mode	254
7.3.1 Roll-to-Sideslip Ratio	254
7.3.2 Roll-to-Sideslip Phase Angle	256
7.3.3 Comparison of Predicted Characteristics With Flight Data	256
7.3.4 Symbols	256
7.4 Roll Performance	261
7.4.1 Derivation of the Roll Equation	261
7.4.2 Steady-State Roll Rate	263

CONTENTS - Concluded

	Page
7.4.3 Apparent Roll Mode Constant	265
7.4.4 Roll and Dutch Roll Mode Coupling	266
7.4.5 Symbols	269
8.0 REFERENCES	281

TABLES RELATED TO SUBJECT AIRPLANE

	Page
3-1 MANUFACTURER'S PHYSICAL CHARACTERISTICS OF THE SUBJECT AIRPLANE	5
PREDICTION OF PROPELLER-OFF AERODYNAMIC CHARACTERISTICS	
4.1.1-1 WING CONTRIBUTION TO C_{Y_β}	28
4.1.2-1 FUSELAGE CONTRIBUTION TO C_{Y_β}	28
4.1.3-1 NACELLES CONTRIBUTION TO C_{Y_β}	29
4.1.4-1 VERTICAL-TAIL CONTRIBUTION TO C_{Y_β}	30
4.1.5-1 C_{Y_β} OF THE COMPLETE AIRPLANE	32
4.2.1-1 WING CONTRIBUTION TO C_{n_β}	48
4.2.2-1 FUSELAGE CONTRIBUTION TO C_{n_β}	49
4.2.3-1 NACELLE CONTRIBUTION TO C_{n_β}	50
4.2.4-1 VERTICAL-TAIL CONTRIBUTION TO C_{n_β}	51
4.2.5-1 WEATHERCOCK STABILITY OF THE AIRPLANE	52
4.3.1-1 WING CONTRIBUTION TO C_{l_β}	64
4.3.2-1 EFFECT OF FUSELAGE ON WING CONTRIBUTION TO C_{l_β}	65
4.3.3-1 VERTICAL-TAIL CONTRIBUTION TO C_{l_β}	66
4.3.4-1 C_{l_β} OF THE COMPLETE AIRPLANE	67
4.4.1-1 ROLLING MOMENTS DUE TO AILERONS, $C_{l_{\delta_a}}$	84
4.4.2-1 YAWING MOMENTS DUE TO AILERONS, $C_{n_{\delta_a}}$	86
4.5.1-1 SIDE FORCE DUE TO RUDDER DEFLECTION, $C_{Y_{\delta_r}}$	103
4.5.2-1 YAWING AND ROLLING MOMENTS DUE TO RUDDER DEFLECTION	104
PREDICTION OF POWER-ON STABILITY AND CONTROL CHARACTERISTICS	
5.1.1-1 EFFECT OF POWER ON C_{Y_β}	119

TABLES - Concluded

	Page
5.1.2-1 EFFECT OF POWER ON C_{n_β}	122
5.1.3-1 EFFECT OF POWER ON C_{l_β}	124
5.3-1 TRANSFORMATION OF DERIVATIVES FROM STABILITY TO BODY AXIS	146
DYNAMIC DERIVATIVE CHARACTERISTICS	
6.1.1-1 WING-FUSELAGE CONTRIBUTION TO C_{l_p}	163
6.1.2-1 HORIZONTAL-TAIL CONTRIBUTION TO C_{l_p}	164
6.1.3-1 VERTICAL-TAIL CONTRIBUTION TO C_{l_p}	165
6.1.4-1 CONTRIBUTION OF NACELLES TO PROPELLER-OFF C_{l_p}	166
6.1.5-1 EFFECT OF POWER ON WING CONTRIBUTION TO C_{l_p}	167
6.1.5-2 CONTRIBUTION OF PROPELLER NORMAL FORCES TO C_{l_p}	168
6.1.5-3 POWER-INDUCED CHANGE IN NACELLE CONTRIBUTION TO C_{l_p}	169
6.1.6-1 SUMMARY OF CONTRIBUTIONS TO C_{l_p}	170
6.2.1-1 WING CONTRIBUTION TO C_{n_r}	187
6.2.3-1 VERTICAL-TAIL CONTRIBUTION TO C_{n_r}	188
6.2.4-1 SUMMARY OF CONTRIBUTIONS TO C_{n_r} INCLUDING POWER . .	189
6.3.1-1 WING CONTRIBUTION TO C_{l_r}	202
6.3.2-1 VERTICAL-TAIL CONTRIBUTION TO C_{l_r}	203
6.3.3-1 EFFECT OF POWER ON WING CONTRIBUTION TO C_{l_r}	205
6.3.4-1 SUMMARY OF CONTRIBUTIONS TO C_{l_r}	205
6.4.1-1 WING CONTRIBUTIONS TO C_{n_p}	214
6.4.2-1 VERTICAL-TAIL CONTRIBUTION TO C_{n_p}	217
6.4.4-1 SUMMARY OF CONTRIBUTIONS TO C_{n_p}	218

**FIGURES COMPARING CALCULATED CHARACTERISTICS
WITH WIND-TUNNEL AND FLIGHT DATA**

	Page
PROPELLER-OFF CHARACTERISTICS	
4.1.5-1 Comparison of calculated $C_{Y\beta}$ with wind-tunnel data. Propellers off.	40
4.2.5-1 Comparison of calculated $C_{n\beta}$ with wind-tunnel data. Propellers off.	56
4.3.4-1 Comparison of calculated $C_{l\beta}$ with wind-tunnel data. Propellers off.	76
4.4.1-6 Comparison of calculated rolling-moment effectiveness of ailerons of subject airplane with wind-tunnel data.	94
4.4.2-2 Comparison of calculated yawing moment due to ailerons of subject airplane with wind-tunnel data.	96
4.5.2-1 Comparison of calculated and wind-tunnel values of rudder side force and yawing- and rolling-moment effectiveness.	107
POWER-ON CHARACTERISTICS	
5.1.1-4 Comparison of calculated $C_{Y\beta}$ with wind-tunnel data as a function of angle of attack and thrust coefficient.	129
5.1.2-1 Comparison of calculated $C_{n\beta}$ with wind-tunnel data as a function of angle of attack and thrust coefficient.	130
5.1.3-1 Comparison of calculated $C_{l\beta}$ with wind-tunnel data as a function of angle of attack and thrust coefficient.	131
5.2.1-1 Comparison of calculated aileron characteristics with wind-tunnel data.	134
5.2.2-1 Comparison of calculated rudder characteristics with wind-tunnel data.	135
5.3.4-1 Comparison of predicted static stability characteristics with flight data relative to body axes.	148
5.3.4-2 Comparison of predicted control characteristics with flight data relative to body axes.	149
6.6.2-1 Comparison of flight-determined and calculated dynamic stability derivatives relative to the body axes as a function of angle of attack.	233
7.2.3-2 Predicted period and damping characteristics of the subject airplane compared with flight data.	253

FIGURES - Concluded

	Page
7.3.3-1 Predicted amplitude ratio and phase angle characteristics of the subject airplane for trim level-flight conditions compared with several flight-determined values.	260
7.4.2-1 Time histories of roll rate response to aileron input and the wing-tip helix angle, $p_{ss} \frac{b_w}{2V}$, shown as a function of δ_a	272

LATERAL-DIRECTIONAL AERODYNAMIC CHARACTERISTICS OF
LIGHT, TWIN-ENGINE, PROPELLER-DRIVEN AIRPLANES

Chester H. Wolowicz and Roxanah B. Yancey
Flight Research Center

SUMMARY

Representative state-of-the-art analytical procedures and design data for predicting the lateral-directional static and dynamic stability and control characteristics of light, twin-engine, propeller-driven airplanes for propeller-off and power-on conditions are documented. Although the consideration of power effects is limited to twin-engine airplanes, the propeller-off considerations are applicable to single-engine airplanes as well.

The procedures are applied to a twin-engine, propeller-driven, semi-low-wing airplane in the clean configuration to determine the lateral and directional control derivatives as well as the static and dynamic stability derivatives as functions of angle of attack and power condition through the linear lift range of the airplane. Also determined are the spiral mode, roll mode, and Dutch roll characteristics for level-flight conditions over the speed range of the airplane. All calculations are documented.

Attempts to calculate the weathercock stability characteristics indicated a need to account for wing-body interference effects on the body contribution as a function of angle of attack and vertical position of the wing relative to the body. Vertical-tail-off wind-tunnel data of a single-engine version of the subject airplane are used to expand the design nomograph from which the body-plus-wing-body contribution to weathercock stability was determined in order to obtain the contribution for a semi-low-wing airplane as a function of angle of attack. Application of the expanded nomograph to the subject airplane resulted in improved correlation of calculated weathercock stability characteristics with wind-tunnel and flight data at low angles of attack. For additional improvement in correlation, there is a need for design data to account for the effects of angle of attack on the sidewash acting on the vertical tail.

The correlation of the calculated effective dihedral with wind-tunnel data was excellent through the linear lift range for all power conditions considered. However, flight-determined values were approximately 40 percent to 50 percent smaller than wind-tunnel values. Within the scope of this study, it was not possible to identify in-flight phenomena which altered the contribution of the wing or the wing-fuselage interference to the variation of rolling-moment coefficient with sideslip and which were not accounted for in the full-scale wind-tunnel tests of the airplane. The effect of the discrepancy on several response characteristics is noted at the end of this summary.

The calculated directional control derivatives correlated well with wind-tunnel and flight data throughout the linear lift range and all power conditions investigated.

The calculated rolling-moment lateral-control derivatives were approximately 10 percent lower than the values obtained from wind-tunnel or flight data. Wind-tunnel and flight data correlated well. The calculated yawing-moment lateral-control derivatives correlated reasonably well with wind-tunnel data; flight values were more adverse than either the wind-tunnel or the calculated values.

Calculated values of the variation of yawing- and rolling-moment coefficients with yaw rate correlated well with flight data. No dynamic wind-tunnel data were available for comparison.

The dynamic derivatives had a significant effect on the calculated Dutch roll frequency. The use of a simplified Dutch roll frequency equation, which included only the static derivatives, would have resulted in a difference of approximately 40 percent in the calculated roll subsidence root.

The calculated Dutch roll period was generally 10 percent lower than the flight values. The calculated Dutch roll damping ratio correlated well with flight data; the correlation was improved when the flight-determined effective dihedral was substituted for the calculated effective dihedral.

The calculated roll-to-sideslip amplitude ratio of the Dutch roll mode did not correlate well with flight data. When the flight values of the effective dihedral were substituted for the calculated values in the response equation, good correlation was obtained.

Calculated roll-rate response to aileron input correlated well with flight data. Substituting the flight values of the effective dihedral for the calculated values in the response equation improved the correlation.

1.0 INTRODUCTION

As part of a NASA program to improve general aviation safety and utility, the NASA Flight Research Center is documenting analytical procedures and design data for predicting the subsonic static and dynamic stability and control characteristics of propeller-driven aircraft.

In partial fulfillment of this project, representative state-of-the-art methods applicable to Mach numbers up to 0.6 have been compiled and, in some instances, extensions in procedures proposed. The results have been applied to a representative light, low-wing, twin-engine, propeller-driven airplane in the clean configuration. The accuracy of the methods, within the Mach number limits (up to 0.25) of the airplane, has been determined by comparing calculated predictions with wind-tunnel and flight data.

Longitudinal characteristics were considered in the first report (ref. 1) of a two-part study. Included were propeller-off and power-on stability and control characteristics in terms of coefficients as functions of angle of attack, elevator position, and power condition. Also included were short-period oscillatory and wind-up-turn characteristics.

This report covers lateral-directional characteristics. In comparisons of the calculated characteristics with wind-tunnel data, the calculated characteristics are related to the stability-axis system to conform to the axis system of the tunnel data (ref. 2). In comparisons of the calculated characteristics with flight data, the calculated characteristics are related to the body-axis system to conform to the axis system of the flight data.

The two reports provide a summary of methods and guidelines which should enable a designer to obtain improved estimates of stability and control characteristics for propeller-off conditions in general and of the effects of power on twin-engine, propeller-driven aircraft in particular.

Axis systems, sign conventions, and definitions of the stability and control derivatives are in accord with standard NASA practices. The positive directions of the X, Y, and Z axes are forward, to the right, and down, respectively. The positive directions of the moments and angular rates are in accord with the right-hand rule. Deflection of the rudder to the left denotes a positive rudder input. The aileron deflection that produces a right roll denotes a positive aileron input. The angle of attack is measured in the XZ plane of symmetry and is the angle between the X-body axis and the component of velocity along the X-stability axis. The sideslip angle is positive when the nose of the airplane is to the left of the velocity vector.

2.0 SCOPE OF THE STUDY

As a logical starting point for the present study, use was made of the USAF Stability and Control Datcom handbook (ref. 3). This is a compendium of methods and design data for predicting the stability and control characteristics of jet and propeller-driven aircraft from subsonic through hypersonic regions of flight. A considerable portion of the material is based on NACA and NASA reports. In the present report, Datcom is listed as the reference when it provides a unique treatment of information from other sources. The basic source is referenced when Datcom repeats pertinent equations and design data. During this study, it became necessary to supplement the Datcom methods and to provide innovations.

The analysis of lateral-directional characteristics in the form of derivatives ranges from zero lift through the linear lift range of the airplane. Propeller-off and power-on conditions are considered in all instances. Included are analyses of the side force due to sideslip, weathercock stability, effective dihedral, yaw control, and roll control, as well as dynamic stability derivatives. Also included are analyses of spiral and roll mode characteristics, lateral-directional oscillatory period and damping characteristics, and roll response characteristics.

The various sections include procedures, design charts, calculations, and figures that compare calculated results with wind-tunnel (ref. 2) or flight data or both. Notations and symbols are defined in each section.

3.0 THE AIRPLANE

The airplane used in the analysis is representative of general aviation, personal-owner aircraft. It is a six-place, low-wing, twin-engine, propeller-driven, all-metal airplane with an all-movable horizontal stabilizer and a single vertical tail. Pertinent physical characteristics, as provided by the manufacturer, are listed in table 3-1. A three-view drawing is presented in figure 3-1.

Adjustable trim is provided longitudinally by the trailing-edge tab on the elevator and directionally by a bungee. No provisions were made for lateral trim adjustment.

TABLE 3-1
MANUFACTURER'S PHYSICAL CHARACTERISTICS OF THE SUBJECT AIRPLANE

Wing -		
Location	Low
Loading, lb/sq ft	20.2
Airfoil section	NACA 64 ₂ , A215 (modified)
Area, sq ft	178.0
Span, ft	35.98
Mean aerodynamic chord, ft	5.00
Aspect ratio	7.30
Dihedral, deg	5.00
Incidence, deg	2.00
Aerodynamic twist	0
Power -		
Horsepower/engine	160.00
Loading, lb/hp	11.3
Engine	2 Lycoming I0-320-B
Propellers -		
Type	Hartzell HC-E2YL-2A constant speed full feathering	
Blades	7663-4
Diameter, in.	72.00
Weight and balance -		
Maximum gross weight, lb	3600.00
Empty gross weight, lb	2160.00
Allowable center of gravity for maximum gross weight, percent mean aerodynamic chord	12.5 to 28.6
Allowable center of gravity for empty gross weight, percent mean aerodynamic chord	3.3 to 21.6
Control-surface deflection, deg -		
Aileron	18 up, 14 down
Elevator (stabilator).	14 up, 4 down
Rudder	22 right, 20 left
Flap (full)	27
Adjustable trim systems -		
Longitudinal	Tab
Directional	Bungee
Lateral	-----

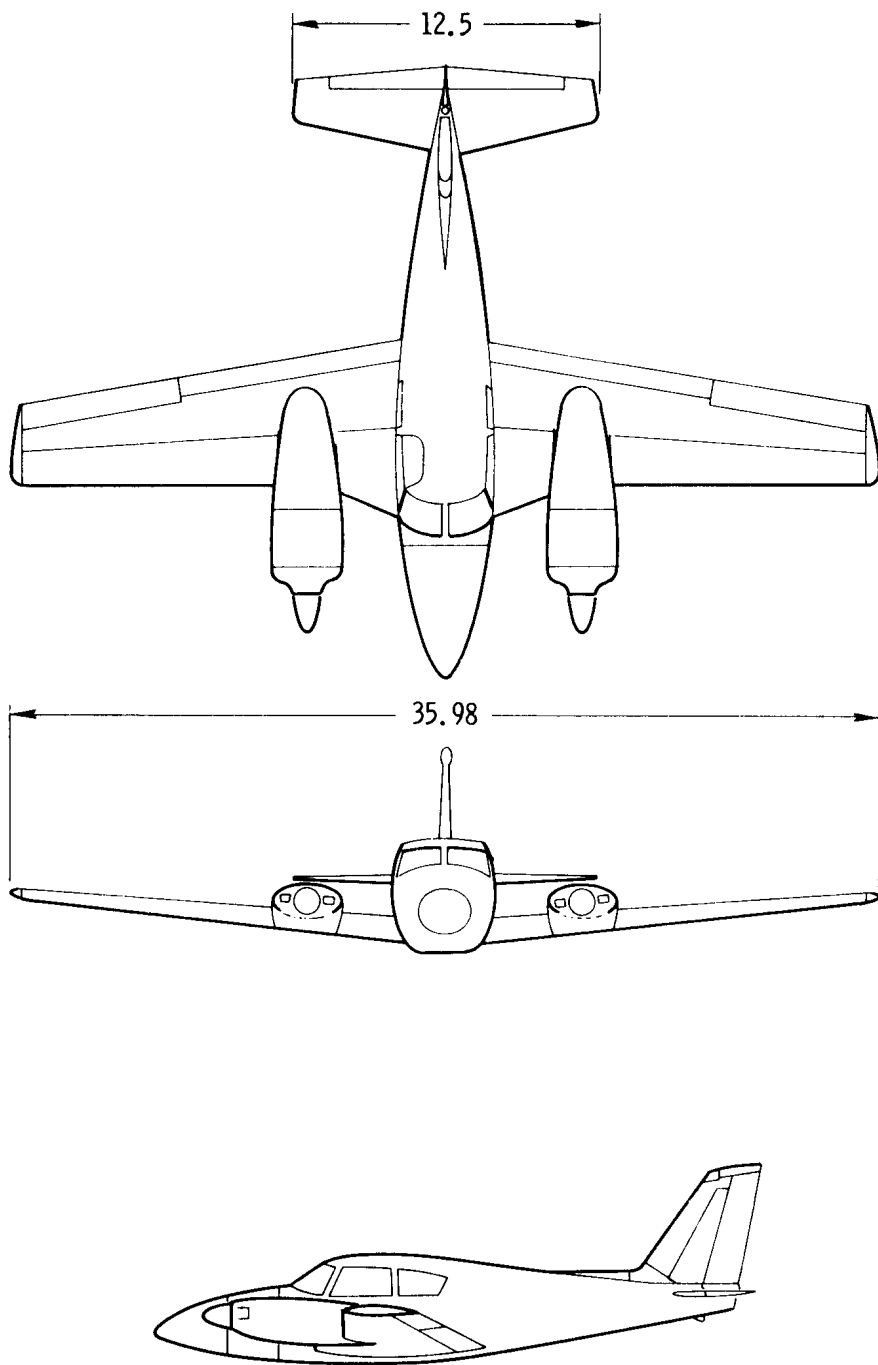


Figure 3-1. Three-view drawing of the test airplane. Dimensions in feet.

3.1 Center-of-Gravity Positions Used in the Analysis

The center of gravity of the airplane, for analytical purposes, was fixed at 10 percent of the wing mean aerodynamic chord and 12 inches below the X-body axis (located on the zero waterline) to conform with the full-scale wind-tunnel data (ref. 2) used in the correlation of analytically predicted characteristics. For preliminary design purposes, a more typical assumption of center-of-gravity position for the start of analysis would be 25 percent of the wing mean aerodynamic chord.

In correlations with flight data, both the analytically predicted characteristics and wind-tunnel data were modified to conform with the 12-percent mean aerodynamic chord center-of-gravity conditions of the flight data.

3.2 Pertinent Geometric Parameters

Figure 3.2-1 shows the geometric parameters associated with the wing and ailerons as well as the general orientation of the wing, ailerons, fuselage, and nacelles. The wing parameters were established in reference 1. Of general interest, and to be considered later, is the proximity of the nacelle relative to the fuselage and the lateral distance of the nacelle from the aileron. The proximity of the nacelle to the fuselage suggests that the curved airflow around the fuselage may interfere with the streamflow on the nacelle during sideslip maneuvers. The lateral position of the nacelle relative to the aileron indicates that the use of a propeller 6 feet in diameter will not immerse any part of the aileron in the propeller slipstream.

Figure 3.2-2 shows the geometric parameters of the fuselage and nacelles pertinent to the analysis of lateral-directional characteristics. Because the design data used in calculating the body and wing-body interference effects were generally based on experimental data obtained from models with axisymmetric bodies, the actual fuselage was replaced by an approximately equivalent circular fuselage as shown. The concept of an equivalent circular fuselage was also used in reference 1.

Figure 3.2-3 shows the geometric parameters of the horizontal tail used to analyze the tail contribution to the damping-in-roll derivative, C_{l_p} . The longitudinal position of the aerodynamic center was used to obtain the effective aspect ratio of the vertical tail.

Figure 3.2-4 shows the geometric parameters required to obtain the effective aspect ratio of the single vertical tail, the lift-curve slope and side force due to sideslip of the tail, and the side force due to rudder deflection. These quantities were basic to the determination of single vertical-tail contribution to lateral-directional stability and control of the airplane. The establishment of the root chord of the vertical tail, c_{r_v} , by extending the leading and trailing edges to the effective centerline of the fuselage, is in accordance with method 1 of reference 3 used to obtain vertical-tail characteristics.

Figure 3.2-5 presents geometric parameters in the XZ plane pertinent to the consideration of power effects on the stability characteristics. The lateral position of the thrust line is shown in figure 3.2-1.

3.2.1 Symbols

A_h, A_v, A_w	aspect ratio of the horizontal tail, vertical tail, and wing, respectively
ac_h, ac_w	aerodynamic center of the horizontal tail and wing, respectively, as a fraction of the mean aerodynamic chord of the surface concerned
b_h, b_v, b_w	span of the horizontal tail, vertical tail, and wing, respectively, in.

c_{fa}	width of the aileron, in.
c_{fr}	width of the rudder, in.
$\left(\frac{c_{fr}}{c_v}\right)_{av}$	average ratio of the rudder chord to the vertical-tail chord
$(c_{fr})_{\eta_i}, (c_{fr})_{\eta_o}$	width of the rudder at the inboard and outboard ends, respectively
c_{rh}, c_{rv}, c_{rw}	root chord of the horizontal tail, vertical tail, and wing, respectively, in.
c_{th}, c_{tv}, c_{tw}	tip chord of the horizontal tail, vertical tail, and wing, respectively, in.
c_v	vertical-tail chord, in.
$(c_v)_h$	vertical-tail chord in the plane of the horizontal tail, in.
$(c_v)_{\eta_i}, (c_v)_{\eta_o}$	chord of the vertical tail at the inboard and outboard edge of the rudder, in.
$\bar{c}_h, \bar{c}_v, \bar{c}_w$	mean aerodynamic chord of the horizontal tail, vertical tail, and wing, respectively, in.
$(d_f)_v$	depth of the fuselage at the quarter-root chord of the vertical tail, in.
d_n	maximum depth of the nacelle forward of the wing leading edge, in.
l_f	length of the fuselage, in.
$l_{n_{eff}}$	effective length of the nacelle (fig. 3.2-2), in.
l_v	distance from the center of gravity to the quarter chord of the vertical-tail mean aerodynamic chord, measured parallel to the X-body axis, in.
$(S_f)_s$	side area of the equivalent circular fuselage, sq ft
S_h, S_v, S_w	area of the horizontal tail, vertical tail, and wing, respectively, sq ft
$(S_{x_n})_{max}$	effective maximum cross-sectional area of a nacelle, assumed to be equal to $\frac{\pi d_n^2}{4(144)}$, sq ft

$(\frac{t}{c})_v, (\frac{t}{c})_w$	thickness ratio of the vertical tail and wing, respectively
$(w_f)_h$	maximum width of the equivalent circular fuselage at the longitudinal station of the quarter-root chord of the exposed horizontal-tail panels, in.
$(w_f)_w$	maximum width of the equivalent circular fuselage at the longitudinal station of the quarter-root chord of the exposed wing panels, in.
$x_{ach(c_v)}_{le}$	distance, parallel to the X-body axis, to the aerodynamic center of the horizontal tail from the leading edge of the vertical-tail chord in the plane of the horizontal tail, in.
x_n	distance, parallel to the X-body axis, from the center of gravity of the airplane to the center of pressure of the nacelle (fig. 3.2-2), in.
x_p	distance, parallel to the X-body axis, from the center of gravity of the airplane to the propeller, in.
$y_{\bar{c}_h}, y_{\bar{c}_w}$	lateral distance from the plane of symmetry to the mean aerodynamic chord of the horizontal tail and the wing, respectively, in.
y_T	lateral distance from the plane of symmetry to the thrust axis, in.
$z_{c_{rh}(c_{rv})}$	vertical distance to the root chord of the horizontal tail from the root chord of the vertical tail, positive down, in.
z_n	vertical distance from the X-body axis to the center of pressure on the effective side area of the nacelle (fig. 3.2-2), positive down, in.
z_p	vertical distance from the X-body axis to the thrust line of the propeller, positive down, in.
z_v	vertical distance from the X-body axis to the mean aerodynamic chord of the vertical tail, positive down, in.
z_w	vertical distance from the X-axis of the equivalent circular fuselage to the quarter chord of the root chord of the exposed wing panel, positive down, in.
z'_w	vertical distance from the X-axis of the airplane to the quarter chord of the root chord of the exposed wing panel, positive down, in.

α_b	angle of attack of the airplane relative to the X-body axis, deg
Γ	geometric dihedral of the wing, deg
Δz_v	vertical distance from the root chord of the vertical tail to the mean aerodynamic chord of the vertical tail, positive down, in.
η_i	ratio of the distance to the inboard edge of the control surface from the root chord of the panel on which the surface is mounted to the panel span
η_o	ratio of the distance to the outboard edge of the control surface from the root chord of the panel on which the surface is mounted to the panel span
$(\Lambda c/2)_v, (\Lambda c/4)_v, (\Lambda l_e)_v$	sweep of the vertical-tail half-chord line, quarter-chord line, and leading edge, respectively, deg
$(\Lambda c/2)_w, (\Lambda c/4)_w, (\Lambda l_e)_w$	sweep of wing half-chord line, quarter-chord line, and leading edge, respectively, deg
$(\Lambda c/4)_h, (\Lambda l_e)_h$	sweep of the horizontal-tail quarter-chord line and leading edge, respectively, deg
$(\Lambda h_l)_a$	sweep of the aileron hinge line, deg
$\lambda_h, \lambda_v, \lambda_w$	taper ratio of the horizontal tail, vertical tail, and wing, respectively
φ_{te}	wing trailing-edge angle, deg

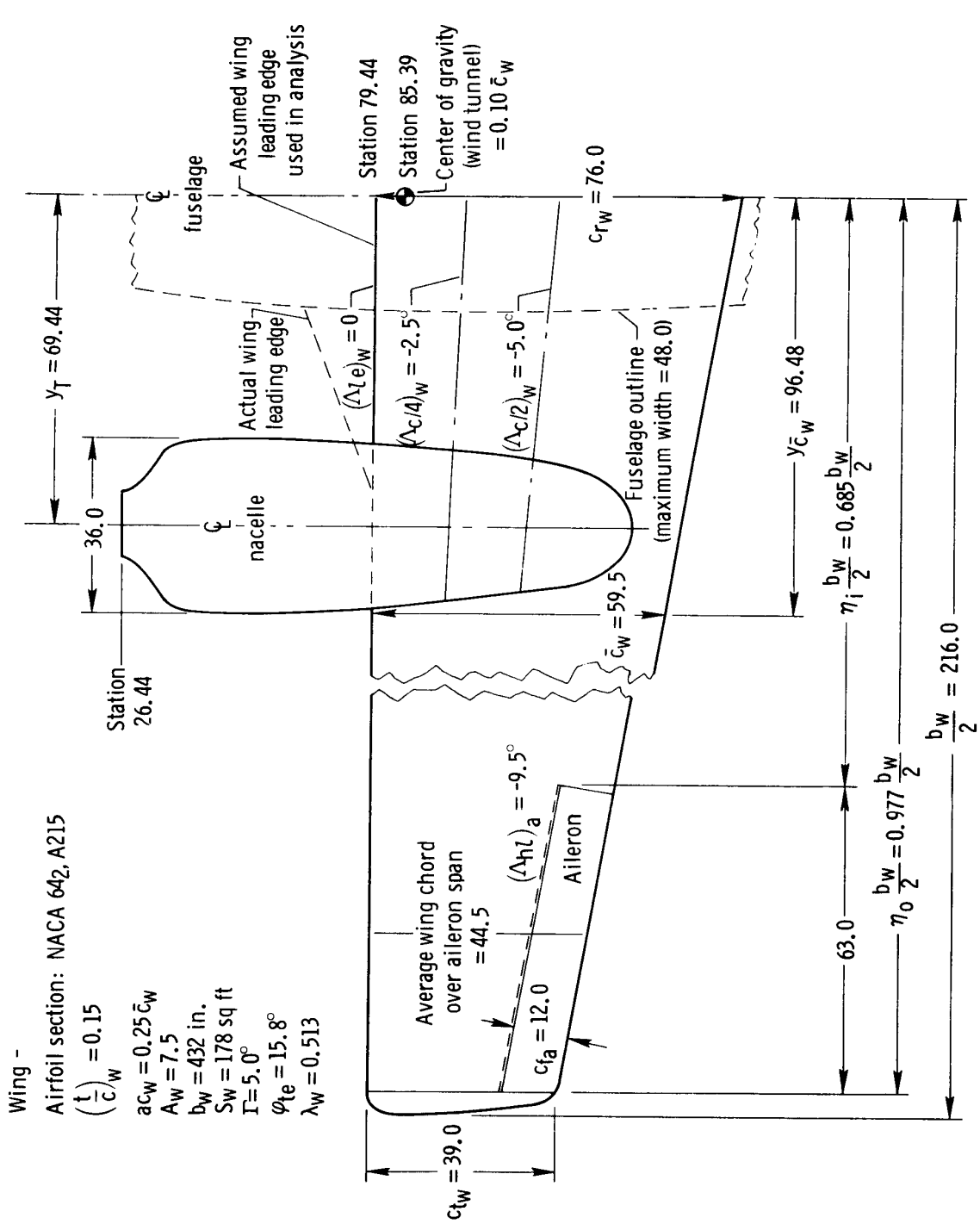


Figure 3.2-1. Geometric relations of wing, ailerons, and nacelle, including geometric parameters of wing and ailerons. Dimensions in inches except as noted.

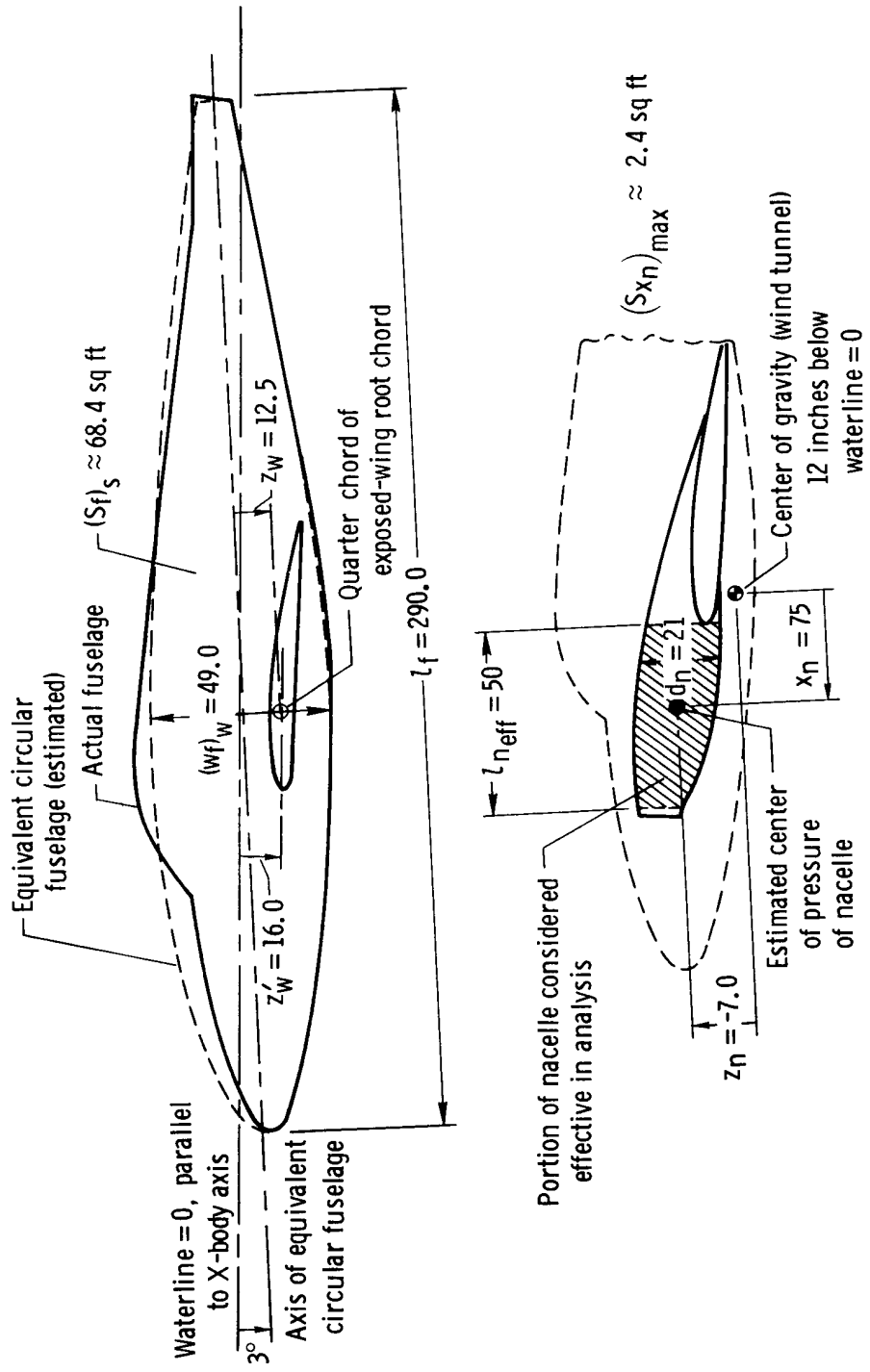


Figure 3.2-2. Geometric parameters of fuselage and nacelle.
Dimensions in inches except as noted.

Horizontal tail -

Airfoil section: NACA 0008

$$a_{ch} = 0.25 \bar{c}_h$$

$$A_h = 4.8$$

$$b_h = 150 \text{ in.}$$

$$S_h = 32.5 \text{ sq ft}$$

$$(w_f)_h = 12 \text{ in.}$$

$$\lambda_h = 0.515$$

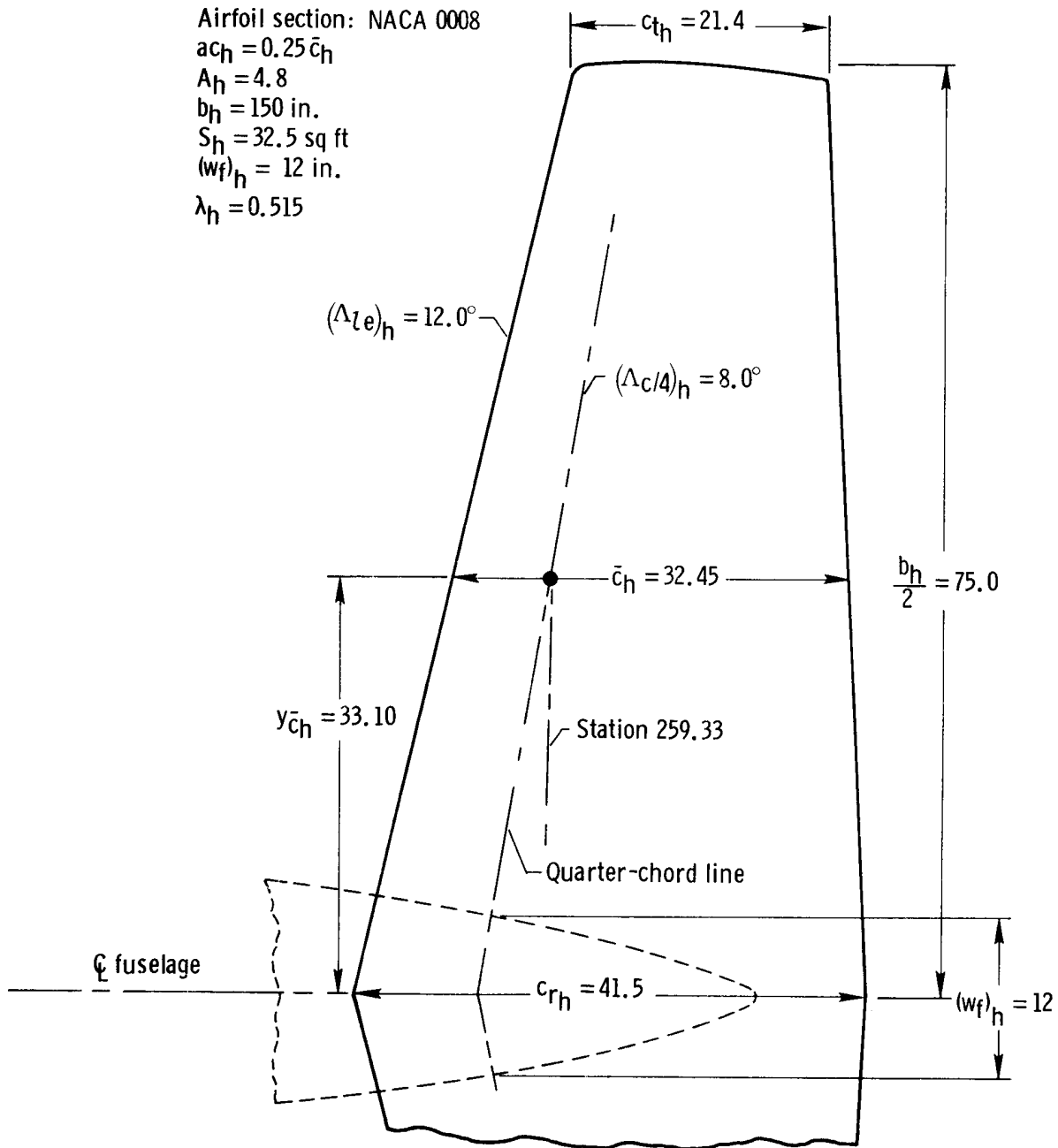


Figure 3.2-3. Geometric parameters of the horizontal tail.
Dimensions in inches except as noted.

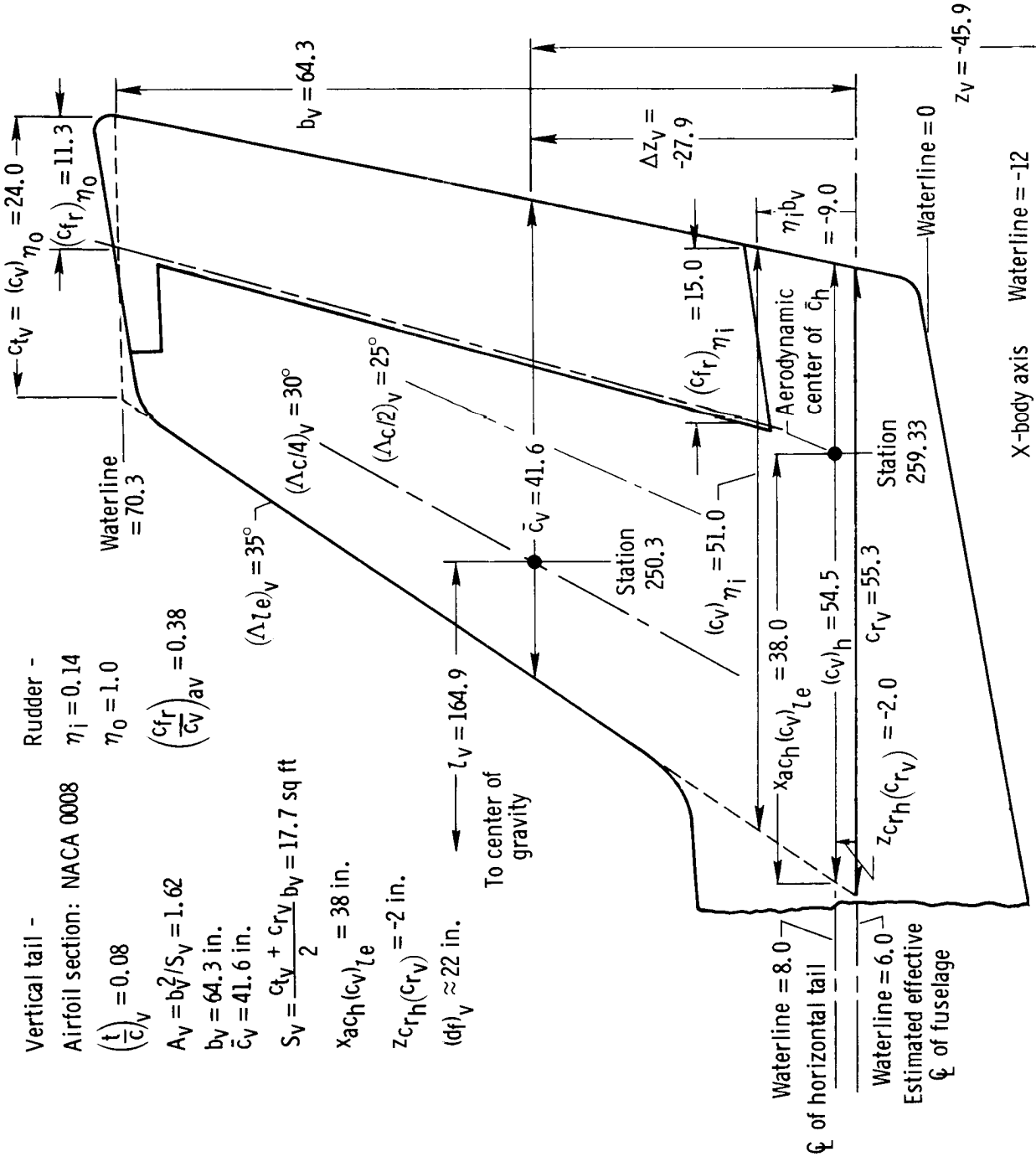


Figure 3.2-4. Geometric parameters of vertical tail and rudder. Dimensions in inches except as noted.

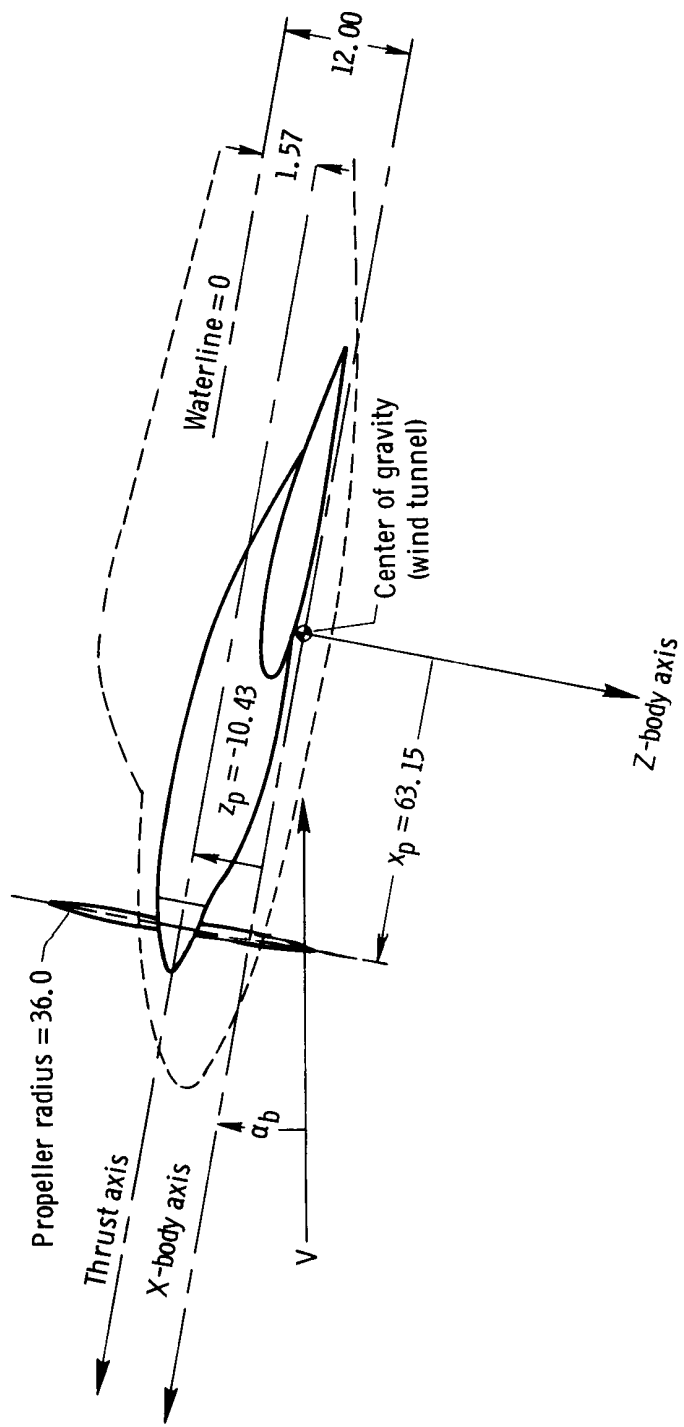


Figure 3.2-5. Longitudinal and vertical orientation of thrust axis relative to body axes. Dimensions in inches.

4. 0 PREDICTION OF PROPELLER-OFF AERODYNAMIC CHARACTERISTICS

4. 1 Side-Force Derivative, $C_{Y\beta}$

The side-force derivative, $C_{Y\beta}$, of the complete airplane in the clean configuration is made up of contributions from the following:

- (1) Wing, including dihedral effects
- (2) Fuselage, including wing-fuselage interference effects
- (3) Nacelles
- (4) Vertical tail, including the interference effects of the wing, fuselage, and horizontal tail

These contributions to $C_{Y\beta}$ can be represented by

$$C_{Y\beta} = (C_{Y\beta})_{w\Gamma=0} + (C_{Y\beta})_\Gamma + K_i (C_{Y\beta})_f + (C_{Y\beta})_n + (C_{Y\beta})_{v(wfh)} \quad (4.1-1)$$

4.1.1 Wing Contribution, $(C_{Y\beta})_{w\Gamma=0} + (C_{Y\beta})_\Gamma$

For subcritical speeds and in the absence of dihedral, the wing contribution to $C_{Y\beta}$ may be obtained from equation (4.1.1-1), the low-speed equation presented in reference 4 (based on strip theory and lifting-line theory) modified to account for the effects of compressibility according to the procedure given in reference 5.

$$(C_{Y\beta})_{w\Gamma=0} = \frac{C_{Lw}^2}{57.3} \left\{ \frac{6 \tan(\Lambda_c/4)_w \sin(\Lambda_c/4)_w}{\pi A_w [A_w B_2 + 4 \cos(\Lambda_c/4)_w]} \right\} \text{per deg} \quad (4.1.1-1)$$

where

C_{Lw} is the lift coefficient of the wing alone from figure 4.1.1-1

A_w is the wing aspect ratio from figure 3.2-1

$(\Lambda_c/4)_w$ is the sweep of the wing quarter-chord line from figure 3.2-1

$$B_2 = \sqrt{1 - M^2 \cos^2 \Lambda_c/4} \quad (4.1.1-2)$$

M is the Mach number

The contribution of the wing dihedral, Γ , to the side-force derivative, $C_{Y\beta}$, can be approximately accounted for at low subsonic speeds by the following expression (from ref. 3):

$$(C_{Y\beta})_\Gamma = -0.0001\Gamma \quad (4.1.1-3)$$

where Γ and β are in degrees.

The preceding expressions show that for general aviation aircraft, for which the wing aspect ratio is of the order of 6 or higher and the quarter-chord sweep is moderate at best, the wing contribution to $C_{Y\beta}$ due to dihedral is the only wing contribution of any significance. As shown in table 4.1.1-1, for the subject airplane

$$(C_{Y\beta})_{w_{\Gamma=0}} = 7.38 \times 10^{-7} C_{L_w}^2 \text{ per deg}$$

$$(C_{Y\beta})_\Gamma = -0.0005 \text{ per deg}$$

The contribution due to dihedral (5° in this instance) is approximately 6.3 percent of the calculated $C_{Y\beta}$ for the complete airplane.

4.1.2 Fuselage Contribution to $C_{Y\beta}$

The fuselage contribution to $C_{Y\beta}$ is composed of the contribution of the fuselage alone plus an increment due to wing-fuselage interference. For subsonic conditions, up to subcritical Mach numbers, the net contribution of the fuselage to $C_{Y\beta}$ in the presence of the wing may be approximated by equation (4.1.2-1) from reference 3. On the basis of wing area, S_w ,

$$(C_{Y\beta})_f = K_i (C_{Y\beta})_{f\bar{V}^{2/3}} \left(\frac{\bar{V}^{2/3}}{S_w} \right) \text{ per deg} \quad (4.1.2-1)$$

where

$(C_{Y\beta})_{f\bar{V}^{2/3}}$ is the contribution of the fuselage alone on the basis of two-thirds fuselage volume and is considered to be equal but of opposite sign to the potential flow portion of the lift-curve slope of the fuselage as obtained from section 4.3 in reference 1

K_i is the wing-fuselage interference factor obtained from figure 4.1.2-1 as a function of only the vertical position of the wing on the body

The interference factor, K_i , is undoubtedly affected by angle of attack as well as wing position on the body. However, until experimental data are assessed on a more

refined basis and presented as a function of angle of attack and wing position, the angle-of-attack effects are not accounted for.

The contribution of the fuselage (including fuselage-wing interference) to $C_{Y\beta}$ of the subject airplane is calculated in table 4. 1. 2-1 to be

$$(C_{Y\beta})_f = -0.00273 \text{ per deg}$$

This contribution is of the order of 34.3 percent of the calculated side-force derivative for the complete airplane (propellers-off).

4.1.3 Nacelles Contribution to $C_{Y\beta}$

The procedure for determining the contribution of the nacelles to $C_{Y\beta}$ is similar to that for determining the contribution of the fuselage. However, a number of uncertainties are involved. No procedures appear to have been established to account for the effects of nacelle size or position relative to the wing and proximity to the fuselage; thus, the following empirical decisions were made for the subject airplane:

- (1) The nacelle's effective length was considered to extend to the wing leading edge only.
- (2) The contribution of a nacelle to $C_{Y\beta}$ may be approximated from equation (4. 1. 3-1), which is based on bodies of circular cross section. The equation is synonymous to the potential-flow part of the lift equation of section 4. 3 of reference 1. On the basis of wing area, S_w ,

$$(C_{Y\beta})_n / \text{Nacelle} = \frac{2(k_2 - k_1)(S_{x_n})_{\max}}{57.3 S_w} \text{ per deg} \quad (4. 1. 3-1)$$

The cross section area of the nacelle, $(S_{x_n})_{\max}$, is an estimated effective area considered to be equal to a circular cross section with a diameter equal to the maximum depth of the nacelle, d_n , as indicated in figure 3. 2-2. The fineness ratio of the nacelle required to obtain $(k_2 - k_1)$ from figure 4. 1. 3-1 (obtained from ref. 6) is based on the effective nacelle length and the maximum depth of the nacelle.

- (3) Because of the proximity of the nacelles to the fuselage and the planform shape of the fuselage in the vicinity of the nacelles, flow interference from the fuselage flow field reduces the $C_{Y\beta}$ contribution of the nacelles. In the absence of design data indicating the extent of the interference, judgment was used in reducing the calculated contribution obtained from equation (4. 1. 3-1) by one-third. Thus, for the subject airplane,

$$(C_{Y\beta})_n \approx -\frac{2}{3} n_n \left[\frac{2(k_2 - k_1)(S_{x_n})_{\max}}{57.3 S_w} \right] \text{ per deg} \quad (4. 1. 3-2)$$

where n_n is the number of nacelles.

On the basis of the summary calculations of table 4.1.3-1, the contribution of the nacelles to $C_{Y\beta}$ is

$$(C_{Y\beta})_n \approx -0.00037 \text{ per deg}$$

This contribution is 4.4 percent of the net calculated $C_{Y\beta}$ of the airplane.

4.1.4 Vertical-Tail Contribution to $C_{Y\beta}$

At subsonic speeds the vertical-tail lift effectiveness, and thus its contribution to $C_{Y\beta}$, is affected by the fuselage crossflow at the tail, the presence of the horizontal tail, and the wing-fuselage sidewash at the vertical tail. All three factors affect the flow on the vertical tail in such a way as to increase its effectiveness.

The characteristics of body crossflow are similar to those of potential flow across a cylinder. Peak local velocity occurs at the top of a cylinder and decays to free-stream crossflow with distance away from the cylinder surface. Thus, tail-body combinations with large bodies and small tails have a greater effectiveness per unit of tail area than combinations with small bodies and large tails (ref. 3).

Horizontal-tail surfaces in the high or low position in the vicinity of the vertical tail increase the pressure loading of the vertical surface. Horizontal surfaces in the mid-span position have relatively little effect (ref. 3).

Sidewash from the wing in sideslip is small compared to the body sidewash due to sideslip. Above the wing-wake centerline, the wing-induced sidewash moves inboard and is stabilizing; below the wing-wake centerline, it moves outboard. A body in sideslip creates a body vortex system, which in turn induces lateral velocity components at the vertical tail. Above or below the body, the body-induced sidewash moves inboard and is stabilizing. For conventional aircraft, the combination of wing-body sidewash flow fields has negligible sidewash effect below the wake centerline.

Of the two procedures presented in reference 3 for obtaining the vertical-tail contribution to $C_{Y\beta}$ (for a single-tail configuration) in the presence of the wing, body, and horizontal tail, only the first is flexible enough to take into account the effects of the horizontal tail mounted on the vertical tail away from the body. This method is used herein. To obtain an effective aspect ratio, it makes use of empirical design charts, based on experimental data, which account for body crossflow and horizontal-tail effects on the vertical-tail lift-curve slope. The effective aspect ratio is then used in conjunction with section lift-curve slope to obtain the net lift-curve slope of the tail. The sidewash effects are then introduced to obtain the vertical-tail contribution to $C_{Y\beta}$.

4.1.4-1 Effective Aspect Ratio of the Vertical Tail, $A_{v\text{eff}}$

To determine the effective aspect ratio of the vertical tail in the single-tail

configuration, the vertical-tail geometric parameters must be determined first. (They are listed in figure 3.2-4 for the subject airplane.)

The effective aspect ratio of the vertical tail in the presence of the body and horizontal tail is obtained from

$$A_{V\text{eff}} = A_V \left(\frac{A_{V(f)}}{A_V} \right) \left\{ 1 + K_h \left[\frac{A_{V(fh)}}{A_{V(f)}} - 1 \right] \right\} \quad (4.1.4-1)$$

where

A_V is the geometric aspect ratio of the isolated vertical tail, obtained from figure 3.2-4

$\frac{A_{V(f)}}{A_V}$ is the ratio of the aspect ratio of the vertical tail in the presence of the body to that of the isolated panel, obtained from figure 4.1.4-1(a) using geometric parameters from figure 3.2-4

$\frac{A_{V(fh)}}{A_{V(f)}}$ is the ratio of the aspect ratio of the vertical tail in the presence of the body and horizontal tail to that of the vertical tail in the presence of the body only, obtained from figure 4.1.4-1(b) using geometric parameters from figure 3.2-4

K_h is a factor accounting for the relative size of the horizontal and vertical tails, obtained from figure 4.1.4-1(c) using horizontal- and vertical-tail areas obtained from figures 3.2-3 and 3.2-4, respectively

For the subject airplane, the summary calculations of table 4.1.4-1(a) show that $A_{V\text{eff}} = 2.67$. In this instance, the horizontal tail is practically coincident with the root chord of the vertical tail (fig. 3.2-4), so the effective aspect ratio is similar to the value that would be obtained using reflection plane principles.

4.1.4-2 Lift-Curve Slope of the Vertical-Tail Panel, $(C_{La})_{v(fh)}$

The lift-curve slope of the single vertical tail in the presence of the fuselage and horizontal tail may be obtained from the following equation. The equation is synonymous with equation (4.2-1) in reference 1. On the basis of the effective vertical-tail area, S_V ,

$$\frac{(C_{La})_{V(fh)}}{A_{V\text{eff}}} = \frac{2\pi}{2 + \sqrt{\frac{(A_{V\text{eff}})^2}{k_V^2} \left[B_1^2 + \tan^2(\Lambda_c/2)_V \right] + 4}} \quad (4.1.4-2)$$

where

$$k_v = \frac{(c_l \alpha)_v}{2\pi} \quad (4.1.4-3)$$

$(c_l \alpha)_v$ is the section lift-curve slope, obtained from section 4.1 in reference 1

$$B_1^2 = 1 - M^2 \quad (4.1.4-4)$$

M is the Mach number

$(\Lambda c/2)_v$ is the sweepback of the vertical-tail half-chord line

For the subject airplane, the summary calculations of table 4.1.4-1(b) show that

$$(C_{L\alpha})_{v(fh)} = 3.01 \text{ per rad} = 0.0525 \text{ per deg}$$

on the basis of $S_v = 17.7$ sq ft.

4.1.4-3 Summary of Vertical-Tail Contribution to $C_{Y\beta}$

The single vertical-tail contribution to $C_{Y\beta}$ is obtained by modifying the single vertical-tail lift curve to account for the effects of wing wake and body sidewash. Thus, in the presence of the wing, body, and horizontal tail, and on the basis of reference 3,

$$(C_{Y\beta})_{v(wfh)} = -k'_1 (C_{L\alpha})_{v(fh)} \left(1 + \frac{\partial \sigma}{\partial \beta}\right) \frac{\bar{q}_v}{\bar{q}_\infty} \frac{S_v}{S_w} \quad (4.1.4-5)$$

where

k'_1 is a factor accounting for the body size relative to the vertical-tail size represented by $\frac{b_v}{(d_f)_v}$ (fig. 3.2-4), obtained from figure 4.1.4-1(d) using tail geometric parameters from figure 3.2-4

The combined effects of wing wake, body sidewash, and dynamic pressure can be approximated from empirical equation (4.1.4-6) from reference 3. A qualitative insight into the angle-of-attack range of applicability of the equation may be obtained from figure 4.1.4-2 (from ref. 7). The figure shows wind-tunnel-determined sidewash characteristics of straight- and swept-wing models with the wings in three vertical positions.

$$\left(1 + \frac{\partial\sigma}{\partial\beta}\right) \frac{\bar{q}_v}{\bar{q}_\infty} = 0.724 + 3.06 \frac{\frac{S_v}{S_w}}{1 + \cos(\Lambda_c/4)} + 0.4 \frac{z_w}{(w_f)_w} + 0.009 A_w \quad (4.1.4-6)$$

where

$(\Lambda_c/4)_v$ is the sweep of the quarter-chord line of the vertical tail, obtained from figure 3.2-4

z_w is the vertical distance from the centerline of the equivalent fuselage to the quarter-chord point of the root chord of the exposed wing panel, obtained from figure 3.2-2

$(w_f)_w$ is the depth of the equivalent circular fuselage at the wing, obtained from figure 3.2-2

For the subject airplane, the summary calculations in table 4.1.4-1(c) indicate the vertical-tail contribution to $C_{Y\beta}$ to be, on the basis of $S_w = 178$ sq ft,

$$(C_{Y\beta})_{v(wfh)} = -0.0049 \text{ per deg}$$

which is of the order of 54.7 percent of the calculated $C_{Y\beta}$ for the complete airplane.

For a twin-vertical-tail configuration, the contribution of the twin tails to $C_{Y\beta}$ may be obtained from the design charts shown in figure 4.1.4-3. The charts are reproduced from reference 3. On the basis of these charts, which include the effects of wing-body wake and sidewash,

$$(C_{Y\beta})_{v(wfh)} = - \left[\frac{(C_{Y\beta})_{v(wfh)}}{(C_{Y\beta})_{v_{eff}}} \right] (C_{Y\beta})_{v_{eff}} \frac{2S_v}{S_w} \quad (4.1.4-7)$$

where

$(C_{Y\beta})_{v_{eff}}$ is the lift-curve slope of one vertical-tail panel, obtained from figure 4.1.4-3, based on the panel area, S_v

$\left[\frac{(C_{Y\beta})_{v(wfh)}}{(C_{Y\beta})_{v_{eff}}} \right]$ is obtained from figure 4.1.4-3

4.1.5 $C_{Y\beta}$ of the Complete Airplane

The side-force-due-to-sideslip derivative, $C_{Y\beta}$, of the subject airplane (obtained

from table 4.1.5-1 on the basis of the contributions of the components as summarized in eq. (4.1-1) was calculated to be

$$\left(C_{Y\beta} \right)_{\substack{\text{prop} \\ \text{off}}} = -0.0085 \text{ per deg}$$

This result shows reasonably good correlation with full-scale wind-tunnel data (fig. 4.1.5-1). Calculated values are less accurate than wind-tunnel data, probably because they do not reflect the effects of angle of attack on wing-body interference and sidewash on the vertical tail.

4.1.6 Symbols

A_v	geometric aspect ratio of the isolated vertical tail, obtained from figure 3.2-4
$A_{v\text{eff}}$	effective aspect ratio of the vertical tail in the presence of the fuselage and the horizontal tail, obtained from equation (4.1.4-1) for single-tail configurations and from figure 4.1.4-3 for twin-vertical-tail configurations
$\frac{A_v(f)}{A_v}$	ratio of the aspect ratio of a single vertical tail in the presence of the fuselage to that of the isolated tail, obtained from figure 4.1.4-1(a) with geometric parameters from figure 3.2-4
$\frac{A_{v(fh)}}{A_{v(f)}}$	ratio of the aspect ratio of the vertical tail in the presence of the fuselage and the horizontal tail to that of the vertical tail in the presence of the fuselage, obtained from figure 4.1.4-1(b)
A_w	aspect ratio of the wing
$B_1 = (1 - M^2)^{1/2}$	
$B_2 = (1 - M^2 \cos^2 \Lambda_c / 4)^{1/2}$	
b_h, b_v	span of the horizontal and vertical tail, respectively, in.
b'_v	span of the twin vertical tail from the horizontal tail to the upper tip of the vertical tail, in.
C_{L_w}	wing-lift coefficient
$(C_{L\alpha})_{f\bar{V}^{2/3}}$	fuselage lift-curve slope due to potential flow, referred to the two-thirds power of the fuselage volume, per deg

$(C_{L\alpha})_{v(fh)}$	vertical-tail lift-curve slope in the presence of the fuselage and horizontal tail, referred to the tail area, per deg
$C_{Y\beta}$	variation of the side-force coefficient with sideslip angle, per deg
$(C_{Y\beta})_f$	fuselage contribution to $C_{Y\beta}$ including wing-body interference, referred to the wing area, per deg
$(C_{Y\beta})_{f\bar{V}^{2/3}}$	isolated fuselage contribution to $C_{Y\beta}$ due to potential flow, considered to be equal to $(C_{L\alpha})_{f\bar{V}^{2/3}}$ for the equivalent circular fuselage
$(C_{Y\beta})_n$	contribution of both nacelles to $C_{Y\beta}$, referred to wing area, per deg
$(C_{Y\beta})_{prop\ off}$	$C_{Y\beta}$ of the complete airplane with propellers off, per deg
$(C_{Y\beta})_{v_{eff}}$	lift-curve slope of one vertical-tail panel in the twin-vertical-tail configuration, obtained from figure 4.1.4-3 based on the area of one panel
$(C_{Y\beta})_{v(wfh)}$	contribution of the vertical tail to $C_{Y\beta}$ in the presence of the wing, fuselage, and horizontal tail, referred to the wing area, per deg
$(C_{Y\beta})_{w_{\Gamma=0}}$	contribution of the wing to $C_{Y\beta}$ in the absence of geometric dihedral, per deg
$(C_{Y\beta})_\Gamma$	contribution of the wing dihedral to $C_{Y\beta}$, per deg
$(c_l)_v$	section lift-curve slope of the vertical tail, per rad
$(c_v)_h$	vertical-tail chord in the plane of the horizontal tail, in.
$(d_f)_{max}$	maximum diameter of the equivalent circular fuselage, obtained from figure 3.2-2, in.
$(d_f)_v$	depth of the fuselage at the quarter-root chord of the vertical tail, obtained from figure 3.2-4, in.
d_n	maximum depth of the nacelle forward of the wing leading edge, obtained from figure 3.2-2, in.

$f(\alpha)$	function of angle of attack
K_h	factor accounting for the relative size of the horizontal and vertical tails, obtained from figure 4.1.4-1
K_i	wing-fuselage interference factor, obtained from figure 4.1.2-1
$k_v = \frac{(c_l \alpha)_v}{2\pi}$	
k'_1	factor accounting for the body size relative to the vertical-tail size, obtained from figure 4.1.4-1(d)
$k_2 - k_1$	reduced mass factor, from potential-flow theory, obtained from figure 4.1.3-1 as a function of fineness ratio
l_f	length of the fuselage, in.
l_n	effective length of the nacelle to the leading edge of the wing, in.
M	Mach number
n_n	number of nacelles
\bar{q}_v	effective dynamic pressure at the vertical tail, lb/sq ft
\bar{q}_∞	free-stream dynamic pressure, lb/sq ft
S_h, S_v, S_w	area of the horizontal tail, vertical tail, and wing, respectively, sq ft
$(S_{x_n})_{max}$	effective maximum cross-sectional area of the nacelle, $\frac{\pi d_n^2}{4(144)}, \text{ sq ft}$
T	thrust of propellers, lb
T'_c	thrust coefficient, $\frac{T}{\bar{q}_\infty S_w}$
$\bar{V}^{2/3}$	two-thirds power of the fuselage volume, sq ft
$(w_f)_w$	depth of the equivalent circular fuselage at the wing, in.
$x_{ach}(c_v)_{le}$	distance to the aerodynamic center of the horizontal tail from the leading edge of the vertical-tail chord in the plane of the horizontal tail, in.

$z_{cr_h}(c_{rv})$	vertical distance to the root chord of the horizontal tail from the root chord of the vertical tail, positive down, in.
z_w	vertical distance from the centerline of the equivalent circular fuselage to the quarter-root chord of the exposed wing panels, positive down, in.
α_b	angle of attack of the airplane relative to the X-body axis, deg
β	sideslip angle, deg
Γ	wing geometric dihedral angle, deg
$(\Lambda_c/2)_v, (\Lambda_c/4)_v$	sweep of the vertical-tail half-chord and quarter-chord line, respectively, deg
$\Lambda_c/4$	sweep of the quarter-chord line, deg
$(\Lambda_c/4)_w$	sweep of the wing quarter-chord line, deg
λ_v	vertical-tail taper ratio
φ_{te}	trailing-edge angle, deg
$\frac{\partial \sigma}{\partial \beta}$	rate of change of the sidewash at the vertical tail with sideslip

TABLE 4.1.1-1

WING CONTRIBUTION TO $C_{Y\beta}$

$$(C_{Y\beta})_{w\Gamma=0} + (C_{Y\beta})_\Gamma = \frac{C_{L_w}^2}{57.3} \left[\frac{6 \tan \Lambda_c/4 \sin \Lambda_c/4}{\pi A_w (A_w B_2 + 4 \cos \Lambda_c/4)} \right] - 0.0001\Gamma$$

Symbol	Description	Reference	Magnitude
M	Mach number	Wind-tunnel Mach number	0.083
A_w	Wing aspect ratio	Figure 3.2-1	7.5
$(\Lambda_c/4)_w$	Sweep of wing quarter-chord line, deg	Figure 3.2-1	-2.5
Γ	Wing dihedral, deg	Figure 3.2-1	5.0
C_{L_w}	Wing-lift coefficient	Figure 4.1.1-1	$f(\alpha)$
Summary: $(C_{Y\beta})_{w\Gamma=0} + (C_{Y\beta})_\Gamma = 7.38 \times 10^{-7} C_{L_w}^2 - 0.0005 \text{ per deg}$			

TABLE 4.1.2-1

FUSELAGE CONTRIBUTION TO $C_{Y\beta}$

$$(C_{Y\beta})_f = K_i (C_{Y\beta})_{f\bar{V}^{2/3}} \left(\frac{\bar{V}^{2/3}}{S_w} \right)$$

Symbol	Description	Reference	Magnitude
$\frac{2z_w}{(wf)_w}$	Wing-body position parameter for obtaining K_i	Figure 3.2-2	0.51
K_i	Wing-body interference factor	Figure 4.1.2-1	1.25
$(C_{Y\beta})_{f\bar{V}^{2/3}}$	$C_{Y\beta}$ of equivalent axisymmetric fuselage on basis of $\bar{V}^{2/3}$ (considered equal but opposite in sign to $(C_{L\alpha})_{f\bar{V}^{2/3}}$ based on potential flow term only), per deg	Table 4.3-1 of reference 1	-0.01256
$\bar{V}^{2/3}$	Fuselage volume to two-thirds power	Table 4.3-1 of reference 1	31.0
S_w	Reference wing area, sq ft	Figure 3.2-1	178.0
Summary: $(C_{Y\beta})_f = -0.00273 \text{ per deg on basis of } S_w = 178 \text{ sq ft}$			

TABLE 4. 1. 3-1
NACELLES CONTRIBUTION TO C_{Y_β}

$$(C_{Y_\beta})_n = -\frac{2}{3} n_n \left[\frac{2(k_2 - k_1) (S_{x_n})_{max}}{57.3 S_w} \right]$$

Symbol	Description	Reference	Magnitude
n_n	Number of nacelles	-----	2
S_w	Reference wing area, sq ft	Figure 3.2-1	178.0
$(S_{x_n})_{max}$	Effective cross-sectional area of nacelle, sq ft	Figure 3.2-2	2.40
$\frac{l_n}{d_n}$	Effective fineness ratio of nacelle	Figure 3.2-2	2.38
$(k_2 - k_1)$	Reduced mass factor of nacelle	Figure 4.1.3-1	.59
Summary: $(C_{Y_\beta})_n = -0.00037$ per deg on basis of $S_w = 178$ sq ft			

TABLE 4.1.4-1
VERTICAL-TAIL CONTRIBUTION TO $C_{Y\beta}$

(a) Effective aspect ratio, $A_{V\text{eff}}$

$$A_{V\text{eff}} = A_V \left(\frac{A_V(f)}{A_V} \right) \left\{ 1 + K_h \left[\frac{A_V(fh)}{A_V(f)} - 1 \right] \right\}$$

Symbol	Description	Reference	Magnitude
S_h	Horizontal-tail area, sq ft	Figure 3.2-3	32.5
S_v	Vertical-tail area, sq ft	Figure 3.2-4	17.7
b_v	Vertical-tail span, in.	Figure 3.2-4	64.3
A_v	Vertical-tail aspect ratio	Figure 3.2-4	1.62
$(c_v)_h$	Vertical-tail chord in plane of horizontal tail, in.	Figure 3.2-4	54.5
$x_{ac_h(c_v)}l_e$	Distance to aerodynamic center of horizontal tail from leading edge of vertical-tail chord in plane of horizontal tail, in.	Figure 3.2-4	38.0
$z_{cr_h(c_{rv})}$	Distance to root chord of horizontal tail from root chord of vertical tail, in.	Figure 3.2-4	-2.0
$(df)_v$	Depth of fuselage at quarter-root chord of vertical tail, in.	Figure 3.2-4	≈ 22.0
λ_v	Vertical-tail taper ratio	Figure 3.2-4	0.433
$\frac{b_v}{(df)_v}$	-----	-----	2.92
$\frac{A_v(f)}{A_v}$	Ratio of aspect ratio of vertical tail in presence of body to tail alone	Figure 4.1.4-1(a)	1.36
$\frac{x_{ac_h(c_v)}l_e}{(c_v)_h}$	Parameter accounting for relative positions of horizontal and vertical tails	-----	0.698
$\frac{z_{cr_h(c_{rv})}}{b_v}$	Parameter accounting for relative positions of horizontal and vertical tails	-----	-0.031
$\frac{A_v(fh)}{A_v(f)}$	Ratio of aspect ratio of vertical tail in presence of body and horizontal tail to that of vertical tail alone	Figure 4.1.4-1(b)	1.19
$\frac{S_h}{S_v}$	Ratio of horizontal- to vertical-tail areas	-----	1.84
K_h	Factor accounting for relative size of horizontal and vertical tails	Figure 4.1.4-1(c)	1.11
Summary: $A_{V\text{eff}} = 2.67$			

TABLE 4.1.4-1 (Concluded)

(b) Lift-curve slope of the vertical tail, $(C_{L\alpha})_{v(fh)}$

$$(C_{L\alpha})_{v(fh)} = A_{v\text{eff}} \frac{\frac{2\pi}{2 + \sqrt{\frac{A_{v\text{eff}}^2}{k_v^2} [B_1^2 + \tan^2(\Lambda_c/2)_v] + 4}}}$$

Symbol	Description	Reference	Magnitude
M	Mach number	Wind-tunnel tests	0.083
B_1^2	$1 - M^2$	-----	.993
$A_{v\text{eff}}$	Effective aspect ratio of vertical tail	Table 4.1.4-1(a)	2.67
$(\Lambda_c/2)_v$	Sweepback of vertical-tail half-chord line, deg	Figure 3.2-4	25
$(C_{L\alpha})_v$	Section lift-curve slope of vertical tail, per rad (same as for horizontal tail; both have NACA 0008 sections)	Table 4.1-1 in reference 1	6.25
k_v	$\frac{(C_{L\alpha})_v}{2\pi}$	-----	.995
Summary: $(C_{L\alpha})_{v(fh)} = 3.01 \text{ per rad} = 0.0525 \text{ per deg based on } S_v = 17.7 \text{ sq ft}$			

(c) Vertical-tail contribution to $C_{Y\beta}$

$$(C_{Y\beta})_{v(wfh)} = -k'_1 (C_{L\alpha})_{v(fh)} \left(1 + \frac{\partial \sigma}{\partial \beta} \right) \frac{\bar{q}_v}{\bar{q}_\infty} \frac{S_v}{S_w}$$

where

$$\left(1 + \frac{\partial \sigma}{\partial \beta} \right) \frac{\bar{q}_v}{\bar{q}_\infty} = 0.724 + 3.06 \frac{S_v}{S_w} \frac{1 + \cos(\Lambda_c/4)_v}{1 + \cos(\Lambda_c/4)_v} + 0.4 \frac{z_w}{(w_f)_w} + 0.009 A_w$$

Symbol	Description	Reference	Magnitude
S_w	Reference wing area, sq ft	Figure 3.2-1	178.0
S_v	Vertical-tail area, sq ft	Figure 3.2-4	17.7
$(\Lambda_c/4)_v$	Sweepback of vertical-tail quarter-chord line, deg	Figure 3.2-4	30.0
z_w	Distance from equivalent fuselage centerline to the wing root quarter chord, in.	Figure 3.2-2	12.5
$(w_f)_w$	Maximum depth of equivalent fuselage at the wing, in.	Figure 3.2-2	49.0
A_w	Aspect ratio of the wing	Figure 3.2-1	7.5
$\left(1 + \frac{\partial \sigma}{\partial \beta} \right) \frac{\bar{q}_v}{\bar{q}_\infty}$	Wing wake and fuselage sidewash factor	Equation (4.1.4-6)	1.054
$\frac{b_v}{(d_f)_v}$	-----	Table 4.1.4-1(a)	2.92
k'_1	Empirical correlation factor	Figure 4.1.4-1(d)	.889
$(C_{L\alpha})_{v(fh)}$	Lift-curve slope of vertical tail in presence of body and horizontal tail	Table 4.1.4-1(b)	0.0525
Summary: $(C_{Y\beta})_{v(wfh)} = -0.00490 \text{ per deg based on } S_w = 178.0 \text{ sq ft}$			

TABLE 4.1.5-1
 $C_{Y\beta}$ OF THE COMPLETE AIRPLANE

$$(C_{Y\beta})_{\text{prop off}} = (C_{Y\beta})_{w\Gamma=0} + (C_{Y\beta})_{\Gamma} + K_i(C_{Y\beta})_f + (C_{Y\beta})_n + (C_{Y\beta})_{v(wfh)} \text{ per deg}$$

Symbol	Description	Reference	Magnitude
$(C_{Y\beta})_{w\Gamma=0}$	Contribution of wing without dihedral	Table 4.1.1-1	$7.38 \times 10^{-7} C_{Lw}^2$
$(C_{Y\beta})_{\Gamma}$	Contribution of wing dihedral	Table 4.1.1-1	-.00050
$K_i(C_{Y\beta})_f$	Contribution of fuselage and fuselage-wing interference	Table 4.1.2-1	-.00273
$(C_{Y\beta})_n$	Contribution of nacelles	Table 4.1.3-1	-.00037
$(C_{Y\beta})_{v(wfh)}$	Contribution of vertical tail in presence of wing, body, and horizontal tail	Table 4.1.4-1(c)	-.0049
Summary: $(C_{Y\beta})_{\text{prop off}} \approx -0.0085 \text{ per deg}$			

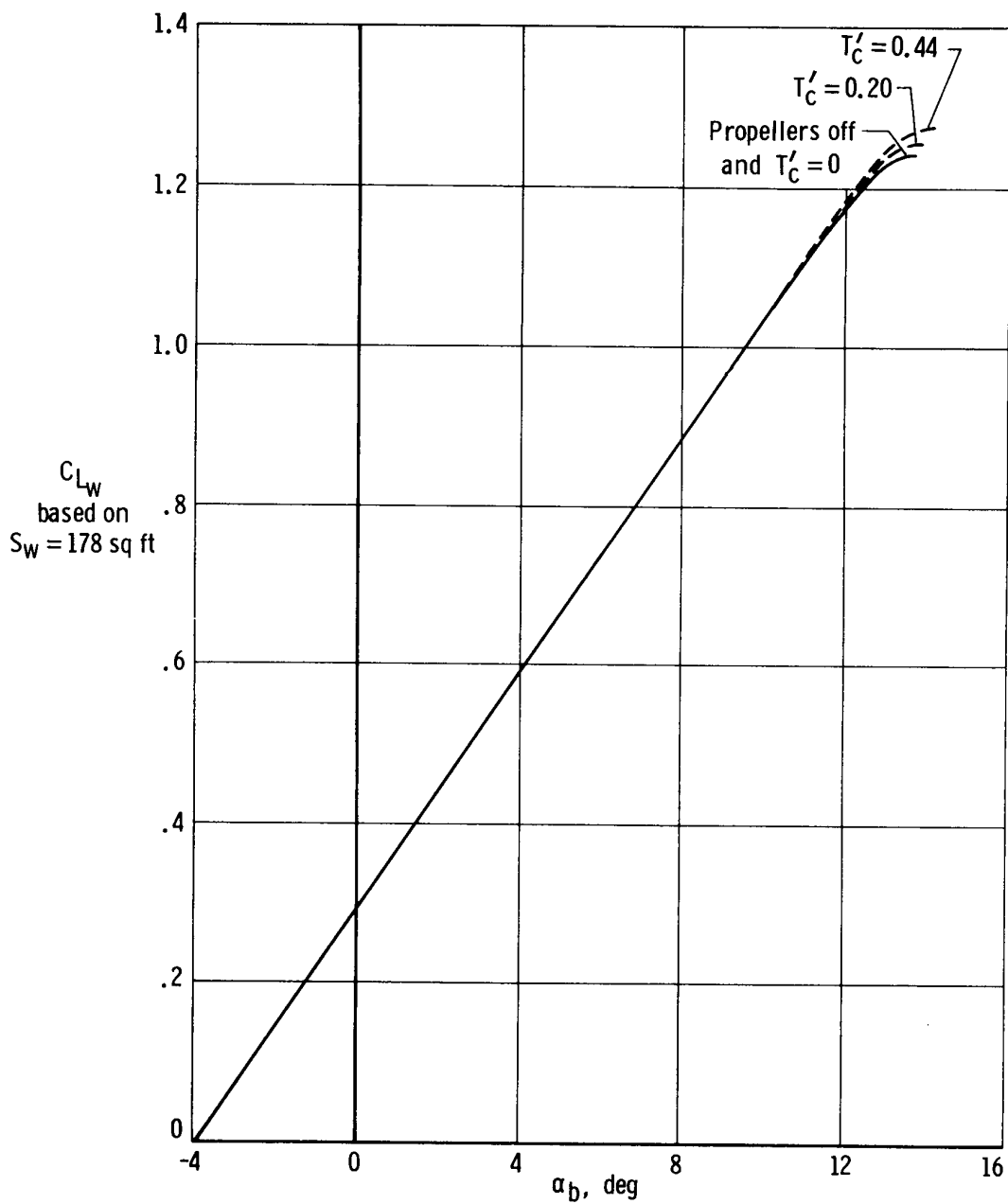


Figure 4.1.1-1. Propeller-off lift characteristics of subject airplane for wing-alone condition with stall extended to power-on stall angles (from fig. 5.1.1-8 of ref. 1).

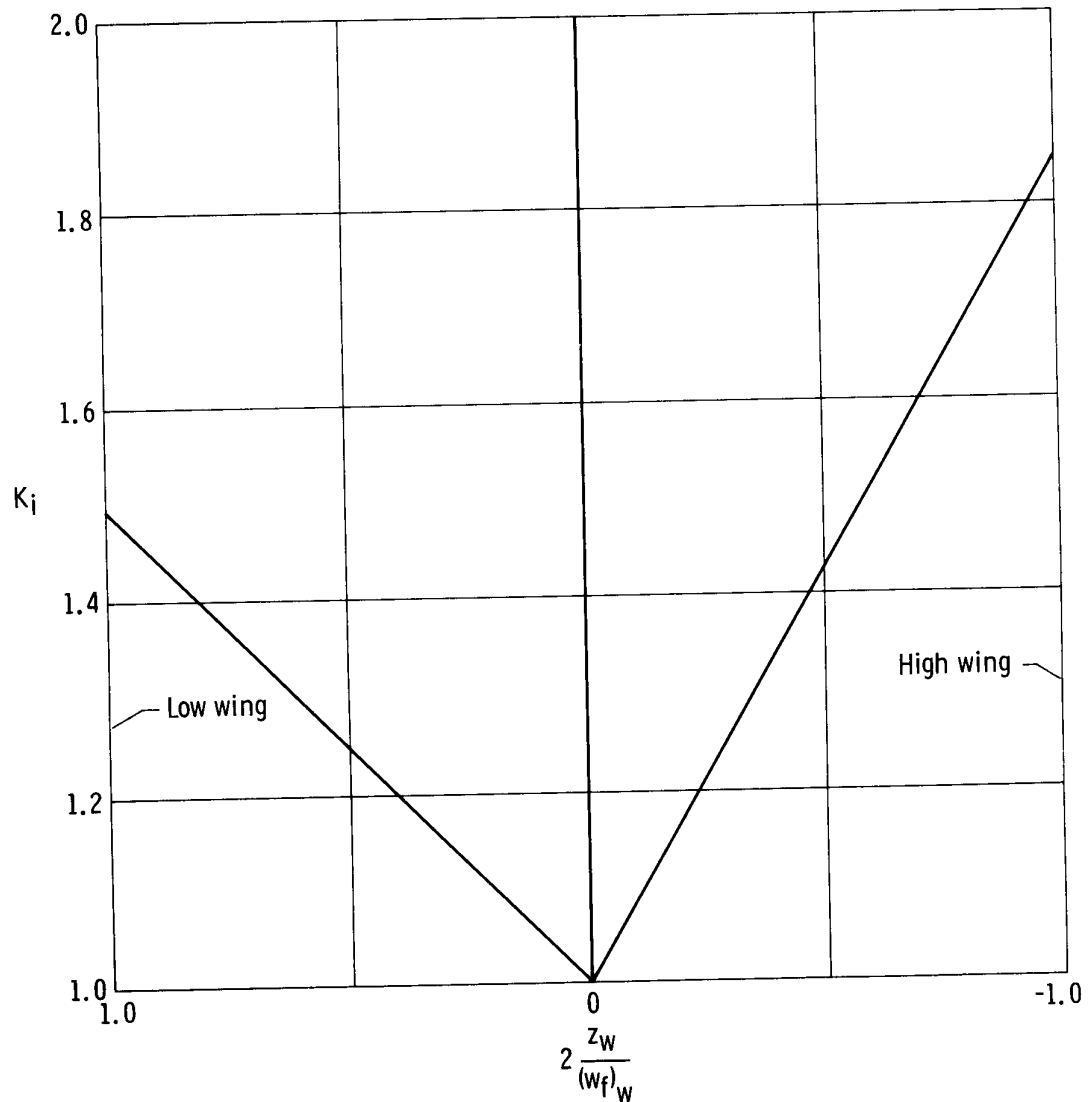


Figure 4.1.2-1. Wing-body interference factor for wing-body side-force derivative, $C_{Y\beta}$ (from ref. 3).

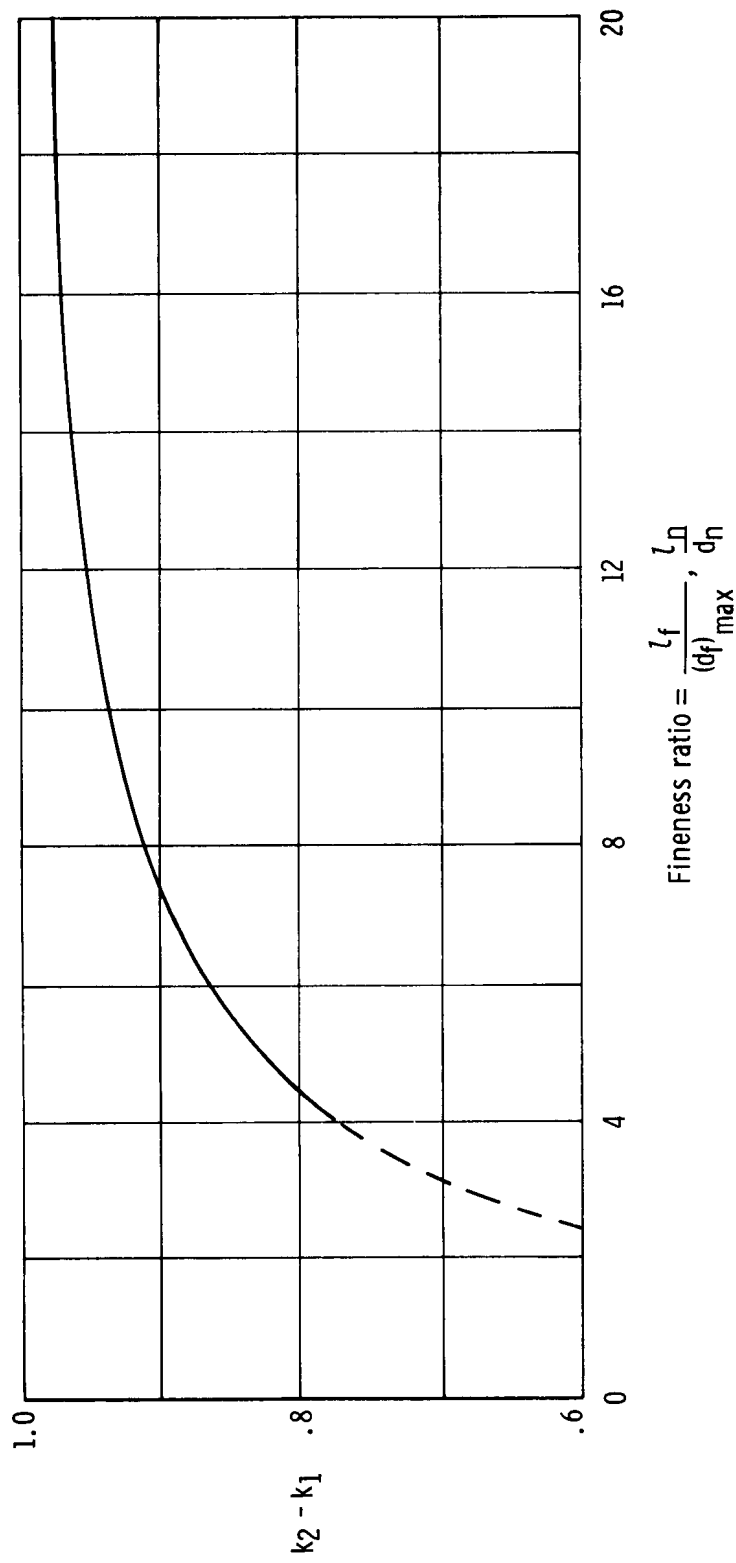
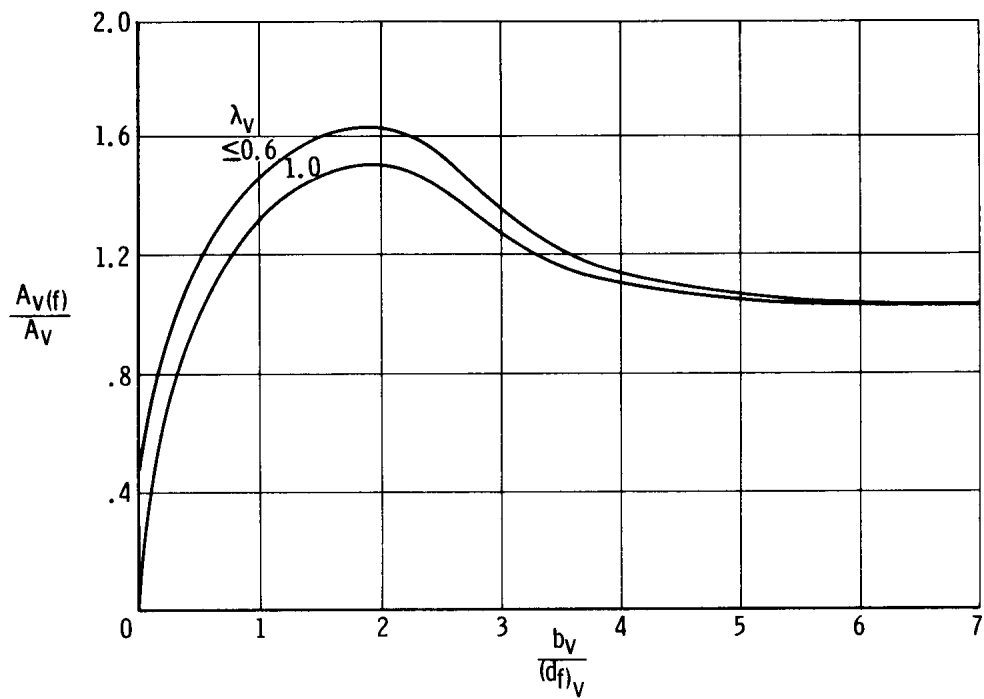
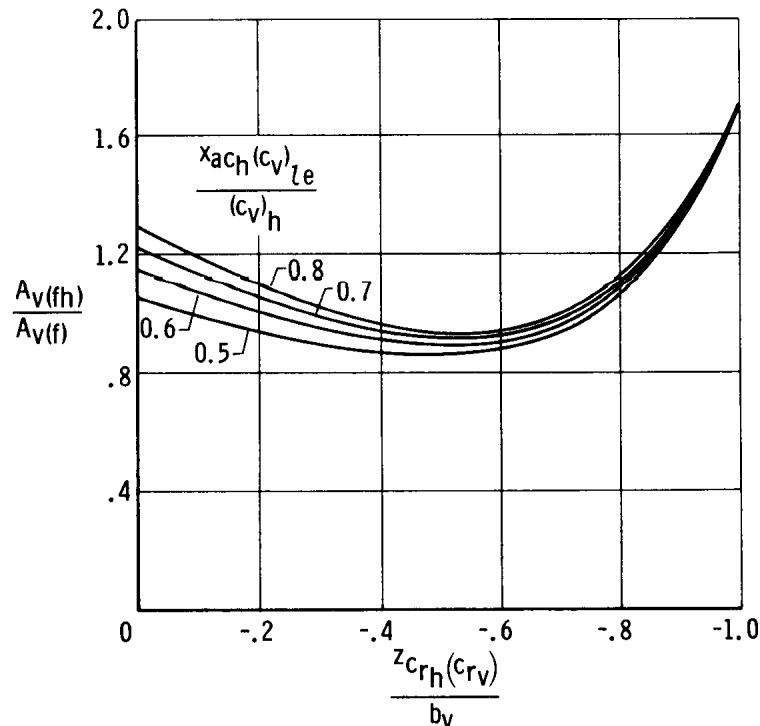


Figure 4.1.3-1. Reduced mass factor (from ref. 6). Subsonic speeds.

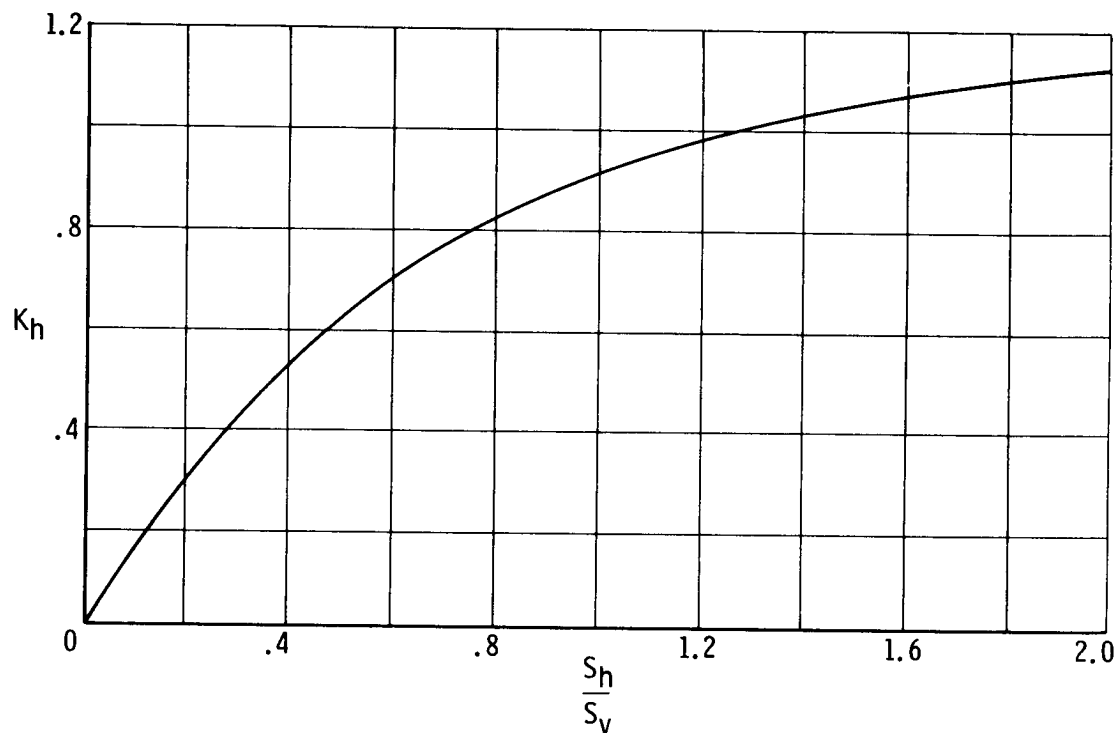


(a) Determination of $\frac{A_{v(f)}}{A_v}$.

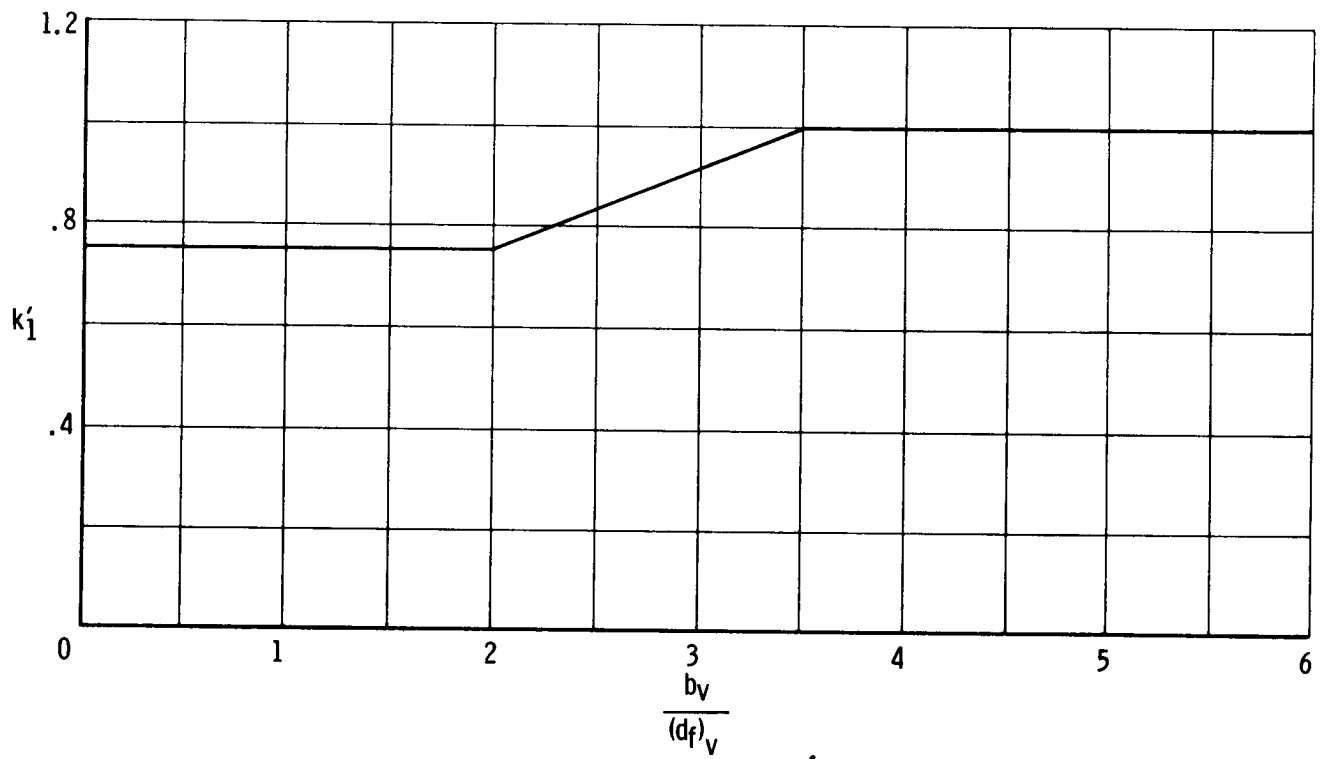


(b) Determination of $\frac{A_{v(fh)}}{A_{v(f)}}$.

Figure 4.1.4-1. Charts for estimating the sideslip derivative parameters for single tails (from ref. 3). Subsonic speeds.



(c) Determination of K_h .



(d) Determination of k'_1 .

Figure 4.1.4-1. Concluded.

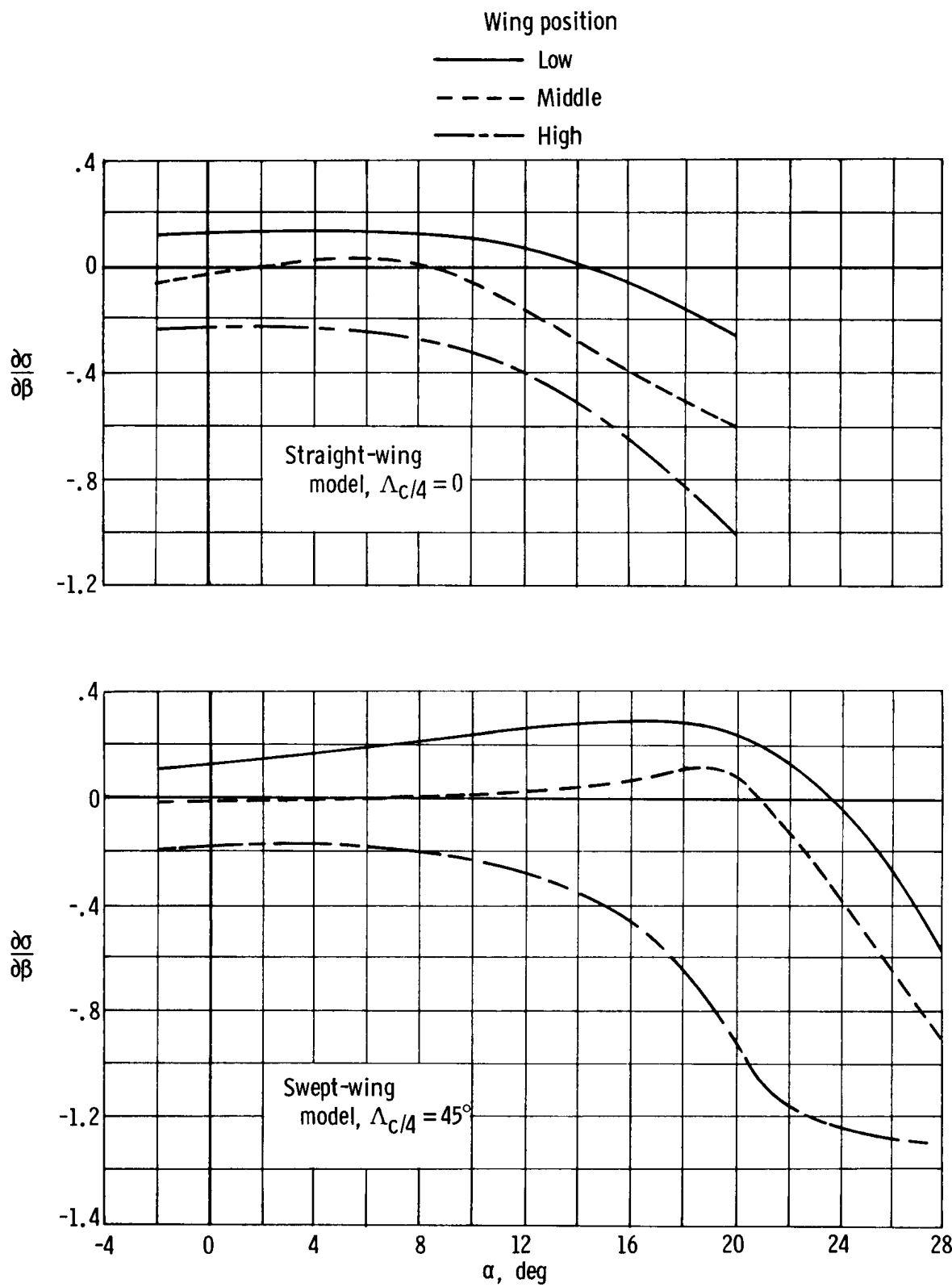


Figure 4.1.4-2. Experimentally determined sidewash characteristics of straight- and swept-wing models with varying wing position (from ref. 7). Aspect ratio = 4; taper ratio = 0.6.

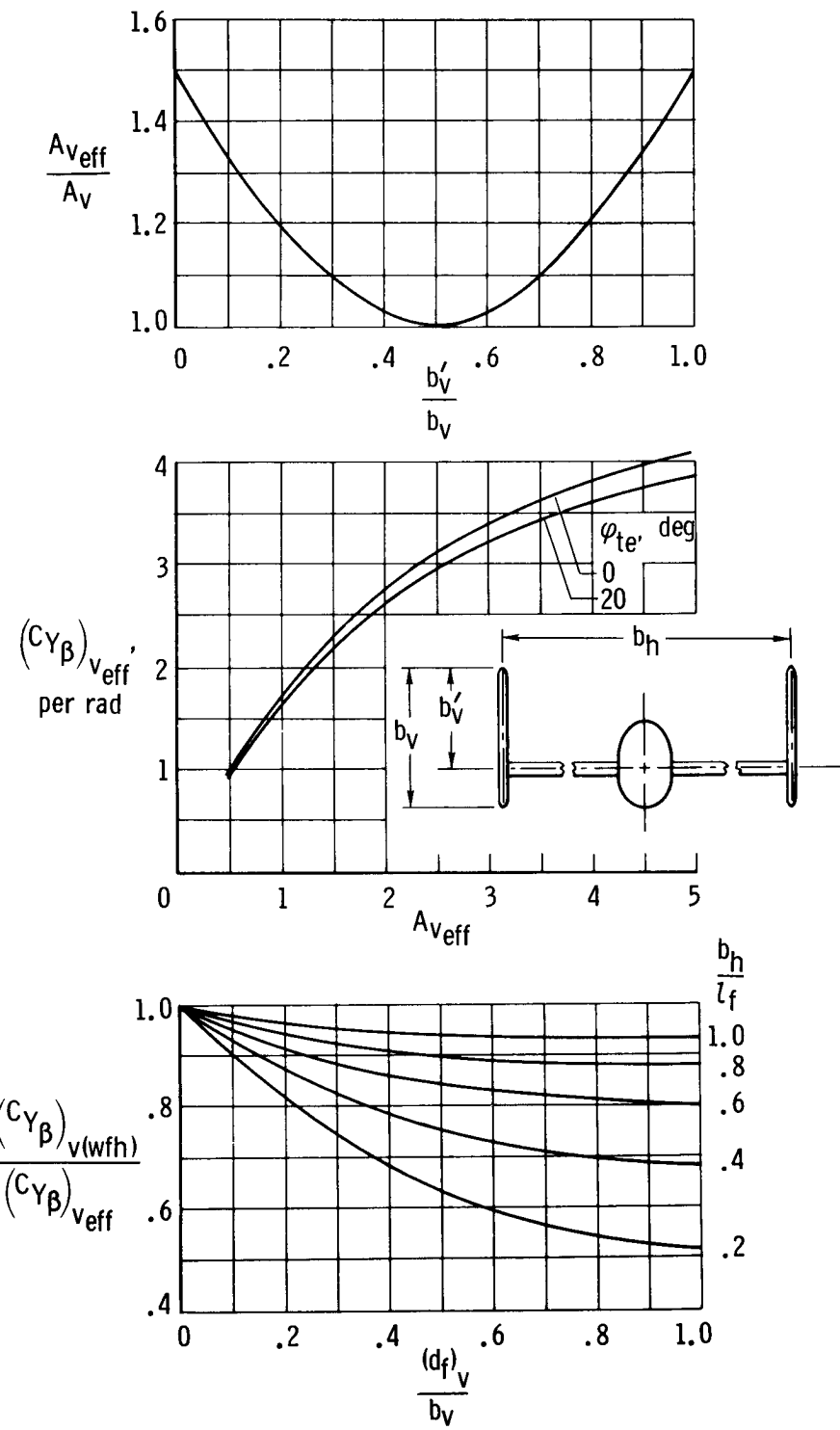


Figure 4.1.4-3. Charts for estimating the side-force derivative, $(C_{Y\beta})_{V(wfh)}$, for twin vertical tails (from ref. 3). Subsonic speeds.

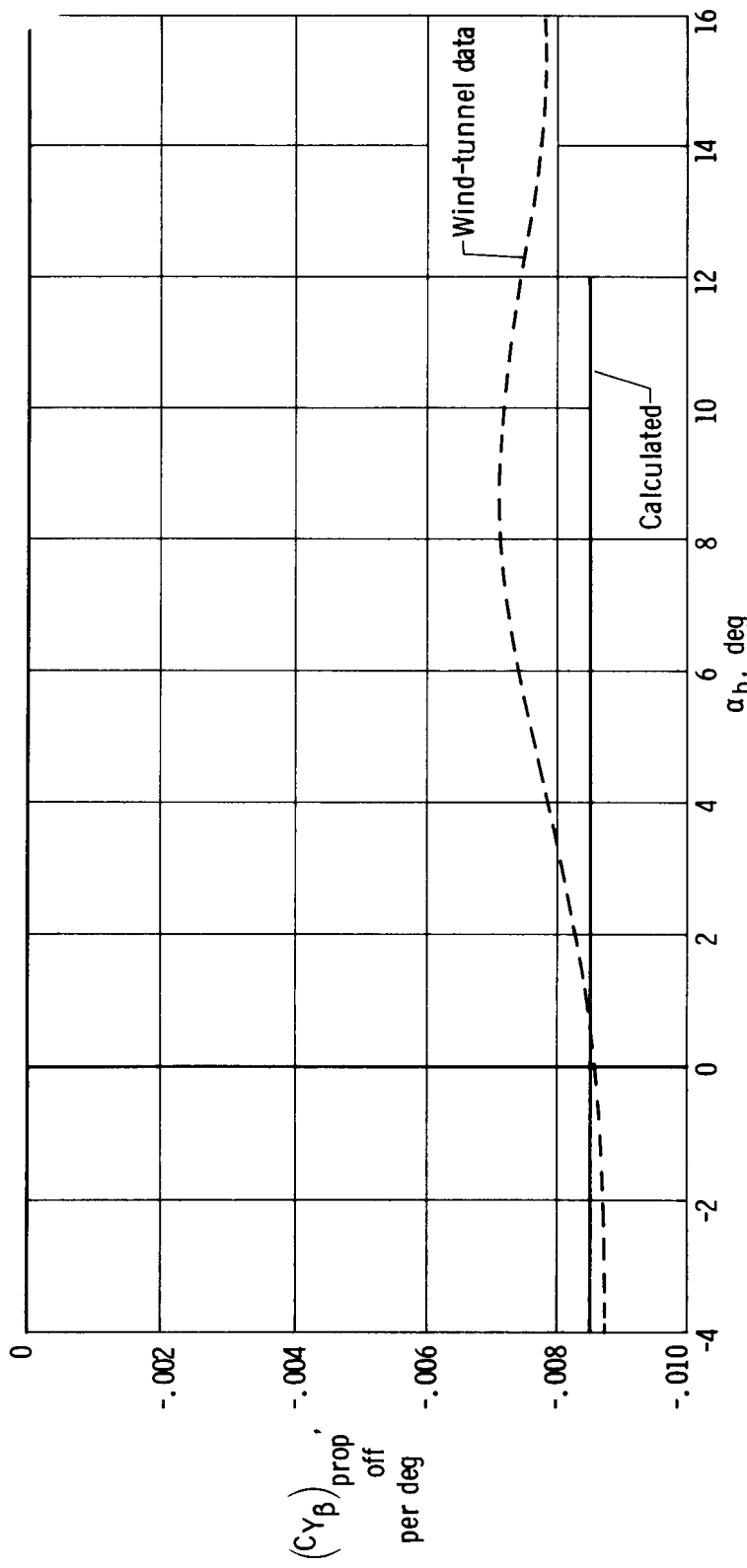


Figure 4.1.5-1. Comparison of calculated $C_{Y\beta}$ with wind-tunnel data. Propellers off

4.2 Weathercock Stability, $C_{n\beta}$

The weathercock stability derivative, $C_{n\beta}$, of the complete airplane in the clean, propeller-off configuration is made up of contributions from the following:

- (1) Wing
- (2) Fuselage and fuselage-wing interference
- (3) Nacelles
- (4) Vertical tail, including the interference and sidewash effects of wing, fuselage, and horizontal tail

These contributions to $C_{n\beta}$, in the order listed, can be represented by

$$\left(C_{n\beta} \right)_{\text{prop off}} = \left(C_{n\beta} \right)_w + \left(C_{n\beta} \right)_{f(w)} + \left(C_{n\beta} \right)_n + \left(C_{n\beta} \right)_{v(wfh)} \quad (4.2-1)$$

4.2.1 Wing Contribution to $C_{n\beta}$

The wing contribution to weathercock stability is primarily due to the asymmetrically induced drag distribution associated with asymmetrical lift distribution. Because the effect of wing taper ratio and dihedral on the contribution can be considered negligible (ref. 3), the wing contribution to $C_{n\beta}$ at low incompressible speeds can be estimated from equation (4.2.1-1) from reference 4. The equation includes the effects of sweep, aspect ratio, and center-of-gravity location.

$$\left(\frac{C_{n\beta}}{C_{L_w}^2} \right)_{\text{low speed}} = \frac{1}{57.3} \left[\frac{1}{4\pi A_w} - \frac{\tan \Lambda_c/4}{\pi A_w (A_w + 4 \cos \Lambda_c/4)} \left(\cos \Lambda_c/4 - \frac{A_w}{2} - \frac{A_w^2}{8 \cos \Lambda_c/4} + 6 \bar{x} \frac{\sin \Lambda_c/4}{\bar{c}_w} \right) \right] \quad (4.2.1-1)$$

where, as obtained from figure 3.2-1,

A_w is the wing aspect ratio

$\Lambda_c/4$ is the sweep of the wing quarter-chord line

\bar{c}_w is the wing mean aerodynamic chord

\bar{x} is the location of the wing aerodynamic center behind the center of gravity on the mean aerodynamic chord

The results obtained above for low speeds can be modified for compressible but subcritical speeds by using equation (4.2.1-2) from reference 5. This equation provides a first-order approximation of wing contribution to $C_{n\beta}$ at compressible flow

conditions.

$$(C_{n\beta})_w = C_{Lw}^2 \left(\frac{A_w + 4 \cos \Lambda_c/4}{A_w B_2 + 4 \cos \Lambda_c/4} \right) \left(\frac{A_w^2 B_2^2 + 4 A_w B_2 \cos \Lambda_c/4 - 8 \cos^2 \Lambda_c/4}{A_w^2 + 4 A_w \cos \Lambda_c/4 - 8 \cos^2 \Lambda_c/4} \right) \left(\frac{C_{n\beta}}{C_{Lw}^2} \right) \quad (4.2.1-2)$$

low speed

where

$$B_2 = \sqrt{1 - M^2 \cos^2 \Lambda_c/4}$$

C_{Lw} is the wing lift coefficient from figure 4.1.1-1.

The contribution of the wing to $C_{n\beta}$ of the subject airplane at $M = 0.083$ is calculated in table 4.2.1-1 to be

$$(C_{n\beta})_w = 0.996 \left(\frac{C_{n\beta}}{C_{Lw}^2} \right) C_{Lw}^2 \quad (4.2.1-3)$$

low speed

$$= 0.000157 C_{Lw}^2 \text{ per deg}$$

Although this contribution seems to be small, it is of the order of 10 percent of the net $C_{n\beta}$ at high angles of attack.

4.2.2 Fuselage Contribution to $C_{n\beta}$

The fuselage contribution to $C_{n\beta}$ is independent of Mach number, according to slender body theory. The contribution of wing-fuselage interference is primarily a function of the vertical position of the wing on the fuselage. It has been concluded, on the basis of experimental evidence, that the interference contribution is independent of wing sweep, taper ratio, and Mach number.

The net contribution of the fuselage and wing-fuselage interference to $C_{n\beta}$ (based on wing area and wing span and referenced to a selected center-of-gravity position) may be obtained from the following equation:

$$(C_{n\beta})_{f(w)} = -K_N \frac{(S_f)_s}{S_w} \frac{l_f}{b_w} \quad (4.2.2-1)$$

where

$(S_f)_s$ is the fuselage side area from figure 3.2-2

S_w is the wing area from figure 3.2-1

l_f is the fuselage length from figure 3.2-2

The quantity K_N in equation (4.2.2-1) is an empirical correlating factor for fuselage plus wing-fuselage interference. It was obtained from the nomograph of figure 4.2.2-1 from reference 3. This nomograph, originally developed in reference 8, was designed for midwing configurations which show negligible angle-of-attack effects on the contribution of the fuselage and wing-fuselage interference to $C_{n\beta}$. In reference 3, on the basis of wind-tunnel data, the effect of wing vertical position is considered to be small, and by implication the use of the nomograph for other than midwing configurations is recommended.

In the absence of more refined procedures for other than midwing configurations, the nomograph provides a first approximation; however, wherever possible, effects of wing vertical position should be taken into account. Wing vertical position, in other than midwing configurations, significantly affects the influence of angle of attack on the contribution of fuselage plus wing-fuselage interference to weathercock stability. This influence is reflected in the full-scale wind-tunnel data of reference 9 for the single-engine version of the subject airplane (fig. 4.2.2-2). The wing-fuselage geometries of the single- and twin-engine versions of the airplane are very similar. The vertical-tail-off data in figure 4.2.2-2 obtained for $T'_c = 0$ conditions show pronounced variations in weathercock stability with angle of attack.

Using the wind-tunnel data of figure 4.2.2-2, the nomograph of figure 4.2.2-1 was extended to be applicable to aircraft with wings positioned below the centerline of the equivalent axisymmetric fuselage a distance of 50 percent of the fuselage radius. As

shown in figure 3.2-2, $\frac{2z_w}{(w_f)_w}$ of the subject airplane is 0.51; however, it was considered to be 0.50 for the nomograph. The angle-of-attack effects on K_N for $\frac{2z_w}{(w_f)_w} \approx 0.50$

were derived by subtracting the wing contributions (using eq. (4.2.1-3)) and the propeller normal-force effects from the data of figure 4.2.2-2. Equation (4.2.2-1) was then used to obtain K_N .

The contribution of the fuselage (including wing-fuselage interference) of the subject airplane to $C_{n\beta}$ is calculated in table 4.2.2-1 following the procedure used in Datcom (ref. 3). In this procedure the midwing configuration is considered to be applicable to other than midwing configurations. The calculations are also based on the extended K_N nomograph (fig. 4.2.2-3), which is more representative of the subject airplane.

The extended nomograph was used in the final calculation of the contribution of the fuselage to $C_{n\beta}$.

The use of the extended nomograph improved the correlation between calculated and wind-tunnel-determined weathercock stability characteristics, as is shown in section 4.2.5.

4.2.3 Nacelles Contribution to C_{n_β}

The contribution of the nacelles to the weathercock stability relative to the stability axes is obtained from

$$(C_{n_\beta})_n = (C_{Y_\beta})_n \left(\frac{x_n \cos \alpha_b + z_n \sin \alpha_b}{b_w} \right) \quad (4.2.3-1)$$

where

$(C_{Y_\beta})_n$ is the contribution of the nacelles to the side force due to sideslip,

obtained from section 4.1.3

x_n, z_n are the distances from the center of gravity of the airplane to the center of pressure of the nacelles parallel and perpendicular to the X-body axis, respectively, obtained from figure 3.2-2

The contribution of the nacelles to the weathercock stability of the subject airplane is calculated in table 4.2.3-1.

4.2.4 Vertical-Tail Contribution to C_{n_β}

The contribution of the vertical tail to the weathercock stability relative to the stability axes and in the presence of the wing, fuselage, and horizontal tail is obtained from

$$(C_{n_\beta})_{v(wfh)} = - (C_{Y_\beta})_{v(wfh)} \left(\frac{l_v \cos \alpha_b - z_v \sin \alpha_b}{b_w} \right) \quad (4.2.4-1)$$

where

$(C_{Y_\beta})_{v(wfh)}$ is the contribution of the vertical tail to the side force due to sideslip,

obtained from section 4.1.4

l_v, z_v are the distances from the center of gravity to the quarter chord of the vertical-tail mean aerodynamic chord, parallel and perpendicular, respectively, to the X-body axis with z_v positive below the center of gravity, obtained from figure 3.2-4

The contribution of the vertical tail to the weathercock stability of the subject airplane is calculated in table 4.2.4-1.

4.2.5 Weathercock Stability of the Complete Airplane

The weathercock stability of the complete airplane is determined by summing the

component contributions discussed in sections 4.2.1 to 4.2.4, or, as expressed previously,

$$\left(C_{n\beta} \right)_{\text{prop off}} = \left(C_{n\beta} \right)_w + \left(C_{n\beta} \right)_{f(w)} + \left(C_{n\beta} \right)_n + \left(C_{n\beta} \right)_{v(wfh)} \quad (4.2-1)$$

The calculated weathercock stability, $C_{n\beta}$, of the complete airplane is summarized in table 4.2.5-1. Values of $C_{n\beta}$ are shown that do and do not take into account the influence of angle of attack and vertical wing position on the wing-body interference contribution.

When compared with full-scale wind-tunnel data, the calculated results that account for the effects of angle of attack and vertical wing position show improved correlation at low angles of attack and a tendency to follow the wind-tunnel data (fig. 4.2.5-1). If suitable design data had been available to account for angle-of-attack effects on the sidewash acting on the vertical tail, the correlation with wind-tunnel data would probably have been improved throughout the angle-of-attack range investigated.

4.2.6 Symbols

A_w	wing aspect ratio
$B_2 = (1 - M^2 \cos^2 \Lambda_c / 4)^{1/2}$	
b_w	wing span, ft
C_{L_w}	wing lift coefficient
$C_{n\beta}$	weathercock stability derivative; variation of yawing-moment coefficient with sideslip, per deg
$\left(C_{n\beta} \right)_{f(w)}$	fuselage contribution to $C_{n\beta}$ in the presence of the wing
$\left(C_{n\beta} \right)_n$	contribution of the nacelles to $C_{n\beta}$
$\left(C_{n\beta} \right)_{\text{prop off}}$	$C_{n\beta}$ of the complete airplane, propellers off
$\left(C_{n\beta} \right)_{v(wfh)}$	vertical-tail contribution to $C_{n\beta}$ in the presence of the wing, fuselage, and horizontal tail
$\left(C_{n\beta} \right)_w$	wing contribution to $C_{n\beta}$
$\left(C_{n\beta} \right)_{\text{wfn}}$	net contribution of the wing, fuselage, and nacelles to $C_{n\beta}$

$(C_{Y\beta})_{v(wfh)}$	contribution of the vertical tail to the variation of the side-force coefficient, C_Y , with sideslip, β , in the presence of the wing, fuselage, and horizontal tail, per deg
\bar{c}_w	mean aerodynamic chord of the wing, in.
$f(\alpha)_b$	function of the angle of attack
h, h_1, h_2	fuselage parameters, defined in figures 4.2.2-1 and 4.2.2-2
K_N	empirical factor accounting for the wing-fuselage interference in calculating the fuselage contribution to $C_{n\beta}$
l_f	fuselage length, ft
l_v	distance along the X-body axis from the center of gravity to the quarter chord of the vertical-tail mean aerodynamic chord, in.
M	Mach number
N_{Re}	Reynolds number
\bar{q}_∞	free-stream dynamic pressure, lb/sq ft
$(S_f)_s$	side area of the fuselage, sq ft
S_w	reference wing area, sq ft
T	thrust due to the propellers, lb
T'_c	thrust coefficient, $\frac{T}{\bar{q}_\infty S_w}$
w_{max}	maximum width of the fuselage, in.
$(w_f)_w$	width of the equivalent circular fuselage at the longitudinal station of the quarter-root chord of the exposed wing panels, in.
\bar{x}	distance from the center of gravity to the wing aerodynamic center as a fraction of the mean aerodynamic chord, in.
x_m	distance from the center of gravity to the nose of the fuselage, in.
x_n	distance along the X-body axis from the center of gravity to the center of pressure of the nacelle side force (fig. 3.2-2), in.
z_n	perpendicular distance from the X-body axis to the center of pressure of the nacelle side force, positive down, in.

z_v	distance along the Z-body axis from the center of gravity to the quarter chord of the vertical-tail mean aerodynamic chord, in.
z_w	vertical distance from the axis of the equivalent circular fuselage to the quarter-root chord of the exposed wing panels (fig. 3.2-2), positive down, in.
α_b	airplane angle of attack relative to the X-body axis, deg
$\lambda_{c/4}$	sweep of the wing quarter-chord line, deg

TABLE 4.2.1-1

WING CONTRIBUTION TO $C_{n\beta}$

$$\left(C_{n\beta} \right)_w = C_{L_w}^2 \left(\frac{A_w + 4 \cos \Lambda_c/4}{A_w B_2 + 4 \cos \Lambda_c/4} \right) \left(\frac{A_w^2 B_2^2 + 4 A_w B_2 \cos \Lambda_c/4 - 8 \cos^2 \Lambda_c/4}{A_w^2 + 4 A_w \cos \Lambda_c/4 - 8 \cos^2 \Lambda_c/4} \right) \left(\frac{C_{n\beta}}{C_{L_w}^2} \right)_{\text{low speed}}$$

$$\left(\frac{C_{n\beta}}{C_{L_w}^2} \right)_{\text{low speed}} = \frac{1}{57.3} \left[\frac{1}{4\pi A_w} - \frac{\tan \Lambda_c/4}{\pi A_w (A_w + 4 \cos \Lambda_c/4)} \left(\cos \Lambda_c/4 - \frac{A_w}{2} - \frac{A_w^2}{8 \cos \Lambda_c/4} + 6 \frac{\bar{x}}{c_w} \frac{\sin \Lambda_c/4}{A_w} \right) \right]$$

Symbol	Description	Reference	Magnitude
M	Mach number	Wind-tunnel test condition	0.083
A _w	Wing aspect ratio	Figure 3.2-1	7.5
$\Lambda_c/4$	Sweep of wing quarter-chord line, deg	Figure 3.2-1	-2.5
\bar{c}_w	Wing mean aerodynamic chord, in.	Figure 3.2-1	59.5
\bar{x}	Wing aerodynamic center - center of gravity = $0.25\bar{c}_w - 0.10\bar{c}_w$	Figure 3.2-1	.15 \bar{c}
B ₂	$\sqrt{1 - M^2 \cos^2 \Lambda_c/4}$	Equation (4.2.1-2)	.997
C _{Lw}	Wing lift coefficient based on S _w = 178 sq ft	Figure 4.1.1-1	f(α_b)
Summary: $\left(C_{n\beta} \right)_w = 0.000157 C_{L_w}^2$ per deg			

(1)	(2)	(3)
-----	Figure 4.1.1-1	-----
α_b , deg	C_{L_w}	$\left(C_{n\beta} \right)_w = 0.000157 (2)^2$
-4	0	0
-2	.145	.000003
0	0.292	0.000013
2	.437	.000030
4	0.584	0.000054
6	.730	.000084
8	0.875	0.000120
10	1.023	.000164
12	1.160	0.000211

TABLE 4.2, 2-1
FUSELAGE CONTRIBUTION TO $C_{n\beta}$

$$(C_{n\beta})_{f(w)} = -K_N \frac{(S_f)_s}{S_w} \frac{l_f}{b_w}$$

Symbol	Description	Reference	Magnitude
$(S_f)_s$	Fuselage side area, sq ft	Figure 3.2-2	68.4
S_w	Wing area, sq ft	Figure 3.2-1	178
l_f	Length of fuselage, ft	Figure 3.2-2	24.2
b_w	Wing span, ft	Figure 3.2-1	36.0
z_w	Vertical position of wing below centerline of equivalent fuselage, in.	Figure 3.2-2	12.5
$(w_f)_w$	Width of equivalent circular fuselage at the quarter-root chord of exposed wing panel, in.	Figure 3.2-2	49.0
$\frac{2z_w}{(w_f)_w}$	-----	-----	.51
N_{Re}	Reynolds number based on body length	Wind-tunnel test N_{Re}	15.7×10^6
x_m, h, h_1, h_2	Geometric fuselage parameters required for K_N	Figure 4.2.2-1	As listed
K_N	Empirical factor for fuselage $C_{n\beta}$ in presence of wing - If α_b and vertical position of wing are negligible If α_b and vertical position of wing are not negligible	Figure 4.2.2-1 Figure 4.2.2-3	0.0018 $f\left(\alpha_b, \frac{2z_w}{(w_f)_w}\right)$

Summary: If α_b and vertical position of wing are assumed to be negligible,

$$(C_{n\beta})_{f(w)} = -0.000465 \text{ per deg}$$

If α_b and vertical position of the wing are taken into account and $\frac{2z_w}{(w_f)_w} = 0.51 \approx 0.50$,

$$(C_{n\beta})_{f(w)} = -0.258 K_N \text{ per deg}$$

(1)	(2)	(3)
-----	Figure 4.2.2-3	-----
α_b , deg	K_N	$(C_{n\beta})_{f(w)} = -0.258 (2)$
-4	0.00036	-0.000093
-2	.00036	-.000093
0	0.00036	-0.000093
2	.00055	-.000142
4	0.00072	-0.000186
6	.00105	-.000271
8	0.00164	-0.000423
10	.00192	-.000495
12	0.00205	-0.000529

TABLE 4.2.3-1

NACELLE CONTRIBUTION TO $C_{n\beta}$

$$(C_{n\beta})_n = (C_{Y\beta})_n \left(\frac{x_n \cos \alpha_b + z_n \sin \alpha_b}{b_w} \right)$$

Symbol	Description	Reference	Magnitude
$(C_{Y\beta})_n$	Contribution of nacelles to side force due to sideslip	Table 4.1.3-1	-0.00037
x_n	Distance along X-body axis from center of gravity to the center of pressure of the nacelle side force, in.	Figure 3.2-2	25.0
z_n	Perpendicular distance from X-body axis to center of pressure of nacelle side force, positive down, in.	Figure 3.2-2	-7.0
b_w	Wing span, in.	Figure 3.2-1	432
Summary: $(C_{n\beta})_n = (C_{Y\beta})_n (0.0579 \cos \alpha_b - 0.0162 \sin \alpha_b)$ per deg $= -0.0000214 \cos \alpha_b + 0.0000060 \sin \alpha_b$			

①	②	③	④
α_b , deg	$\cos \alpha_b$	$\sin \alpha_b$	$(C_{n\beta})_n = -0.0000214(2) + 0.0000060(3)$
-4	0.9976	-0.0698	-0.000022
-2	.9994	-.0349	-.000022
0	1.0000	0	-0.000021
2	.9994	.0349	-.000021
4	0.9976	0.0698	-0.000021
6	.9945	.1045	-.000021
8	0.9903	0.1392	-0.000020
10	.9848	.1736	-.000020
12	0.9781	0.2079	-0.000020

TABLE 4.2.4-1
VERTICAL-TAIL CONTRIBUTION TO $C_{n\beta}$

$$(C_{n\beta})_{v(wfh)} = -(C_{Y\beta})_{v(wfh)} \left(\frac{l_v \cos \alpha_b - z_v \sin \alpha_b}{b_w} \right)$$

Symbol	Description	Reference	Magnitude
$(C_{Y\beta})_{v(wfh)}$	Contribution of vertical tail to side force due to sideslip, per deg	Table 4.1.4-1(c)	-0.0049
l_v	Distance along X-body axis from center of gravity to quarter chord of vertical-tail mean aerodynamic chord, in.	Figure 3.2-4	164.9
z_v	Perpendicular distance from X-body axis to quarter chord of vertical-tail mean aerodynamic chord, in.	Figure 3.2-4	-45.9
b_w	Wing span, in.	Figure 3.2-1	432.0
Summary: $(C_{n\beta})_{v(wfh)} = 0.00187 \cos \alpha_b + 0.000521 \sin \alpha_b$			

(1)	(2)	(3)	(4)
α_b , deg	$\cos(1)$	$\sin(1)$	$(C_{n\beta})_{v(wfh)} = 0.00187(2) + 0.000521(3)$
-4	0.9976	-0.0698	0.001829
-2	.9994	-.0349	.001851
0	1.0000	0	0.001870
2	.9994	.0349	.001887
4	0.9976	0.0698	0.001902
6	.9945	.1045	.001914
8	0.9903	0.1392	0.001924
10	.9848	.1736	.001932
12	0.9781	0.2079	0.001937

TABLE 4.2.5-1
WEATHERCOCK STABILITY OF THE AIRPLANE

$$(C_{n\beta})_{\text{prop off}} = (C_{n\beta})_w + (C_{n\beta})_{f(w)} + (C_{n\beta})_n + (C_{n\beta})_{v(wfh)}$$

		Vertical tail off						Complete airplane	
①	②	③a (a)	③b (b)	④	⑤a (a)	⑤b (b)	⑥	⑦a (a)	⑦b (b)
Table 4.2.1-1	Table 4.2.2-1	Table 4.2.2-1	Table 4.2.3-1	Table 4.2.3-1	-----	-----	-----	Table 4.2.4-1	-----
α_b , deg	$(C_{n\beta})_w$	$(C_{n\beta})_{f(w)}$	$(C_{n\beta})_n$	$(C_{n\beta})_{wfh}$ $(2) + (3a) + (4)$	$(C_{n\beta})_{wfh}$ $(2) + (3b) + (4)$	$(C_{n\beta})_{v(wfh)}$ $(2) + (3b) + (4)$	$(C_{n\beta})_{v(wfh)}$ $(5a) + (6)$	$(C_{n\beta})_{\text{prop off}}$ $(5b) + (6)$	$(C_{n\beta})_{\text{prop off}}$ $(5b) + (6)$
-4	0	-0.000465	-0.000093	-0.000022	-0.000487	-0.000115	0.001829	0.001342	0.001714
-2	.000003	-.000465	-.000093	-.000022	-.000484	-.000112	.001851	.001367	.001739
0	0.000013	-0.000465	-0.000093	-0.000021	-0.000473	-0.000101	0.001870	0.001397	0.001769
2	.000030	-.000465	-.000142	-.000021	-.000456	-.000133	.001887	.001431	.001754
4	0.000054	-0.000465	-0.000186	-0.000021	-0.000432	-0.000153	0.001902	0.001470	0.001749
6	.000084	-.000465	-.000271	-.000021	-.000402	-.000208	.001914	.001512	.001706
8	0.000120	-0.000465	-0.000423	-0.000020	-0.000365	-0.000233	0.001924	0.001559	0.001601
10	.000164	-.000465	-.000495	-.000020	-.000321	-.000351	.001932	.001611	.001581
12	0.000211	-0.000465	-0.000529	-0.000020	-0.000274	-0.000338	0.001937	0.001663	0.001599

^aEffect of a_b and vertical position of the wing on the wing-body interference neglected.

^bEffect of a_b and vertical position of the wing on the wing-body interference accounted for.

For subject airplane -

$$x_m = 99.14 \text{ in.} \quad h = 54.0 \text{ in.}$$

$$l_f = 290.0 \text{ in.} \quad h_1 = 38.0 \text{ in.}$$

$$w_{\max} = 48.0 \text{ in.} \quad h_2 = 29.0 \text{ in.}$$

$$(S_f)_S = 68.4 \text{ sq ft}$$

$$N_{Re} = 15.7 \times 10^6$$

$$\frac{x_m}{l_f} = 0.342 \quad \sqrt{\frac{h_1}{h_2}} = 1.146$$

$$\frac{l_f^2}{(S_f)_S} = 8.56 \quad \frac{h}{w_{\max}} = 1.125$$

$$\frac{l_f^2}{(S_f)_S} \quad \sqrt{\frac{h_1}{h_2}}$$

$$0.8 \quad 1.0$$

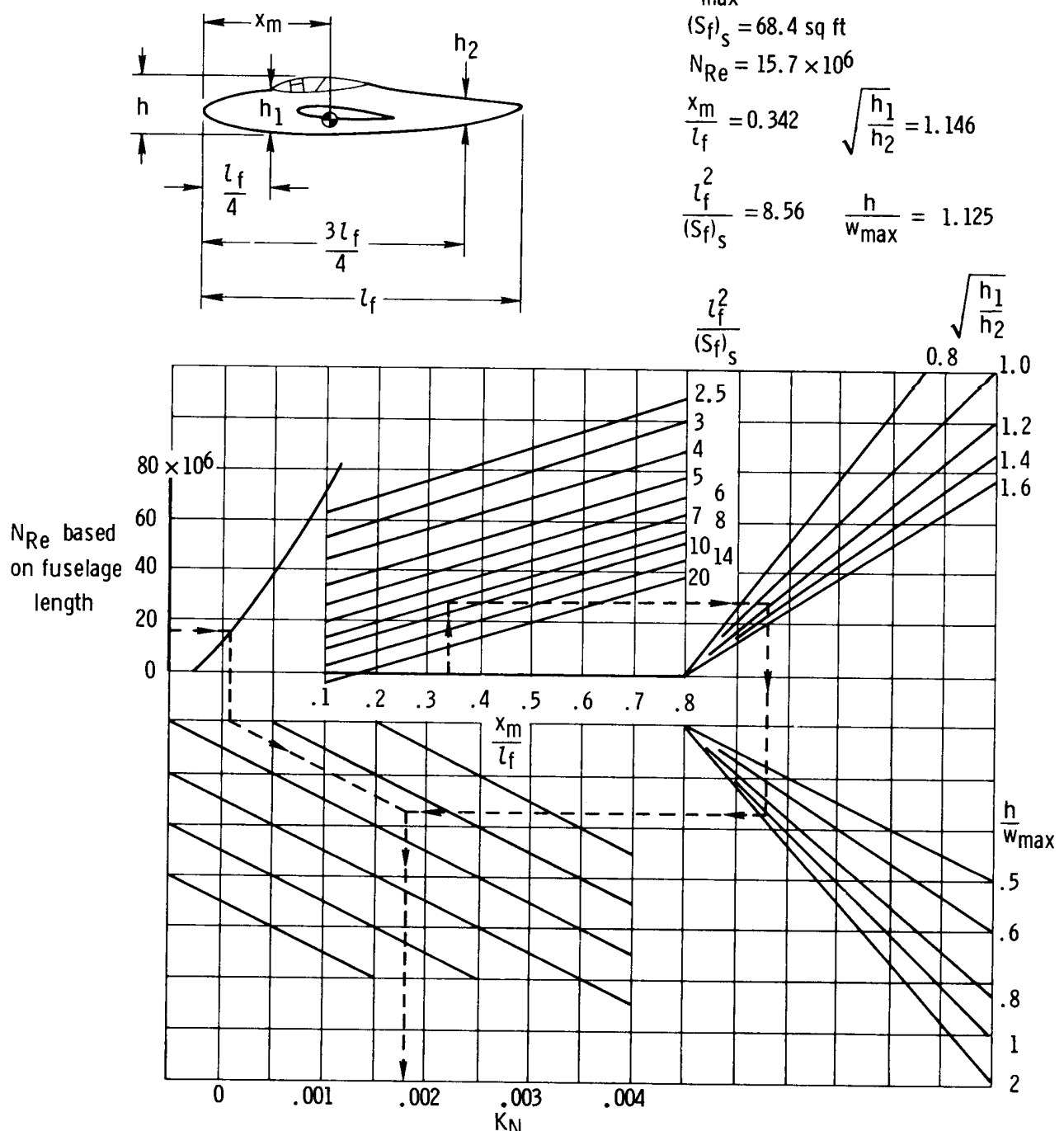


Figure 4.2.2-1. Empirical factor, K_N , related to the derivative $C_{n\beta}$ for the fuselage plus wing-fuselage interference (from ref. 3). Midwing configuration.

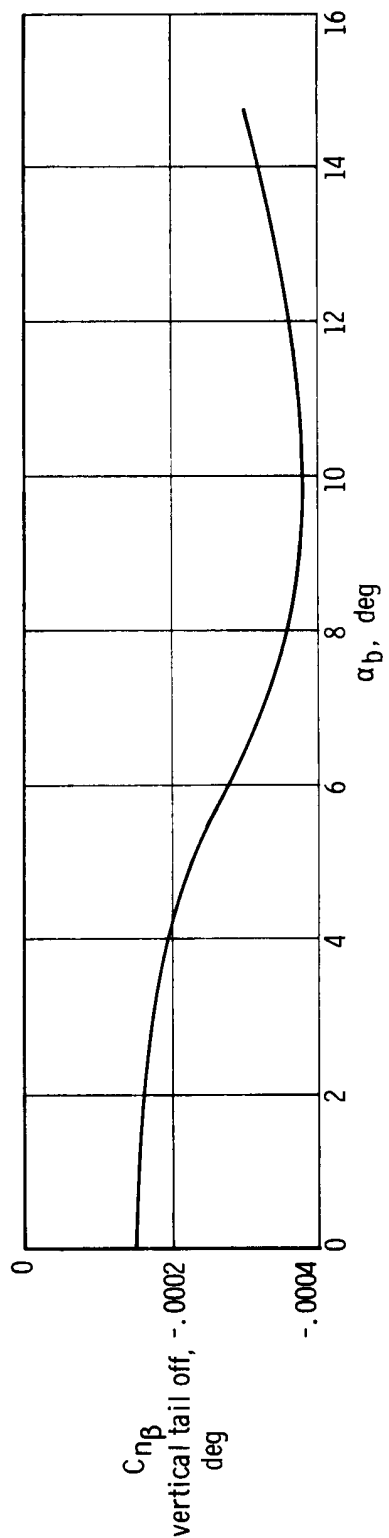


Figure 4.2.2-2. Wind-tunnel-determined vertical-tail-off weathercock stability characteristics of a single-engine version of the subject airplane at $T'_C = 0$.

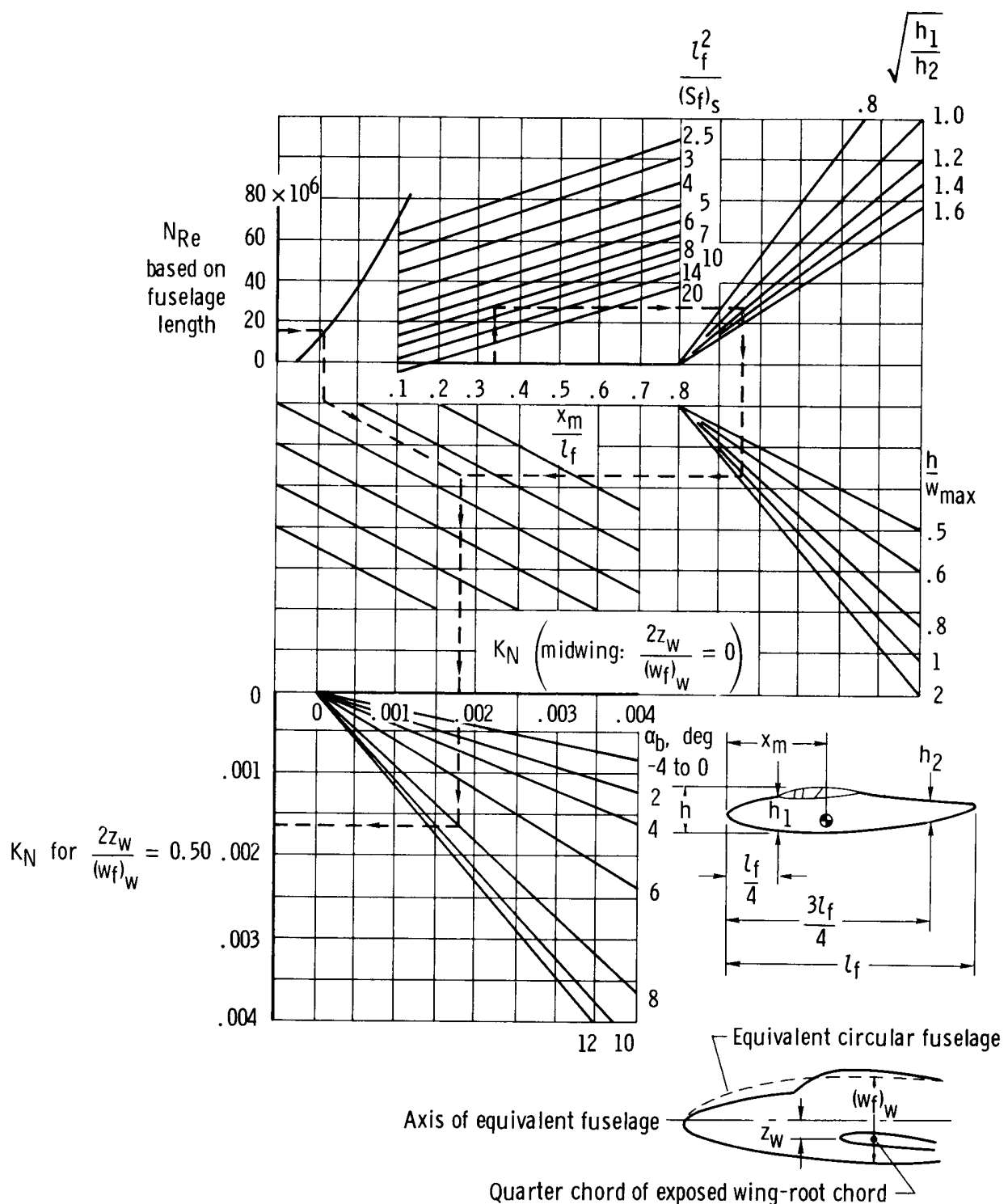


Figure 4.2.2-3. Extension of the nomograph of figure 4.2.2-1 to obtain the empirical factor K_N for low-wing configuration where $\frac{2z_w}{(w_f)_w} = 0.50$.

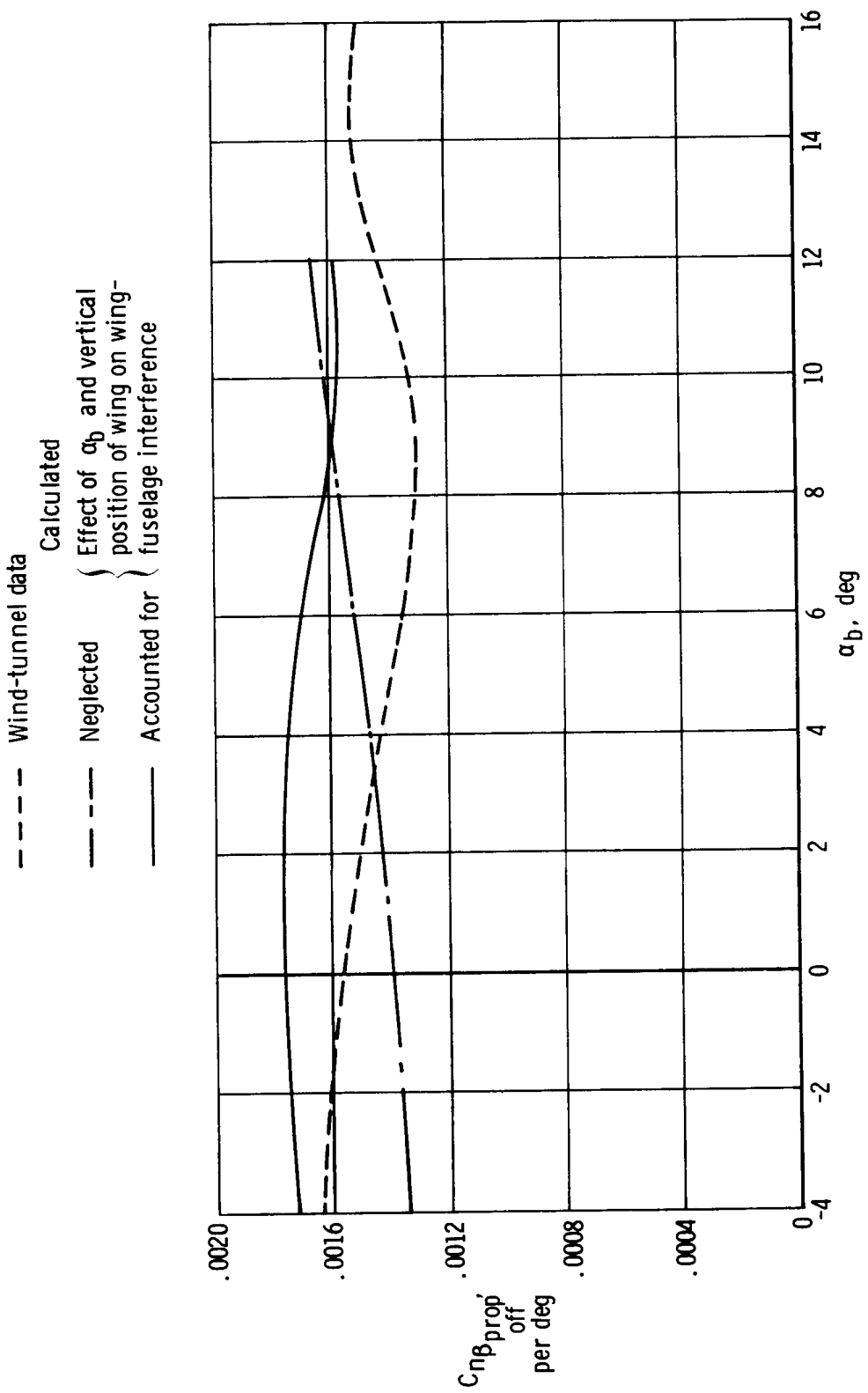


Figure 4.2.5-1. Comparison of calculated $C_{n\beta}$ with wind-tunnel data. Propellers off.

4.3 Effective Dihedral, $C_{l\beta}$

The effective dihedral derivative, $C_{l\beta}$, of the complete airplane in its clean configuration is considered to be made up of contributions from the following:

- (a) Wing in the absence of geometric dihedral
- (b) Wing geometric dihedral
- (c) Wing-fuselage interference effects in the absence of geometric dihedral
- (d) Fuselage interference effects on wing geometric dihedral
- (e) Vertical tail in the presence of the wing, fuselage, and horizontal tail

These contributions to the airplane effective dihedral are represented, in the order listed, by

$$(C_{l\beta})_{\text{prop off}} = (C_{l\beta})_{w\Gamma=0} + (C_{l\beta})_\Gamma + (C_{l\beta})_{f(w)\Gamma=0} + (C_{l\beta})_{f(\Gamma)} + (C_{l\beta})_{v(wfh)} \quad (4.3-1)$$

It should be noted that a negative value of $C_{l\beta}$ signifies positive effective dihedral and a positive value of $C_{l\beta}$ signifies negative effective dihedral.

The horizontal-tail contribution, for most general aviation configurations, is taken to be negligible. When the horizontal tail has significant geometric dihedral and a relatively large area, its contribution is accounted for by analyzing it as another wing. For the subject airplane, the horizontal-tail contribution to $C_{l\beta}$ of the complete airplane was of the order of 1 percent. This is much less than the contributions listed and, consequently, is not included in the calculations.

4.3.1 Wing Contribution to $C_{l\beta}$

For the subsonic speed conditions and angles of attack within the linear lift range, the wing contribution to $C_{l\beta}$ is primarily a function of aspect ratio, taper ratio, sweep, and geometric dihedral. Wing twist generally has a negligible effect on the $C_{l\beta}$ of general aviation aircraft. The wing contribution is accounted for by considering its contribution in the absence of geometric dihedral, adding the effect of geometric dihedral, and adding the effect of wing twist if pertinent. Thus,

$$(C_{l\beta})_w = (C_{l\beta})_{w\Gamma=0} + (C_{l\beta})_\Gamma + (C_{l\beta})_\theta \quad (4.3.1-1)$$

In the absence of wing twist and geometric dihedral, $C_{l\beta}$ may be obtained to a good degree of accuracy from equation (4.3.1-2) which was derived in reference 10 on the

basis of a modified lifting-line theory using a vortex system.

$$\left(C_{l\beta}\right)_{w_{\Gamma=0}} = C_{LW} \left[\left(\frac{C_{l\beta}}{C_{LW}}\right)_{M=0} + \left(\frac{\Delta C_{l\beta}}{C_{LW}}\right)_M \right] \quad (4.3.1-2)$$

where

C_{LW} is the lift coefficient of the wing, from figure 4.1.1-1

$\left(\frac{C_{l\beta}}{C_{LW}}\right)_{M=0}$ is the low-speed derivation, obtained from figure 4.3.1-1, which

is a graphical representation of

$$\left(\frac{C_{l\beta}}{C_{LW}}\right)_{M=0} = -\frac{1}{2} \left[\frac{3}{A_w(1+\lambda)} + \bar{y}^* \left(\tan \Lambda_c/4 - \frac{6}{A_w} \frac{1-\lambda}{1+\lambda} \right) \right] + 0.05 \text{ per rad} \quad (4.3.1-3)$$

$\left(\frac{\Delta C_{l\beta}}{C_{LW}}\right)_M$ is the influence of the compressible flow which is accounted for by

$$\left(\frac{\Delta C_{l\beta}}{C_{LW}}\right)_M = -\frac{1}{2} \bar{y}^* \frac{A_w^2 M^2 \tan \Lambda_c/4}{\left[\left(\frac{A_w}{\cos \Lambda_c/4} \right)^2 - A_w^2 M^2 + 4 \right]^{1/2} \left\{ 2 + \left[\left(\frac{A_w}{\cos \Lambda_c/4} \right)^2 - A_w^2 M^2 + 4 \right]^{1/2} \right\}} \text{ per rad} \quad (4.3.1-4)$$

In equation (4.3.1-4), \bar{y}^* is the spanwise position of the centroid of the angle-of-attack span loading as a ratio of the wing semispan, $\frac{b_w}{2}$, obtained from figure 4.3.1-2.

The contribution of uniform geometric dihedral to $C_{l\beta}$ is accounted for by equation (4.3.1-5) from references 11 and 3. (Nonuniform geometric dihedral effects are considered in references 12 and 13.)

$$\left(C_{l\beta}\right)_{\Gamma} = \Gamma \left(\frac{C_{l\beta}}{\Gamma}\right)_{M=0} K_{M\Gamma} \text{ per deg} \quad (4.3.1-5)$$

where

Γ is the geometric dihedral in degrees

$\left(\frac{C_{l\beta}}{\Gamma}\right)_{M=0}$ is the effect of uniform geometric dihedral on $C_{l\beta}$ at low speeds, obtained from figure 4.3.1-3

$K_{M\Gamma}$ is the compressibility correction factor (fig. 4.3.1-4)

The effect of wing twist on $C_{l\beta}$, although generally negligible for general aviation wing configurations, can be accounted for by the following equation from reference 3:

$$(C_{l\beta})_\theta = \theta \tan \Lambda_c / 4 \left(\frac{\Delta C_{l\beta}}{\theta \tan \Lambda_c / 4} \right) \text{ per deg} \quad (4.3.1-6)$$

where

θ is the wing twist between root and tip chord, deg

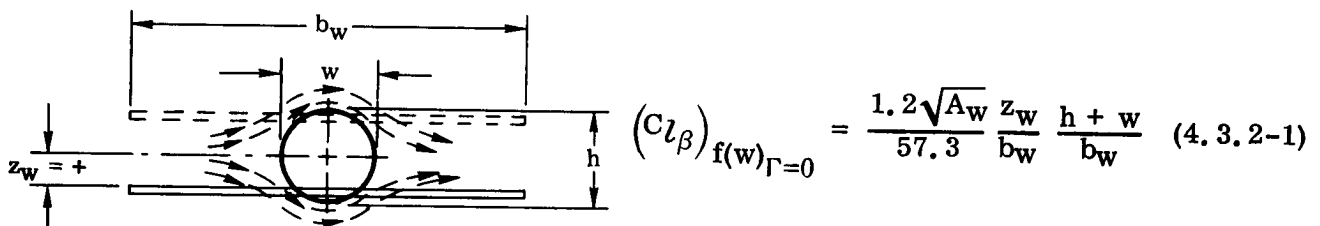
$\frac{\Delta C_{l\beta}}{\theta \tan \Lambda_c / 4}$ is the wing-twist correction factor (fig. 4.3.1-5)

The contribution of the wing to $C_{l\beta}$ of the subject airplane is calculated in table 4.3.1-1. It should be pointed out that the compressibility correction for a Mach number of 0.083 is insignificant in this instance.

4.3.2 Effect of Fuselage on Wing Contribution to $C_{l\beta}$

The contribution of the fuselage alone to $C_{l\beta}$ is negligible. However, the addition of the fuselage to the wing results in several wing-fuselage interference effects which can alter the wing contributions significantly.

One well-known interference effect is related to the vertical location of the wing on the fuselage. A high wing results in a more positive effective dihedral and a low wing in a less-positive effective dihedral than obtained for an isolated wing. A midwing position on the fuselage results in essentially zero interference effect. Wing position affects $C_{l\beta}$ because it affects the crossflow around the body. Changing the crossflow causes changes in the local angle of attack of the wing. This effect was treated theoretically in reference 14 and was simplified to the following format in reference 15:



A second interference effect, which is an extension of the first, involves geometric dihedral. Because the vertical position of the wing relative to the fuselage varies along the span of a wing having geometric dihedral, the fuselage-induced crossflow effect on the wing must be modified. This fuselage interference effect may be accounted

for by the following equation developed in reference 11:

$$(C_{l\beta})_{f(\Gamma)} = -0.0005 \sqrt{A_w} \left[\frac{(df)_w}{b_w} \right]^2 \Gamma \text{ per deg} \quad (4.3.2-2)$$

where

$(df)_w$ is the diameter of the equivalent circular fuselage at the wing, from figure 3.2-2

b_w is the wing span, from figure 3.2-1

A_w is the wing aspect ratio, from figure 3.2-1

Γ is the geometric dihedral, from figure 3.2-1

A third interference effect was shown by reference 11 to be associated with the length, l'_f , of the fuselage forebody (from the nose to the midchord point of the tip chord), wing span, and wing sweep. A decrease in $C_{l\beta}$ with increasing $\frac{l'_f}{b_w}$ and sweep was observed. At zero sweep the effect was nil. This additional fuselage effect, as indicated in reference 11, may be the result of a reduction of the wing effective sideslip angle due to the flow field of the fuselage. More research is required with regard to this fuselage effect. For the subject airplane, this effect may be considered to be negligible.

The wing-fuselage interference effects on $C_{l\beta}$ of the subject airplane are calculated in table 4.3.2-1.

4.3.3 Vertical-Tail Contribution to $C_{l\beta}$

The contribution of the vertical tail to $C_{l\beta}$ in the presence of the wing, fuselage, and horizontal tail is obtained from equation (4.3.3-1). Relative to the stability system of axes,

$$(C_{l\beta})_{v(wfh)} = - (C_{Y\beta})_{v(wfh)} \frac{z_v \cos \alpha_b + l_v \sin \alpha_b}{b_w} \quad (4.3.3-1)$$

where

$(C_{Y\beta})_{v(wfh)}$ is the side force due to the sideslip of the vertical tail in the presence of the wing, fuselage, and horizontal tail, obtained from table 4.1.4-1(c)

z_v, l_v are the distances from the center of gravity to the quarter chord of the vertical-tail mean aerodynamic chord perpendicular and parallel, respectively, to the X-body axes; z_v is positive below the center of gravity, obtained from figure 3.2-4

b_w is the wing span

The contribution of the vertical tail to the $C_{l\beta}$ of the subject airplane is calculated in table 4.3.3-1.

4.3.4 $C_{l\beta}$ of the Complete Airplane

The $C_{l\beta}$ of the complete airplane is determined by summing the component contributions discussed in sections 4.3.1 through 4.3.3 or

$$(C_{l\beta})_{\text{prop off}} = (C_{l\beta})_{w_{\Gamma=0}} + (C_{l\beta})_{\Gamma} + (C_{l\beta})_{f(w)_{\Gamma=0}} + (C_{l\beta})_{f(\Gamma)} + (C_{l\beta})_{v(wfh)} \quad (4.3-1)$$

The component contributions are summarized in table 4.3.4-1. The calculated results, when compared with analyzed full-scale wind-tunnel tabulated data (fig. 4.3.4-1), show good correlation through the linear range of the lift curve.

4.3.5 Symbols

A_w	wing aspect ratio
b_w	wing span, in.
C_{Lw}	wing lift coefficient
$C_{l\beta}$	effective dihedral parameter, variation of the rolling-moment coefficient with sideslip, per deg
$(C_{l\beta})_{\text{prop off}}$	effective dihedral of the complete airplane with propellers off
$(C_{l\beta})_{v(wfh)}$	vertical-tail contribution to $C_{l\beta}$
$(C_{l\beta})_w$	wing contribution to $C_{l\beta}$
$(C_{l\beta})_{f(w)_{\Gamma=0}}$	contribution of the fuselage interference to the wing contribution to $C_{l\beta}$ in the absence of geometric dihedral
$(C_{l\beta})_{w_{\Gamma=0}}$	contribution of the wing to $C_{l\beta}$ in the absence of geometric dihedral
$(C_{l\beta})_{\Gamma}$	contribution of the wing geometric dihedral to $C_{l\beta}$

$(C_{l\beta})_{f(\Gamma)}$	contribution of the fuselage interference to the wing geometric-dihedral contribution to $C_{l\beta}$
$(C_{l\beta})_\theta$	contribution of the wing twist to $C_{l\beta}$
$\left(\frac{C_{l\beta}}{C_{Lw}}\right)_{M=0}$	incompressible-flow contribution to $(C_{l\beta})_{w_{\Gamma}=0}$ as a function of the wing-lift coefficient
$\left(\frac{C_{l\beta}}{\Gamma}\right)_{M=0}$	incompressible-flow contribution to $(C_{l\beta})_\Gamma$ as a function of the geometric dihedral, obtained from figure 4.3.1-3
$\left(\frac{\Delta C_{l\beta}}{C_{Lw}}\right)_M$	influence of subsonic flow compressibility on $(C_{l\beta})_{w_{\Gamma}=0}$ as a function of the wing-lift coefficient
$\frac{\Delta C_{l\beta}}{\theta \tan \Lambda_c / 4}$	wing-twist correction factor from figure 4.3.1-5 used to obtain $(C_{l\beta})_\theta$
$(C_{Y\beta})_{v(wfh)}$	contribution of the vertical tail to the variation of the side-force coefficient with sideslip in the presence of the wing, fuselage, and horizontal tail, per deg
$(df)_w$	diameter of the equivalent circular fuselage at the wing (similar to $(wf)_w$), in.
$f(\alpha)$	function of the angle of attack
h	height of the fuselage at the wing location (similar to $(wf)_w$), in.
K_{M_Γ}	compressibility correction factor from figure 4.3.1-4 used to obtain $(C_{l\beta})_\Gamma$
l'_f	length of the fuselage forebody extending from the nose to the midchord point of the tip chord, in.
l_v	distance along the X-body axis from the airplane center of gravity to the quarter chord of the vertical-tail mean aerodynamic chord, in.
M	Mach number

w	width of the fuselage at the wing location (similar to $(w_f)_w$), in.
$(w_f)_w$	maximum width of the equivalent circular fuselage at the longitudinal station of the quarter-root chord of the exposed wing panels, in.
\bar{y}^*	spanwise position of the centroid of span loading as a fraction of the semispan
z_v	distance from the X-body axis to the quarter chord of the vertical-tail mean aerodynamic chord (fig. 3.2-4), positive down, in.
z_w	vertical distance from the axis of the equivalent circular fuselage to the quarter-root chord of the exposed wing panels (fig. 3.2-2), positive down, in.
α_b	airplane angle of attack relative to the X-body axis, deg
β	sideslip angle, deg
Γ	wing geometric dihedral, deg
θ	wing twist between the root and tip chord, deg
$\Lambda_c/2, \Lambda_c/4$	wing sweep of the half-chord and quarter-chord line, respectively, deg
λ_w	wing taper ratio

TABLE 4.3.1-1

WING CONTRIBUTION TO $C_{l\beta}$

$$(C_{l\beta})_w = (C_{l\beta})_{w\Gamma=0} + (C_{l\beta})_\Gamma$$

$$(a) \quad (C_{l\beta})_{w\Gamma=0} = C_{L_w} \left\{ \left(\frac{C_{l\beta}}{C_{L_w}} \right)_{M=0} - \frac{1}{2} \bar{y}^* \frac{A_w^2 M^2 \tan \Lambda_c/4}{\left[\left(\frac{A_w}{\cos \Lambda_c/4} \right)^2 - A_w^2 M^2 + 4 \right]^{1/2} \left\{ 2 + \left[\left(\frac{A_w}{\cos \Lambda_c/4} \right)^2 - A_w^2 M^2 + 4 \right]^{1/2} \right\}} \right\}$$

Symbol	Description	Reference	Magnitude
M	Mach number	Wind-tunnel test condition	0.083
C_{L_w}	Wing lift coefficient	Figure 4.1.1-1	$f(\alpha)$
A_w	Wing aspect ratio	Figure 3.2-1	7.5
λ_w	Wing taper ratio	Figure 3.2-1	.513
$\Lambda_c/4$	Sweep of wing quarter-chord line, deg	Figure 3.2-1	-2.5
$\left(\frac{C_{l\beta}}{C_{L_w}} \right)_{M=0}$	Low-speed derivation of $C_{l\beta}$ as a function of C_{L_w}	Figure 4.3.1-1	-0.02 per rad -0.000349 per deg
\bar{y}^*	Spanwise position of the centroid of span loading as a fraction of the semispan	Figure 4.3.1-2	.423
Summary: $(C_{l\beta})_{w\Gamma=0} = - (0.020 - 0.00047) C_{L_w}$ per rad $= - 0.000348 C_{L_w}$ per deg			

$$(b) \quad (C_{l\beta})_\Gamma = \Gamma \left(\frac{C_{l\beta}}{\Gamma} \right) K_M \Gamma$$

Symbol	Description	Reference	Magnitude
M	Mach number	Wind-tunnel test condition	0.083
A_w	Wing aspect ratio	Figure 3.2-1	7.5
λ_w	Wing taper ratio	Figure 3.2-1	.513
$\Lambda_c/2$	Sweep of wing half-chord line, deg	Figure 3.2-1	-5.0
$\left(\frac{C_{l\beta}}{\Gamma} \right)_{M=0}$	Effect of geometric dihedral on $C_{l\beta}$ at low speeds	Figure 4.3.1-3	-0.00023
$K_M \Gamma$	Compressibility correction factor	Figure 4.3.1-4	1.00
Γ	Geometric dihedral of wing, deg	Figure 3.2-1	5.0
Summary: $(C_{l\beta})_\Gamma = -0.00115$ per deg			

$$(c) \quad (C_{l\beta})_w = (C_{l\beta})_{w\Gamma=0} + (C_{l\beta})_\Gamma$$

$$(C_{l\beta})_w = -0.000348 C_{L_w} - 0.00115 \text{ per deg}$$

TABLE 4.3.2-1
EFFECT OF FUSELAGE ON WING CONTRIBUTION TO $C_{l\beta}$

$$(C_{l\beta})_{f(w)} + (C_{l\beta})_{f(\Gamma)} = \frac{1.2\sqrt{A_w}}{57.3} \frac{z_w}{b_w} \frac{h+w}{b_w} - 0.0005 \sqrt{A_w} \left[\frac{(df)_w}{b_w} \right]^2 \Gamma \text{ per deg}$$

Symbol	Description	Reference	Magnitude
A_w	Wing aspect ratio	Figure 3.2-1	7.5
b_w	Wing span, in.	Figure 3.2-1	432.0
z_w	Vertical position of wing relative to centerline of equivalent circular fuselage, in.	Figure 3.2-2	12.5
$(df)_w = h = w$	Diameter of equivalent circular fuselage at wing, in.	Figure 3.2-2	49
Γ	Geometric dihedral of wing, deg	Figure 3.2-1	5.0
Summary: $(C_{l\beta})_{f(w)} + (C_{l\beta})_{f(\Gamma)} = 0.000376 - 0.000088$			
		= 0.000288 per deg	

TABLE 4.3.3-1
VERTICAL-TAIL CONTRIBUTION TO $C_{l\beta}$

$$(C_{l\beta})_{v(wfh)} = - (C_{Y\beta})_{v(wfh)} \frac{z_v \cos \alpha_b + l_v \sin \alpha_b}{b_w}$$

Symbol	Description	Reference	Magnitude
$(C_{Y\beta})_{v(wfh)}$	Vertical-tail side force due to sideslip in presence of wing, fuselage, and horizontal tail, per deg	Table 4.1.4-1(c)	-0.0049
z_v	Distance from X-body axis to quarter chord of vertical-tail mean aerodynamic chord, in.	Figure 3.2-4	-45.9
l_v	Distance along X-body axis from center of gravity to quarter chord of vertical-tail mean aerodynamic chord, in.	Figure 3.2-4	164.9
b_w	Wing span, in.	Figure 3.2-1	492.0
Summary: $(C_{l\beta})_{v(wfh)} = -0.000521 \cos \alpha_b + 0.00187 \sin \alpha_b$			

(1)	(2)	(3)	(4)
α_b , deg	$\cos (1)$	$\sin (1)$	$(C_{l\beta})_{v(wfh)} = -0.000521(2) + 0.00187(3)$
-4	0.9976	-0.0698	-0.000650
-2	.9994	-.0349	-.000586
0	1.0000	0	-0.000521
2	.9994	.0349	-.000455
4	0.9976	0.0698	-0.000389
6	.9945	.1045	-.000323
8	0.9903	0.1392	-0.000256
10	.9848	.1736	-.000188
12	0.9781	0.2079	-0.000121

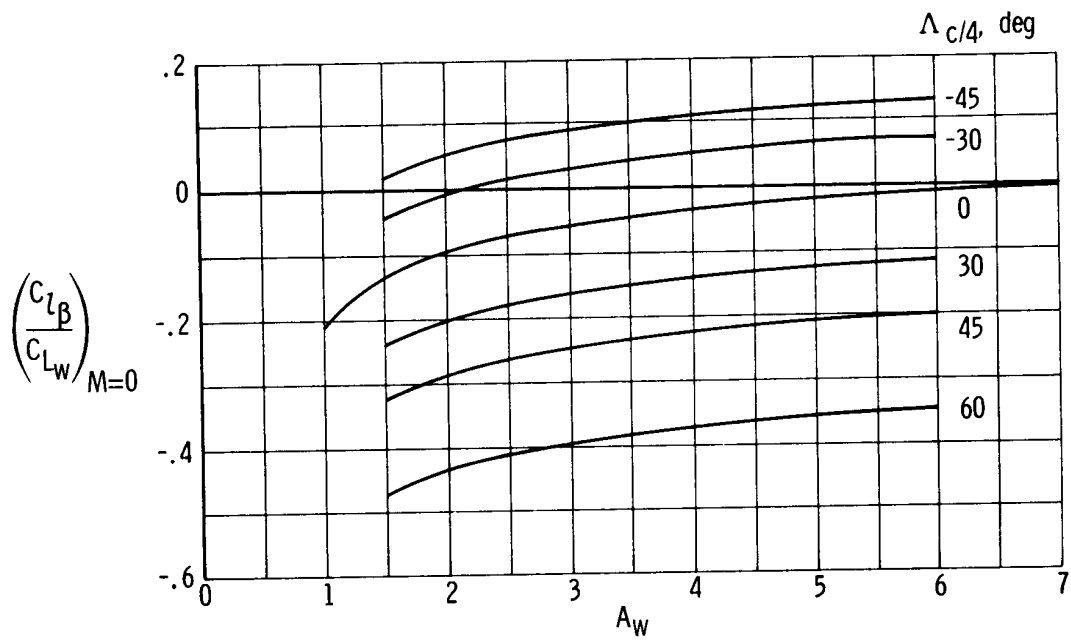
TABLE 4.3. 4-1
 c_{l_β} OF THE COMPLETE AIR PLANE

$$(c_{l_\beta})_{\text{prop}} = (c_{l_\beta})_{w_{\Gamma=0}} + (c_{l_\beta})_{\Gamma} + (c_{l_\beta})_{f(w)_{\Gamma=0}} + (c_{l_\beta})_{f(\Gamma)} + (c_{l_\beta})_{v(wfh)}$$

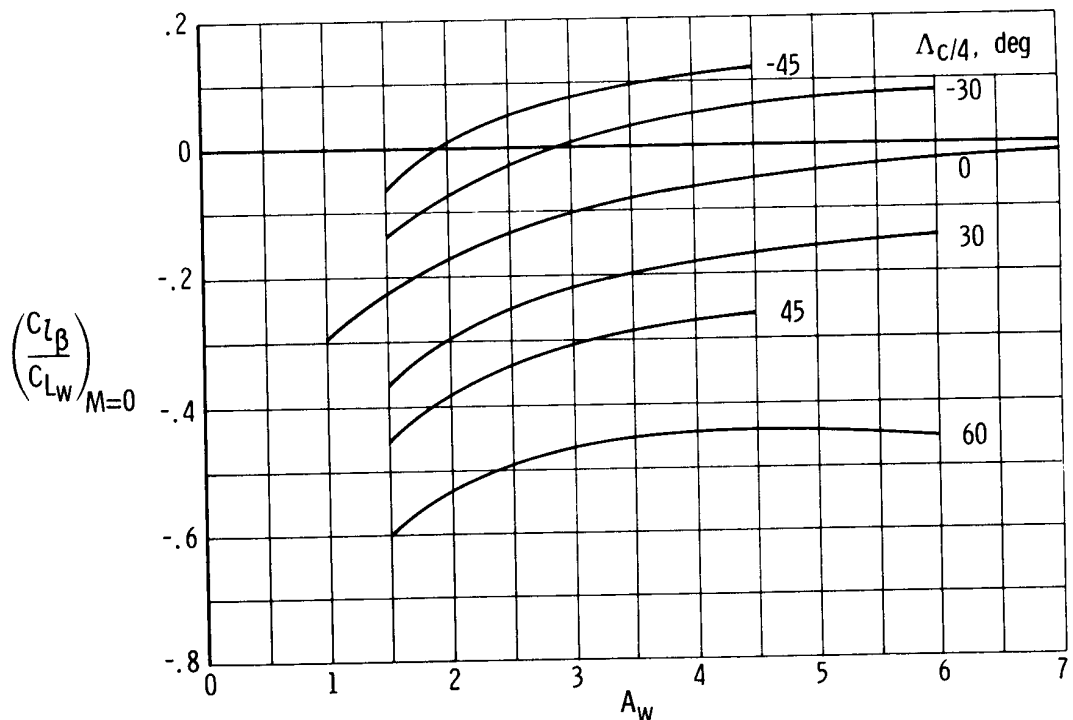
off

(1)	(2)	(3)	(4)	(5)	(6)
---	Figure 4.1. 1-1	Table 4.3. 1-1(c)	Table 4.3. 2-1	Table 4.3. 3-1	---
α_b , deg	c_{L_w}	$(c_{l_\beta})_{w_{\Gamma=0}} + (c_{l_\beta})_{\Gamma} =$ $-0.000348(2) - 0.00115$	$(c_{l_\beta})_{f(w)_{\Gamma=0}} + (c_{l_\beta})_{f(\Gamma)}$	$(c_{l_\beta})_{v(wfh)}$	$c_{l_\beta} =$ $(3) + (4) + (5)$
-4	0	-0.00115	0.000288	-0.000650	-0.001512
-2	.145	-.00120	.000288	-.000586	-.001498
0	0.292	-0.00125	0.000288	-0.000521	-0.001483
2	.437	-.00130	.000288	-.000455	-.001467
4	0.584	-0.00135	0.000288	-0.000389	-0.001451
6	.730	-.00140	.000288	-.000323	-.001435
8	0.875	-0.00145	0.000288	-0.000256	-0.001418
a ₁₀	1.023	-.00151	.000288	-.000188	-.001410
12	1.160	-0.00155	0.000288	-0.000121	-0.001383

^aLimit of linearity of lift curve.

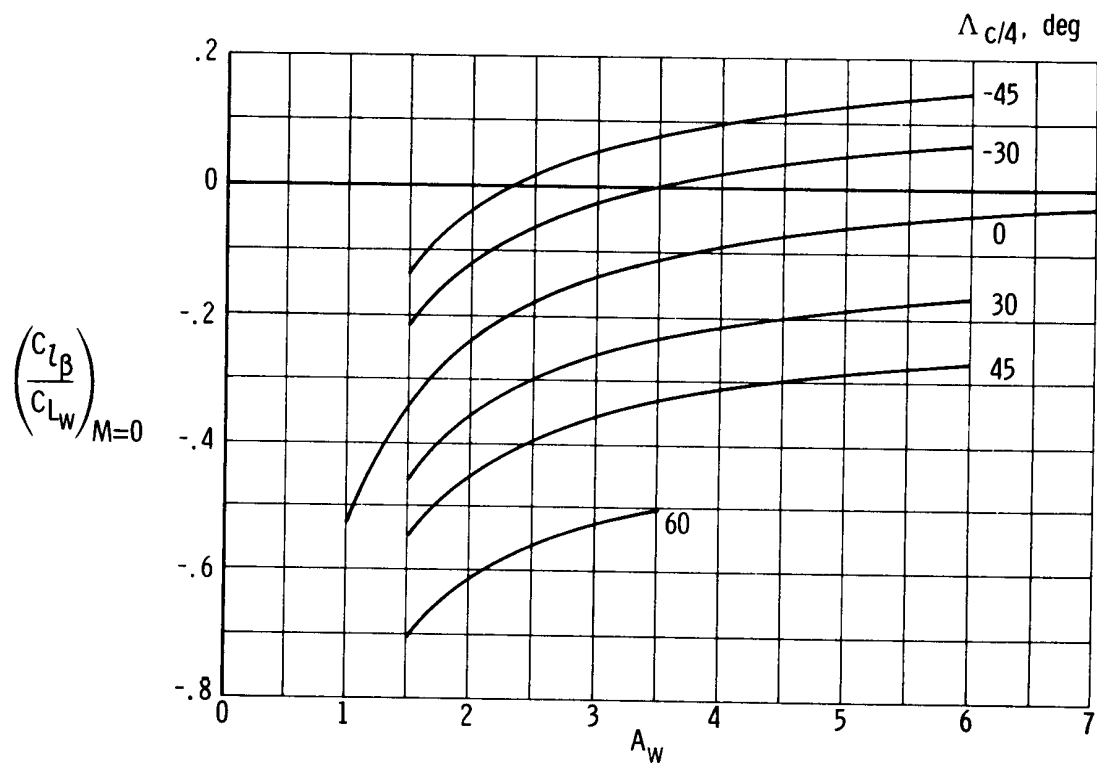


(a) $\lambda_w = 0.$

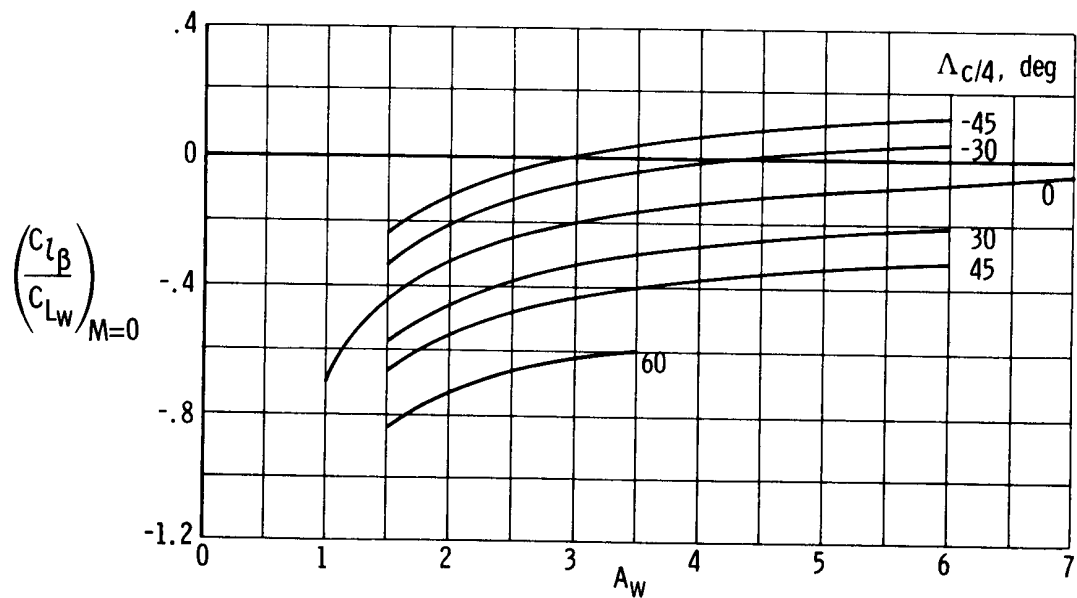


(b) $\lambda_w = 0.25.$

Figure 4.3.1-1. Variation of $\frac{C_l\beta}{C_{Lw}}$ with aspect ratio, sweep, and taper ratio (from ref. 10). $M = 0.$



(c) $\lambda_W = 0.50$.



(d) $\lambda_W = 1.0$.

Figure 4.3.1-1. Concluded.

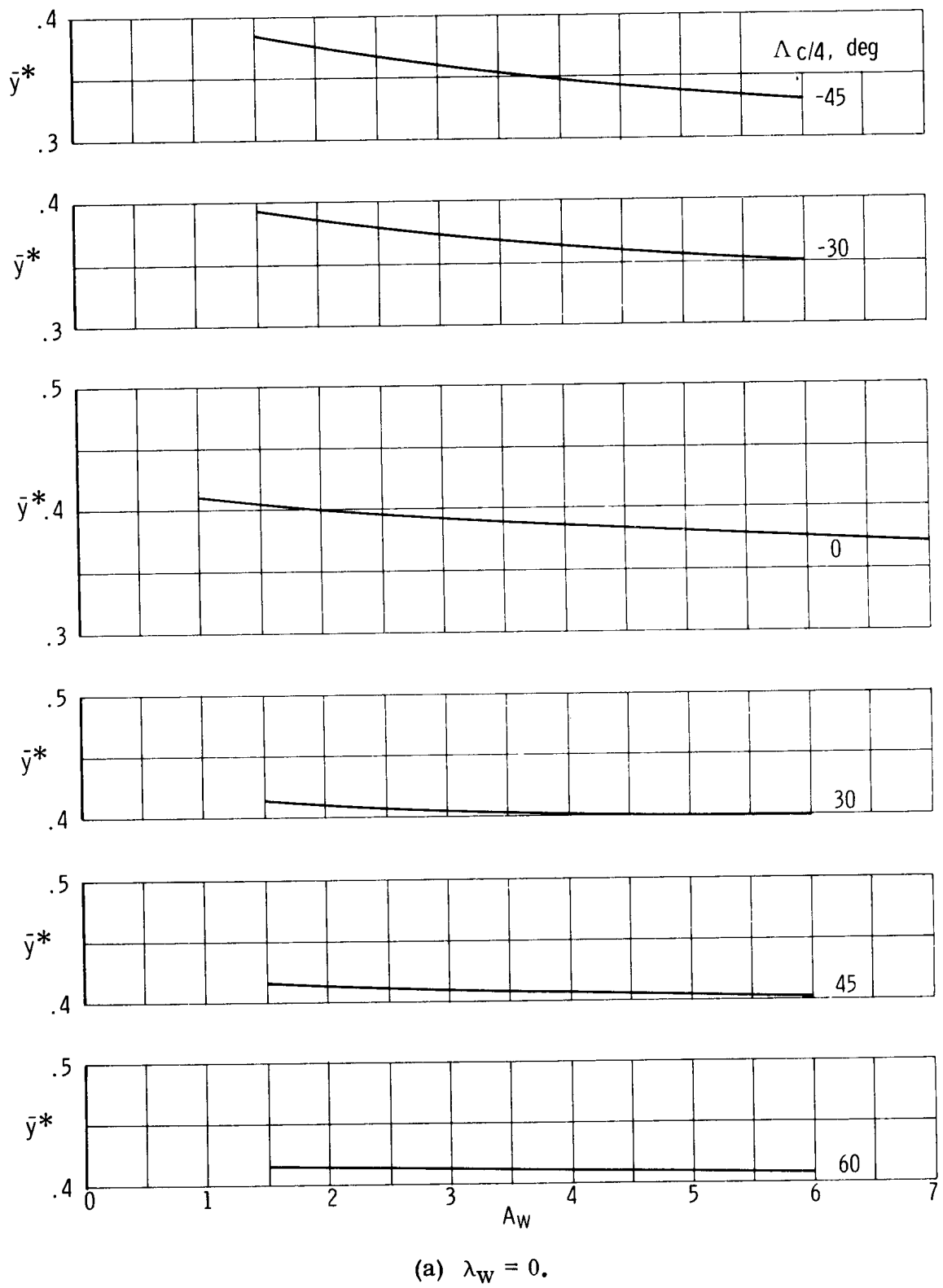
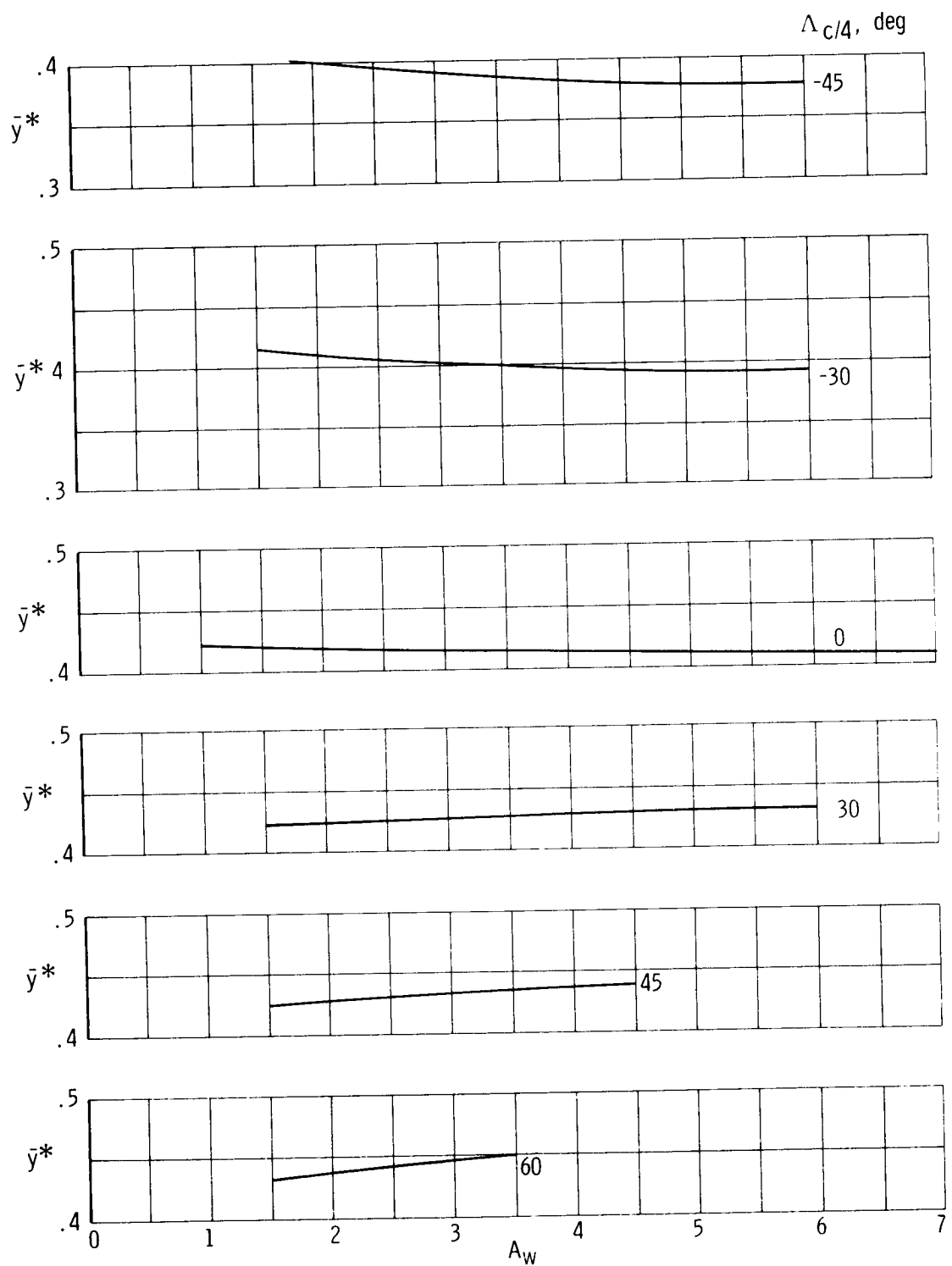
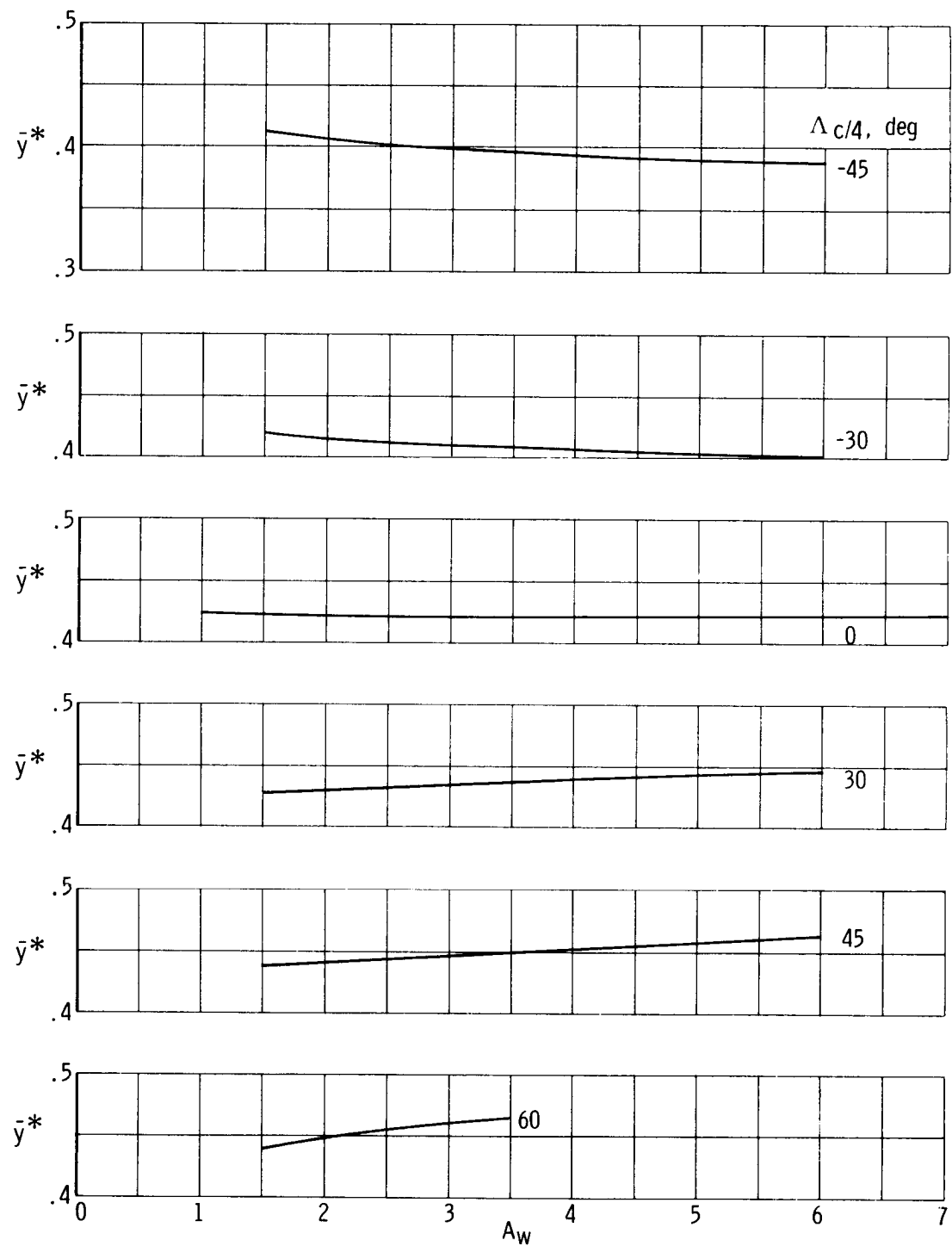


Figure 4.3.1-2. Spanwise location of centroid of angle-of-attack loading (from ref. 10).



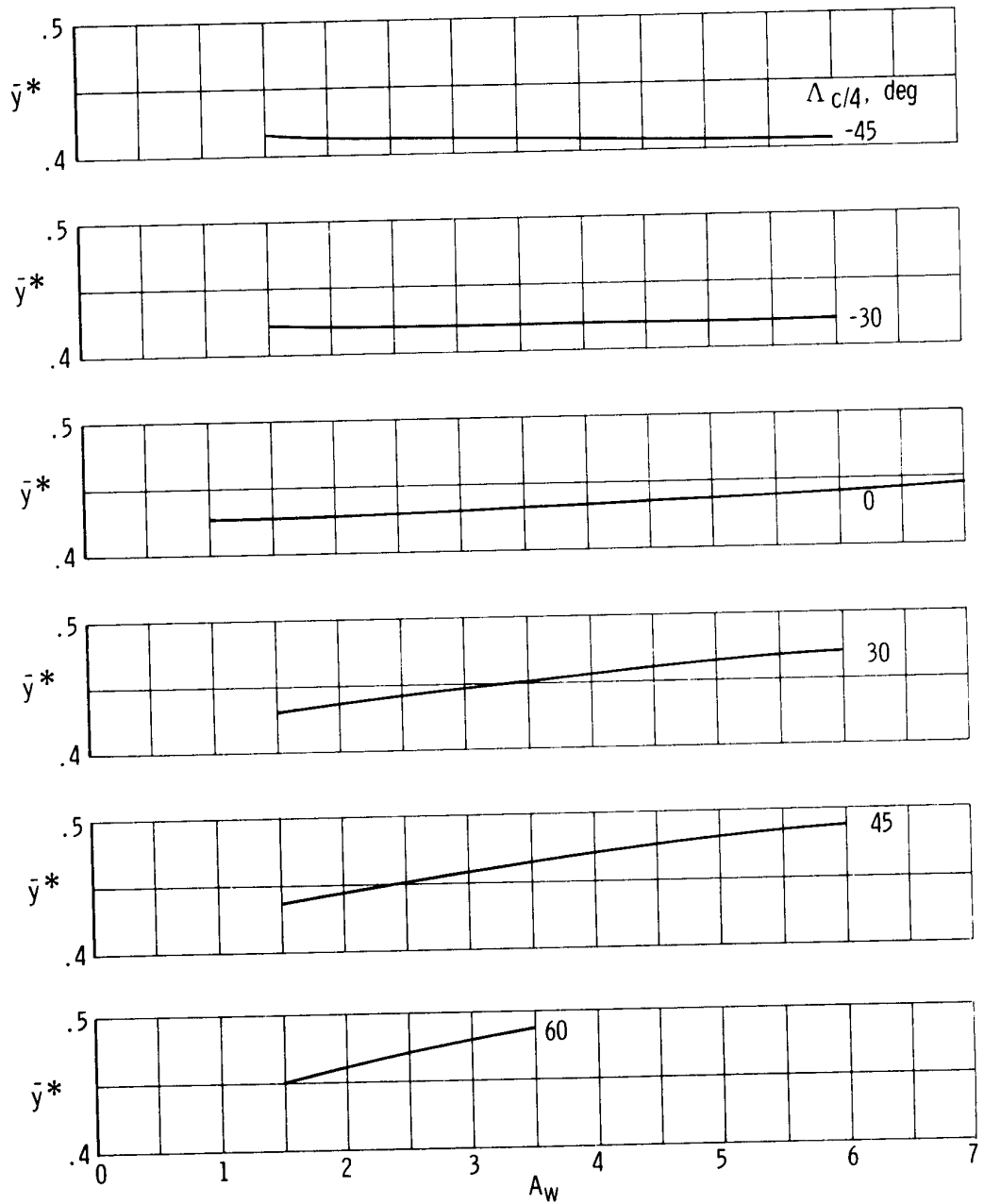
(b) $\lambda_W = 0.25$.

Figure 4.3.1-2. Continued.



(c) $\lambda_w = 0.5$.

Figure 4.3.1-2. Continued.



(d) $\lambda_w = 1.0$.

Figure 4.3.1-2. Concluded.

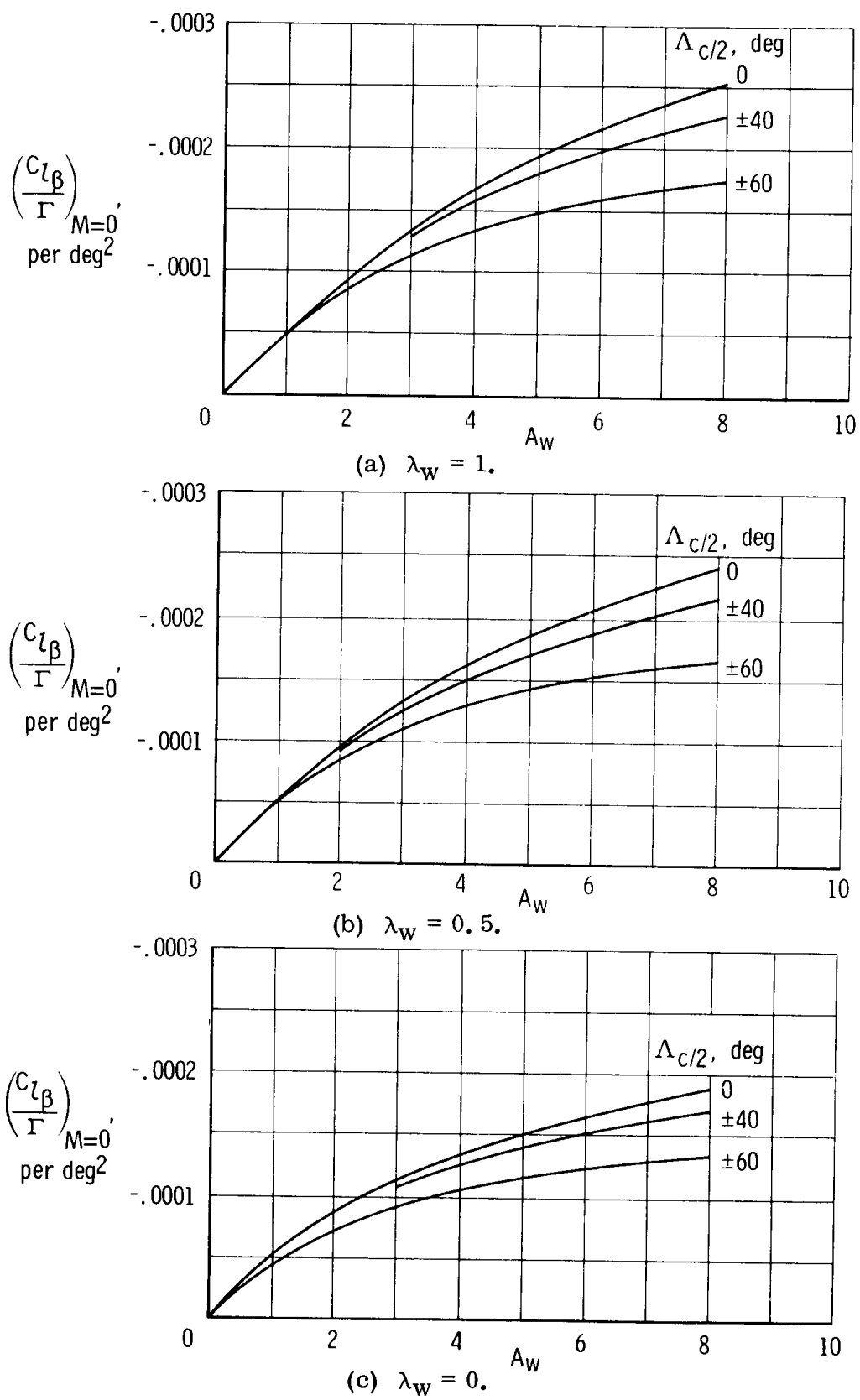


Figure 4.3.1-3. Effect of uniform geometric dihedral on wing $C_{l\beta}$ (from ref. 3). Subsonic speeds.

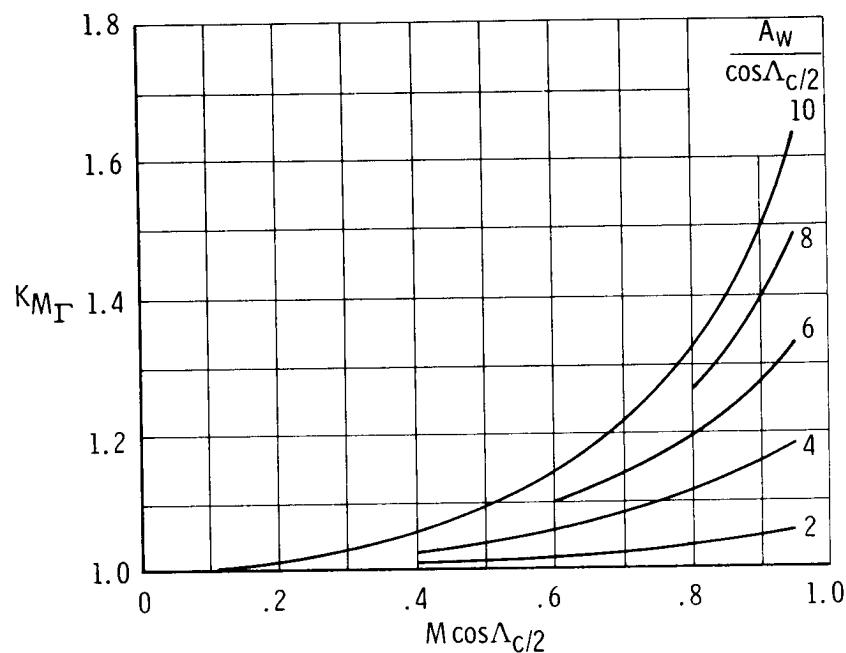


Figure 4.3.1-4. Compressibility correction to dihedral effect on wing $C_{l\beta}$ (from ref. 3). Subsonic speeds.

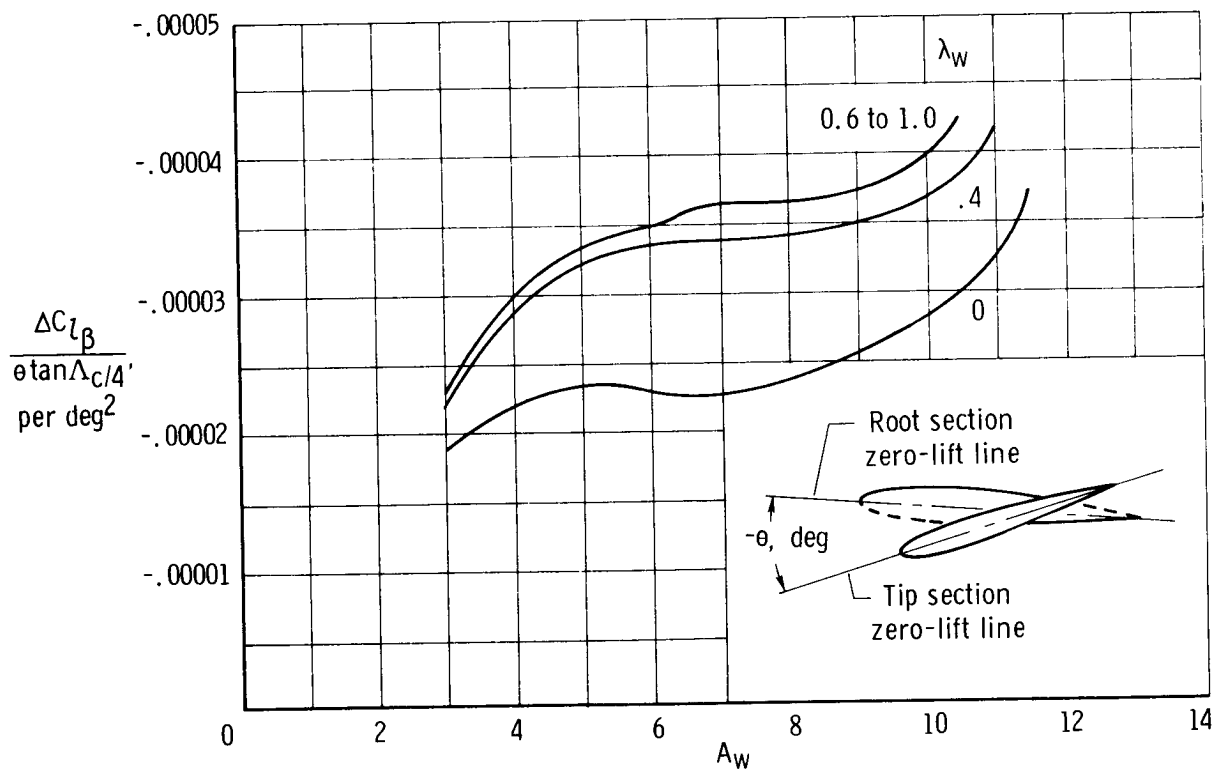


Figure 4.3.1-5. Effect of wing twist on wing $C_{l\beta}$ (from ref. 3).

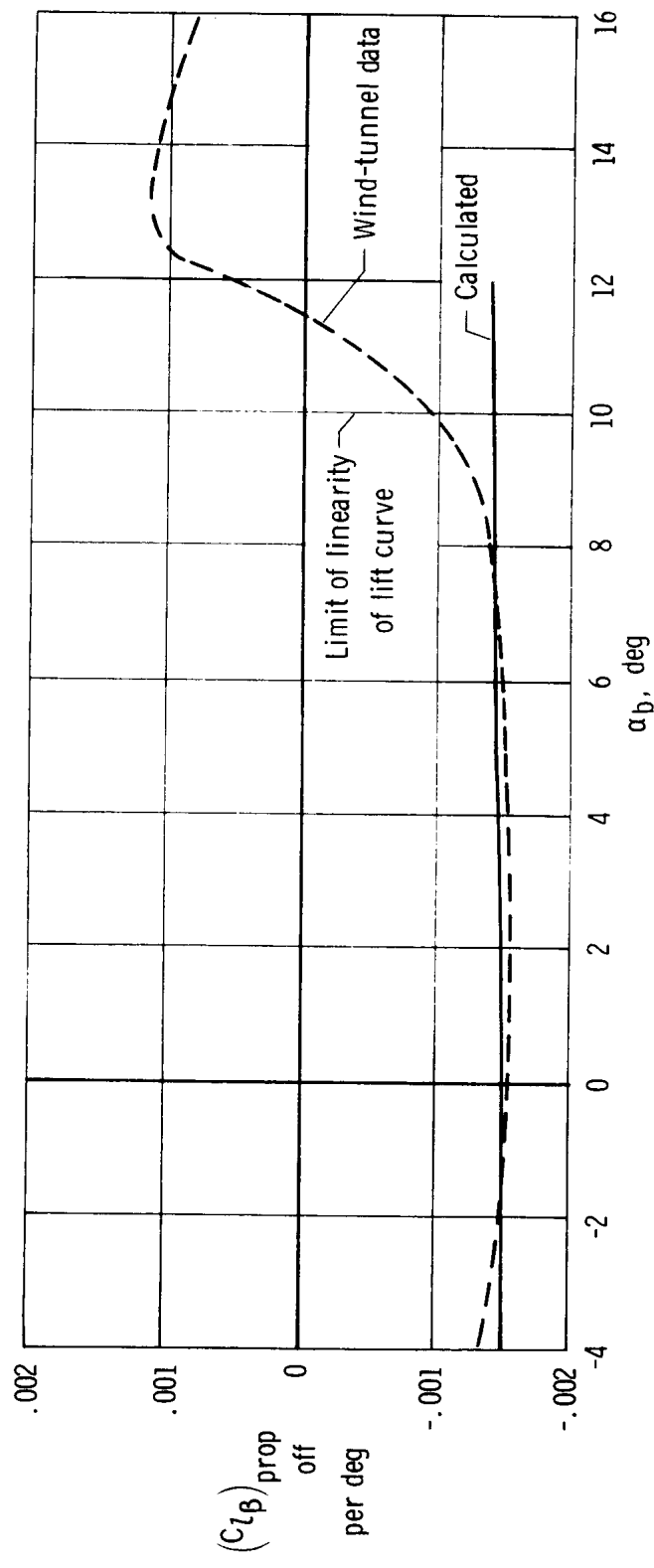


Figure 4.3.4-1. Comparison of calculated Cl_{β} with wind-tunnel data. Propellers off.

4.4 Rolling and Yawing Moments Due to Aileron Deflection

The rolling and yawing moments due to aileron deflection to be considered are for ailerons made up of plain, differentially operated trailing-edge flaps. The method to be used to obtain yawing moments due to aileron deflection, $C_{n\delta_a}$, is contingent on knowledge of the rolling moment due to aileron deflection, $C_{l\delta_a}$; thus, this is discussed first.

4.4.1 Rolling Moment Due to Aileron Deflection, $C_{l\delta_a}$

The method described in reference 13 was used to obtain the rolling-moment effectiveness, $C_{l\delta_a}$, for plain, differentially operated trailing-edge flaps. The method, based on simplified lifting-surface theory, is applicable up to a Mach number of approximately 0.6 and is valid if no flow separation exists for the wing angle of attack and surface deflection being considered.

For aileron panels rigged to have equal and opposite displacement, this method can be summarized by the following equation, in which the total aileron deflection is measured in a plane parallel to the plane of symmetry:

$$C_{l\delta'_a} = -\frac{1}{2} \frac{k}{B_1} (\alpha\delta)_{cl} \Delta \left(\frac{B_1}{k} C'_{l\delta'_a} \right) \quad (4.4.1-1a)$$

For differentially operated ailerons, that is, aileron panels having unequal and opposite displacement ($\delta'_{aL} \neq \delta'_{aR}$), this equation takes the following form:

$$C_{l\delta'_a} = -\frac{1}{2} \frac{k}{B_1} \Delta \left(\frac{B_1}{k} C'_{l\delta'_a} \right) \frac{\left\{ [(\alpha\delta)_{cl}]_L \delta_{aL} - [(\alpha\delta)_{cl}]_R \delta_{aR} \right\}}{\delta_{aL} - \delta_{aR}} \quad (4.4.1-1b)$$

When the aileron deflection is measured normal to the hinge line,

$$C_{l\delta_a} = \frac{C_{l\delta'_a}}{\cos \Lambda_{hl}} \quad (4.4.1-2)$$

In equations (4.4.1-1a) and (4.4.1-1b), loss in aileron panel effectiveness is accounted for by the section lift-effectiveness parameter, $(\alpha\delta)_{cl}$, which is based on the deflection of the individual aileron panels. For ailerons having chords equal to or less than 25 percent of the wing chord, the loss in effectiveness does not start until the aileron panel is deflected beyond about 12° . Thus, for equally deflected aileron panels, loss in effectiveness does not begin until the total aileron deflection, δ_a , is about 24° . For the subject airplane, which has differentially operated ailerons, the loss in effectiveness does not begin until the aileron deflection, δ_a , is about 21° . Because the

predicted aileron effectiveness is to be compared eventually with wind-tunnel and flight data from which $C_{l\delta_a}$ is based on aileron deflections of less than 21° , the two equations are identical for present purposes. Thus the first format (eq. (4.4.1-1a)) will be used.

In equations (4.4.1-1a) and (4.4.1-1b),

Δ_{hl} is the sweep of the hinge line, obtained from figure 3.2-1

$$B_1 = \sqrt{1 - M^2} \quad (4.4.1-3)$$

$$k = \frac{c_l \alpha}{2\pi} \quad (4.4.1-4)$$

where $c_{l\alpha}$ is the section lift-curve slope in radians, from section 4.1 in reference 1

The section lift-effectiveness parameter, $(\alpha\delta)_{cl}$, in equations (4.4.1-1a) and (4.4.1-1b) is obtained from

$$(\alpha\delta)_{cl} = - \frac{c_l \delta}{c_{l\alpha}} \quad (4.4.1-5)$$

where

$c_{l\alpha}$ is as defined from equation (4.4.1-4)

$c_{l\delta}$ is the section-lift effectiveness of plain trailing-edge flaps, defined by

$$c_{l\delta} = \frac{1}{B_1} \frac{c_{l\delta}}{(c_{l\delta})_{\text{theory}}} \left(c_{l\delta} \right)_{\text{theory}}^{K'} \quad (\text{ref. 3}) \quad (4.4.1-6)$$

where

$\left(c_{l\delta} \right)_{\text{theory}}$ is the theoretical section lift effectiveness of plain trailing-edge flaps (obtained from fig. 4.4.1-1) as a function of the airfoil section thickness ratio, t/c ,

and the effective ratio of the flap chord to the wing chord, $\left(\frac{c_f}{c} \right)_{av}$, within the aileron span

$\frac{c_{l\delta}}{(c_{l\delta})_{\text{theory}}}$ is the empirical correction for the section lift effectiveness of

plain trailing-edge flaps (obtained from fig. 4.4.1-2) as a function of $\left(\frac{c_f}{c}\right)_{av}$ and

$$\frac{c_l \alpha}{(c_l \alpha)_{theory}}$$

$(c_l \alpha)_{theory}$ in the ratio of $\frac{c_l \alpha}{(c_l \alpha)_{theory}}$ is obtained from the following equation

(eq. (4.1-1) in ref. 1), in radians:

$$(c_l \alpha)_{theory} = 6.28 + 4.7(t/c)(1 + 0.00375 \varphi_{te}) \quad (4.4.1-7)$$

K' is an empirical correction factor for the section-lift effectiveness of plain trailing-edge flaps at high flap deflections (obtained from fig. 4.4.1-3) as a function

of flap deflection, δ_f , and $\left(\frac{c_f a}{c_w}\right)_{av}$

The parameter $\Delta\left(\frac{B_1}{k} C_l' \delta_a'\right)$ in equations (4.4.1-1a) and (4.4.1-1b) defines the difference in the roll effectiveness of a full-chord aileron extending from the plane of symmetry to the outboard tip of the aileron, $\eta_o = y_o/(b/2)$, and a full-chord aileron extending to the inboard tip, $\eta_i = y_i/(b/2)$. This parameter (obtained from fig. 4.4.1-4) is a function of η , $\frac{B_1 A}{k}$, wing taper ratio, λ , and

$$\Lambda_{B_1} = \tan^{-1} \frac{\tan \Lambda c/4}{B_1} \text{ in degrees} \quad (4.4.1-8)$$

Figure 4.4.1-5 shows a cross plot of figure 4.4.1-4 used to obtain $\Delta\left(\frac{B_1}{k} C_l' \delta_a'\right)$ for the subject airplane. The cross plots were obtained at $\eta_o = 0.977$ and $\eta_i = 0.685$ for a wing taper ratio of 0.51 and $\Lambda_{B_1} = -2.5^\circ$.

The calculations for the rolling-moment effectiveness of the ailerons of the subject airplane are summarized in table 4.4.1-1. A comparison of the calculated $C_l \delta_a$ for the propeller-off condition with wind-tunnel data obtained at $T_c' = 0$ (fig. 4.4.1-6) shows reasonably good correlation.

4.4.2 Yawing Moment Due to Aileron Deflection, $C_n \delta_a$

Yawing moments due to aileron deflection depend upon the aileron geometry and are primarily the result of antisymmetric change in induced drag of the wing due to the displacement of the ailerons. The yawing moments could be affected by a net antisymmetric

change in profile drag due to aileron deflection, depending on the nose shape and gearing of the ailerons.

The antisymmetric change in induced drag due to aileron displacement produces an "adverse aileron yaw" which yaws the nose of the airplane away from the turn roll produced by the ailerons. This antisymmetric change in induced drag is not affected by differential gearing of the ailerons in normal aileron operation. For ailerons having equal and opposite displacement, the change in profile drag for each aileron is approximately equal and does not contribute to the yawing moments. However, for differentially geared ailerons, there is a net antisymmetric change in the profile drag which tends to alleviate the "adverse aileron yaw."

Although the subject airplane has differentially geared ailerons and both antisymmetric induced drag and profile drag changes due to aileron deflection should be calculated, there is a lack of design data from which to estimate the effect of the profile drag changes. Thus, for a first approximation, only the antisymmetric induced-drag effect is calculated.

The antisymmetric induced effect has been recognized as being proportional to the wing lift coefficient, C_{L_w} , and aileron rolling-moment effectiveness, $C_{l\delta_a}$. As a result of these proportionalities, the yawing moments due to aileron deflection can be represented by

$$C_{n\delta_a} = \left[\frac{(C_n/C_l)}{C_{L_w}} \right] C_{L_w} C_{l\delta_a} \cos \Lambda h l \quad (4.4.2-1)$$

or

$$C_{n\delta_a} = K C_{L_w} C_{l\delta_a} \cos \Lambda h l \quad (4.4.2-2)$$

where

K is an empirical factor dependent on planform geometry

C_{L_w} is the wing lift coefficient for zero aileron deflection

$C_{l\delta_a}$ is the rolling-moment effectiveness of the ailerons with aileron deflection measured perpendicular to the hinge line

For plain flap-type ailerons extending to the wing tip, the factor K may be obtained from figure 4.4.2-1 as a function of wing taper ratio, λ , wing aspect ratio, A , and inboard-tip location, $\eta_i = y_i/(b/2)$, of the aileron. This design chart, from reference 3, was originally presented in reference 8.

For ailerons not extending to the wing tip, equation (4.4.2-2) is used to obtain the difference in the yawing moments of two hypothetical ailerons. One of the hypothetical ailerons is assumed to extend from the inboard tip of the actual aileron to the wing tip,

and the other to extend from the outboard tip of the actual aileron to the wing tip. The difference in the yawing moments per unit δ_a thus obtained is the $C_{n\delta_a}$ of the actual aileron.

The calculations for the yawing moment due to aileron deflection of the subject airplane are summarized in table 4.4.2-1. A comparison of the calculated $C_{n\delta_a}$ for the propeller-off condition with wind-tunnel data obtained at $T'_c = 0$ (fig. 4.4.2-2) shows reasonably good correlation.

4.4.3 Symbols

A	wing aspect ratio
$B_1 = (1 - M^2)^{1/2}$	
b	wing span, in.
C_{L_w}	wing-lift coefficient
$C_{l\delta_a}$	aileron rolling-moment effectiveness derivative with the aileron deflection measured perpendicular to the hinge line, per rad of differential aileron deflection unless otherwise noted
$C_{l\delta'_a}$	$C_{l\delta_a}$ with aileron deflection measured in the plane parallel to the airplane plane of symmetry
$C_{n\delta_a}$	rate of change of the yawing-moment coefficient with the aileron deflection, per rad unless otherwise noted
c	airfoil section chord, in.
c_f	flap chord, in.
$\left(\frac{c_f}{c}\right)_{av}$	average ratio of the flap chord to the airfoil-section chord within the flap span
$\left(\frac{c_{f_a}}{c_w}\right)_{av}$	average (effective) ratio of the aileron chord to the wing chord within the aileron span
c_{f_a}	aileron-flap chord (aileron width), in.
$c_l \alpha$	experimental lift-curve slope of the wing airfoil section, per rad

$(c_l \alpha)_{\text{theory}}$	theoretical lift-curve slope of the airfoil section obtained from equation (4.4.1-7), per rad
$c_l \delta$	section lift effectiveness of a plain trailing-edge flap, per rad
$(c_l \delta)_{\text{theory}}$	theoretical section lift effectiveness of a plain trailing-edge flap, obtained from figure 4.4.1-1, per rad
$\frac{c_l \delta}{(c_l \delta)_{\text{theory}}}$	empirical correction factor (fig. 4.4.1-2) to obtain $c_l \delta$ from $(c_l \delta)_{\text{theory}}$
c_w	wing chord, in.
K	empirical correlation factor for determining $C_{n\delta_a}$ (considered proportional to the wing lift coefficient, C_{L_w} , and the aileron roll effectiveness, $C_l \delta_a$), obtained from figure 4.4.2-1
K'	empirical correction factor for the section-lift effectiveness of plain trailing-edge flaps at high flap deflections, obtained from figure 4.4.1-3
$k = \frac{c_l \alpha}{2\pi}$	
M	Mach number
\bar{q}	free-stream dynamic pressure, lb/sq ft
S_w	reference wing area, sq ft
T	thrust due to propellers
$T'_c = \frac{T}{\bar{q} S_w}$	
t/c	airfoil section thickness ratio
y	distance from and normal to the plane of symmetry to the point of interest on the flap, in.
y_i, y_o	distance from and normal to the plane of symmetry to the inboard and outboard edge of the aileron, respectively, in.
α_b	angle of attack of the airplane relative to the X-body axis, deg

$(\alpha\delta)_{c_l}$	section lift effectiveness parameter, $- \frac{c_l \delta}{c_l \alpha}$
Δ	difference
$\Delta \left(\frac{B_1}{k} c_l' \delta_a' \right)$	parameter defining the difference in the roll effectiveness of a full-chord aileron extending from the plane of symmetry to the outboard tip of the aileron and a full-chord aileron extending to the inboard tip, obtained from figure 4.4.1-4 as shown in figure 4.4.1-5
δ_a	differential aileron deflection measured normal to the hinge line, rad unless otherwise noted
δ_a'	differential aileron deflection measured in the plane parallel to the plane of symmetry, rad
δ_f	flap deflection measured normal to the hinge line, rad
η	aileron lateral coordinate, the distance y as a ratio of the wing semispan
η_i, η_o	distance y_i and y_o as a ratio of the wing semispan, respectively
φ_{te}	wing trailing-edge angle, deg
ΛB_1	compressible sweep parameter, $\tan^{-1} \left(\frac{\tan \Lambda c/4}{B_1} \right)$, deg
$\Lambda c/4, \Lambda h l$	sweep of the wing quarter-chord line and aileron hinge line, respectively, deg
λ	wing taper ratio
Subscripts:	
av	average
L, R	left and right, respectively

TABLE 4.4.1-1

ROLLING MOMENTS DUE TO AILERONS, $C_l \delta_a$

$$C_l \delta_a = -\frac{1}{2} \frac{k}{B_1} (\alpha_\delta)_{c_l} \Delta \left(\frac{B_1}{k} C'_l \delta'_a \right) \frac{1}{\cos \Lambda_{hl}}$$

(a) Section lift-effectiveness parameter of ailerons, $(\alpha_\delta)_{c_l}$

Symbol	Description	Reference	Magnitude
M	Mach number	Wind-tunnel test condition	0.083
$\left(\frac{c_f a}{c_w}\right)_{av}$	Effective ratio of aileron chord to wing chord within the aileron span	Figure 3.2-1	0.27
t/c	Thickness ratio of wing-airfoil section (NACA 64 ₂ A215)	Table 4.1-1 of reference 1	.15
φ_{te}	Wing section trailing-edge angle, deg	Table 4.1-1 of reference 1	15.8
$c_l \alpha$	Wing section lift-curve slope, rad	Table 4.1-1 of reference 1	5.444
$(c_l \alpha)_{theory}$	$6.28 + 4.7(t/c)(1 + 0.00375\varphi_{te})$	Equation (4.4.1-7)	7.027
$\frac{c_l \alpha}{(c_l \alpha)_{theory}}$	-----	-----	.775
$(c_l \delta)_{theory}$	Theoretical effectiveness of flap (aileron) section, function of $\left(\frac{c_f}{c}\right)_{av}$ and (t/c), rad	Figure 4.4.1-1	4.35
$\frac{c_l \delta}{(c_l \delta)_{theory}}$	Empirical correction to $(c_l \delta)_{theory}$, function of $\left(\frac{c_f}{c}\right)_{av}$ and $\frac{c_l \alpha}{(c_l \alpha)_{theory}}$	Figure 4.4.1-2	.622
B ₁	$\sqrt{1 - M^2}$, compressibility correction factor	-----	0.997
K'	Empirical correction factor for large flap deflections	Figure 4.4.1-3	1.0 up to 12° per flap
$c_l \delta$	$\frac{1}{B_1} \frac{c_l \delta}{(c_l \delta)_{theory}} (c_l \delta)_{theory} K'$, rad	Equation (4.4.1-6)	2.71
Summary: $(\alpha_\delta)_{c_l} = -\frac{c_l \delta}{c_l \alpha} = -\frac{2.71}{5.44} = -0.498$			

TABLE 4.4.1-1 (Concluded)

$$(b) \text{ Aileron roll-effectiveness parameter, } \Delta \left(\frac{B_1}{k} C_{l\delta_a}' \right)$$

Symbol	Description	Reference	Magnitude
M	Mach number	Wind-tunnel test condition	0.083
B ₁	$\sqrt{1 - M^2}$, compressibility correction factor	Equation (4.4.1-3)	.997
A	Wing aspect ratio	Figure 3.2-1	7.5
λ	Wing taper ratio	Figure 3.2-1	.513
$\Lambda_c/4$	Wing sweep along quarter-chord line, deg	Figure 3.2-1	-2.5
Λ_{B_1}	$\tan^{-1} \left(\frac{\tan \Lambda_c/4}{B_1} \right)$ compressible sweep parameter	Equation (4.4.1-8)	≈ -2.5
$c_{l\alpha}$	Wing section lift-curve slope, rad	Table 4.4.1-1(a)	5.44
k	$\frac{c_{l\alpha}}{2\pi}$	Equation (4.4.1-4)	.867
$\frac{B_1 A}{k}$	-----	-----	8.62
η_i	Inboard edge of aileron, $y_i/(b/2)$	Figure 3.2-1	0.685
η_o	Outboard edge of aileron, $y_o/(b/2)$	Figure 3.2-1	.977
Summary: On basis of figure 4.4.1-5, which shows cross plots of figure 4.4.1-4 at $\eta_i = 0.685$ and $\eta_o = 0.997$ for $\Lambda_{B_1} = -2.5^\circ$ and $\lambda = 0.51$, $\Delta \left(\frac{B_1}{k} C_{l\delta_a}' \right) = 0.305$ per rad			

$$(c) \text{ Roll effectiveness of ailerons, } C_{l\delta_a}$$

Symbol	Description	Reference	Magnitude
B ₁	Compressibility correction factor	Table 4.4.1-1(b)	0.997
k	$\frac{c_{l\alpha}}{2\pi}$	Table 4.4.1-1(b)	.867
$(\alpha\delta)_{cl}$	Section lift-effectiveness parameter of ailerons	Table 4.4.1-1(a)	-.498
$\Delta \left(\frac{B_1}{k} C_{l\delta_a}' \right)$	Aileron roll-effectiveness parameter	Table 4.4.1-1(b)	.305
Λ_{hl}	Wing sweep along aileron hinge line, deg	Figure 3.2-1	-9.5
Summary: $C_{l\delta_a} = -\frac{1}{2} \frac{k}{B_1} (\alpha\delta)_{cl} \Delta \left(\frac{B_1}{k} C_{l\delta_a}' \right) \frac{1}{\cos \Lambda_{hl}} = 0.0670$ per rad $= 0.00117$ per deg			

TABLE 4.4.2-1

YAWING MOMENTS DUE TO AILERONS, $C_{n\delta_a}$

$$C_{n\delta_a} = K C_{L_w} C_{l\delta_a} \cos \alpha_h l$$

Symbol	Description	Reference	Magnitude
A	Wing aspect ratio	Figure 3.2-1	7.5
λ	Wing taper ratio	Figure 3.2-1	.513
η_i	Inboard edge of aileron as ratio of semispan	Table 4.4.1-1(b)	.685
η_o	Outboard edge of aileron as ratio of semispan	Table 4.4.1-1(b)	.977 (≈ 1.0)
K	Empirical factor, $f(A_w, \lambda, \eta)$	Figure 4.4.2-1	-.160
C_{L_w}	Wing lift coefficient based on $S_w = 178$ sq ft	Figure 4.1.1-1	$f(\alpha_b)$
$C_{l\delta_a}$	Aileron effectiveness in roll, per deg	Table 4.4.1-1(c)	0.00117
$\alpha_h l$	Wing sweep along aileron hinge line, deg	Figure 3.2-1	-9.5
Summary: $C_{n\delta_a} = -0.160(C_{L_w})(0.00117)(0.9863)$ $= -0.000185 C_{L_w}$ per deg			

(1)	(2)	(3)
-----	Figure 4.1.1-1	-----
α_b , deg	C_{L_w}	$C_{n\delta_a} = -0.000185(2)$
-4	0	0
0	.292	-.000054
4	.584	-.000108
8	.875	-.000162
12	1.160	-.000215

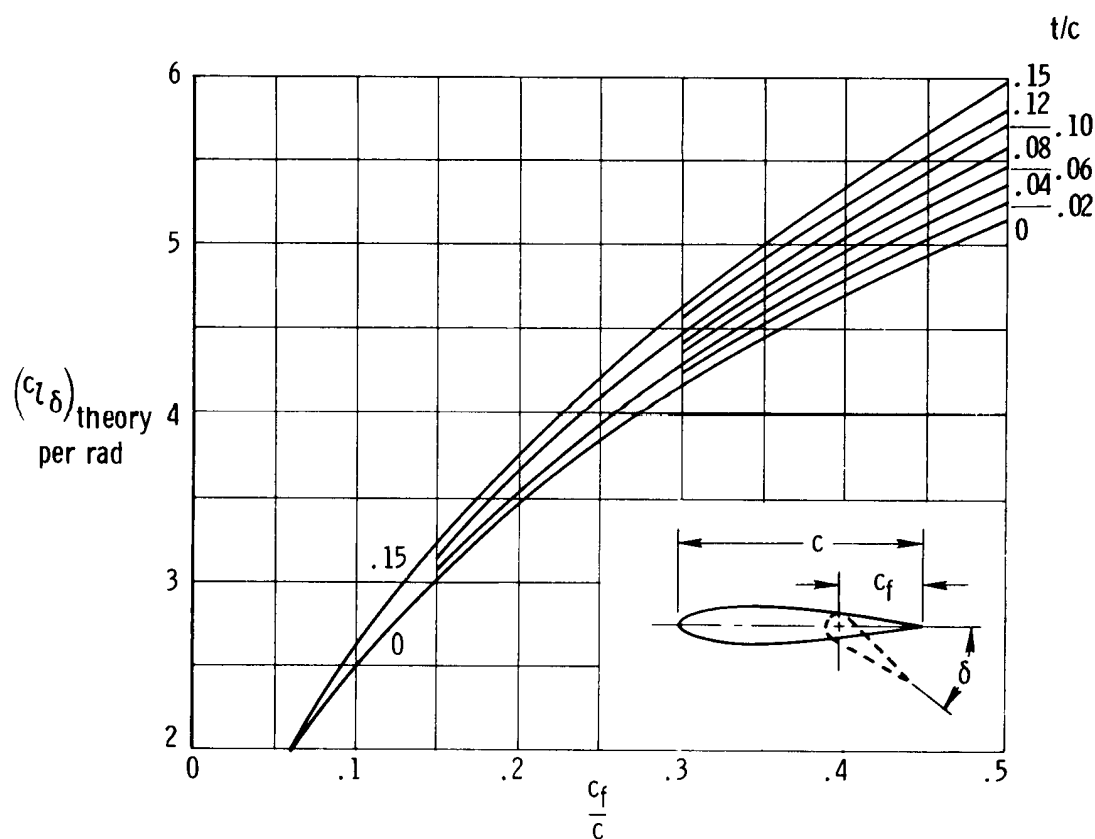


Figure 4.4.1-1. Theoretical lift effectiveness of plain trailing-edge flaps (from ref. 3).

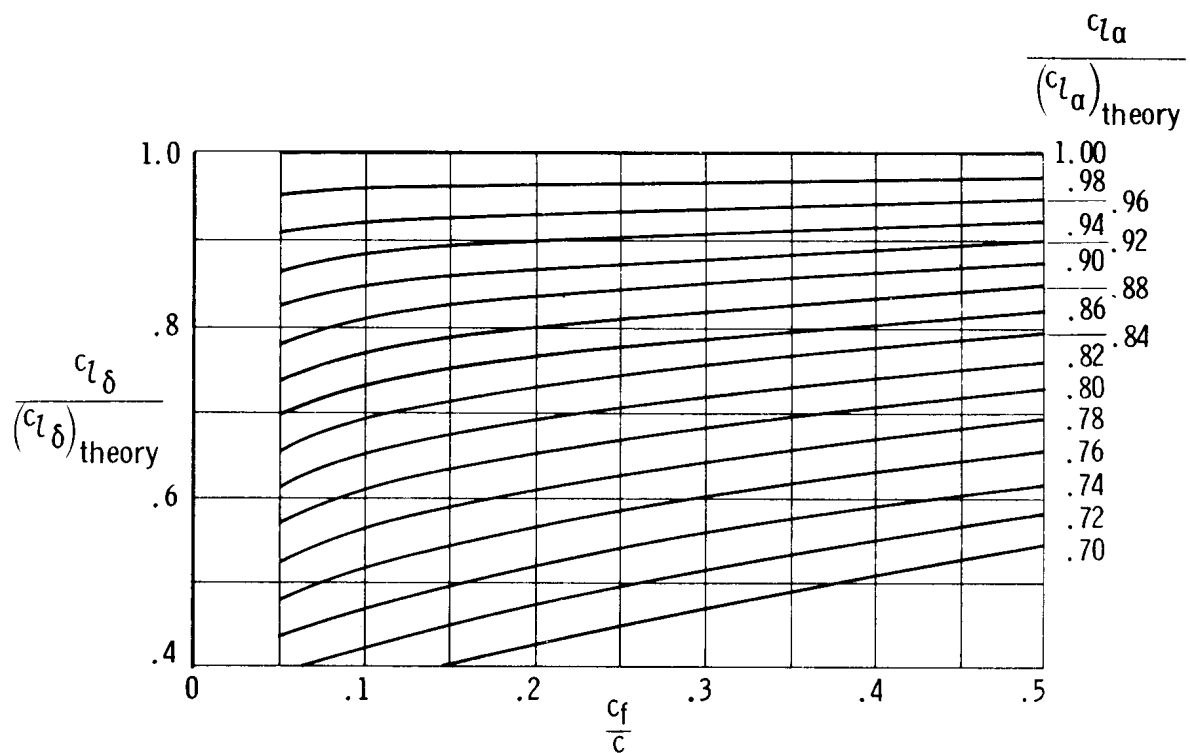


Figure 4.4.1-2. Empirical correction for lift effectiveness of plain trailing-edge flaps (from ref. 3).

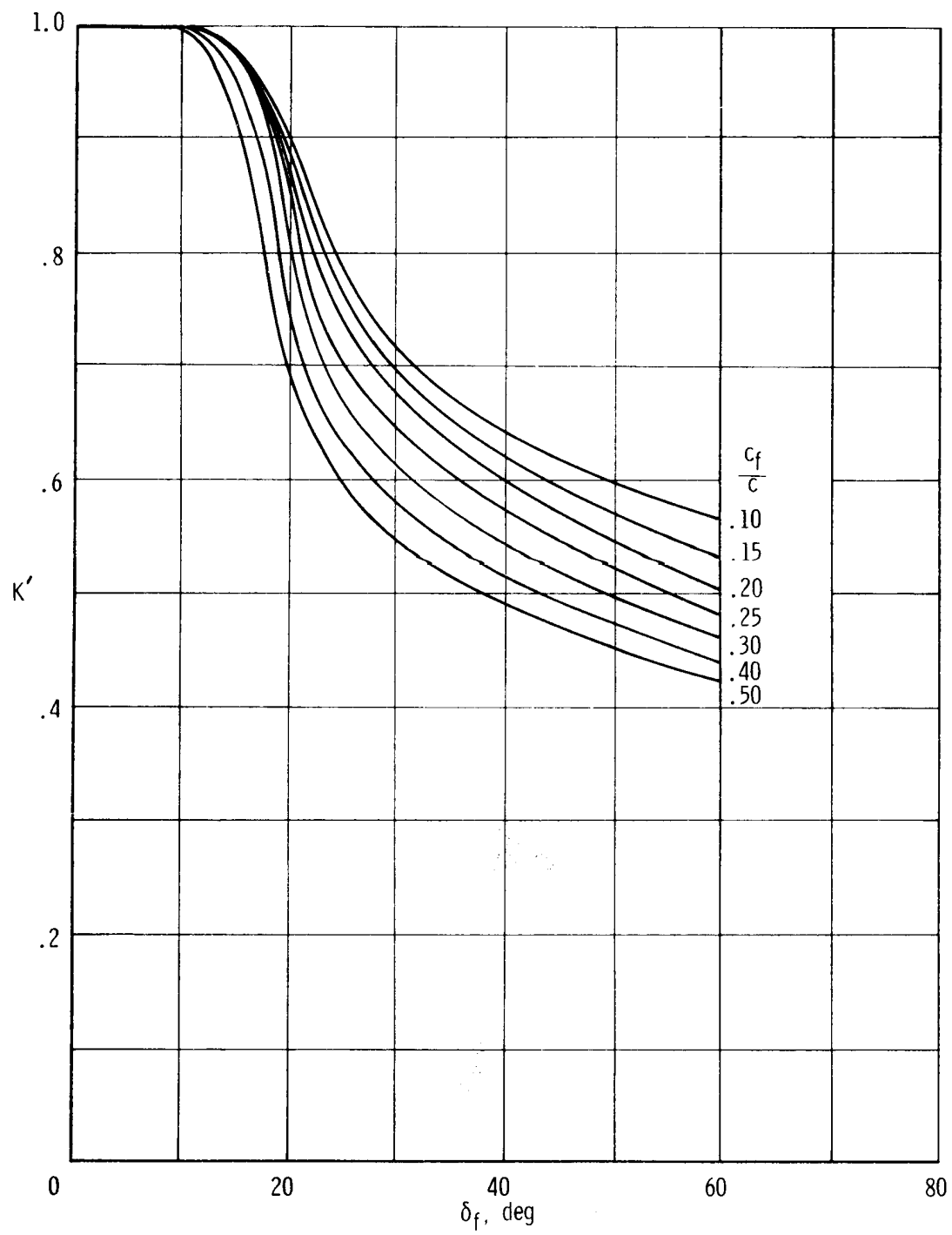
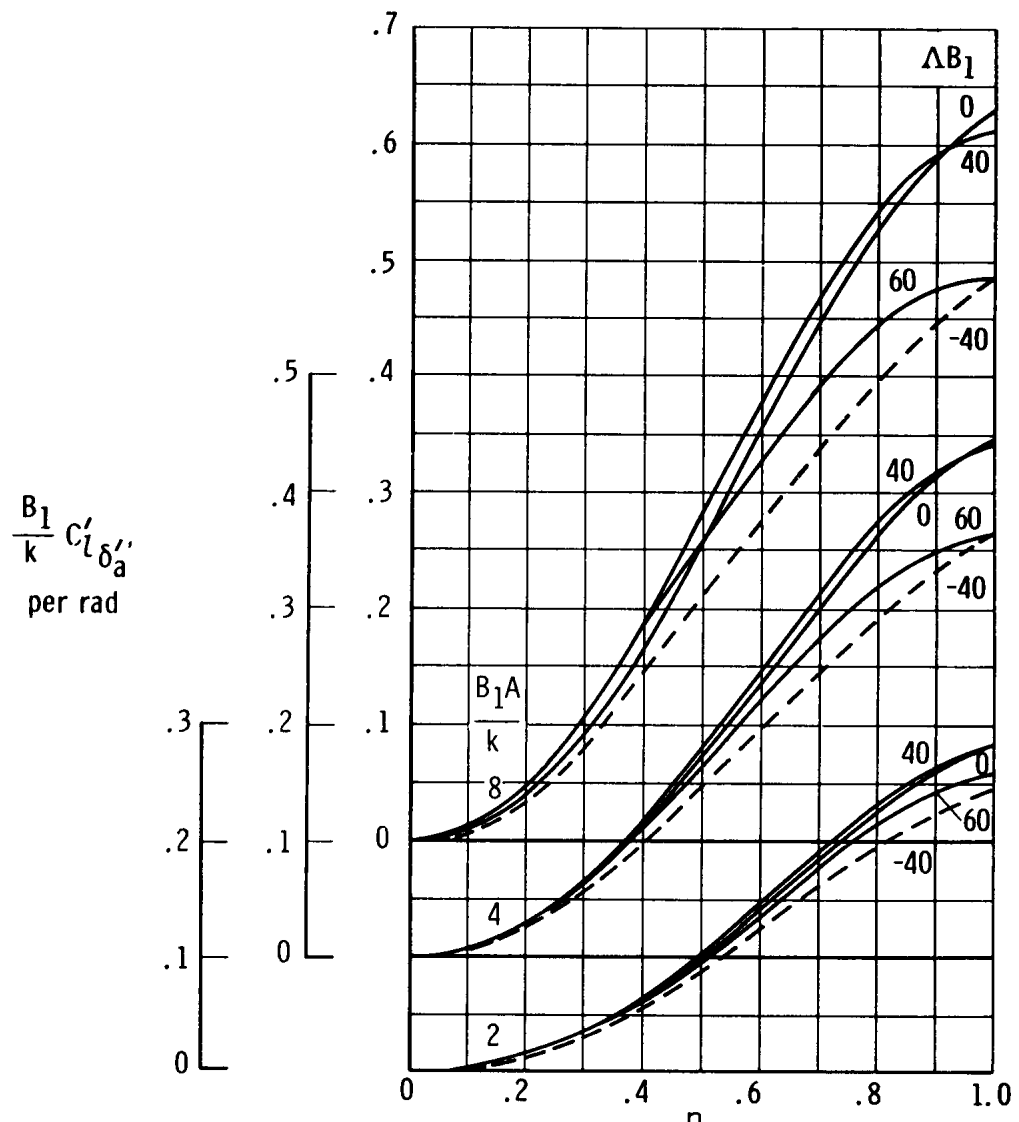
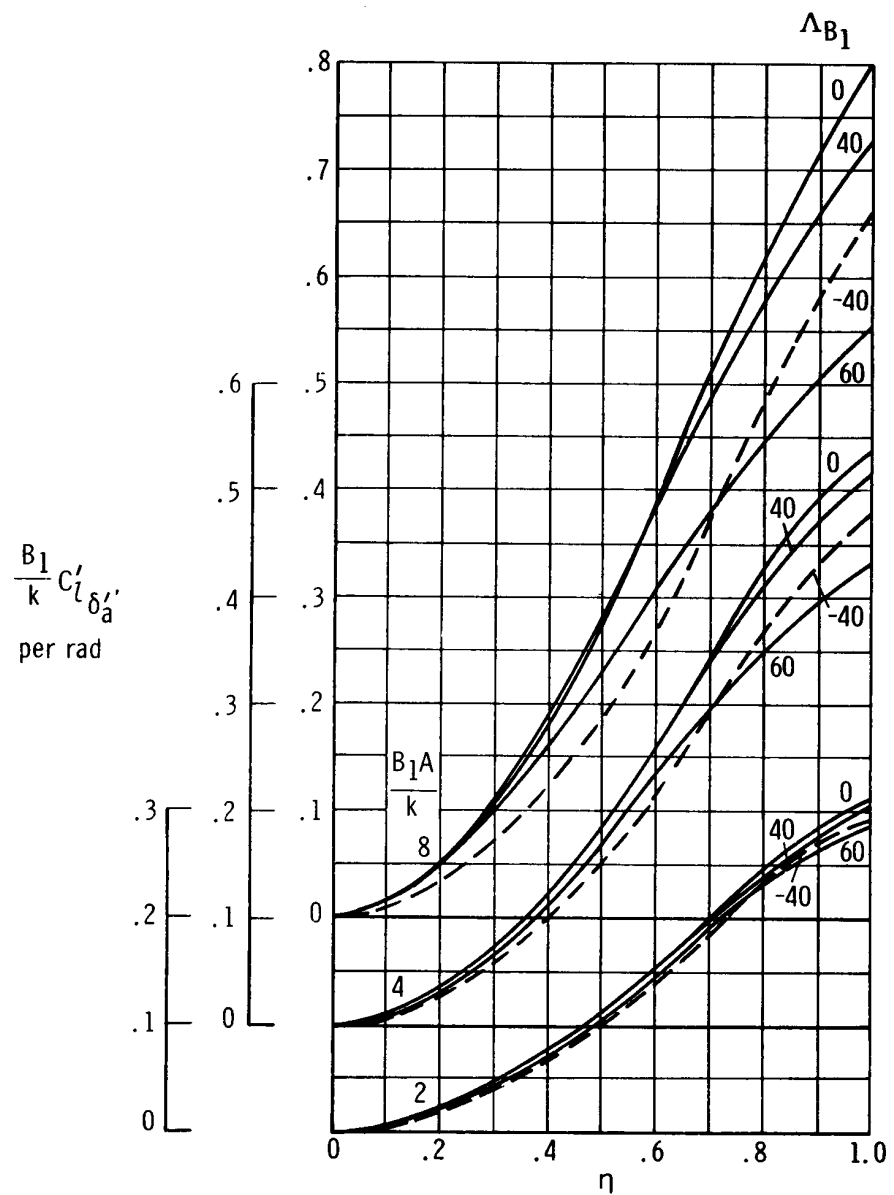


Figure 4.4.1-3. Empirical correction for lift effectiveness of plain trailing-edge flaps at high flap deflections (from ref. 3).



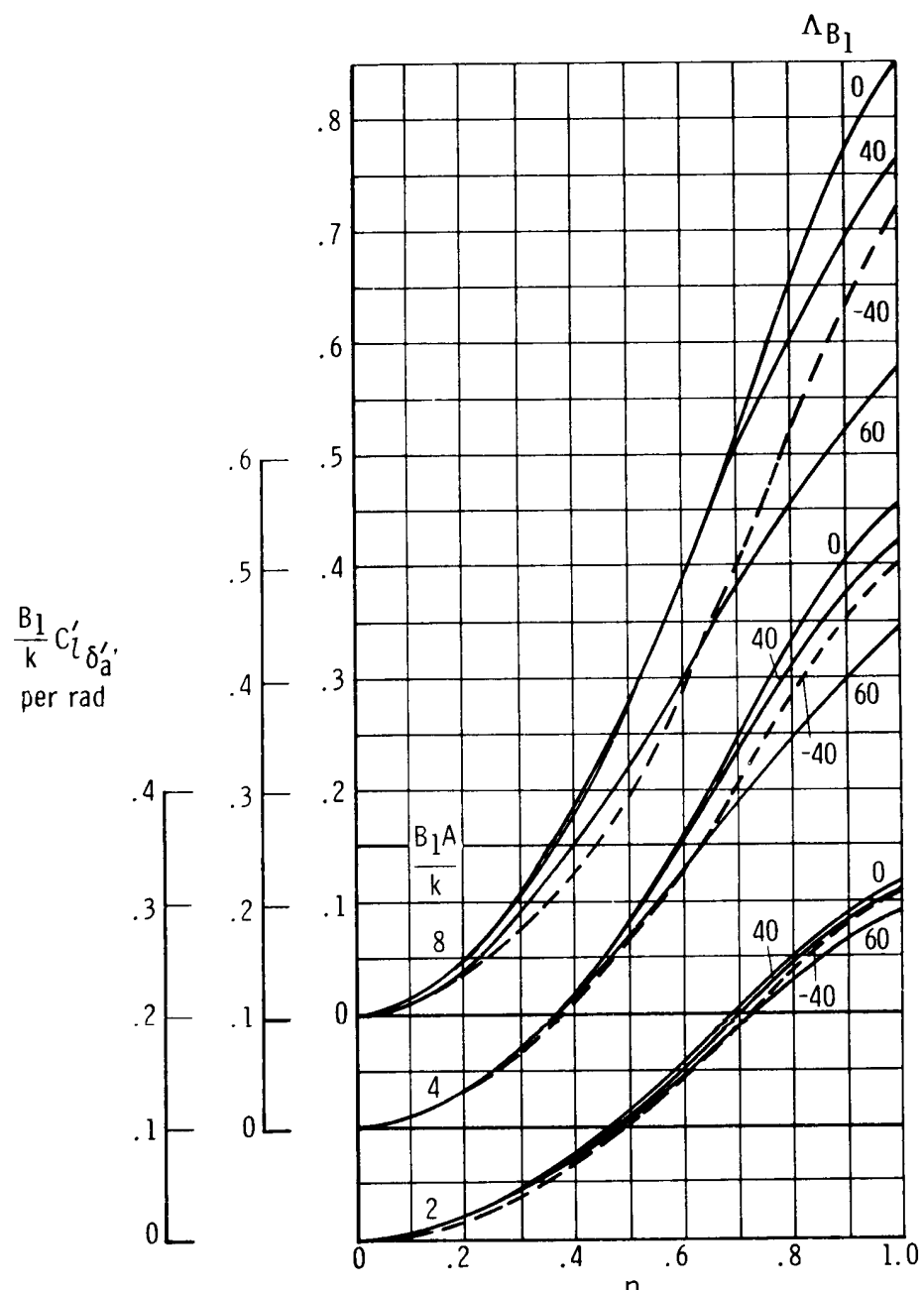
(a) $\lambda = 0.$

Figure 4.4.1-4. Subsonic aileron rolling-moment parameter (from ref. 13).



(b) $\lambda = 0.5.$

Figure 4, 4, 1-4. Continued.



(c) $\lambda = 1.0$.

Figure 4.4. 1-4. Concluded.

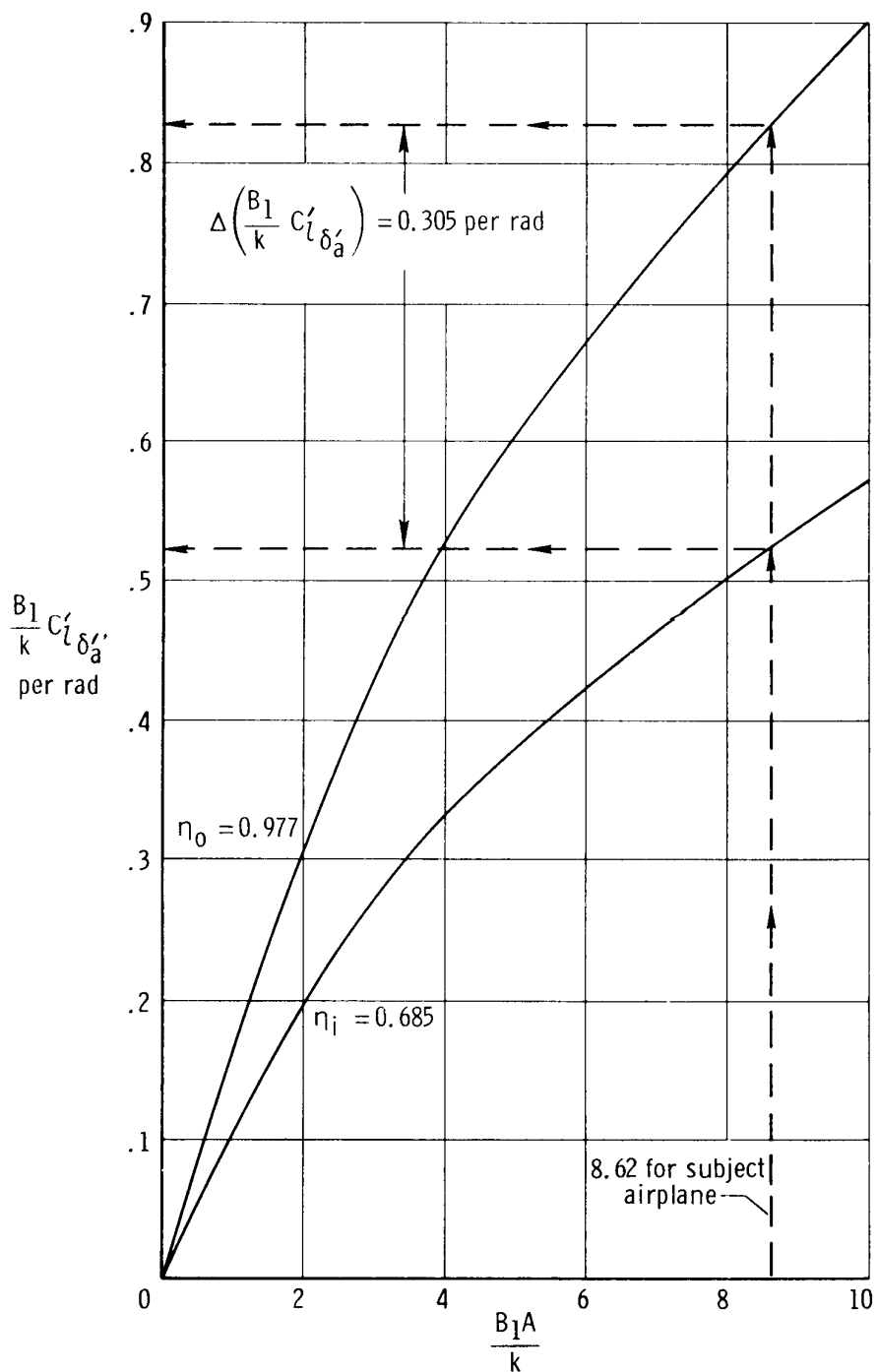


Figure 4.4.1-5. Cross plot of figure 4.4.1-4 to obtain $\Delta\left(\frac{B_1}{k} C_l' \delta_a'\right)$ for subject airplane. $\Delta B_1 = -2.5$; $\lambda = 0.51$.

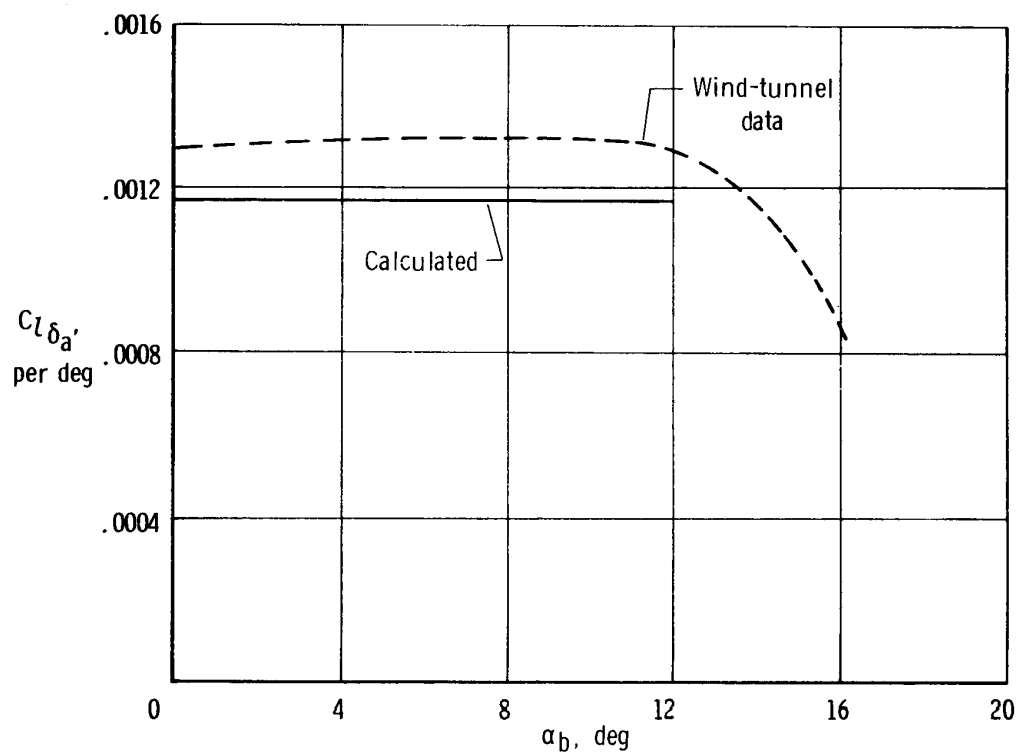


Figure 4.4.1-6. Comparison of calculated rolling-moment effectiveness of ailerons of subject airplane with wind-tunnel data.

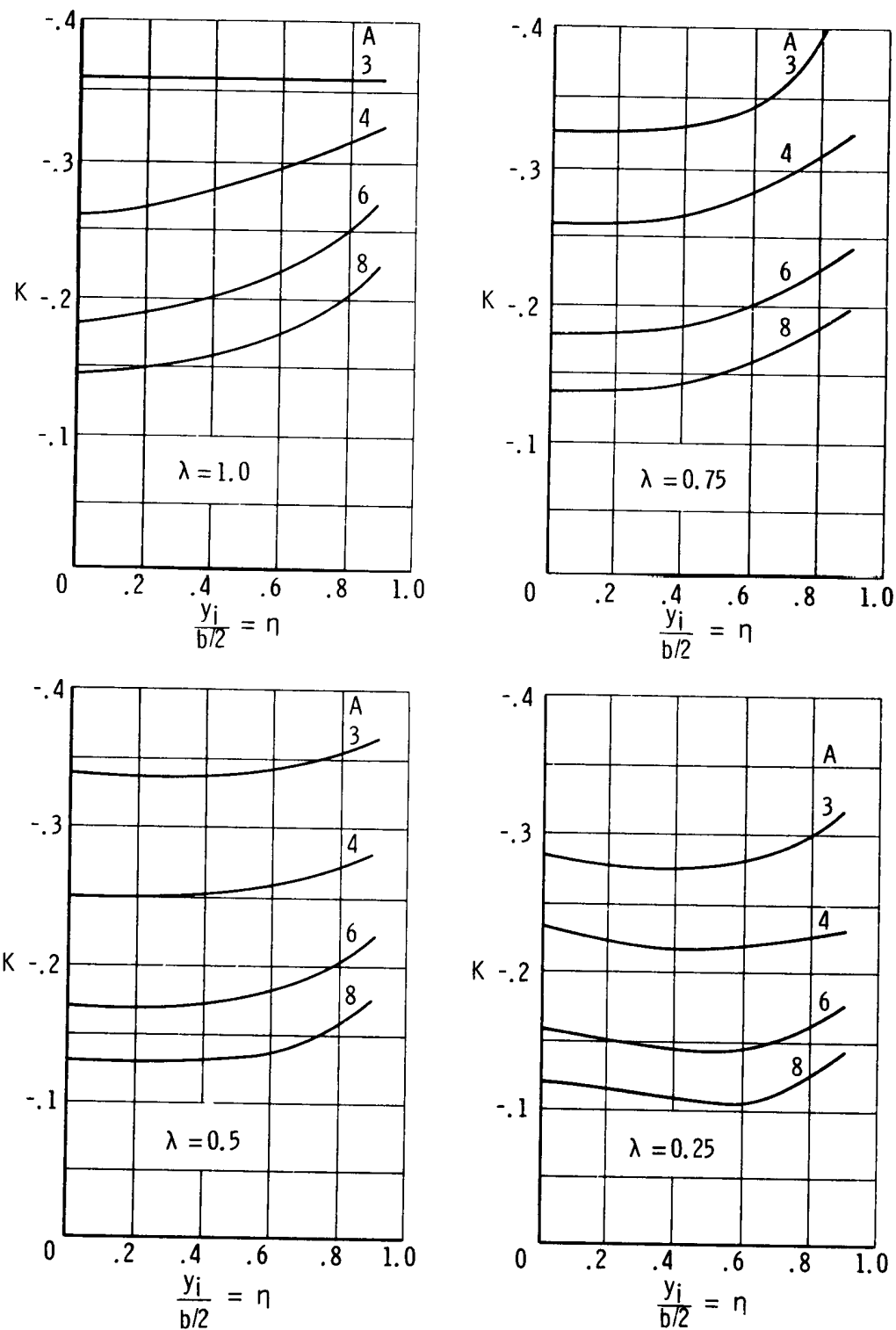


Figure 4.4.2-1. Correlation constant for determining yawing moment due to aileron deflection (from ref. 8).

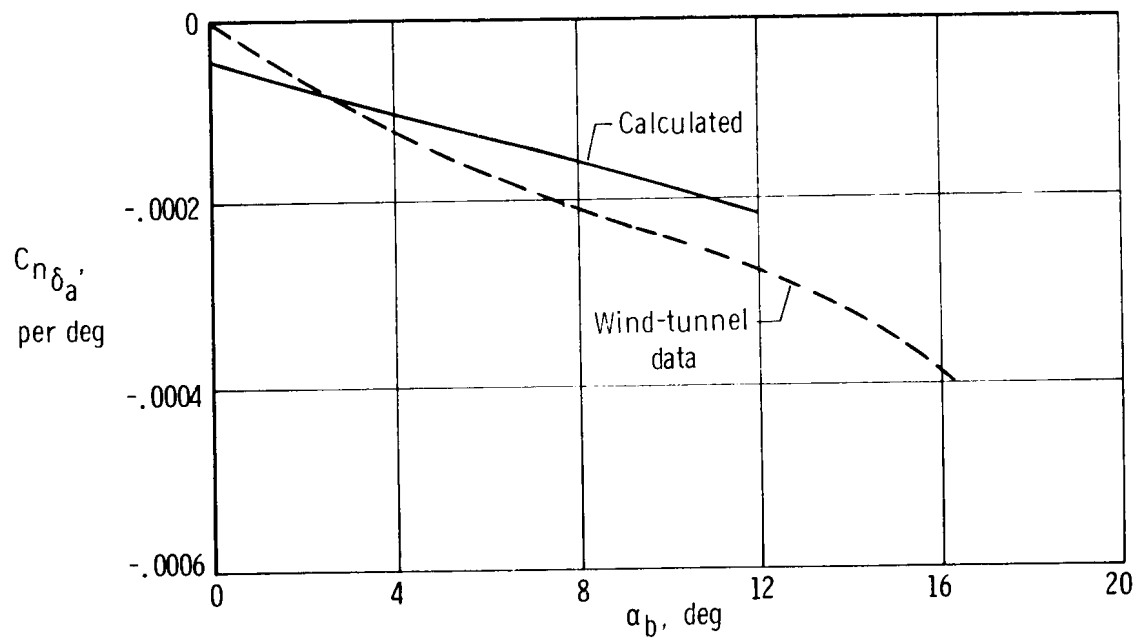


Figure 4.4.2-2. Comparison of calculated yawing moment due to ailerons of subject airplane with wind-tunnel data.

4.5 Yawing and Rolling Moments Due to Rudder Deflection

The yawing and rolling moments due to rudder deflection to be considered are for conventional rudders, which are essentially plain trailing-edge flaps. The method used to estimate these moments involves the determination of the side force due to rudder deflection, which is then multiplied by the appropriate moment arms to obtain the desired moments.

4.5.1 Side Force Due to Rudder Deflection, $C_{Y\delta_r}$

The side force due to rudder deflection, $C_{Y\delta_r}$, in the linear lift range of the vertical tail can be obtained by using equation (4.5.1-1). This equation was developed in reference 16 to obtain the lift increment of high-lift flaps and was used in reference 1 to determine the lift on the horizontal tail due to tab deflection. The equation, adapted to the present situation and based on wing area, gives

$$C_{Y\delta_r} = c_l \delta_r \frac{(C'_{L\alpha})_v}{(c_l \alpha)_v} \left[\frac{(\alpha \delta_r)_{CL}}{(\alpha \delta_r)_{cl}} \right]_v K_b \quad (4.5.1-1)$$

where

$(C'_{L\alpha})_v$ is the effective lift-curve slope of the vertical tail as obtained from $(C_{Y\beta})_v$ with wing-wake and body-sidewash effects equal to zero; thus, from equation (4.1.4-5),

$$(C'_{L\alpha})_v = k'_1 (C_{L\alpha})_{v(fh)} \frac{\bar{q}_v}{\bar{q}_\infty} \frac{S_v}{S_w} \quad (4.5.1-2)$$

$(c_l \alpha)_v$ is the section lift-curve slope of the vertical tail, obtained from section 4.1 of reference 1

K_b is the rudder-span factor (obtained from fig. 4.5.1-1) as a function of the taper ratio, λ_v , and the span ratio, η (fig. 3.2-4)

$c_l \delta_r$ is the section lift effectiveness of the rudder (obtained from eq. (4.4.1-6), which was applied in section 4.4.1 to obtain the section-lift effectiveness of the ailerons; the pertinent required geometric parameters of the rudder are obtained from fig. 3.4-2)

$\left[\frac{(\alpha \delta_r)_{CL}}{(\alpha \delta_r)_{cl}} \right]_v$ is the rudder-chord factor (obtained from fig. 4.5.1-2) as a function

of the vertical-tail aspect ratio, $A_{v\text{eff}}$, (from eq. (4.1.4-1)) and $(\alpha_{\delta_r})_{c_l}$.

The $(\alpha_{\delta_r})_{c_l}$ required to obtain $\left[\frac{(\alpha_{\delta_r})_{CL}}{(\alpha_{\delta_r})_{c_l}} \right]_v$ from figure 4.5.1-2 may be obtained, for a rudder having a constant ratio of flap chord to airfoil-section chord, from $-\frac{c_l \delta_r}{c_l \alpha}$ based on experimental data or from the insert in figure 4.5.1-2 based on theory. When $(\alpha_{\delta_r})_{c_l}$ varies along the span, as for a constant-chord rudder on a tapered surface, an average value of the chord ratio may be used with good accuracy. Otherwise, as discussed in reference 16, the effective $(\alpha_{\delta_r})_{c_l}$ may be found by determining the value of $(\alpha_{\delta_r})_{c_l}$ at each of several locations across the rudder span and plotting these values against corresponding values of K_b . The area under the curve divided by ΔK_b is the effective value of $(\alpha_{\delta_r})_{c_l}$.

The calculations for the side force due to rudder deflection, $C_{Y\delta_r}$, of the subject airplane, based on the preceding relations, are summarized in table 4.5.1-1. A comparison of the calculated $C_{Y\delta_r}$ with full-scale wind-tunnel data obtained at the power condition of $T'_c = 0$ is shown in figure 4.5.2-1.

4.5.2 Yawing and Rolling Moments Due to Rudder Deflection

The yawing and rolling moments due to rudder deflection are readily obtainable from the following simple relations, relative to the stability system of axes:

$$C_{n\delta_r} = -C_{Y\delta_r} \frac{l'_v \cos \alpha_b - z'_v \sin \alpha_b}{b_w} \quad (4.5.2-1)$$

$$C_{l\delta_r} = C_{Y\delta_r} \frac{-z'_v \cos \alpha_b - l'_v \sin \alpha_b}{b_w} \quad (4.5.2-2)$$

where l'_v and z'_v are distances, relative to the X- and Z-body axes, respectively, from the center of gravity to the quarter chord of the mean aerodynamic chord of that portion of the vertical tail spanned by the rudder, $(\bar{c}_{\Delta\eta})_r$. This mean aerodynamic chord is obtained from

$$(\bar{c}_{\Delta\eta})_r = \frac{2}{3} (\alpha_v)_{\eta_1} \left(\frac{1 + \lambda_{\Delta\eta} + \lambda^2 \Delta\eta}{1 + \lambda_{\Delta\eta}} \right) \quad (4.5.2-3)$$

where

$$\lambda \Delta \eta = \frac{(c_v)_{\eta_o}}{(c_v)_{\eta_i}} \quad (4.5.2-4)$$

and where $(c_v)_{\eta_o}$ and $(c_v)_{\eta_i}$ are the chords of the vertical tail at the outboard and inboard ends of the rudder, respectively.

The spanwise location of $(\bar{c}_{\Delta \eta})_r$ from the inboard end of the rudder $(c_v)_{\eta_i}$ is obtained from

$$\Delta z_{\Delta \eta} = -\frac{1}{3} \left(\frac{1 + 2\lambda \Delta \eta}{1 + \lambda \Delta \eta} \right) b_r \quad (4.5.2-5)$$

where b_r is the rudder span.

The calculations for the yawing and rolling moments due to rudder deflection, $C_{n\delta_r}$ and $C_{l\delta_r}$, of the subject airplane, based on the preceding relations, are summarized in table 4.5.2-1. The correlation of calculated $C_{Y\delta_r}$, $C_{n\delta_r}$, and $C_{l\delta_r}$ with analyzed full-scale wind-tunnel data obtained at the power condition of $T_c' = 0$ (no propeller-off wind-tunnel data were available) is shown in figure 4.5.2-1. The correlation is considered to be good, although the calculated values are slightly larger than the wind-tunnel values.

4.5.3 Symbols

$A_{v\text{eff}}$	effective aspect ratio of the vertical tail in the presence of the fuselage and the horizontal tail, obtained from equation (4.1.4-1) for a single-tail configuration
$B_1 = (1 - M^2)^{1/2}$	
b_r	rudder span parallel to the Z-body axis, in.
b_v	vertical-tail span, in.
b_w	wing span, in.
$(C'_L)_\alpha$	effective lift-curve slope of the vertical tail referred to the wing area, obtained from equation (4.5.1-2), per deg
$(C_L)_v(fh)$	vertical-tail lift-curve slope referred to the tail area, obtained from equation (4.1.4-2), per rad or deg

$C_{L\delta_r}$	vertical-tail lift effectiveness of the rudder, referred to the wing area, per deg
$C_{l\delta_r}$	rate of change of the rolling-moment coefficient with rudder deflection, per deg
$C_{n\delta_r}$	rudder effectiveness in yaw; rate of change in the yawing-moment coefficient with rudder deflection, per deg
$(C_{Y\beta})_v$	vertical-tail contribution to the variation of the side-force coefficient with the sideslip
$C_{Y\delta_r}$	rate of change of the side-force coefficient with rudder deflection, per rad or deg
c_{f_r}	rudder-flap chord, in.
$\left(\frac{c_{f_r}}{c_v}\right)_{av}$	average ratio of the rudder chord to the vertical-tail chord within the rudder span
c_{r_v}	root chord of the vertical tail, in.
c_v	vertical-tail chord, in.
$(c_v)_{\eta_i}, (c_v)_{\eta_o}$	vertical-tail chord at the inboard and outboard edge of the rudder, respectively, in.
$(c_l \alpha)_v$	section lift-curve slope of the vertical tail, per rad
$(c_l \alpha)_{v\text{theory}}$	theoretical section lift-curve slope of the vertical tail, per rad
$c_{l\delta_r}$	section lift effectiveness of the rudder, per rad
$(c_{l\delta_r})_{\text{theory}}$	theoretical section lift effectiveness of the rudder, per rad
$(\bar{c}_{\Delta\eta})_r$	mean aerodynamic chord of the portion of the vertical tail spanned by the rudder, in.
K'	empirical correction factor for the section lift effectiveness of plain trailing-edge flaps at high flap deflections, obtained from figure 4.4.1-3
K_b	rudder span factor, obtained from figure 4.5.1-1
k'_1	factor accounting for the body size relative to the vertical-tail size, obtained from figure 4.1.4-1(d)

l_v, z_v	distance relative to the X- and Z-body axes, respectively, from the center of gravity to the quarter chord of the mean aerodynamic chord of the vertical tail, in.
l'_v, z'_v	distance, relative to the X- and Z-body axes, respectively, from the center of gravity to the quarter chord of the mean aerodynamic chord, $(\bar{c}_{\Delta\eta})_r$, of the portion of the vertical tail spanned by the rudder, in.
M	Mach number
\bar{q}_∞	free-stream dynamic pressure, lb/sq ft
\bar{q}_v	dynamic pressure at the vertical tail, lb/sq ft
S_v	vertical-tail area, sq ft
S_w	wing area, sq ft
T	thrust due to the propellers, lb
$T'_c = \frac{T}{\bar{q}_\infty S_w}$	
t/c	airfoil-section thickness ratio of the vertical tail
α_b	angle of attack relative to the X-body axis, deg
$(\alpha_{\delta_r})_{C_L} = - \frac{C_{L\delta_r}}{(C'_{L\alpha})_v}$	
$(\alpha_{\delta_r})_{cl} = - \frac{c_l \delta_r}{(c_{l\alpha})_v}$	
$\left[\frac{(\alpha_{\delta_r})_{C_L}}{(\alpha_{\delta_r})_{cl}} \right]_v$	flap- (rudder) chord factor (obtained from fig. 4.5.1-2) as a function of the vertical-tail aspect ratio, $A_{v_{eff}}$, and $(\alpha_{\delta_r})_{cl}$
Δ	difference
Δz_v	spanwise location of the vertical-tail mean aerodynamic chord from the root chord, $(c_r)_v$, of the tail, in.

$\Delta z_{\Delta\eta}$	spanwise location of $(\bar{c}_{\Delta\eta})_r$ from $(c_v)_{\eta_i}$, in.
$\Delta\eta = \eta_i - \eta_o$	
η	span ratio
η_i, η_o	distance from the root chord of the vertical tail to the inboard and outboard edge of the rudder, respectively, as a ratio of the vertical-tail span
φ_{te}	vertical-tail trailing-edge angle, deg
$\Lambda \bar{c}/4$	sweep of the quarter-chord line of the vertical tail, deg
λ_v	vertical-tail taper ratio
$\lambda_{\Delta\eta}$	taper ratio of the portion of the vertical tail spanned by the rudder

TABLE 4.5.1-1
SIDE FORCE DUE TO RUDDER DEFLECTION, $C_{Y\delta_r}$

$$C_{Y\delta_r} = c_{l\delta_r} \left[\frac{(c'_{L\alpha})_v}{(c_{l\alpha})_v} \right] \left[\frac{(\alpha\delta_r)_{C_L}}{(\alpha\delta_r)_{c_l}} \right] K_b$$

$$(c'_{L\alpha})_v = k'_1 (c_{L\alpha})_{v(fh)} \frac{\bar{q}_v}{\bar{q}_\infty} \frac{S_v}{S_w}$$

Symbol	Description	Reference	Magnitude
S_v	Vertical-tail area, sq ft	Figure 3.2-4	17, 7
S_w	Reference wing area, sq ft	Figure 3.2-1	178, 0
$(c_{L\alpha})_{v(fh)}$	Lift-curve slope of vertical tail, referred to tail area, per deg	Table 4.1.4-1(b)	.0525
k'_1	Empirical correction factor accounting for body size relative to vertical-tail size	Table 4.1.4-1(c)	.889
$\frac{\bar{q}_v}{\bar{q}_\infty}$	Dynamic-pressure ratio at vertical tail	-----	$\approx 1, 0$
$(c'_{L\alpha})_v$	Effective lift-curve slope of vertical tail, referred to wing area, per deg	Equation (4.5.1-2)	.00464
t/c	Thickness ratio of vertical-tail section	NACA 0008	0, 08
φ_{te}	Vertical-tail trailing-edge angle, deg	-----	Negligible
$(c_{l\alpha})_{v\text{theory}}$	6.28 + 4.7(t/c)(1 + 0.00375 φ_{te}), per rad	Equation (4.4.1-7)	6, 66
$(c_{l\alpha})_v$	Section lift-curve slope of vertical tail, per rad	Table 4.1.4-1(b)	6, 25
$(c_{l\alpha})_v$	-----	-----	.938
$(\frac{c_{fr}}{c_v})_{av}$	$\left(\frac{\text{Rudder chord}}{\text{Vertical-tail chord within rudder span}} \right)_{\text{average}}$	Figure 3.2-4	0, 38
$(c_{l\delta_r})_{\text{theory}}$	Theoretical rudder effectiveness of section, $f(t/c, \frac{c_{fr}}{c_v})$	Figure 4.4.1-1	4, 88
$\frac{c_{l\delta_r}}{(c_{l\delta_r})_{\text{theory}}}$	$f \left[\left(\frac{c_{fr}}{c_v} \right), \frac{(c_{l\alpha})_v}{(c_{l\alpha})_{v\text{theory}}} \right]$	Figure 4.4.1-2	.91
B_1	$\sqrt{1 - M^2}$ for wind-tunnel Mach number = 0, 083	Wind-tunnel test condition	.997
K'	Empirical correction factor for large flap deflections, deg	Figure 4.4.1-3	1, 0 to 10
$c_{l\delta_r}$	$\frac{1}{B_1} \left(\frac{c_{l\delta_r}}{(c_{l\delta_r})_{\text{theory}}} \right) (c_{l\delta_r})_{\text{theory}} K', \text{ rad}$	Equation (4.4.1-6)	4, 45
$A_{v\text{eff}}$	Effective aspect ratio of vertical tail	Table 4.1.4-1(a)	2, 67
$(\alpha\delta_r)_{c_l}$	$-\frac{c_{l\delta_r}}{(c_{l\alpha})_v}$	-----	-.712
$\frac{(\alpha\delta_r)_{C_L}}{(\alpha\delta_r)_{c_l}}$	$f[A_{v\text{eff}}, (\alpha\delta_r)_{c_l}]$	Figure 4.5.1-2	1, 07
λ_v	Vertical-tail taper ratio	Figure 3.2-4	0, 433
η_i	Distance from root chord of vertical tail to inboard edge of rudder as fraction of vertical-tail span	Figure 3.2-4	.14
η_o	Distance from root chord of vertical tail to outboard edge of rudder as fraction of vertical-tail span	Figure 3.2-4	1, 00
K_b	Span factor for rudder, $f(\lambda_v, \eta_i, \eta_o)$	Figure 4.5.1-1	.80
<p>Summary: $C_{Y\delta_r} = c_{l\delta_r} \left[\frac{(c'_{L\alpha})_v}{(c_{l\alpha})_v} \right] \left[\frac{(\alpha\delta_r)_{C_L}}{(\alpha\delta_r)_{c_l}} \right] K_b$</p> $= 4, 45 \left(\frac{0, 00464}{6, 25/57, 3} \right) (1, 07)(0, 80)$ $= 0, 16204 \text{ per rad}$ $= 0, 00283 \text{ per deg referenced to } S_w = 178 \text{ sq ft}$			

TABLE 4.5.2-1
YAWING AND ROLLING MOMENTS DUE TO RUDDER DEFLECTION

$$C_{n\delta_r} = -C_{Y\delta_r} \frac{l'_v \cos \alpha_b - z'_v \sin \alpha_b}{b_w}$$

$$C_{l\delta_r} = C_{Y\delta_r} \frac{-z'_v \cos \alpha_b - l'_v \sin \alpha_b}{b_w}$$

Symbol	Description	Reference	Magnitude
b_w	Wing span, in.	Figure 3.2-1	432.0
b_r	Rudder span parallel to Z-body axis, in.	Figure 3.2-4	55.3
l_v	Distance from center of gravity to quarter chord of vertical-tail mean aerodynamic chord, in.	Figure 3.2-4	164.9
z_v	Vertical distance from center of gravity to quarter chord of vertical-tail mean aerodynamic chord, in.	Figure 3.2-4	-45.9
$\Delta c/4$	Sweepback of vertical-tail quarter-chord line, deg	Figure 3.2-4	30.0
Δz_v	Spanwise location of vertical-tail mean aerodynamic chord from c_{rv} , in.	Figure 3.2-4	-27.9
$(c_v)_{\eta_0}$	Chord of vertical tail at outboard end of rudder, in.	Figure 3.2-4	24.0
$(c_v)_{\eta_i}$	Chord of vertical tail at inboard end of rudder, in.	Figure 3.2-4	51.0
$\lambda \Delta \eta$	$\frac{(c_v)_{\eta_0}}{(c_v)_{\eta_i}}$	-----	.471
$(\bar{c}_{\Delta \eta})_r$	Mean aerodynamic chord of portion of tail spanned by rudder, $\frac{2}{3}(c_v)_{\eta_i} \left(\frac{1 + \lambda \Delta \eta + \lambda \Delta \eta^2}{1 + \lambda \Delta \eta} \right)$, in.	-----	39.0
$\Delta z_{\Delta \eta}$	Spanwise location of $(\bar{c}_{\Delta \eta})_r$ from $(c_v)_{\eta_i} = -\frac{1}{3} \left(\frac{1 + 2 \lambda \Delta \eta}{1 + \lambda \Delta \eta} \right) b_r$, in.	Equation (4.5.2-4)	-24.3
$\eta_i b_v$	Spanwise location of $(c_v)_{\eta_i}$ from c_{rv} , in.	Figure 3.2-4	-9.0
l'_v	$l_v - (\eta_i b_v + \Delta z_{\Delta \eta} - \Delta z_v) \sin \Delta c/4$, in.	-----	167.6
z'_v	$z_v + (\eta_i b_v + \Delta z_{\Delta \eta} - \Delta z_v) \cos \Delta c/4$, in.	-----	-50.6
$C_{Y\delta_r}$	Referenced to $S_w = 178$ sq ft, per deg	Table 4.5.1-1	0.00283
Summary: $C_{n\delta_r} = -0.001098 \cos \alpha_b - 0.000331 \sin \alpha_b$ $C_{l\delta_r} = 0.000331 \cos \alpha_b - 0.001098 \sin \alpha_b$			

α_b , deg	$C_{n\delta_r}$	$C_{l\delta_r}$
-4	-0.001072	0.000407
0	-.001098	.000330
4	-.001118	.000253
8	-.001133	.000175
12	-.001143	.000096

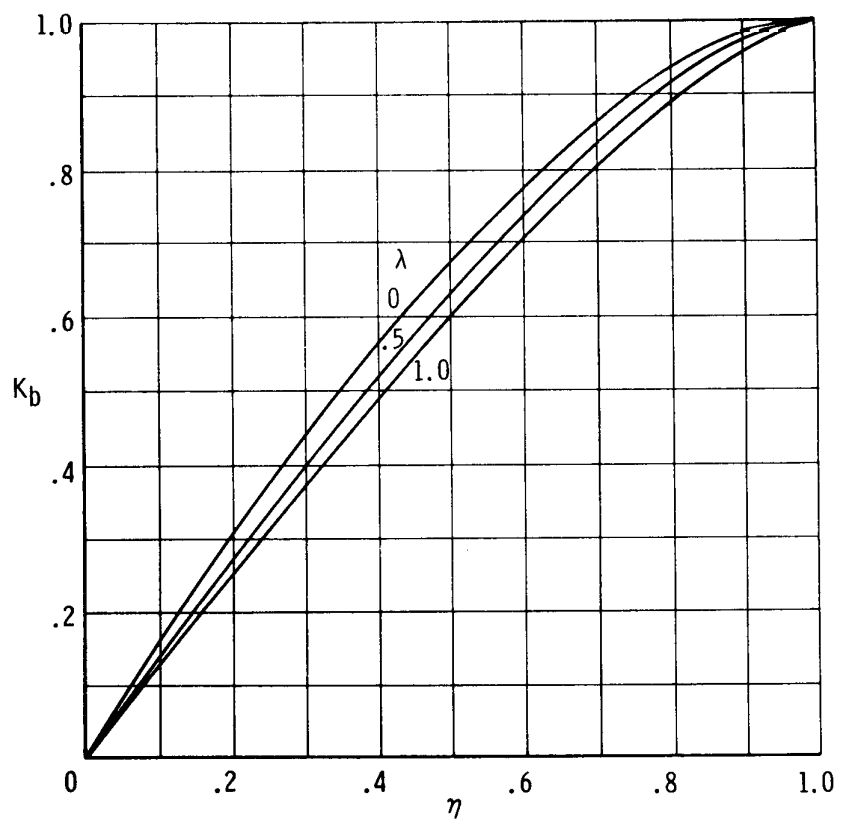
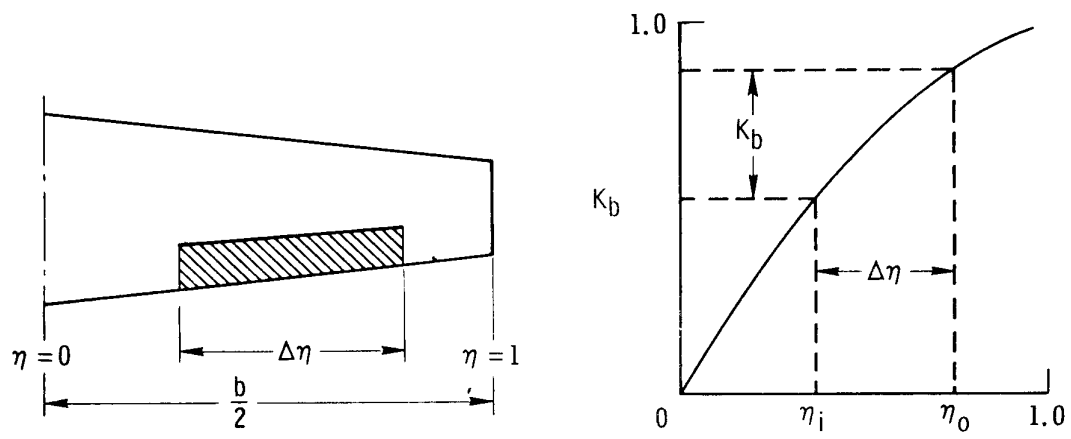


Figure 4.5.1-1. Span factor for inboard flaps (from ref. 16).

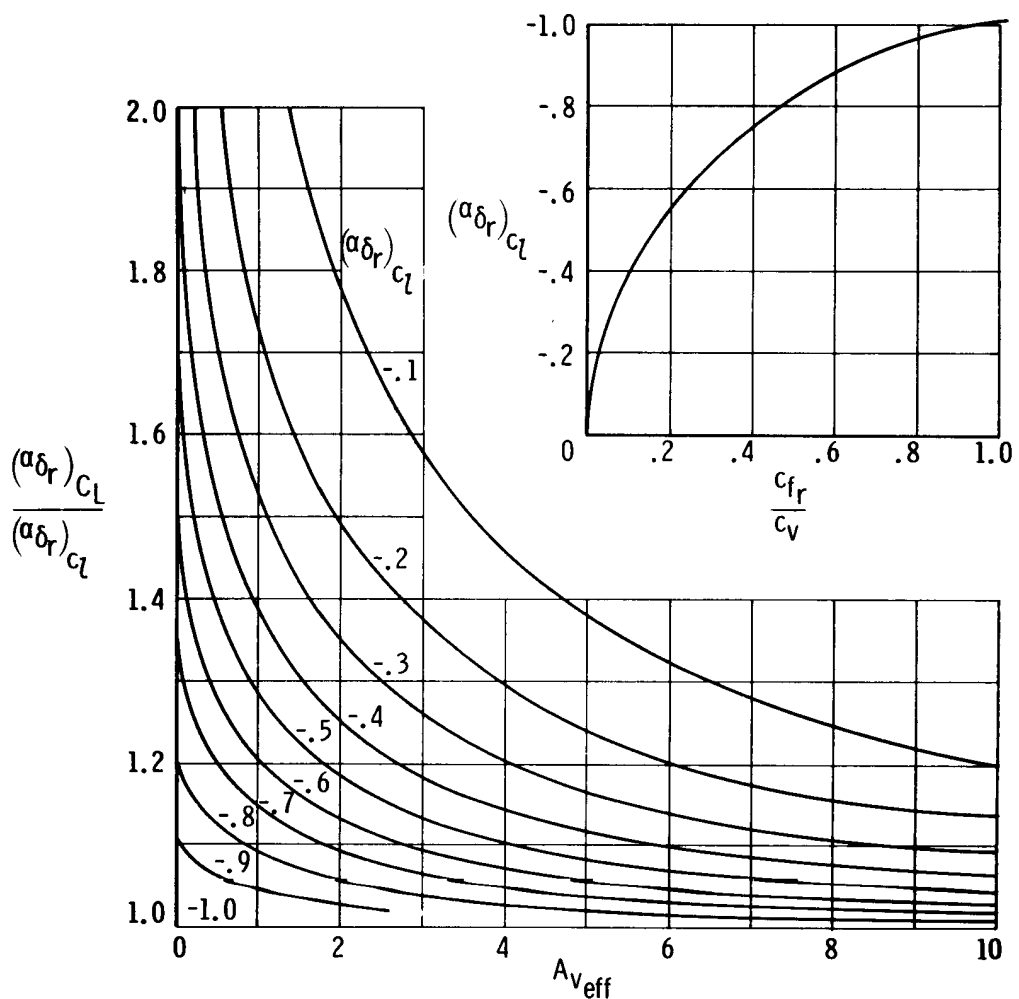


Figure 4.5.1-2. Flap-chord factor (from ref. 16).

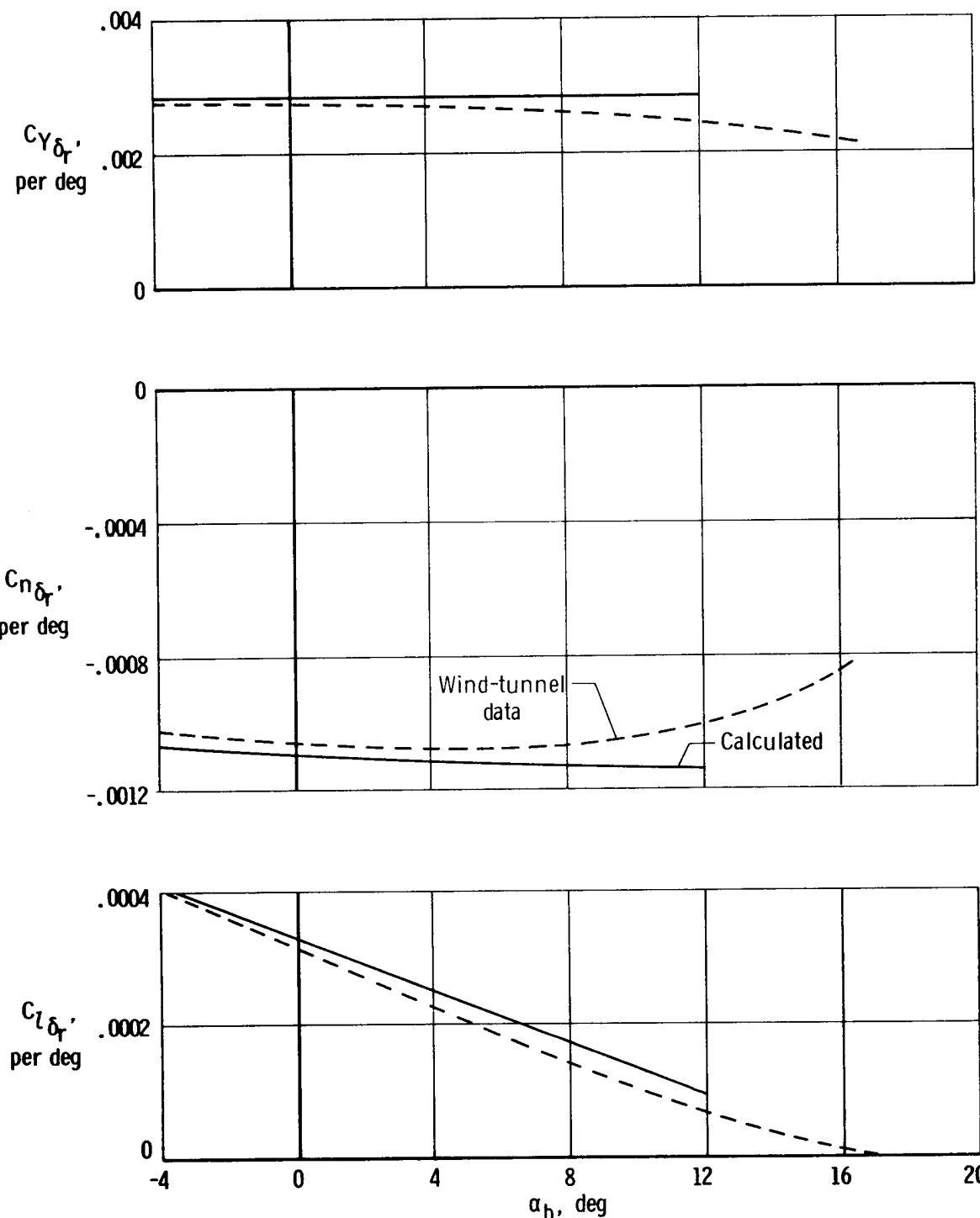


Figure 4.5.2-1. Comparison of calculated and wind-tunnel values of rudder side force and yawing- and rolling-moment effectiveness.

5.0 PREDICTION OF POWER-ON STATIC STABILITY AND CONTROL CHARACTERISTICS

A general design procedure for determining the effects of power on the lateral-directional static stability and control characteristics of propeller-driven aircraft does not appear to be available. In single-engine airplanes the effects of power are particularly significant because the vertical tail is strongly affected by the propeller slipstream and the wing-body interference with the slipstream. In the absence of reliable data for preliminary design purposes, tests of powered models in wind tunnels or practical experience with similar airplane configurations is used.

For twin-engine, propeller-driven aircraft, the vertical tail is normally outside the main propeller slipstream. Although the propeller slipstream may have some effect on the vertical tail—particularly with increasing power—the effect is usually small enough to be neglected in preliminary design calculations.

5.1 Power-On Static Stability Characteristics

The effect of power on the sidewash of the vertical tail of a twin-engine airplane for normal operating conditions is assumed to be negligible in a first order of approximation. Inasmuch as the tail is outside the main propeller slipstream under these operating conditions, the dynamic-pressure ratio is considered to be similar to 1.0.

5.1.1 Power Effects on $C_{Y\beta}$

Three power effects are added to the propeller-off side-force derivative to arrive at the power-on value. These are the normal force (side force) of the propellers, the increased dynamic pressure behind the propeller as it affects the contribution of the nacelles, and the power-induced sidewash behind the propeller, which also affects the contribution of the nacelles. With these three power effects taken into account, the power-on equation for $C_{Y\beta}$ can be represented by

$$C_{Y\beta} = \left(C_{Y\beta}\right)_{\substack{\text{prop} \\ \text{off}}} + \left(\Delta C_{Y\beta}\right)_{N_p} + \left(\Delta C_{Y\beta}\right)_{n(\Delta \bar{q})} + \left(\Delta C_{Y\beta}\right)_{n(\sigma_p)} \quad (5.1.1-1)$$

Propeller-off side-force derivative, $\left(C_{Y\beta}\right)_{\substack{\text{prop} \\ \text{off}}}$, was considered in section 4.1.

As calculated, the derivative provided reasonably good preliminary correlation with wind-tunnel data for the subject airplane. Because of a lack of design data, the calculations did not show the influence of angle of attack on wing-body interference which was reflected in the wind-tunnel data.

The increment of the side-force derivative due to propeller normal force, $\left(\Delta C_{Y\beta}\right)_{N_p}$, is accounted for by equation (5.1.1-2). This equation is an adaptation of equation (5.1.1-2) in reference 1, which accounted for the propeller normal-force contribution to lift.

$$\left(\Delta C_{Y\beta}\right)_{N_p} = - \frac{nf}{57.3} \left(C_{N\alpha}\right)_p \left(\frac{S_p/\text{prop}}{S_w} \right) \quad (5.1.1-2)$$

where

n is the number of propellers

f is the propeller inflow factor, the ratio of propeller normal-force (side-force) coefficient at power-on to power-off conditions, obtained from figure 5.1.1-1 (from ref. 17)

S_p/prop is the disk area of the propeller, equal to πR_p^2

$(C_{N\alpha})_p$ is the propeller normal-force parameter at $T'_c = 0$, per radian, obtained from the following equation from reference 8:

$$(C_{N\alpha})_p = \left[(C_{N\alpha})_p \right]_{K_N=80.7} \left[1 + 0.8 \left(\frac{K_N}{80.7} - 1 \right) \right] \quad (5.1.1-3)$$

where

K_N is the side-force factor obtained from the propeller manufacturer or approximated by

$$K_N = 262 \left(\frac{b_p}{R_p} \right)_{0.3R_p} + 262 \left(\frac{b_p}{R_p} \right)_{0.6R_p} + 135 \left(\frac{b_p}{R_p} \right)_{0.9R_p} \quad (5.1.1-4)$$

in which $\frac{b_p}{R_p}$ is the ratio of the blade width, b_p , to the propeller radius, R_p , and the subscripts $0.3R_p$, $0.6R_p$, and $0.9R_p$ indicate the radial station of the ratio

$\left[(C_{N\alpha})_p \right]_{K_N=80.7}$ is the propeller normal-force derivative given by figure 5.1.1-2

as a function of the blade angle, β' , and the type of propeller

The contributions of the propeller normal force to the side-force derivative of the subject airplane are summarized in table 5.1.1-1(a).

The increment of the side-force derivative, $C_{Y\beta}$, due to propeller-induced increase in dynamic pressure acting on the nacelles is accounted for by

$$(\Delta C_{Y\beta})_{n(\Delta \bar{q})} = \left[(\Delta C_{Y\beta})_n \right]_{\substack{\text{prop} \\ \text{off}}} \frac{\Delta \bar{q}_n}{\bar{q}_\infty} \quad (5.1.1-5)$$

where

$\left[(\Delta C_{Y\beta})_n \right]_{\substack{\text{prop} \\ \text{off}}}$ is the propeller-off contribution of the nacelles to $C_{Y\beta}$, obtained from table 4.1.3-1

$\frac{\Delta \bar{q}_n}{\bar{q}_\infty}$ is the increase in dynamic-pressure ratio at the nacelle due to power,

obtained from

$$\frac{\Delta \bar{q}_n}{\bar{q}_\infty} = \frac{S_w(T'_c/\text{prop})}{\pi R_p^2} \quad (5.1.1-6)$$

The contribution of $(\Delta C_{Y\beta})_{n(\Delta \bar{q})}$ to the side-force derivative of the subject airplane is summarized in table 5.1.1-1(b).

The increment of $C_{Y\beta}$ due to power-induced sidewash acting on the nacelles is accounted for by

$$(\Delta C_{Y\beta})_{n(\sigma_p)} = -[(\Delta C_{Y\beta})_n]_{\text{prop off}} \left(\frac{\partial \sigma_p}{\partial \beta} \right) \left(1 + \frac{\Delta \bar{q}_n}{\bar{q}_\infty} \right) \quad (5.1.1-7)$$

where

$\left(\frac{\partial \sigma_p}{\partial \beta} \right)$ is the propeller-induced sidewash factor behind the propeller obtained from the following relation (from ref. 8):

$$\frac{\partial \sigma_p}{\partial \beta} = C_1 + C_2 (C_{N\alpha})_p \quad (5.1.1-8)$$

in which the factors C_1 and C_2 are obtained from figure 5.1.1-3. The contribution of $(\Delta C_{Y\beta})_{n(\sigma_p)}$ to the side-force derivative of the subject airplane is summarized in table 5.1.1-1(c).

Summary calculations for power-on $C_{Y\beta}$ characteristics of the subject airplane for vertical-tail-off and vertical-tail-on conditions are presented in table 5.1.1-1(d) as a function of power conditions. In figure 5.1.1-4 the calculated characteristics are compared with wind-tunnel data. The vertical-tail-off data imply that the contribution of the fuselage in the presence of the wing is a function of angle of attack. The difference in the tail-on and tail-off values for this twin-engine configuration when thrust coefficient is equal to zero and 0.44 indicates the vertical-tail contribution to $C_{Y\beta}$ to be a function of angle of attack with some dependence on the power condition over most of the linear angle-of-attack range. Because of the lack of appropriate design data, the contribution of the fuselage in the presence of the wing and the contribution of the vertical tail were considered to be independent of angle of attack in calculating the $C_{Y\beta}$ characteristics.

5.1.2 Power Effects on $C_{n\beta}$

Power effects to be added onto the propeller-off weathercock stability, $C_{n\beta}$, are considered to be due to the same factors that affected the side-force derivative, $C_{Y\beta}$. The factors are propeller normal force (side force), increased lateral forces on the nacelles due to propeller-induced increase in dynamic pressure, and propeller-induced sidewash. With these factors taken into account, the power-on equation for $C_{n\beta}$ can be represented by

$$C_{n\beta} = \left(C_{n\beta} \right)_{\substack{\text{prop} \\ \text{off}}} + \left(\Delta C_{n\beta} \right)_{N_p} + \left(\Delta C_{n\beta} \right)_{n(\Delta \bar{q})} + \left(\Delta C_{n\beta} \right)_{n(\sigma_p)} \quad (5.1.2-1)$$

where

$\left(C_{n\beta} \right)_{\substack{\text{prop} \\ \text{off}}}$ is the propeller-off $C_{n\beta}$ accounted for in section 4.2.1.

$\left(C_{n\beta} \right)_{N_p}$ is the contribution due to the propeller side force and is determined by

$$\left(\Delta C_{n\beta} \right)_{N_p} = \left(\Delta C_{Y\beta} \right)_{N_p} \left(\frac{x_p \cos \alpha_b + z_p \sin \alpha_b}{b_w} \right) \quad (5.1.2-2)$$

where

$\left(\Delta C_{Y\beta} \right)_{N_p}$ is obtained from section 5.1.1-1

x_p and z_p are the distances from the center of gravity to the propeller, from figure 3.2-5

b_w is the wing span, from figure 3.2-1

$\left(\Delta C_{n\beta} \right)_{n(\Delta \bar{q})} + \left(\Delta C_{n\beta} \right)_{n(\sigma_p)}$ are the changes in nacelle contribution to $C_{n\beta}$ due

to the propeller-induced increase in dynamic pressure and sidewash, respectively. Their net contribution is determined by

$$\left(\Delta C_{n\beta} \right)_{n(\Delta \bar{q})} + \left(\Delta C_{n\beta} \right)_{n(\sigma_p)} = \left[\left(\Delta C_{Y\beta} \right)_{n(\Delta \bar{q})} + \left(\Delta C_{Y\beta} \right)_{n(\sigma_p)} \right] \left(\frac{x_n \cos \alpha_b + z_n \sin \alpha_b}{b_w} \right) \quad (5.1.2-3)$$

where

$\left(\Delta C_{Y\beta} \right)_{n(\Delta \bar{q})}$ and $\left(\Delta C_{Y\beta} \right)_{n(\sigma_p)}$ are obtained from section 5.1.1-1

x_n and z_n are the distances from the center of gravity to the nacelle center of pressure (fig. 3.2-2)

Summary calculations of power-on $C_{l\beta}$ characteristics of the subject airplane for vertical-tail-on and vertical-tail-off conditions are presented in tables 5.1.2-1(a) and 5.1.2-1(b) as a function of angle of attack and power condition. In table 5.1.2-1(b) the propeller-off $C_{n\beta}$ characteristics listed in columns 2 and 3 were obtained from table 4.2.5-1 for the condition where wing-fuselage interference was accounted for as a function of angle of attack but vertical-tail effectiveness, $(C_{Y\beta})_{v(wfh)}$, was not accounted for as a function of angle of attack because of the lack of appropriate design data.

In figure 5.1.2-1 the calculated $C_{n\beta}$ characteristics are compared with wind-tunnel data. The vertical-tail-off data show some increase in wing-fuselage interference with increasing power which was approximately accounted for in the calculations. The tail-on and tail-off data also show some change in tail effectiveness with increasing angle of attack. As was noted for $C_{n\beta}$ for propeller-off conditions (section 4.2.5), lack of appropriate design data for sidewash effects as a function of angle of attack precluded the consideration of the angle-of-attack effects on the vertical tail.

5.1.3 Power Effects on $C_{l\beta}$

Power effects on the effective dihedral derivative, $C_{l\beta}$, to be added to the propeller-off derivative were considered to be the results of rolling moments due to propeller normal force (side force) and rolling moments due to the sideslip-induced lateral displacement of the portion of the wing immersed in the propeller slipstream. The portion of the wing in the slipstream is affected by a propeller-induced increase in dynamic pressure and downwash. With these factors taken into account, the power-on equation for $C_{l\beta}$ is represented by

$$C_{l\beta} = (C_{l\beta})_{\text{prop off}} + (\Delta C_{l\beta})_{N_p} + (\Delta C_{l\beta})_{w(\Delta \bar{q} + \epsilon_p)} \quad (5.1.3-1)$$

The $C_{l\beta}$ with propeller off, $(C_{l\beta})_{\text{prop off}}$, is accounted for in section 4.3.

The contribution of the propeller side force to $C_{l\beta}$ is obtained from

$$(\Delta C_{l\beta})_{N_p} = (\Delta C_{Y\beta})_{N_p} \left(\frac{-z_p \cos \alpha_b + x_p \sin \alpha_b}{b_w} \right) \quad (5.1.3-2)$$

where

$(\Delta C_{Y_\beta})_{N_p}$ is the propeller side-force derivative as obtained from equation (5.1.1-2) and table 5.1.1-1(a)

x_p and z_p are distances from the center of gravity to the propeller, from figure 3.2-5

b_w is the wing span, from figure 3.2-1

The contribution of the portion of the wing immersed in the propeller slipstream to C_{l_β} is the result of a lateral shift of the immersed part of the wing. In sideslip, in the absence of secondary effects, the centerline of the propeller slipstream is yawed from the thrust line by an amount equal to $(\beta - \sigma_p)$, where σ_p is the propeller-induced sidewash.

The increments of lift, $(\Delta C_L)_{w(\Delta \bar{q})}$ and $(\Delta C_L)_{w(\epsilon_p)}$, of the immersed portion of the wing due to the power-induced increase in dynamic pressure and downwash are assumed to be effectively centered at the quarter chord of the wing. With the lateral shift in center of pressure considered to be equal to $x'_p \tan(\beta - \sigma_p)$, the contribution of the immersed portion of the wing to C_{l_β} is obtained from

$$(\Delta C_{l_\beta})_{w(\Delta \bar{q} + \epsilon_p)} = \frac{\partial}{\partial \beta} \left\{ \left[(\Delta C_L)_{w(\Delta \bar{q})} + (\Delta C_L)_{w(\epsilon_p)} \right] \frac{x'_p \tan(\beta - \sigma_p)}{b_w} \right\} \quad (5.1.3-3)$$

However, the proximity of the fuselage and the curvature of the fuselage flow field alter the shift in propeller slipstream centerline. In the absence of more specific information, personal judgment was used in applying an interference factor of 0.5 to equation (5.1.3-3), which for the normal range of sideslip angles was used in the following format:

$$(\Delta C_{l_\beta})_{w(\Delta \bar{q} + \epsilon_p)} = \frac{0.5}{57.3} \frac{x'_p}{b_w} \left[(\Delta C_L)_{w(\Delta \bar{q})} + (\Delta C_L)_{w(\epsilon_p)} \right] \left(1 - \frac{\partial \sigma_p}{\partial \beta} \right) \quad (5.1.3-4)$$

where

x'_p is the distance from the propeller to the quarter chord of the wing at the thrust line, scaled from figure 3.2-1

b_w is the wing span, from figure 3.2-1

$(\Delta C_L)_{w(\Delta \bar{q})}$ is the increment of lift on the immersed wing area due to the power-induced increase in dynamic pressure, obtained from table 5.1.1-2(a)-3 of reference 1

$(\Delta C_L)_{w(\epsilon_p)}$ is the increment of lift on the immersed wing area due to power-induced downwash, obtained from table 5.1.1-2(b)-2 of reference 1

$\frac{\partial \sigma_p}{\partial \beta}$ is the power-induced sidewash factor behind the propeller, obtained from equation (5.1.1-8)

Summary calculations of power-on $C_{l\beta}$ characteristics of the subject airplane are presented in tables 5.1.3-1(a) and 5.1.3-1(b) as a function of angle of attack and power condition. As indicated in table 5.1.3-1(b), the propeller side force (column 5) tends to increase the effective dihedral, and the sideslip-induced lateral displacement of the immersed portion of the wing (column 7) decreases the effective dihedral with increasing angle of attack and thrust coefficient. At a 12° angle of attack, with $(C_{l\beta})_{\text{prop off}}$ as a base, the propeller side force increases the effective dihedral about 3 and 4 percent at thrust coefficients of 0.20 and 0.44, respectively. At the same angle of attack, the sideslip-induced lateral displacement of the immersed portion of the wing decreases the effective dihedral about 8 and 14 percent at thrust coefficients at 0.20 and 0.44, respectively. Had an interference factor not been included in equation (5.1.3-4) to obtain the latter contributions, the decrease in effective dihedral would have been 16 and 28 percent instead of 8 and 14 percent. Because the interference factor used was based on personal judgment, it is apparent that a more rational basis is required for determining the interference factor to be used.

A comparison of the calculated $C_{l\beta}$ characteristics with wind-tunnel data in figure 5.1.3-1 shows good correlation.

5.1.4 Symbols

b_p	width of the propeller blade, ft
b_w	wing span, in.
C_1, C_2	factors for determining the propeller-induced sidewash and downwash behind the propeller, obtained from figure 5.1.1-3
$(\Delta C_L)_{w(\Delta \bar{q})}, (\Delta C_L)_{w(\epsilon_p)}$	increment of the lift coefficient due to the power-induced increase in the dynamic pressure and downwash, respectively, on the portion of the wing immersed in the propeller slipstreams
$C_{l\beta}$	effective dihedral derivative; rate of change of the rolling-moment coefficient with sideslip, per deg
$(C_{l\beta})_{\text{prop off}}$	airplane $C_{l\beta}$ for propeller-off conditions

$(\Delta C_{l_\beta})_{N_p}$	contribution of the normal propeller force to C_{l_β}
$(\Delta C_{l_\beta})_{w(\Delta \bar{q} + \epsilon_p)}$	change in the wing contribution to C_{l_β} due to the power-induced change in the dynamic pressure in the propeller slipstream and the power-induced downwash of the slipstream acting on the wing
$(C_{N_\alpha})_p$	propeller normal-force parameter at $T'_c = 0$, per rad
$[(C_{N_\alpha})_p]_{K_N=80.7}$	propeller normal-force parameter, $(C_{N_\alpha})_p$, at the reference side-force factor, $K_N = 80.7$ (condition obtained from fig. 5.1.1-2)
C_{n_β}	weathercock stability derivative; variation of the yawing-moment coefficient with sideslip, per deg
$(C_{n_\beta})_{\text{prop off}}$	airplane C_{n_β} for propeller-off conditions
$(\Delta C_{n_\beta})_{N_p}$	contribution of the propeller side force to C_{n_β}
$(\Delta C_{n_\beta})_{n(\Delta \bar{q})}, (\Delta C_{n_\beta})_{n(\sigma_p)}$	change in the nacelle contributions to C_{n_β} due to the propeller-induced increase in the dynamic pressure and sidewash, respectively, acting on the nacelles
$(\Delta C_{n_\beta})_{n(\Delta \bar{q} + \sigma_p)} = (\Delta C_{n_\beta})_{n(\Delta \bar{q})} + (\Delta C_{n_\beta})_{n(\sigma_p)}$	
$(\Delta C_{n_\beta})_p$	increment of the weathercock stability due to the power effects
$(C_{n_\beta})_{\text{wfn}}$	vertical-tail-off C_{n_β}
$[(C_{n_\beta})_{\text{wfn}}]_{\text{prop off}}$	vertical-tail-off C_{n_β} at propeller-off conditions
C_{Y_β}	rate of change of the side-force coefficient with sideslip angle, per deg
$(C_{Y_\beta})_{\text{prop off}}$	airplane C_{Y_β} for propeller-off conditions

$(\Delta C_{Y\beta})_{N_p}$	contribution of the propeller side force to $C_{Y\beta}$
$[(\Delta C_{Y\beta})_n]_{\substack{\text{prop} \\ \text{off}}}$	contribution of the nacelles to $C_{Y\beta}$ for propeller-off conditions
$(\Delta C_{Y\beta})_{n(\Delta\bar{q})}, (\Delta C_{Y\beta})_{n(\sigma_p)}$	change in the nacelle contributions to $C_{Y\beta}$ due to the propeller-induced increase in the dynamic pressure and sidewash, respectively, acting on the nacelles
$(C_{Y\beta})_{v(wfh)}$	contribution of the vertical tail to $C_{Y\beta}$ in the presence of the wing, fuselage, and horizontal tail, per deg
$(C_{Y\beta})_{wfh}$	vertical-tail-off $C_{Y\beta}$
$[(C_{Y\beta})_{wfh}]_{\substack{\text{prop} \\ \text{off}}}$	vertical-tail-off $C_{Y\beta}$ at propeller-off conditions
f	propeller inflow factor, obtained from figure 5.1.1-1
$K = \frac{0.5}{57.3} \frac{x_p'}{b_w} \left(1 - \frac{\partial \sigma}{\partial \beta}\right)$, a function of T'_c	
K_N	propeller side-force factor, obtained from equation (5.1.1-4)
n	number of propellers
\bar{q}_∞	free-stream dynamic pressure, lb/sq ft
$\Delta\bar{q}_n$	power-induced increase in the dynamic pressure acting on the nacelles, lb/sq ft
R_p	propeller radius, ft
S_p/prop	propeller disk area, πR_p^2 , sq ft
S_w	wing area, sq ft
T	thrust due to the propellers, lb
T'_c	thrust coefficient, $\frac{T}{\bar{q}_\infty S_w}$
T'_c/prop	thrust coefficient of one propeller

V	airplane velocity, ft/sec
x_n, x_p	distance, parallel to the X-body axis, from the center of gravity to the nacelle center of pressure and to the propeller, respectively, obtained from figure 3.2-5, in.
x'_p	distance, parallel to the X-body axis, from the propeller to the quarter chord of the wing at the thrust line, obtained from figure 3.2-1, in.
z_n, z_p	distance, parallel to the Z-body axis, from the center of gravity to the nacelle center of pressure and to the propeller, respectively, obtained from figure 3.2-5, positive down, in.
α_b	airplane angle of attack relative to the X-body axis, deg
β	sideslip angle, deg
β'	propeller blade angle at $0.75R_p$, deg
σ_p	power-induced sidewash of the slipstream behind the propeller, deg
$\frac{\partial \sigma_p}{\partial \beta}$	rate of change of the power-induced sidewash behind the propeller with sideslip angle

TABLE 5.1.1-1

EFFECT OF POWER ON $C_{Y\beta}$ (a) Increment of $C_{Y\beta}$ due to propeller normal force, $(\Delta C_{Y\beta})_{N_p}$

$$(\Delta C_{Y\beta})_{N_p} = - \frac{nf}{57.3} (C_{N\alpha})_p \left(\frac{S_p/\text{prop}}{S_w} \right)$$

Symbol	Description	Reference	Magnitude
n	Number of propellers	-----	2
R _p	Propeller radius, ft	Table 3-1	.3.0
S _p /prop	Propeller disk area, πR_p^2 , sq ft	-----	28.27 per propeller
S _w	Reference wing area, sq ft	Figure 3.2-1	178
$\frac{S_w(T'_c/\text{prop})}{8R_p^2}$	Power parameter for obtaining inflow factor, f	-----	$2.47(T'_c/\text{prop})$
f	Propeller inflow factor (function of $\frac{S_w(T'_c/\text{prop})}{8R_p^2}$)	Figure 5.1.1-1	$f(T'_c/\text{prop})$
b _p	Width of propeller blade, ft	Manufacturer	0.416 at 0.3R _p .492 at 0.6R _p .419 at 0.9R _p
K _N	Side-force factor, $262\left(\frac{b_p}{R_p}\right)_{0.3R_p} + 262\left(\frac{b_p}{R_p}\right)_{0.6R_p} + 135\left(\frac{b_p}{R_p}\right)_{0.9R_p}$	Equation (5.1.1-4)	98.2
β'	Propeller blade angle, (function of $\frac{V}{(\text{Revolutions per second})2R_p}$ and T'_c/prop), deg	Propeller group	As selected
$(C_{N\alpha})_p _{K_N=80.7}$	Propeller normal-force parameter	Figure 5.1.1-2	$f(\beta')$
$(C_{N\alpha})_p$	Propeller normal-force derivative, $[(C_{N\alpha})_p]_{K_N=80.7} [1 + 0.8 \left(\frac{K_N}{80.7} - 1 \right)]$, per rad	Equation (5.1.1-3)	$1.17 [(C_{N\alpha})_p]_{K_N=80.7}$
Summary: $(\Delta C_{Y\beta})_{N_p} = -0.00554 f(C_{N\alpha})_p$			

(1)	(2)	(3)	(4)	(5)	(6)	(7)
----	-----	Figure 5.1.1-1	As set in wind-tunnel tests of the airplane	Figure 5.1.1-2	-----	-----
T'_c	$\frac{S_w(T'_c/\text{prop})}{8R_p^2} =$ $2.47(1/2)$	f	β' , deg	$[(C_{N\alpha})_p]_{K_N=80.7}$	$(C_{N\alpha})_p =$ 1.17(5)	$(\Delta C_{Y\beta})_{N_p} =$ $-0.00554 \cdot 3 \cdot 6$, per deg
0 .20 .44	0 .247 .543	1.00 1.19 1.37	14.8 19.3 21.5	0.080 .098 .104	0.0936 .1147 .1217	-0.000519 -.000756 -.000924

TABLE 5.1.1-1 (Continued)

(b) Increment of $C_{Y\beta}$ due to propeller-induced increase in dynamic pressure on nacelles, $(\Delta C_{Y\beta})_{n(\Delta \bar{q})}$

$$(\Delta C_{Y\beta})_{n(\Delta \bar{q})} = \left[(\Delta C_{Y\beta})_n \right]_{\substack{\text{prop} \\ \text{off}}} \frac{\Delta \bar{q}_n}{\bar{q}_{\infty}}$$

Symbol	Description	Reference	Magnitude
$\left[(\Delta C_{Y\beta})_n \right]_{\substack{\text{prop} \\ \text{off}}}$	Propeller-off increment of $C_{Y\beta}$ due to nacelles, deg	Table 4.1.3-1	-0.00037
R_p	Propeller radius, ft	Table 3-1	3.0
S_w	Reference wing area, sq ft	Figure 3.2-1	178.0
$\frac{\Delta \bar{q}_n}{\bar{q}_{\infty}}$	Increase in dynamic-pressure ratio at nacelle, $\frac{S_w(T'_c/\text{prop})}{\pi R_p^2}$	Equation (5.1.1-6)	6.295(T'_c/prop)

Total T'_c	T'_c/prop	$(\Delta C_{Y\beta})_{n(\Delta \bar{q})} \approx -0.00233 (T'_c/\text{prop})$, per deg
0	0	0
.20	.10	-.000233
.44	.22	-.000513

TABLE 5.1.1-1 (Concluded)

(c) Increment of $C_{Y\beta}$ due to power-induced sidewash at nacelles, $(\Delta C_{Y\beta})_{n(\sigma_p)}$

$\textcircled{1}$	$\textcircled{2}$	$\textcircled{3}$	$\textcircled{4}$	$\textcircled{5}$	$\textcircled{6}$	$\textcircled{7}$	$\textcircled{8}$	$\textcircled{9}$
Table 4.1.3-1	Table 5.1.1-1(a)	Figure 5.1.1-3	Table 5.1.1-1(a)	Table 5.1.1-1(b)	Equation (5.1.1-8)	Table 5.1.1-1(b)	Table 5.1.1-1(b)	Equation (5.1.1-7)
T'_c	$\left[(\Delta C_{Y\beta})_n \right]_{\text{prop off}}^{\text{prop}}$ per deg	$\frac{S_w(T'_c/\text{prop})}{8R_p^2} =$ $2.47(\textcircled{1}/2)$	C_1	C_2	$(C_N)_p$	$\frac{\partial \sigma_p}{\partial \beta} =$ $\textcircled{4} + \textcircled{6}$	$\frac{\Delta \bar{q}_n}{\bar{q}_\infty} =$ $6.295(T'_c/\text{prop})$	$(\Delta C_{Y\beta})_{n(\sigma_p)} =$ $\textcircled{2} \textcircled{7}(1 + \textcircled{8})$
0	-0.00037	0	0	0.250	0.0936	0.0234	0	Equation (5.1.1-1)
.20	-.00037	.247	.170	.250	.1147	.1987	.6295	$C_{Y\beta} = (\Delta C_{Y\beta})_{\text{prop}} + (\Delta C_{Y\beta})_{N_p} + (\Delta C_{Y\beta})_{n(\Delta \bar{q})} + (\Delta C_{Y\beta})_{n(\sigma_p)}$
.44	-.00037	.543	.260	.243	.1217	.2896	1.3850	Complete airplane.

(d) Power-on $C_{Y\beta}$

$\textcircled{1}$	$\textcircled{2}$	$\textcircled{3}$	$\textcircled{4}$	$\textcircled{5}$	$\textcircled{6}$	$\textcircled{7}$	$\textcircled{8}$
Table 4.1.5-1	Table 5.1.1-1(a)	Table 5.1.1-1(b)	Table 5.1.1-1(c)	Table 5.1.1-1(c)	Table 5.1.1-1(c)	Table 5.1.1-1(c)	Equation (5.1.1-1)
T'_c	Vertical tail off, $\left[(C_{Y\beta})_{\text{wfh}} \right]_{\text{prop off}}$	Complete airplane, $(C_{Y\beta})_{N_p}$	$(\Delta C_{Y\beta})_{n(\Delta \bar{q})}$	$(\Delta C_{Y\beta})_{n(\sigma_p)}$	$(C_{Y\beta})_{\text{wfh}}$	Vertical tail off, $(C_{Y\beta})_{\text{wfh}} = \textcircled{2} + \textcircled{4} + \textcircled{5} + \textcircled{6}$	Complete airplane. $C_{Y\beta} = \textcircled{3} + \textcircled{4} + \textcircled{5} + \textcircled{6}$
0	-0.0036	-0.0085	-0.0052	0	0.0001	-0.00411	-0.00901
.20	-.0036	-.0085	-.0076	-.00023	.00012	-.00447	-.00937
.44	-.0036	-.0085	-.0092	-.00051	.00026	-.00477	-.00967

TABLE 5.1-2-1
EFFECT OF POWER ON $C_{n\beta}$

(a) Increment of $C_{n\beta}$ due to propeller side force and power effects on nacelles

(1)		(2)		(3)		(4)		(5)		(6)		(7)		(8)	
$\cos \alpha_b =$	$\cos \Theta$	$\sin \alpha_b =$	$\sin \Theta$	$x_p \cos \alpha_b + z_p \sin \alpha_b =$	b_w	$x_n \cos \alpha_b + z_n \sin \alpha_b =$	b_w	$(\Delta C_{n\beta})_{N_p} =$	$(\Delta C_{Y\beta})_{N_p} \left(\frac{x_p \cos \alpha_b + z_p \sin \alpha_b}{b_w} \right) + \left[(\Delta C_{Y\beta})_{n(\sigma_p)} + \left(\frac{x_n \cos \alpha_b + z_n \sin \alpha_b}{b_w} \right) \right]$	$(\Delta C_{n\beta})_{N_p} =$	$(\Delta C_{Y\beta})_{N_p} \left(\frac{x_n \cos \alpha_b + z_n \sin \alpha_b}{b_w} \right)$	$(\Delta C_{n\beta})_{n(\Delta \bar{q})} =$	$(\Delta C_{Y\beta})_{n(\Delta \bar{q})} + (\Delta C_{Y\beta})_{n(\sigma_p)}$	$(\Delta C_{n\beta})_p =$	$(\Delta C_{Y\beta})_p =$
-4	0.9976	-0.0698	0.1475	0.0589	-0.000077	-0.000112	-0.000136	≈ 0	-0.00009	-0.00009	-0.000113	-0.000257	0	0.20	0.44
-2	.9994	-.0349	.1470	.0584	-.000076	-.000111	-.000136	≈ 0	-0.00007	-0.00007	-0.000116	-0.000277	0.000119	-0.000151	
0	1.0000	0	0.1462	0.0579	-0.000076	-.000111	-0.000135	≈ 0	-0.00007	-0.00007	-0.000115	-0.000276	0.000118	-0.000151	
2	.9994	-.0349	.1453	.0573	-.000075	-.000110	-.000134	≈ 0	-0.00006	-0.00006	-0.000115	-0.000275	0.000118	-0.000150	
4	0.9976	0.0698	0.1442	0.0566	-0.000075	-0.000109	-0.000133	≈ 0	-0.00006	-0.00006	-0.000115	-0.000275	0.000116	-0.000149	
6	.9945	.1045	.1429	.0559	-.000074	-.000108	-.000132	≈ 0	-0.00006	-0.00006	-0.000114	-0.000274	0.000114	-0.000146	
8	0.9903	0.1392	0.1414	0.0551	-0.000073	-0.000107	-0.000131	≈ 0	-0.00006	-0.00006	-0.000113	-0.000273	0.000113	-0.000145	
10	.9848	.1736	.1398	.0542	-.000073	-.000106	-.000129	≈ 0	-0.00006	-0.00006	-0.000112	-0.000273	0.000112	-0.000143	
12	0.9781	0.2079	0.1380	0.0533	-0.000072	-0.000104	-0.000128	≈ 0	-0.00006	-0.00006	-0.000110	-0.000272	0.000110	-0.000142	

TABLE 5, L.2-1 (Concluded)

(b) Power-on $C_{n\beta}$

$$C_{n\beta} = \left(C_{n\beta} \right)_{\text{prop off}} + \left(\Delta C_{n\beta} \right)_p$$

α_b , deg	$\left[\left(C_{n\beta} \right)_{\text{wfn}} \right]_{\text{prop off}}$	$\textcircled{1}$		$\textcircled{2}$		$\textcircled{3}$		$\textcircled{4}$		$\textcircled{5}$		$\textcircled{6}$	
		Table 4.2.5-1 $\textcircled{5b}$	Table 4.2.5-1 $\textcircled{7b}$	Table 5.1.2-1(a)		$\left(\Delta C_{n\beta} \right)_p$	Vertical tail off, Complete airplane, $\left(C_{n\beta} \right)_{\text{prop off}}$	$\left(C_{n\beta} \right)_{\text{wfn}}$	Vertical tail off, $\left(C_{n\beta} \right)_{\text{wfn}}$	$\textcircled{2}$ + $\textcircled{4}$	Complete airplane, $C_{n\beta} = \textcircled{3} + \textcircled{4}$	T'_c	T'_c
-4	-0.000115	0.001714	-0.000077	-0.000119	-0.000151	-0.000192	-0.000234	-0.000266	0.001637	0.001595	0.001563		
-2	-0.000112	0.001739	-0.000076	-0.000118	-0.000151	-0.000188	-0.000230	-0.000263	.001663	.001621	.001588		
0	-0.000101	0.001769	-0.000076	-0.000118	-0.000150	-0.000177	-0.000219	-0.000251	0.001693	0.001651	0.001619		
2	-0.000133	0.001754	-0.000075	-0.000116	-0.000149	-0.000208	-0.000249	-0.000282	.001679	.001638	.001605		
4	-0.000153	0.001749	-0.000075	-0.000115	-0.000148	-0.000228	-0.000268	-0.000301	0.001674	0.001634	0.001601		
6	-0.000208	0.001706	-0.000074	-0.000114	-0.000146	-0.000242	-0.000322	-0.000354	.001632	.001592	.001560		
8	-0.000323	0.001601	-0.000073	-0.000113	-0.000145	-0.000386	-0.000436	-0.000468	0.001528	0.001488	0.001456		
10	-0.000351	0.001581	-0.000073	-0.000112	-0.000143	-0.000424	-0.000463	-0.000494	.001508	.001469	.001438		
12	-0.000338	0.001599	-0.000072	-0.000110	-0.000142	-0.000410	-0.000448	-0.000480	0.001527	0.001489	0.001457		

TABLE 5. 1. 3-1

EFFECT OF POWER ON $C_{l\beta}$

$$C_{l\beta} = (C_{l\beta})_{\text{prop off}} + (\Delta C_{Y\beta})_{N_p} \left(\frac{-z_p \cos \alpha_b + x_p \sin \alpha_b}{b_w} \right) + \frac{0.5}{57.3} \frac{x'_p}{b_w} \left(1 - \frac{\partial \sigma}{\partial \beta} \right) \left[(\Delta C_L)_{w(\Delta \bar{q})} + (\Delta C_L)_{w(\epsilon_p)} \right]$$

(a) Pertinent parameters

Symbol	Description	Reference	Magnitude
$(C_{l\beta})_{\text{prop off}}$	Propeller-off $C_{l\beta}$	Table 4. 3. 4-1	$f(\alpha_b)$
x_p	Distance from center of gravity to propeller along X-body axis, in.	Figure 3. 2-5	63. 15
z_p	Distance from center of gravity to propeller along Z-body axis, in.	Figure 3. 2-5	-10. 43
b_w	Wing span, in.	Figure 3. 2-1	432. 0
$(\Delta C_{Y\beta})_{N_p}$	Increment of $C_{Y\beta}$ due to propeller side force, deg For: $T'_c = 0$ $T'_c = 0.20$ $T'_c = 0.44$	Table 5. 1. 1-1(a)	-0.000519 .000756 .000924
x'_p	Distance from propeller to wing quarter chord along thrust line, in.	Scaled from figure 3. 2-1	72
$\frac{\partial \sigma}{\partial \beta}$	Power-induced sidewash factor behind propeller For: $T'_c = 0$ $T'_c = 0.20$ $T'_c = 0.44$	Table 5. 1. 1-1(c)	0.0234 .1987 .2896
$(\Delta C_L)_{w(\Delta \bar{q})}$	Increment of lift on immersed wing area due to power-induced increase in dynamic pressure	Table 5. 1. 1-2(a)-3 of reference 1	$f(\alpha_b)$
$(\Delta C_L)_{w(\epsilon_p)}$	Increment of lift on immersed wing area due to power-induced downwash	Table 5. 1. 1-2(b)-2 of reference 1	$f(\alpha_b)$

Summary:

For $T'_c = 0$

$$C_{l\beta} = (C_{l\beta})_{\text{prop off}} + (\Delta C_{Y\beta})_{N_p} (0.0241 \cos \alpha_b + 0.1462 \sin \alpha_b) + 0.00142 [(\Delta C_L)_{w(\Delta \bar{q})} + (\Delta C_L)_{w(\epsilon_p)}]$$

For $T'_c = 0.20$

$$C_{l\beta} = (C_{l\beta})_{\text{prop off}} + (\Delta C_{Y\beta})_{N_p} (0.0241 \cos \alpha_b + 0.1462 \sin \alpha_b) + 0.00117 [(\Delta C_L)_{w(\Delta \bar{q})} + (\Delta C_L)_{w(\epsilon_p)}]$$

For $T'_c = 0.44$

$$C_{l\beta} = (C_{l\beta})_{\text{prop off}} + (\Delta C_{Y\beta})_{N_p} (0.0241 \cos \alpha_b + 0.1462 \sin \alpha_b) + 0.00103 [(\Delta C_L)_{w(\Delta \bar{q})} + (\Delta C_L)_{w(\epsilon_p)}]$$

TABLE 5. 1. 3-1 (Concluded)

①	②	③	④	⑤		⑥		⑦		⑧	
---	---	---	Table 4, 3-4-1	Equation (5, 1, 3-2) and table 5, 1, 3-1(a)		Tables 5, 1, 1-2(a)-3 and 5, 1, 1-2(b)-2 of reference 1		Equation (5, 1, 3-4) and table 5, 1, 3-1(a)		Equation (5, 1, 3-1)	
α_b deg	$\cos(1)$	$\sin(1)$	$(C_{l_\beta})_{\text{off}}^{\text{prop}}$	$(\Delta C_{l_\beta})_{N_p} = (\Delta C_{Y_\beta})_{N_p} (0, 0241 \odot + 0, 1462 \odot)$	T'_c	$(\Delta C_L)_{W(\Delta \bar{q})} + (\Delta C_L)_{W(\epsilon_p)}$	T'_c	$(\Delta C_{l_\beta})_{W(\Delta \bar{q} + \epsilon_p)} = K(6)$	T'_c	$C_{l_\beta} = \odot + \odot + \odot$	
				From table 5, 1, 3-1(a), $(\Delta C_{Y_\beta})_{N_p} =$		From table 5, 1, 3-1(a), $K =$					
-4	0.9976	-0.0698	-0.000519	-0.000756	-0.000924	0	0.20	0.44	0.00142	0.00117	0.00103
-2	.9994	-.0349	-0.001512	-0.00001	-0.00001	0.00211	0.02910	0.06194	0.00003	0.00006	-0.00152
0	1.0000	0	-0.001498	-.00001	-.00001	.00083	.04228	.08675	0.00005	.00009	-.00151
2	.9994	.0349	-0.001483	-0.00001	-0.00002	-0.00002	-0.00042	0.05459	0.10569	0.00011	0.00149
4	0.9976	0.0698	-0.000519	-0.000756	-0.000924	0	0.20	0.44	0.00142	0.00117	0.00103
6	.9945	.1045	-0.001451	-0.00002	-0.00003	-0.00003	-0.00263	0.07527	0.14569	0.00015	0.00147
8	0.9903	0.1392	-0.001418	-0.00002	-0.00003	-0.00004	-.00004	.03355	.05389	0.00010	0.00017
10	.8848	.1736	-.001410	-.00003	-.00004	-.00005	-.00474	0.09643	0.17790	0.00011	0.00018
12	0.9781	0.2079	-0.001383	-0.00003	-0.00004	-0.00005	-0.00486	.09336	.18731	0.00011	0.00019

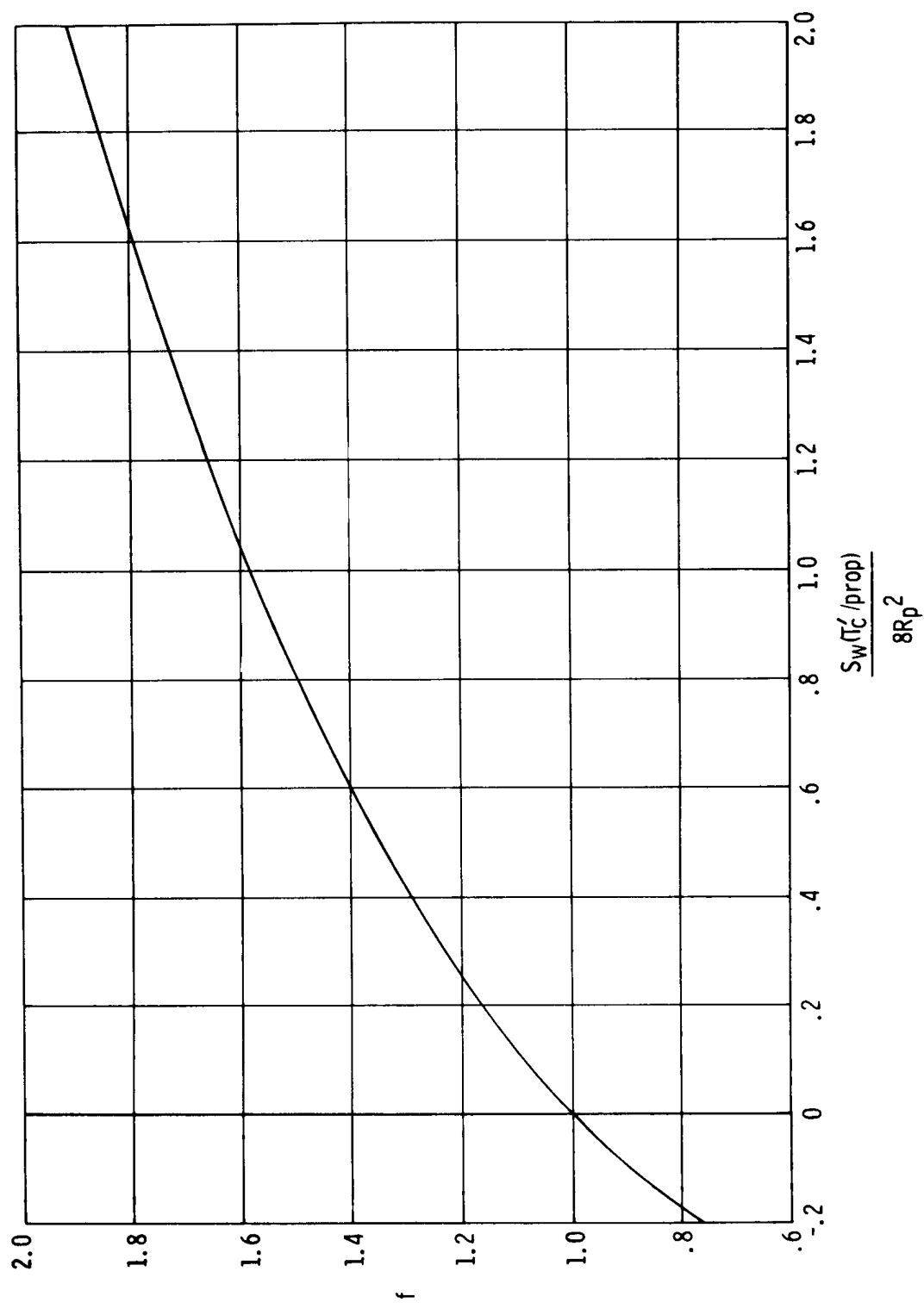


Figure 5.1.1-1. Propeller inflow factor (from ref. 17).

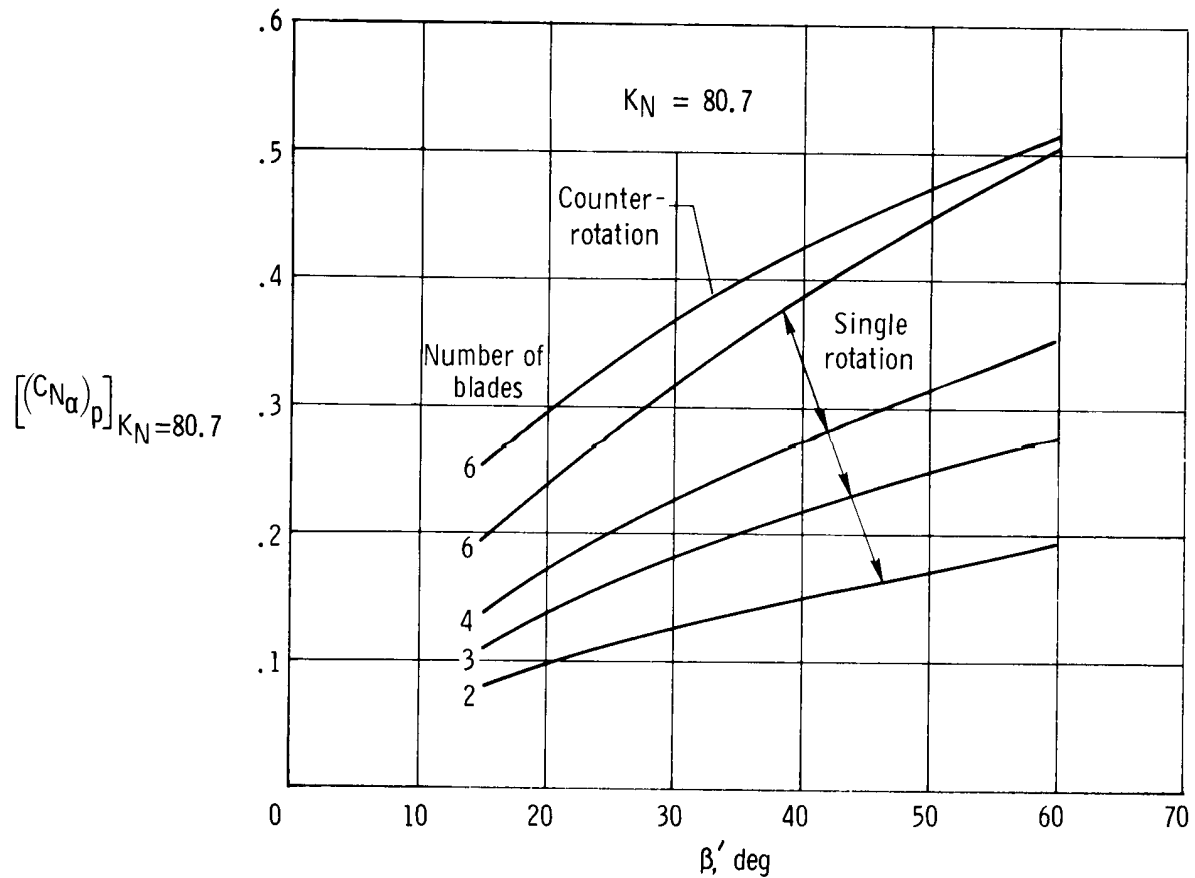


Figure 5.1.1-2. Propeller normal-force parameter (from ref. 17).

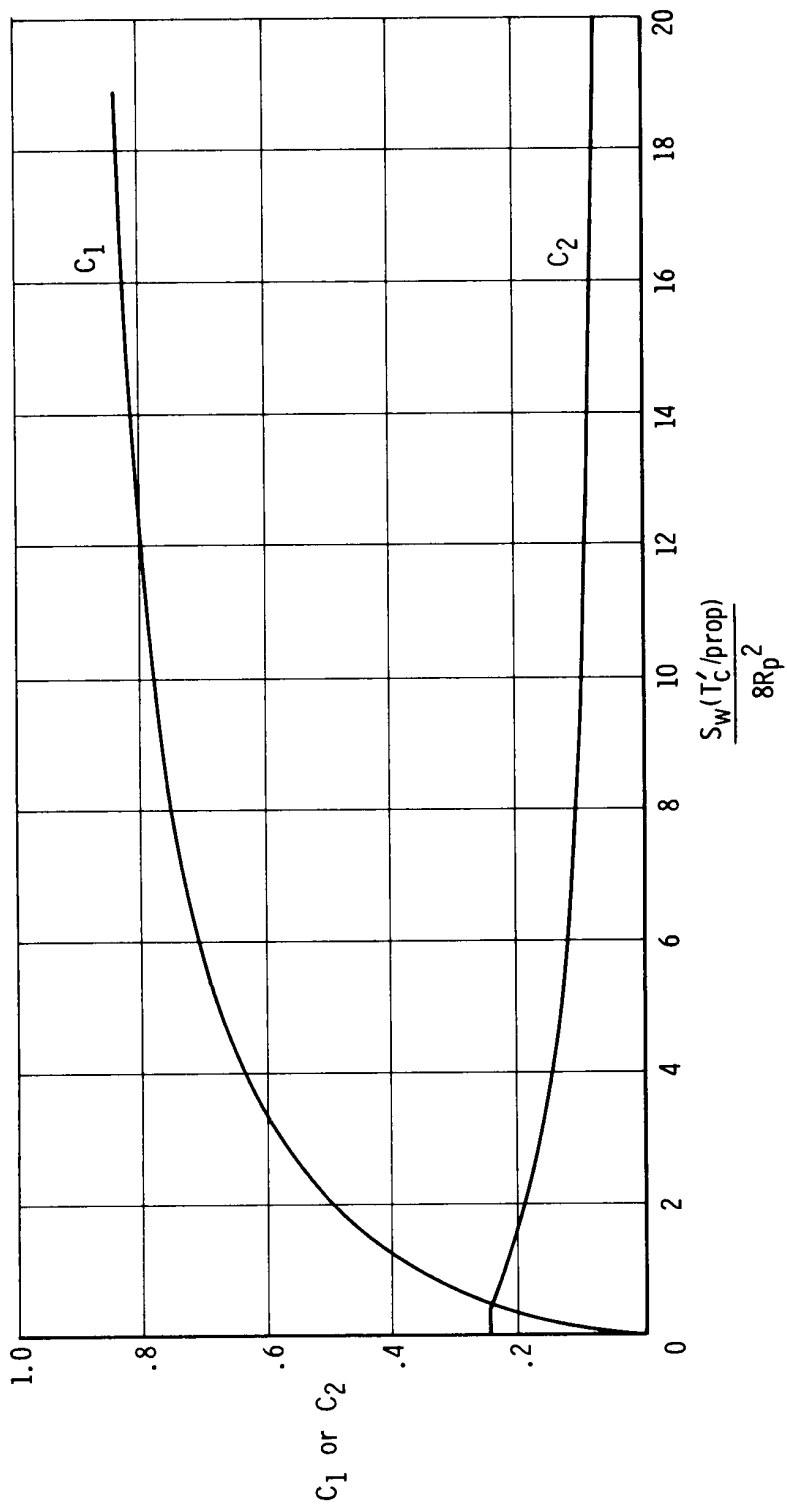


Figure 5.1.1-3. Factors for determining propeller downwash (from ref. 8).

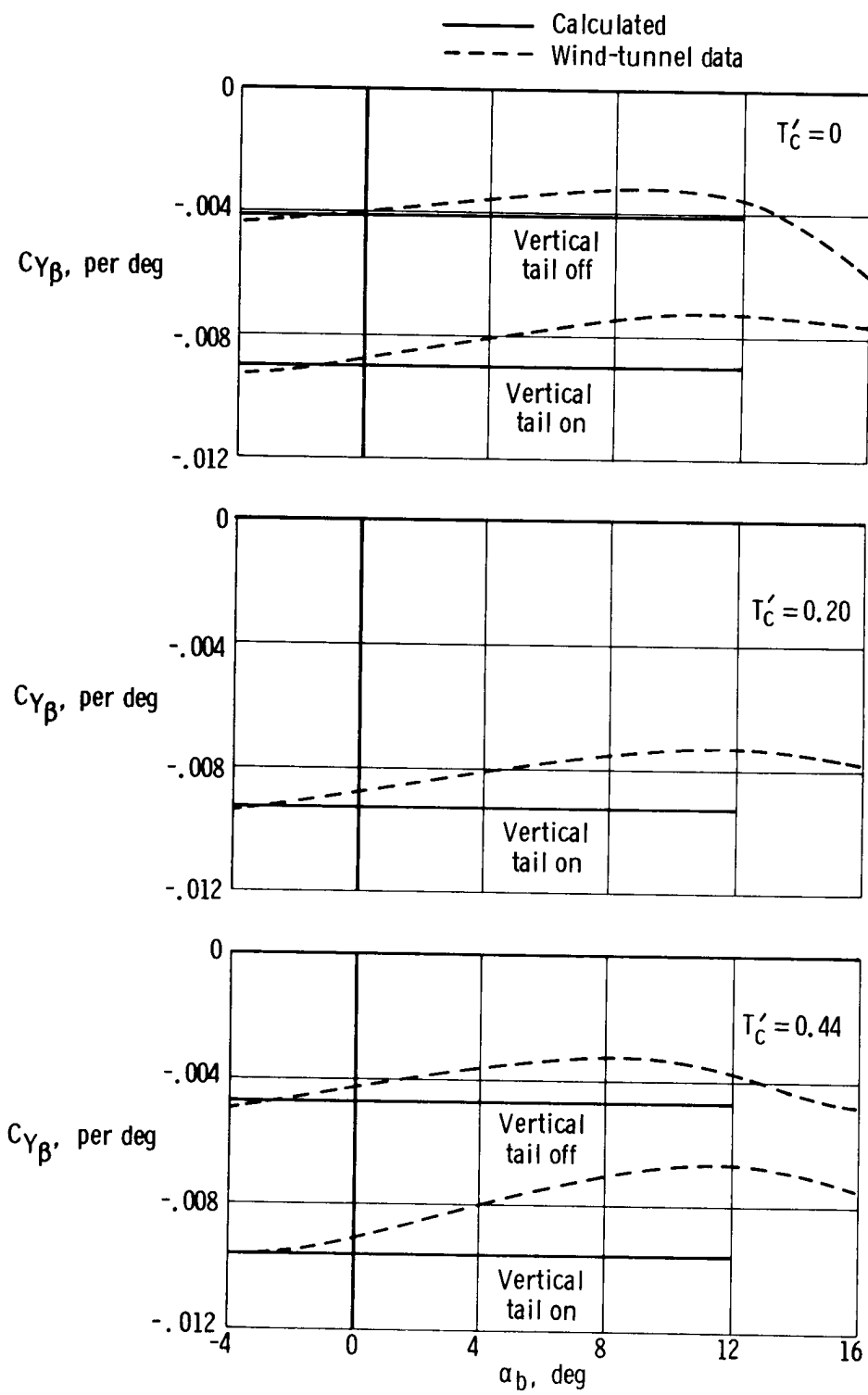


Figure 5.1.1-4. Comparison of calculated $C_{Y\beta}$ with wind-tunnel data as a function of angle of attack and thrust coefficient.

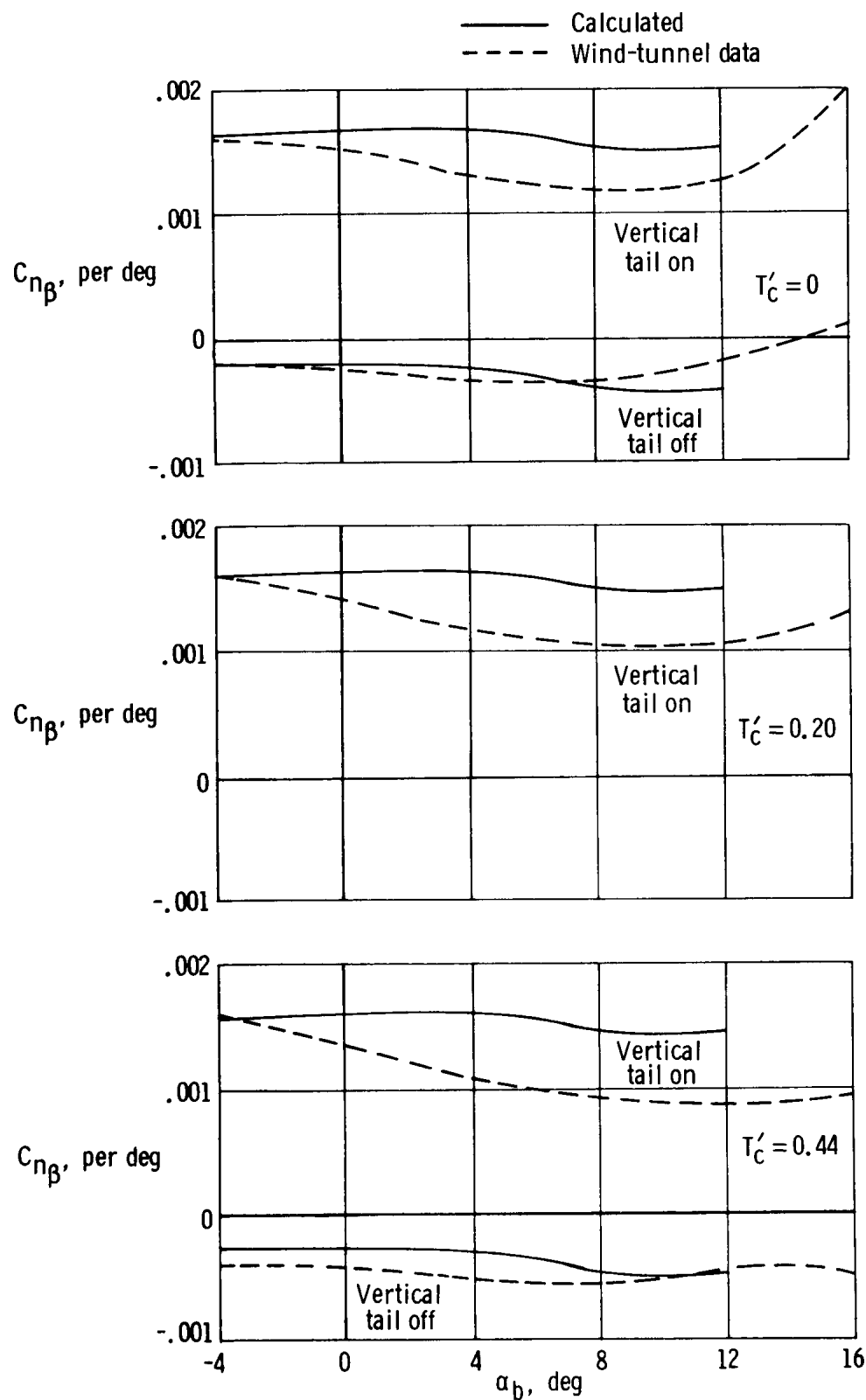


Figure 5.1.2-1. Comparison of calculated $C_{n\beta}$ with wind-tunnel data as a function of angle of attack and thrust coefficient.

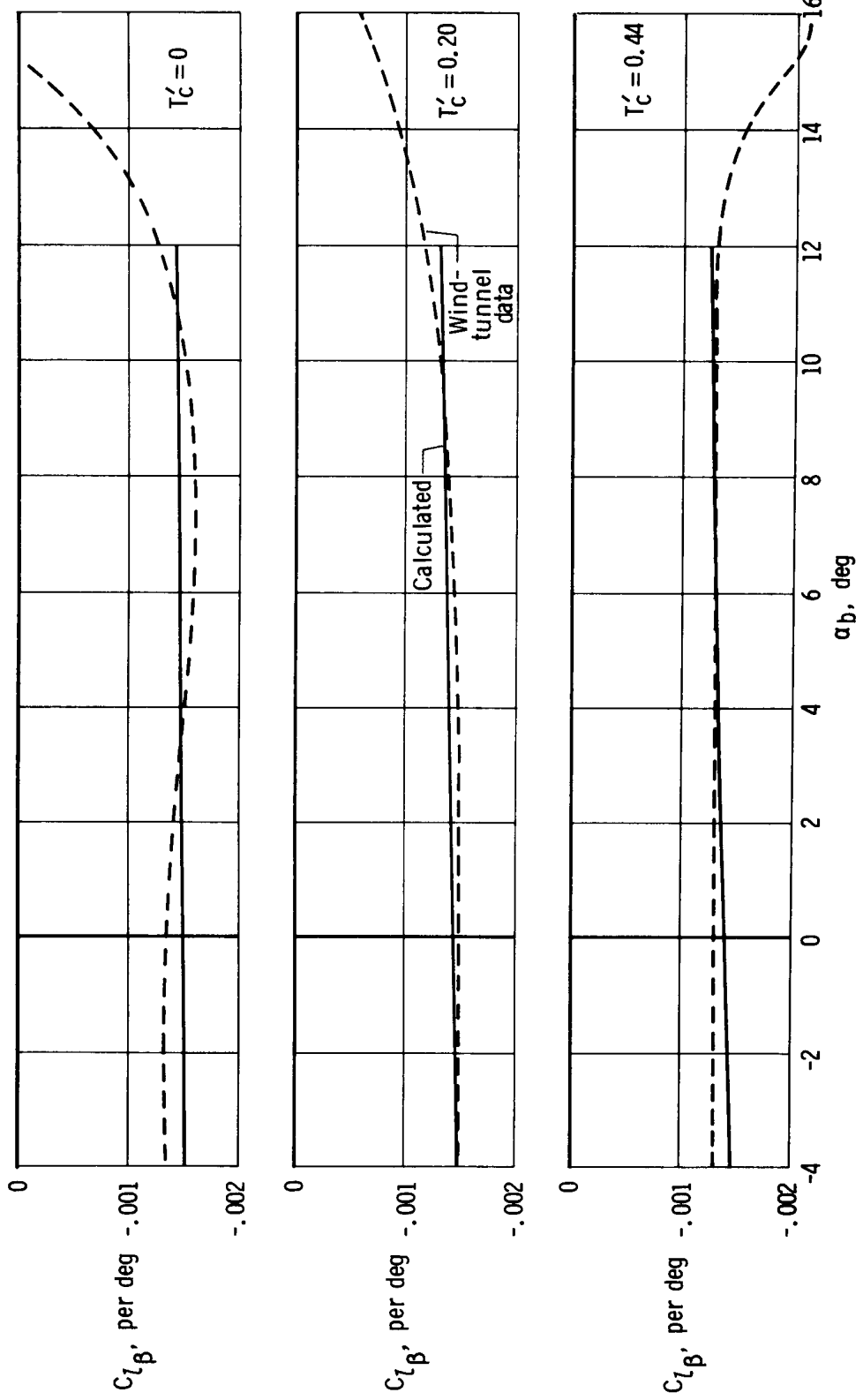


Figure 5.1.3-1. Comparison of calculated $C_{l\beta}$ with wind-tunnel data as a function of angle of attack and thrust coefficient.

5.2 Power-On Control Characteristics

5.2.1 Aileron Parameters

The ailerons on light aircraft are normally not significantly affected by the propeller slipstream. They are far enough away from the slipstream to be on the edge of or outside the influence of power-induced change in wing-span loading. Consequently, the values of the propeller-off aileron parameters, $C_l \delta_a$ and $C_n \delta_a$, calculated in section 4.4, are considered to be valid estimates for all power conditions.

The calculated characteristics of the aileron parameters, $C_l \delta_a$ and $C_n \delta_a$, for the subject airplane (from tables 4.4.1-1 and 4.4.2-1, respectively) are compared with wind-tunnel data in figure 5.2.1-1. The wind-tunnel data for $C_l \delta_a$ show some inconsistency in variation with angle of attack for the different power conditions. This may be more a matter of test technique than power effects, inasmuch as the tunnel data were based on aileron settings of -32° , -18° , 0° , 16° , and 32° , which are rather coarse for accurate determination of aileron characteristics. With this factor taken into consideration, the calculated aileron characteristics have been obtained to a reasonably good degree of accuracy.

5.2.2 Rudder Parameters

The rudder on a single vertical-tail installation on a twin-engine airplane can be considered to be outside the propeller slipstream for normal maneuvering and unaffected by power conditions. Thus the values of the propeller-off rudder parameters, $C_Y \delta_r$, $C_n \delta_r$, and $C_l \delta_r$, calculated in section 4.5, are considered to be valid estimates for all power conditions.

The calculated characteristics of the rudder parameters, $C_Y \delta_r$, $C_n \delta_r$, and $C_l \delta_r$, for the subject airplane (from tables 4.5.1-1 and 4.5.2-1) are compared with wind-tunnel data in figure 5.2.2-1. The calculated $C_Y \delta_r$ and $C_l \delta_r$ parameters show the same good correlation with the power-on tunnel data as was shown in figure 4.5.2-1 for propeller-off conditions. Calculated $C_n \delta_r$, which showed good correlation with propeller-off wind-tunnel data (fig. 4.5.2-1), shows poorer but reasonably good correlation with the power-on wind-tunnel data. It should be noted that although the power-on wind-tunnel data do not show any significant change with power in the linear angle-of-attack range, the values are smaller than the propeller-off values shown in figure 4.5.2-1. The reason for this difference is not clear.

5.2.3 Symbols

$C_l \delta_a$ rate of change of the rolling-moment coefficient with the aileron deflection, per deg

$C_l \delta_r$ rate of change of the rolling-moment coefficient with the rudder deflection, per deg

$C_{n\delta_a}$	rate of change of the yawing-moment coefficient with the aileron deflection, per deg
$C_{n\delta_r}$	rate of change of the yawing-moment coefficient with the rudder deflection, per deg
$C_{Y\delta_r}$	rate of change of the side-force coefficient with the rudder deflection, per deg
T_c'	thrust coefficient
α_b	angle of attack relative to the X-body axis, deg

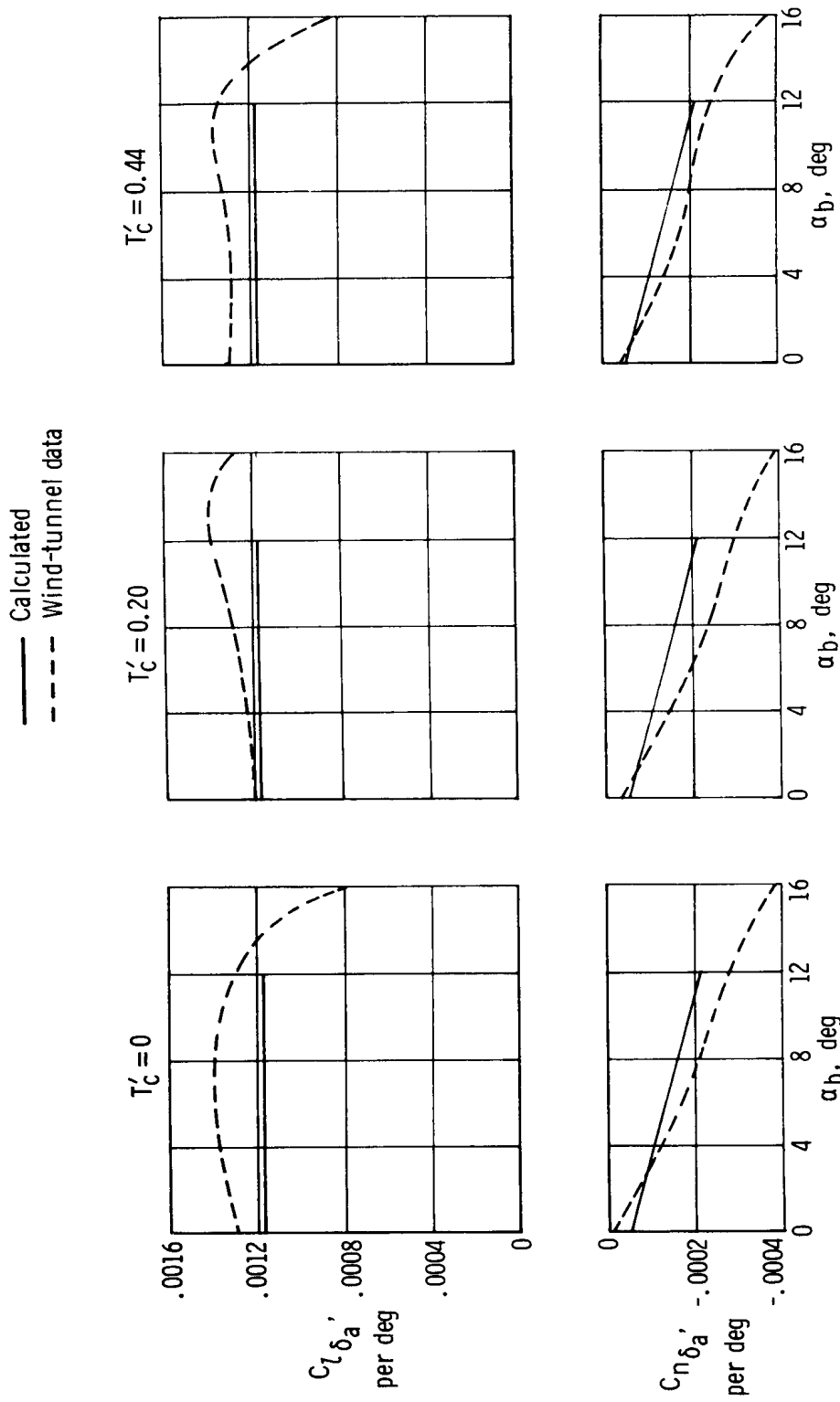


Figure 5.2.1-1. Comparison of calculated aileron characteristics with wind-tunnel data.

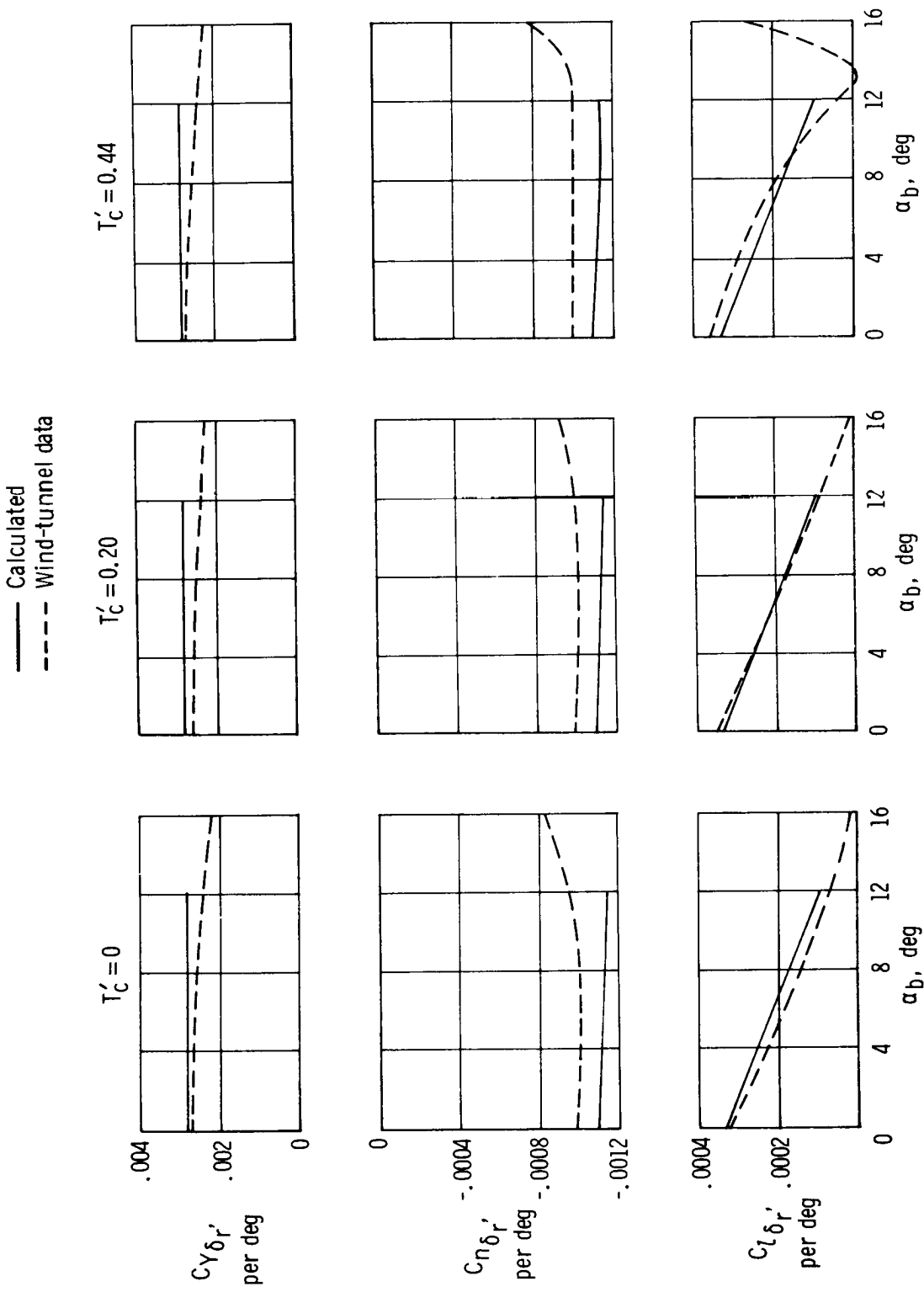


Figure 5.2.2-1. Comparison of calculated rudder characteristics with wind-tunnel data.

5.3 Comparison of Predicted Static Stability and Control Characteristics With Flight Data

Although the calculated static stability and control characteristics were compared with wind-tunnel data for validation, it is desirable to compare both calculated and wind-tunnel predictions with flight data. The methods by which the flight-determined derivatives used in the comparisons were obtained are discussed in this section, and the flight results are compared with predictions. In previous sections, calculated and wind-tunnel predictions were referenced to the stability system of axes. In comparing predictions with flight results the predicted characteristics will be referenced to the body system of axes to conform with the flight data. Table 5.3-1 lists a complete set of transformation equations that reorient the predicted characteristics from stability to body axis.

5.3.1 Flight-Test Conditions and Maneuvers

The flight data for the subject airplane were obtained at a pressure altitude of 6000 feet and over a velocity range of 133 to 254 feet per second, with the airplane center of gravity at 12 percent of the mean aerodynamic chord. The data were obtained from Dutch roll oscillations and sideslip maneuvers.

The Dutch roll maneuver was initiated by an aileron or rudder input when the airplane was at a steady-state 1g condition. Aileron inputs were of an abrupt pulse type to excite the transient oscillatory mode with the controls held fixed at pre-maneuver trim position during the oscillatory responses. The rudder inputs were of a doublet type to minimize rolloff tendencies which became evident when rudder pulse inputs were attempted.

The increasing-sideslip maneuver was initiated from stabilized wings-level conditions. Sideslip was increased slowly to provide essentially zero roll and yaw rates and accelerations.

5.3.2 Analysis of the Dutch Roll Maneuver Flight Data

Flight data from Dutch roll maneuvers were analyzed using the simplest procedures, commensurate with the need, to obtain the flight derivatives by manual manipulation of the data at a desk. Thus primary consideration was given to the use of approximate equations (ref. 18), with due regard to the limitations of their application. When the application of an approximate equation was questionable, as for $C_{l\beta}$, complete graphical time-vector solutions involving dynamic derivatives (ref. 18) were used to supplement or replace the simpler approach.

By using the graphical time-vector technique, $C_{Y\beta}$ was obtained from

$$C_{Y\beta} = -\frac{W}{qS} \frac{|a_t|}{|\beta|} \text{ per deg} \quad (5.3.2-1)$$

where

W is the airplane weight, lb

\bar{q} is the free-stream dynamic pressure, lb/sq ft

$\frac{|a_t|}{|\beta|}$ is the amplitude ratio of the lateral acceleration (corrected to the center of gravity, in g units) to the sideslip angle (in deg)

S is the wing area, sq ft

In considering the application of an approximate equation to obtain $C_{n\beta}$ from the oscillatory flight data, several factors were taken into account. The product of inertia of the subject airplane is small and negligible for present purposes; also, a study of the control-fixed oscillatory responses to a control input showed the roll-rate vector to be approximately 180° out of phase with the sideslip vector. Consequently, the following equation, which is a refinement of an equation presented in reference 18, was formulated and used to obtain $C_{n\beta}$:

$$C_{n\beta} = \frac{1}{57.3} \left(\frac{I_Z}{\bar{q}Sb} \frac{|r|}{|\beta|} \omega_n + C_{n_p} \frac{|p|}{|\beta|} \frac{b}{2V} \right) \text{ per deg} \quad (5.3.2-2)$$

where

I_Z is the moment of inertia about the Z-body axis, slug-ft²

$\frac{|r|}{|\beta|}$ is the amplitude ratio of the yaw rate relative to sideslip, obtained directly from flight records in the manner described in reference 18, (rad/sec)/rad

$\frac{|p|}{|\beta|}$ is the amplitude ratio of the roll rate relative to sideslip (Because only a limited number of p traces of suitable quality for analysis were available, a representative constant value was used for all maneuvers analyzed.)

ω_n is the undamped oscillatory frequency of the responses as obtained from

$$\omega_n = \frac{2\pi}{P(1 - \xi^2)} \quad (5.3.2-3)$$

and where

P is the period of the oscillations obtained from flight records, sec

ξ is the damping ratio obtained from

$$\xi = \tan^{-1} \left(\frac{0.1103P}{T_{1/2}} \right) \quad (5.3.2-4)$$

$T_{1/2}$ is the time to damp to half amplitude, obtained from flight records

C_{n_p} is the calculated yawing-moment-due-to-roll-rate derivative, obtained from section 6.4.

As a check on the flight-determined values of C_{n_β} (obtained by the approximate equation (5.3.2-2)), complete graphical time-vector solutions were obtained when the quality of the p traces permitted. The check cases involved refined techniques (described in ref. 18) to obtain $\frac{|r|}{|\beta|}$ and its corresponding phase angle, $\Phi_{r\beta}$, more precisely than was possible using the flight records directly.

The approximate equations for C_{l_β} (ref. 18) showed excessive sensitivity to slight experimental errors, because small differences in two large numbers caused a disproportionately large variation in the derivative. This unreliability, along with an indication that there was a discrepancy between flight-determined and predicted values of C_{l_β} , resulted in use of the graphical time-vector solution of the rolling-moment equation whenever suitable data were available. As described in reference 18, the solution of the rolling-moment equation involves refined techniques for obtaining fairly precise values of $\frac{|r|}{|\beta|}$ and its corresponding phase relationship, $\Phi_{r\beta}$, thus reducing experimental error. Although C_{l_β} is of prime concern at this time, the use of the complete vector solution involves dynamic derivatives.

The graphical time-vector solution of the rolling-moment equation involves the derivatives C_{l_β} , C_{l_p} , and C_{l_r} . Only two of these can be solved for at the same time. For the subject airplane the p and β vectors were almost 180° out of phase and, as a consequence, it was not possible to solve for C_{l_p} and C_{l_β} . Slight experimental errors in the phase relationship of p and β resulted in large changes in C_{l_p} and C_{l_β} . Because C_{l_p} can be theoretically predicted within 5 percent, it was decided to use calculated values of C_{l_p} as the known quantity and to solve for C_{l_β} and C_{l_r} .

A typical vector diagram showing the rolling-moment equation being solved for C_{l_β} and C_{l_r} is shown in figure 5.3.2-1. The orientation of the vectors shows that C_{l_β} is obtained with good accuracy (within 5 percent), since $\frac{|\beta|}{|r|}$, $\Phi_{\beta r}$, $\frac{|p|}{|r|}$, and C_{l_p} are known with a good degree of accuracy. The derivative C_{l_r} is determined with a smaller degree of accuracy (within 20 percent) because of the probable $\pm 5^\circ$ error in the phase angle between the p and r vectors.

The control derivatives relative to the body axes may be obtained by manual calculations from the initial portion of the maneuvers (from initiation of the input to the first peak of the dominant angular acceleration) using abbreviated yawing- and rolling-moment perturbation equations of motion related to the body-axes system. The degree of abbreviation permitted is a function of the type of airplane input as well as of airplane response characteristics. The following equations were used to obtain the aileron

derivatives for the subject airplane from the initial portion of Dutch roll maneuvers initiated by abrupt, pulse-type inputs:

$$C_{l\delta_a} = \frac{1}{\Delta\delta_a} \left(\frac{I_X}{qSb} \Delta\dot{p} - C_{l_p} \Delta p \frac{b}{2V} - C_{l_\beta} \Delta\beta \right) \quad (5.3.2-5)$$

$$C_{n\delta_a} = \frac{1}{\Delta\delta_a} \left(\frac{I_Z}{qSb} \Delta\dot{r} - \frac{I_{XZ}}{qSb} \Delta\dot{p} - C_{n_r} \Delta r \frac{b}{2V} - C_{n_\beta} \Delta\beta \right) \quad (5.3.2-6)$$

The following equations were used to obtain the rudder derivatives from the initial portion of the Dutch roll maneuvers initiated by abrupt, doublet-type rudder inputs:

$$C_{n\delta_r} = \left(\frac{I_Z}{qSb} \Delta\dot{r} - C_{n_r} \Delta r \frac{b}{2V} - C_{n_\beta} \Delta\beta \right) \quad (5.3.2-7)$$

$$C_{l\delta_r} = \left(\frac{I_X}{qSb} \Delta\dot{p} - C_{l_p} \Delta p \frac{b}{2V} - C_{l_\beta} \Delta\beta \right) \quad (5.3.2-8)$$

In these equations, p , \dot{p} , r , and \dot{r} are in radians; β is in degrees.

After studying the variation of the product of inertia, I_{XZ} , for the range of airplane weight encompassed by the flight-test data and after several spot checks of its influence on the results, the product of inertia of the subject airplane was considered to be negligible in all instances except in the determination of $C_{n\delta_a}$ (eq. (5.3.2-6)). The product of inertia was between 20 and 40. The moments of inertia about the X-axis and Z-axis were of the order of 2700 and 4400, respectively.

The static body-referenced stability derivatives, C_{n_β} and C_{l_β} , used in the equations were obtained from equation (5.3.2-2) and from graphical time-vector techniques, respectively.

The dynamic derivatives, C_{l_p} and C_{n_r} , used in the equations are calculated values (from section 6) transformed from the stability- to the body-axes system. The calculated values of C_{l_p} , used in the absence of flight values, are considered to be within 5 percent of the true value. Although flight-determined values of C_{n_r} could have been used, calculated values, which correlated well with the flight data, were given preference because of the scatter in the flight data.

The increment changes in \dot{r} , \dot{p} , r , p , and β correspond to the time increment, Δt , of the initial rapid control input, $\Delta\delta$. Corrections for the phase lag in the response of the sensed quantities were applied as required.

5.3.3 Analysis of the Increasing-Sideslip-Maneuver Flight Data

The flight data from the increasing-sideslip maneuvers were analyzed for $C_{n\beta}$ and $C_{l\beta}$, using the following equations from reference 18, to substantiate the values obtained from the analysis of the Dutch roll flight data, particularly the values of $C_{l\beta}$:

$$C_{n\beta} = - \left(C_{n\delta_r} \delta_{r\beta} + C_{n\delta_a} \delta_{a\beta} \right) \quad (5.3.3-1)$$

$$C_{l\beta} = - \left(C_{l\delta_r} \delta_{r\beta} + C_{l\delta_a} \delta_{a\beta} \right) \quad (5.3.3-2)$$

where

$\delta_{r\beta}$, $\delta_{a\beta}$ are the variations of trim values of rudder and aileron settings, respectively, with sideslip

$C_{n\delta_r}$, $C_{n\delta_a}$, $C_{l\delta_a}$, $C_{l\delta_r}$ are the control-effectiveness parameters previously discussed

Unless the sideslip maneuver is performed carefully, the sideslip parameters, $\delta_{r\beta}$ and $\delta_{a\beta}$, are obtained inaccurately, thus precluding the successful application of equations (5.3.3-1) and (5.3.3-2). For the subject airplane the sideslip maneuvers were performed with precision, thus minimizing the error in determining these sideslip parameters. Also, faired values of flight-determined $C_{n\delta_r}$, $C_{n\delta_a}$, and $C_{l\delta_a}$ were used to minimize the level of uncertainty of these parameters. Because $C_{l\delta_r}$ could not be determined from the flight data available, calculated values were used.

5.3.4 Comparison of Predicted Stability and Control Characteristics With Flight Data

In figures 5.3.4-1 and 5.3.4-2 the predicted static stability and control characteristics are compared with the flight-determined characteristics of the subject airplane.

5.3.4-1 Static Stability Derivatives

As indicated in figure 5.3.4-1, flight-determined $C_{Y\beta}$ shows excellent correlation with wind-tunnel data. Calculated $C_{Y\beta}$ shows good agreement at low angles of attack, but correlation deteriorates with increasing angle of attack. This deterioration is probably due to the inadequate allowance for wing-body interference and vertical-tail sidewash effects as a function of angle of attack.

Considering the scatter of the data and the various techniques used in the analysis, flight values of $C_{n\beta}$ show good correlation with the wind-tunnel data through most of the flight range. The calculated values show an increasing discrepancy with wind-tunnel and flight data with increasing angle of attack; however, the correlation is

reasonably good. The increasing discrepancy is undoubtedly due to some extent to inadequate allowance for vertical-tail sidewash effects as a function of angle of attack.

Flight-determined $C_{l\beta}$ obtained from the graphical time-vector solution generally shows the same variation with angle of attack as predicted by calculations and wind-tunnel data; however, it does not correlate in magnitude. Flight $C_{l\beta}$ is approximately 40 to 50 percent less than predicted. Although calculated values of C_{l_p} were used in the graphical time-vector technique to obtain $C_{l\beta}$, this usage of calculated C_{l_p} was not a factor in the discrepancy. This is verified by the somewhat less accurate but reasonable values of $C_{l\beta}$ obtained from increasing-sideslip maneuvers, which tend to correlate with the values obtained from the time-vector technique. The validity of flight-determined values of $C_{l\beta}$ is substantiated in sections 7.3 and 7.4.2, in which it is shown that improved correlation of the calculated response parameters $\frac{|\varphi|}{|\beta|}$ and $\left(\frac{pb}{2V}\right)_{\delta_a}$ were obtained when flight values of $C_{l\beta}$ were used in the response equations.

A study of the factors that contributed to $C_{l\beta}$ under propeller-off conditions (table 4.3.4-1) and of the effect of power on $C_{l\beta}$ (table 5.1.3-1(b)) showed wing and wing-fuselage interference to be the most likely sources for the discrepancy. The vertical tail was not considered to be a potential source of discrepancy, because its contribution is much smaller than the magnitude of the discrepancy shown.

A similar discrepancy in $C_{l\beta}$ was encountered in a Princeton University study (ref. 19) in correlating wind-tunnel and flight data for a light, single-engine, propeller-driven airplane. Obviously, the discrepancy should be investigated further.

5.3.4-2 Control Derivatives

The correlation between flight, wind-tunnel, and calculated control derivatives, $C_{l\delta_a}$, $C_{n\delta_r}$, and $C_{n\delta_a}$ is shown in figure 5.3.4-2. The derivative $C_{l\delta_r}$ is not included because the quality of the flight data would not permit the determination of this parameter to any reasonable degree of reliability with the method of analysis used.

The correlation is excellent between flight and wind-tunnel $C_{l\delta_a}$ and $C_{n\delta_r}$. The calculated value of $C_{l\delta_a}$ is approximately 8 percent low at an angle of attack of 0° and 14 percent low at an angle of attack of 10° . The calculated value of $C_{n\delta_r}$ is approximately 10 percent high at an angle of attack of 0° and 15 percent high at an angle of attack of 10° .

Although calculated and wind-tunnel values of $C_{n\delta_a}$ show reasonably good correlation, flight data indicate larger negative values than predicted. The reason for this

discrepancy has not been determined.

5.3.5 Symbols

Unless otherwise indicated, the mass properties and aerodynamic characteristics defined are related to the body system of axes. Calculated and wind-tunnel-determined aerodynamic characteristics can be transformed to the body system, for use in section 5.3, by using table 5.3-1.

a_t	lateral (transverse) acceleration, g units
b	wing span, ft
C_c	coefficient of the axial force along the X-body axis, positive to the rear
$C_{c\alpha} = \frac{\partial C_c}{\partial \alpha}$	
C_D	drag coefficient; coefficient of the axial force along the X-stability axis, positive to the rear
$C_{D\alpha} = \frac{\partial C_D}{\partial \alpha}$	
C_L	lift coefficient; coefficient of the lift force along the X-stability axis
$C_{L\alpha} = \frac{\partial C_L}{\partial \alpha}$	
C_l	rolling-moment coefficient
$C_{l_p} = \frac{\partial C_l}{\partial (\frac{pb}{2V})}$	
$C_{l_r} = \frac{\partial C_l}{\partial (\frac{rb}{2V})}$	
$C_{l\beta} = \frac{\partial C_l}{\partial \beta}$	
$C_{l\dot{\beta}} = \frac{\partial C_l}{\partial (\frac{\dot{\beta}b}{2V})}$	
$C_{l\delta}, C_{n\delta}$	variation of the rolling-moment coefficient and the yawing- moment coefficient, respectively, with control deflec- tion

$C_{l\delta_a} = \frac{\partial C_l}{\partial \delta_a}$	
$C_{l\delta_r} = \frac{\partial C_l}{\partial \delta_r}$	
C_m	pitching-moment coefficient
$C_{m\alpha} = \frac{\partial C_m}{\partial \alpha}$	
C_N	normal-force coefficient; coefficient of the force parallel to the Z-body axis
$C_{N\alpha} = \frac{\partial C_N}{\partial \alpha}$	
C_n	yawing-moment coefficient
$C_{n_p} = \frac{\partial C_n}{\partial \left(\frac{pb}{2V} \right)}$	
$C_{n_r} = \frac{\partial C_n}{\partial \left(\frac{rb}{2V} \right)}$	
$C_{n\beta} = \frac{\partial C_n}{\partial \beta}$	
$C_{n\dot{\beta}} = \frac{\partial C_n}{\partial \left(\frac{\dot{\beta}b}{2V} \right)}$	
$C_{n\delta_a} = \frac{\partial C_n}{\partial \delta_a}$	
$C_{n\delta_r} = \frac{\partial C_n}{\partial \delta_r}$	
C_Y	side-force (lateral-force) coefficient
$C_{Y_p} = \frac{\partial C_Y}{\partial \left(\frac{pb}{2V} \right)}$	
$C_{Y_r} = \frac{\partial C_Y}{\partial \left(\frac{rb}{2V} \right)}$	

$C_{Y\beta} = \frac{\partial C_Y}{\partial \beta}$	
I_X, I_Z	mass moment of inertia about the X-body axis and the Z-body axis, respectively, slug-ft ²
I_{XZ}	mass product of inertia referred to the X- and Z-body axes, slug-ft ²
P	period of the Dutch roll oscillation, sec
p, r	rolling and yawing velocity about the X-body axis and the Z-body axis, respectively, rad/sec
\dot{p}, \dot{r}	rolling and yawing acceleration about the X-body axis and the Z-body axis, respectively, rad/sec ²
\bar{q}	free-stream dynamic pressure, lb/sq ft
S	wing area, sq ft
T'_c	thrust coefficient of the propellers, $\frac{\text{Thrust}}{\bar{q}S}$
$T_{1/2}$	time required for the Dutch roll oscillation to damp to one-half amplitude, sec
V	true airspeed, ft/sec
W	airplane weight, lb
α, α_b	airplane angle of attack relative to the X-body axis, deg
α_b^*	upper limit of linearity of the lift-curve slope
β	angle of sideslip, deg (unless noted otherwise)
$\dot{\beta}$	rate of change of sideslip with time, rad/sec
Δ	increment
δ_a, δ_r	differential aileron and rudder deflection, respectively, deg
$\delta_{a\beta} = \frac{\partial \delta_a}{\partial \beta}$	
$\delta_{r\beta} = \frac{\partial \delta_r}{\partial \beta}$	
ξ	damping ratio

Φ_{ij}	phase angle of a vector quantity i relative to a vector quantity j during the Dutch roll oscillation, deg
φ	bank angle, deg
ω_n	undamped natural frequency of the Dutch roll oscillation, rad/sec
$\frac{ i }{ j }$	amplitude ratio of a vector quantity i relative to a vector quantity j during the Dutch roll oscillation
Subscript:	
s	relative to stability axis

TABLE 5.3-1

TRANSFORMATION OF DERIVATIVES FROM STABILITY TO BODY AXIS

$$C_{N_\alpha} = C_{L_\alpha} \cos \alpha + C_{D_\alpha} \sin \alpha + C_c$$

$$C_{c_\alpha} = C_{D_\alpha} \cos \alpha - C_{L_\alpha} \sin \alpha - C_N$$

$$C_{m_\alpha} = (C_{m_\alpha})_s$$

$$C_{n_\beta} = (C_{n_\beta})_s \cos \alpha + (C_{l_\beta})_s \sin \alpha$$

$$C_{n_r} = (C_{n_r})_s \cos^2 \alpha + (C_{l_p})_s \sin^2 \alpha + (C_{n_p} + C_{l_r})_s \sin \alpha \cos \alpha$$

$$C_{n_{\dot{\beta}}} = (C_{n_{\dot{\beta}}})_s \cos \alpha + (C_{l_{\dot{\beta}}})_s \sin \alpha$$

$$C_{n_p} = (C_{n_p})_s \cos^2 \alpha - (C_{l_r})_s \sin^2 \alpha - (C_{n_r} - C_{l_p})_s \sin \alpha \cos \alpha$$

$$C_{n_\delta} = (C_{n_\delta})_s \cos \alpha + (C_{l_\delta})_s \sin \alpha$$

$$C_{l_\beta} = (C_{l_\beta})_s \cos \alpha - (C_{n_\beta})_s \sin \alpha$$

$$C_{l_r} = (C_{l_r})_s \cos^2 \alpha - (C_{n_p})_s \sin^2 \alpha - (C_{n_r} - C_{l_p})_s \sin \alpha \cos \alpha$$

$$C_{l_{\dot{\beta}}} = (C_{l_{\dot{\beta}}})_s \cos \alpha - (C_{n_\beta})_s \sin \alpha$$

$$C_{l_p} = (C_{l_p})_s \cos^2 \alpha + (C_{n_r})_s \sin^2 \alpha - (C_{n_p} + C_{l_r})_s \sin \alpha \cos \alpha$$

$$C_{l_\delta} = (C_{l_\delta})_s \cos \alpha - (C_{n_\delta})_s \sin \alpha$$

$$C_{Y_\beta} = (C_{Y_\beta})_s$$

$$C_{Y_p} = (C_{Y_p})_s \cos \alpha - (C_{Y_r})_s \sin \alpha$$

$$C_{Y_r} = (C_{Y_r})_s \cos \alpha + (C_{Y_p})_s \sin \alpha$$

$$\frac{|X|}{qSb} \frac{|\dot{p}|}{|r|} \angle \Phi_{\dot{p}r} - \frac{|Xz|}{qSb} \frac{|\dot{r}|}{|r|} \angle \Phi_{\dot{r}r} - C_{l_p} \frac{|\dot{p}|}{|r|} \frac{b}{2V} \angle \Phi_{pr} - C_{l_\beta} \frac{|\beta|}{|r|} \angle \Phi_{\beta r} - C_{l_r} \frac{|\dot{r}|}{|r|} \frac{b}{2V} \angle \Phi_{rr} = 0$$

$$0.0172 \angle 7.95^\circ - 0.0004 \angle 98.95^\circ + 0.0323 \angle -91.0^\circ - 36.5 C_{l_\beta} \angle 89.15^\circ - 0.12 C_{l_r} \angle 0^\circ = 0$$

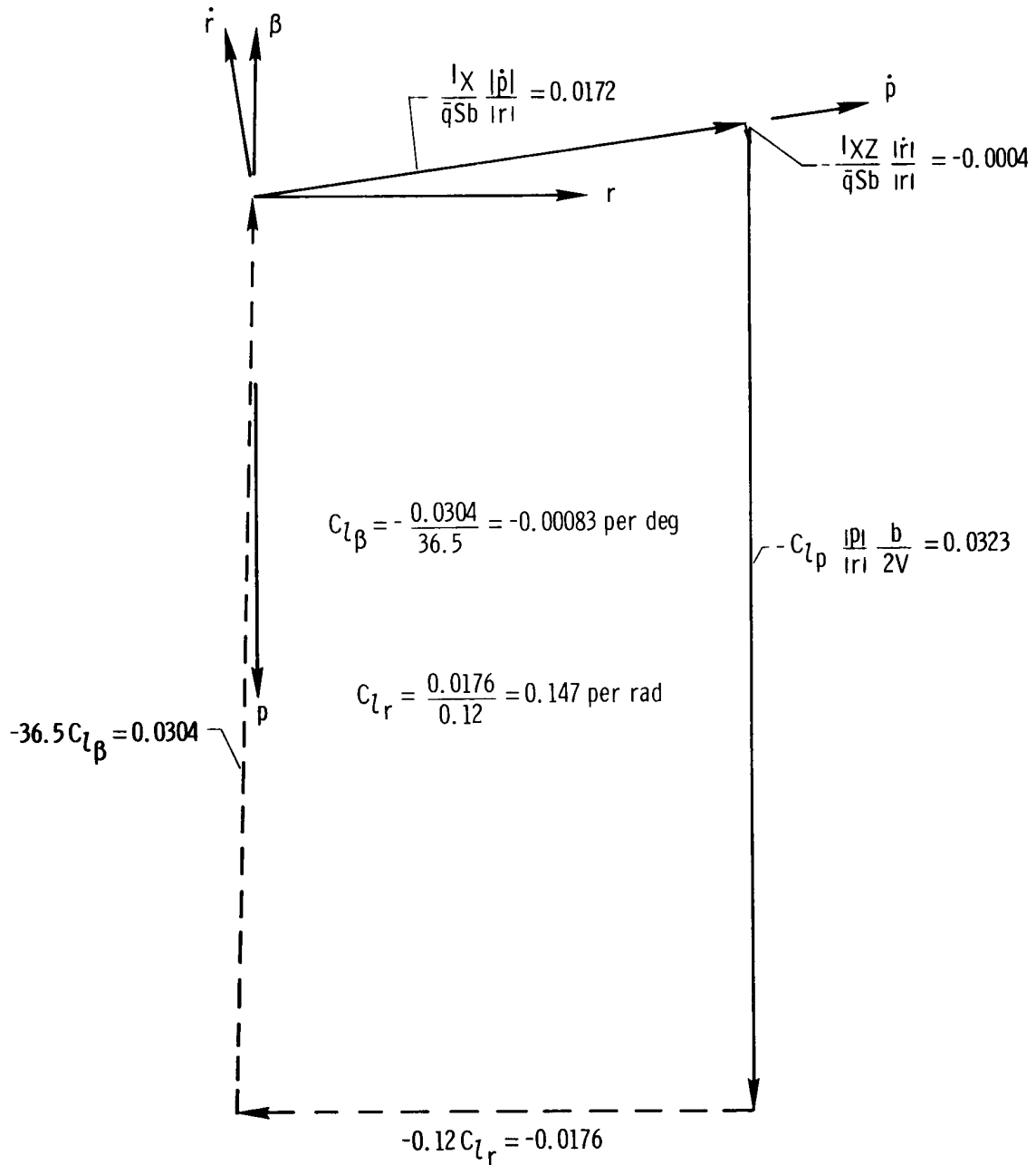


Figure 5.3.2-1. Typical graphical time-vector solution of C_{l_β} and C_{l_r} for the subject airplane using calculated C_{l_p} as a known quantity. $\alpha = 6^\circ$.

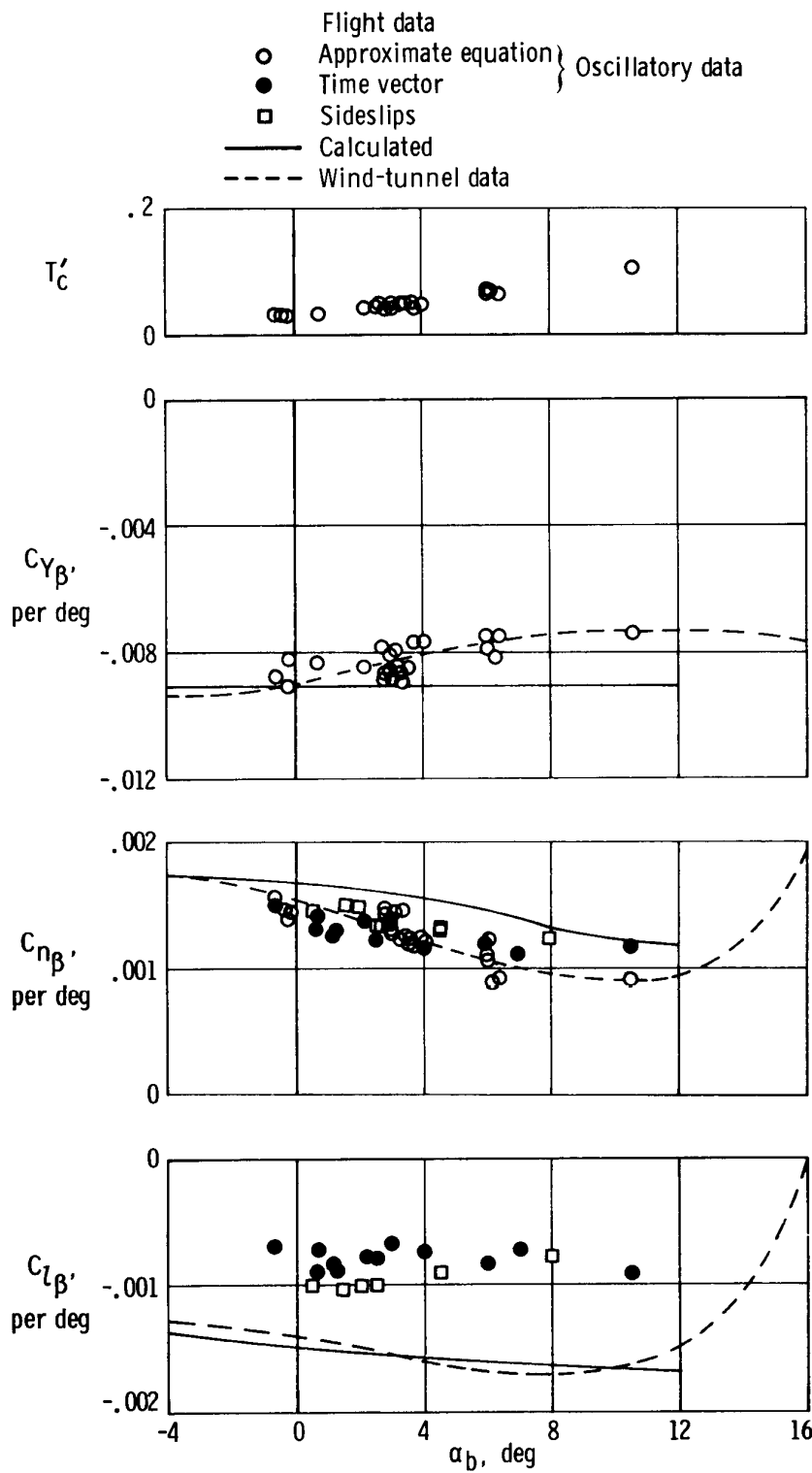


Figure 5.3.4-1. Comparison of predicted static stability characteristics with flight data relative to body axes.

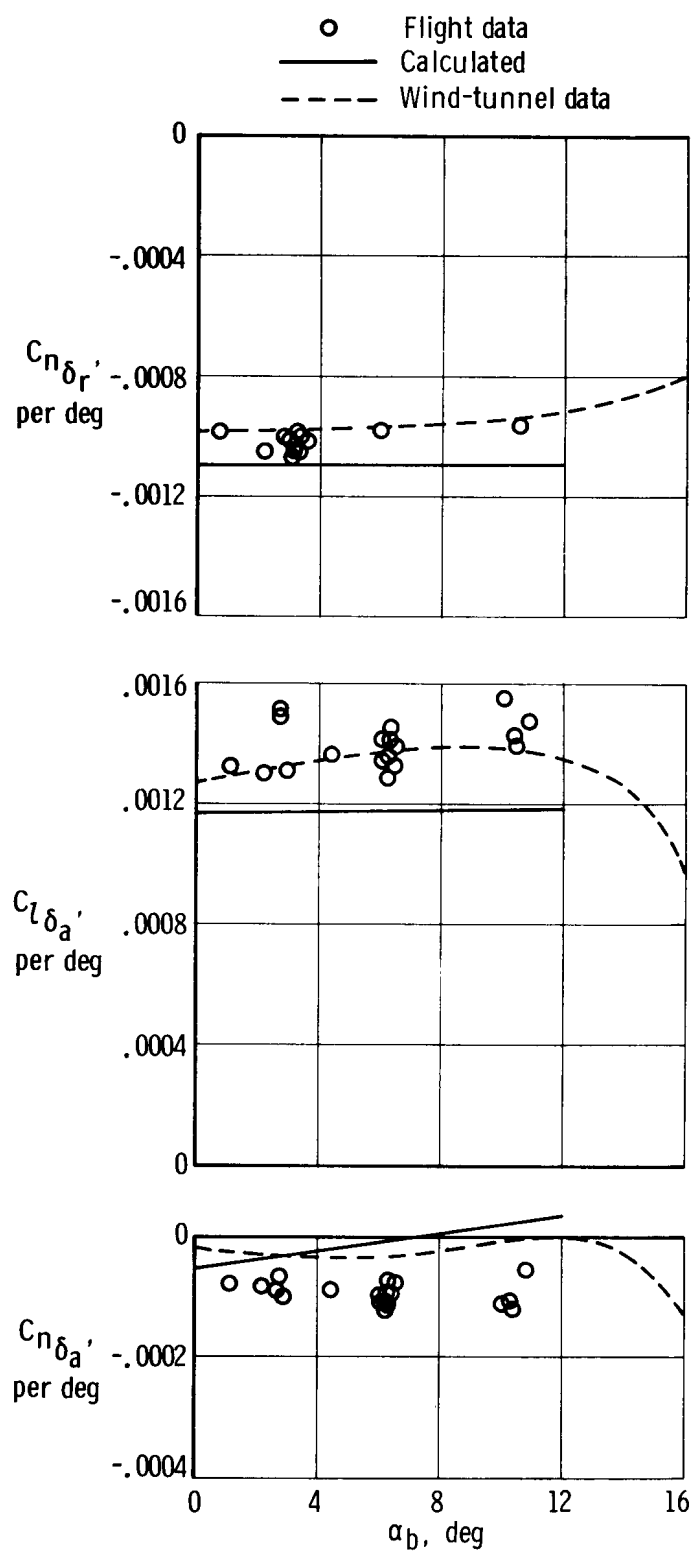


Figure 5.3.4-2. Comparison of predicted control characteristics with flight data relative to body axes.

6.0 DYNAMIC DERIVATIVE CHARACTERISTICS

The calculations of the lateral-directional dynamic derivatives considered in this section take into account the effects of power when feasible.

The methods used in calculating the contributions of the lifting surfaces to the dynamic derivatives are based on lifting-surface theory and, as a consequence, on attached-flow conditions. Because the attached-flow conditions prevail up to stall angles for the high-aspect-ratio lifting surfaces, the methods used are valid up to near-stall conditions for the purposes of this report. As a result of the attached-flow conditions, the dynamic derivatives of conventional general aviation airplanes are frequency-independent over the practical frequency range of operation of the airplane.

In the following discussion of the methods for calculating the various dynamic derivatives, the derivatives are referred to the stability-axes system. When the calculated dynamic derivatives are compared with flight data, the calculated characteristics are transformed to the body-axes system (using table 5.3-1) to be compatible with the flight data.

6.1 Damping-in-Roll Derivative, C_{l_p}

Although the wing is generally the only significant contributor to C_{l_p} , the contributions of the horizontal- and vertical-tail surfaces, the nacelles, and the propellers are also accounted for. The modifying influence of the fuselage on the wing and horizontal-tail contributions is taken into account.

In considering power effects, the power-induced change in dynamic pressure at the horizontal tail is accounted for as a normal consideration in discussing the horizontal-tail contribution to C_{l_p} . The effects of power on the wing, nacelles, and propeller contribution to C_{l_p} are discussed separately.

Taking into account the types of contribution to the damping-in-roll derivative to be discussed, the C_{l_p} of the airplane may be represented by

$$C_{l_p} = (C_{l_p})_{wf} + (C_{l_p})_{hf} + (C_{l_p})_v + (C_{l_p})_n + (\Delta C_{l_p})_{power} \quad (6.1-1)$$

6.1.1 Wing-Body Contribution to C_{l_p}

At low speeds (Mach numbers of less than 0.20), lift coefficients near zero, and fuselage-width to wing-span ratios of 0.25 or less, the contribution of a wing-fuselage combination to C_{l_p} is similar to the contribution of the wing alone and may be obtained, for zero dihedral conditions, from figure 6.1.1-1 (from ref. 12) as a function of aspect ratio, taper ratio, and sweep angle of the quarter-chord line. In lieu of figure 6.1.1-1 or when fuselage width may be an influencing factor, C_{l_p} for near zero-lift conditions may be obtained from the nomograph of figure 6.1.1-2 (from ref. 3). This figure is based on lifting-surface theory (ref. 20) corrected for sweep by the method of reference 4 and empirically modified, on the basis of available wind-tunnel data, for the effects of the fuselage.

The effect of dihedral and change in the lift-curve slope at the higher lift coefficients on C_{l_p} at low-speed conditions are accounted for by the following equation:

$$[(C_{l_p})_{wf}]_{M=0} = (C_{l_p})_{wC_L=0} \frac{(C_{L\alpha})_{wC_L}}{(C_{L\alpha})_{wC_L=0}} \frac{(C_{l_p})_\Gamma}{(C_{l_p})_{\Gamma=0}} + (\Delta C_{l_p})_{wdrag} \quad (6.1.1-1)$$

where

$(C_{L\alpha})_{wC_L=0}$ is the propeller-off lift-curve slope of the wing at zero lift

$(C_{L\alpha})_{wC_L}$ is the propeller-off lift-curve slope of the wing at the airplane angle of attack being considered, obtained from a figure like figure 4.1.1-1 with stall extended

to power-on stall angles

$\frac{(C_l p)_\Gamma}{(C_l p)_{\Gamma=0}}$ is the correction factor for dihedral, obtained from figure 6.1.1-3 from reference 21; as can be noted in the figure, the influence of dihedral on the wing contribution to $C_l p$ is a function of the vertical displacement of the center of gravity from the wing-root chord and can be significant

$(\Delta C_l p)_{w\text{drag}}$ is the increment of $C_l p$ due to wing drag in roll. For high-aspect-ratio wings this increment is negligible; however, its effect is larger than the separate or combined contributions of the tail surfaces. As accounted for by reference 22,

$$(\Delta C_l p)_{w\text{drag}} = -\frac{1}{8} \frac{C_L w^2}{\pi A_w \cos^2(\Lambda_c/4)_w} \left[1 + 2 \sin^2(\Lambda_c/4)_w \frac{A_w + 2 \cos(\Lambda_c/4)_w}{A_w + 4 \cos(\Lambda_c/4)_w} \right] - \frac{1}{8} (C_D 0)_w \quad (6.1.1-2)$$

To account for Mach number (compressibility) effects, the low-speed wing-body contribution to $C_l p$ is modified by the application of the Prandtl-Glauert rule. In accordance with reference 5,

$$\left[(C_l p)_{wf} \right]_M = \frac{A_w + 4 \cos(\Lambda_c/4)_w}{A_w B_{2w} + 4 \cos(\Lambda_c/4)_w} \left[(C_l p)_{wf} \right]_{M=0} \quad (6.1.1-3)$$

where

$$B_{2w} = \sqrt{1 - M^2 \cos^2(\Lambda_c/4)_w}$$

The calculations pertaining to the contribution of the wing-fuselage of the subject airplane, using the preceding relations, are summarized in table 6.1.1-1 for propeller-off conditions. In the nonlinear lift region (near stall), the stall characteristics of the propeller-off lift curve have been extended to the stall angles of the various power conditions (fig. 4.1.1-1) to obtain to a first order of approximation the propeller-off $(C_l p)_{wf}$ near the stall angles for the powered conditions. From the results of table 6.1.1-1, plotted in figure 6.1.1-4, it can be observed that $(C_l p)_{wf}$ is relatively constant throughout the linear lift range of the wing. From the limit of linearity (between 10° and 11° of angle of attack) there is a rapid decrease in damping in roll of the wing to a value near zero at stall. Beyond stall, damping in roll becomes negative.

6.1.2 Horizontal-Tail Contribution to $C_l p$

The contribution of the horizontal tail to $C_l p$ is usually negligible. When the tail is large, however, its influence may not be negligible. In such instances, its contribution may be determined by applying the procedures of section 6.1.1 and multiplying the

result by the factor $0.5 \frac{S_h}{S_w} \left(\frac{b_h}{b_w} \right)^2 \left(\frac{\bar{q}_h}{\bar{q}_\infty} \right)$. This adjusts the results to the reference wing area and span and accounts for the rotation of flow at the tail produced by the wing, as noted in reference 15.

When the tail has zero dihedral and only the linear range of the tail lift-curve slope is of practical interest, the expanded form of equation (6.1.1-3) applied to the horizontal tail will result in

$$(C_{l_p})_{hf} = 0.5 \frac{S_h}{S_w} \left(\frac{b_h}{b_w} \right)^2 \left(\frac{\bar{q}_h}{\bar{q}_\infty} \right) \left[\frac{A_h + 4 \cos(\Lambda_c/4)_h}{A_h B_2 h + 4 \cos(\Lambda_c/4)_h} \right] \left[(C_{l_p})_{h C_L=0} + (\Delta C_{l_p})_{h \text{drag}} \right] \quad (6.1.2-1)$$

where, with the quantities referenced to tail area and geometry,

$$(\Delta C_{l_p})_{h \text{drag}} = -\frac{1}{8} \left[\frac{C_{L_h}^2}{\pi A_h \cos(\Lambda_c/4)_h} \right] \left[1 + 2 \sin^2(\Lambda_c/4)_h \frac{A_h + 2 \cos(\Lambda_c/4)_h}{A_h + 4 \cos(\Lambda_c/4)_h} \right] - \frac{1}{8} (C_{D_0})_h \quad (6.1.2-2)$$

Applied to the subject airplane, the preceding relations indicate that the horizontal-tail contribution in the presence of the fuselage is of the order of 1 percent of the wing-body contribution (table 6.1.2-1) and is due almost entirely to quantities involving $(C_{l_p})_{h C_L=0}$ in equation (6.1.2-1).

6.1.3 Vertical-Tail Contribution to C_{l_p}

The contribution of the vertical tail to C_{l_p} may be obtained from the following equation (based on ref. 22) which accounts for the sidewash caused by the unsymmetrical span loading on the wing during rolling:

$$(C_{l_p})_v = -57.3 (C'_{L_\alpha})_v \left(\frac{z_v \cos \alpha_b + l_v \sin \alpha_b}{b_w} \right) \left[\frac{2(z_v \cos \alpha_b + l_v \sin \alpha_b)}{b_w} + \frac{\partial \sigma}{\partial \frac{pb_w}{2V}} \right] \quad (6.1.3-1)$$

where

$(C'_{L_\alpha})_v$ is the effective lift-curve slope of the vertical tail, obtained from equation (4.5.1-2) referenced to the wing area, S_w , per deg

z_v is the vertical distance parallel to the Z-body axis from the center of gravity to the vertical-tail mean aerodynamic chord, positive when measured down from the center of gravity, obtained from figure 3.2-4

l_v is the distance parallel to the X-body axis from the center of gravity to the quarter chord of the vertical-tail mean aerodynamic chord, obtained from figure 3.2-4

b_w is the wing span, obtained from figure 3.2-1

$\frac{\partial \sigma}{\partial \frac{pb_w}{2V}}$ is the rate of change of sidewash with wing-tip helix angle; positive value indicates a sidewash at the tail in the same direction as the wing roll

The sidewash factor, $\frac{\partial \sigma}{\partial \frac{pb_w}{2V}}$, is not easily determined. In reference 23, analysis

of wind-tunnel data of a single-tail model indicated that the effect of the angle of attack on this factor was small through approximately 12° of angle of attack. It was concluded that a value of 0.25 was a fairly good approximate average value for the sidewash factor. In reference 24 it was determined that the magnitude of the factor and its variation with angle of attack were functions of wing aspect ratio and sweepback, vertical-tail span, and considerations associated with airplane geometry. As a result of a study of reference 24, a value of 0.20 was used in calculating the vertical-tail contribution of the subject airplane to C_{l_p} .

The calculations in table 6.1.3-1 of the contribution of the vertical tail of the subject airplane to C_{l_p} show that the vertical tail contributes less than one half of 1

percent of that contributed by the wing. The contribution of the sidewash factor (column 9 in the table) tends to cancel out the effectiveness of the tail in roll.

6.1.4 Nacelles Contribution to C_{l_p}

The propeller-off contribution of the nacelles to C_{l_p} is the result of roll-rate-induced increments in angle of attack at the nacelle. This contribution is accounted for by the following equation:

$$(C_{l_p})_n = -114.6 (C_{L\alpha})_n \left(\frac{y_T}{b_w} \right)^2 \quad (6.1.4-1)$$

where

y_T is the lateral distance, parallel to the Y-axis, from the X-axis to the thrust axis

The lift-curve slope of the nacelles, $(C_{L\alpha})_n$, is obtained graphically from the lift curve of the two nacelles in figure 6.1.4-1 for the particular angle of attack being considered. The lift curve in figure 6.1.4-1 was plotted from the data in columns 5 and 6 of table 4.4-2 in reference 1.

Table 6.1.4-1 summarizes the propeller-off contribution of the nacelles of the subject airplane.

6.1.5 Power Contributions to C_{l_p}

Power contributions to the damping-in-roll derivative of the subject airplane arise from:

- (1) The power-induced increase in dynamic-pressure ratio on the horizontal tail, obtained from section 5.1.2 of reference 1. This was accounted for in the calculations for the horizontal-tail contribution to C_{l_p} (table 6.1.2-1).
- (2) The power-induced change in wing contribution to C_{l_p} resulting from the incremental change in lift of the portions of the wing immersed in the propeller slipstream. Because the change in lift of the immersed portion of the wing per propeller is a function of power-induced change in dynamic pressure and downwash behind the propeller, both of which are functions of thrust coefficient and angle of attack,

$$\begin{aligned} (\Delta C_{l_p})_{w(\Delta \bar{q} + \epsilon_p)} &= (\Delta C_{l_p})_{w(\Delta \bar{q})} + (\Delta C_{l_p})_{w(\epsilon_p)} \\ &= -57.3(2n) \left[(\Delta C_{L_\alpha})_{w(\Delta \bar{q})}/\text{propeller} + (\Delta C_{L_\alpha})_{w(\epsilon_p)}/\text{propeller} \right] \left(\frac{y_T}{b_w} \right)^2 \quad (6.1.5-1) \end{aligned}$$

where

n is the number of propellers

$(\Delta C_{L_\alpha})_{w(\Delta \bar{q})}/\text{propeller}$ is the change in lift-curve slope due to the change in dynamic pressure acting on the wing immersed in the slipstream of one propeller, obtained by measuring the slope of $(\Delta C_L)_{w(\Delta \bar{q})}$ versus α_b in figure 6.1.5-1 (obtained from table 5.1.1-2 of ref. 1)

$(\Delta C_{L_\alpha})_{w(\epsilon_p)}/\text{propeller}$ is the change in lift-curve slope due to power-induced change in the downwash behind the propeller acting on the wing area immersed in the slipstream of one propeller, obtained from figure 6.1.5-1 in the same manner as $(\Delta C_{L_\alpha})_{w(\Delta \bar{q})}/\text{propeller}$

The calculations of table 6.1.5-1 that account for the power-induced change in wing contribution to C_{l_p} of the subject airplane indicate that:

- (a) The power-induced change in dynamic pressure increases the wing contribution to C_{l_p} with increasing power at any one angle of attack through the linear lift range

with a maximum effect at zero lift and a minimum positive effect at the limit of linearity of the lift-curve slope.

(b) The influence of the power-induced change in downwash, ϵ_p , is similar to $\Delta\bar{q}$ but of opposite sign, which tends to cancel the $\Delta\bar{q}$ effects. (A proper assessment of power effects on the wing requires that both $\Delta\bar{q}$ and ϵ_p effects be accounted for.)

(3) The power-induced contribution of the propeller normal force to C_{l_p} results from roll-rate-induced change in angle of attack of the propeller plane. This is readily accounted for by the following equation (for two propellers):

$$(\Delta C_{l_p})_{N_p} = -114.6(C_{L\alpha})_{N_p} \left(\frac{y_T}{b_w} \right)^2 \quad (6.1.5-2)$$

The lift-curve slope of the propeller normal force is obtained graphically from the lift curve of the propeller in figure 6.1.5-2 for the particular angle of attack being considered. The lift curve was plotted from the data in column 6 of table 5.1.1-1(c) in reference 1.

Table 6.1.5-2 summarizes the contributions of the normal forces of the propellers to C_{l_p} of the subject airplane.

(4) The power-induced change in nacelle contribution to C_{l_p} results from the power-induced change in dynamic pressure and downwash behind the propeller acting on the nacelles immersed in the propeller slipstreams.

The change in nacelle contribution to C_{l_p} due to power-induced change in dynamic pressure is accounted for by

$$(\Delta C_{l_p})_{n(\Delta\bar{q})} = \left(\frac{\Delta\bar{q}}{\bar{q}_\infty} \right) (C_{l_p})_{n_{prop\ off}} \quad (6.1.5-3)$$

where

$\frac{\Delta\bar{q}}{\bar{q}_\infty}$ is the change in the dynamic-pressure ratio behind the propeller, obtained from table 5.1.1-2(a)-2 in reference 1

$(C_{l_p})_{n_{prop\ off}}$ is the propeller-off contribution of the nacelles to C_{l_p} , obtained from equation (6.1.4-1)

The change in nacelle contribution to C_{l_p} due to the power-induced increment of downwash on the nacelles is obtained from the following equation, derived from relations given in section 5.1 of reference 1:

$$(\Delta C_{l_p})_{n(\epsilon_p)} = 114.6 (C_{L_\alpha})_{n_{\text{prop off}}} \left(\frac{\frac{\partial \epsilon_p}{\partial \alpha_p}}{1 - \frac{\partial \epsilon_u}{\partial \alpha_w}} \right) \left(1 + \frac{\Delta \bar{q}}{\bar{q}_\infty} \right) \left(\frac{y_T}{b_w} \right)^2 \quad (6.1.5-4)$$

where

$\frac{\partial \epsilon_p}{\partial \alpha_p}$ is the rate of change of the propeller downwash with the propeller angle of attack, obtained from table 5.1.1-2(a)-2 in reference 1

$\frac{\partial \epsilon_u}{\partial \alpha_w}$ is the upwash gradient at the propeller, obtained from table 5.1.1-1 in reference 1

A comparison of equation (6.1.5-4) with equation (6.1.4-1) shows that equation (6.1.5-4) can be modified to

$$(\Delta C_{l_p})_{n(\epsilon_p)} = - (C_{l_p})_{n_{\text{prop off}}} \left(\frac{\frac{\partial \epsilon_p}{\partial \alpha_p}}{1 - \frac{\partial \epsilon_u}{\partial \alpha_w}} \right) \left(1 + \frac{\Delta \bar{q}}{\bar{q}_\infty} \right) \quad (6.1.5-5)$$

The net effect of the power-induced dynamic pressure and downwash increments on the contribution of the nacelles to C_{l_p} is accounted for by combining equations (6.1.5-3) and (6.1.5-5). This results in

$$\begin{aligned} (\Delta C_{l_p})_{n(\Delta \bar{q} + \epsilon_p)} &= (\Delta C_{l_p})_{n(\Delta \bar{q})} + (\Delta C_{l_p})_{n(\epsilon_p)} \\ &= (C_{l_p})_{n_{\text{prop off}}} \left[\frac{\Delta \bar{q}}{\bar{q}_\infty} - \left(\frac{\frac{\partial \epsilon_p}{\partial \alpha_p}}{1 - \frac{\partial \epsilon_u}{\partial \alpha_w}} \right) \left(1 + \frac{\Delta \bar{q}}{\bar{q}_\infty} \right) \right] \end{aligned} \quad (6.1.5-6)$$

Table 6.1.5-3 summarizes the contributions to C_{l_p} of the subject airplane due to power-induced increments of dynamic pressure and downwash acting on the nacelles.

6.1.6 Summary of Contributions to C_{l_p}

Table 6.1.6-1 summarizes the contributions to C_{l_p} of the subject airplane. For propellers-off conditions, the wing is the only significant contributor. With the wing contribution as a base value, the horizontal tail and the nacelles each contribute approximately 1 percent. The vertical-tail contribution is negligible.

The effect of power on the C_{l_p} of the subject airplane is a function of thrust coefficient, T'_c . At $T'_c = 0$, the effect of power is nil. The small but negligible increase in damping in roll due to the propeller normal force (column 7) is canceled by the adverse effects of power on the immersed wing area and the nacelles (columns 6 and 8). With increase in thrust, the propeller normal forces and the power-induced effects on the nacelles and immersed wing areas increase the damping in roll. At $T'_c = 0.44$ the largest power-induced effect is due to the immersed wing area (column 6), which contributes from approximately 8 percent (at $\alpha_b = -4^\circ$) to 4 percent (at $\alpha_b = 8^\circ$) to the damping in roll. At this high thrust condition, the propeller normal forces and the power-induced effects on the nacelles each contribute less than 1 percent.

Figure 6.1.6-1 shows the variation of the calculated C_{l_p} of the subject airplane as a function of angle of attack and thrust coefficient. No wind-tunnel data were available for comparison. Comparisons with flight data are made in section 6.5.

6.1.7 Symbols

A	aspect ratio
A_h, A_w	aspect ratio of the horizontal tail and wing, respectively
$B_{2h} = \sqrt{1 - M^2 \cos^2(\Lambda_c/4)_h}$	
$B_{2w} = \sqrt{1 - M^2 \cos^2(\Lambda_c/4)_w}$	
b	span of the lifting surface, in.
b_h, b_w	span of the horizontal tail and wing, respectively, in.
$(C_{D0})_h, (C_{D0})_w$	zero-lift drag coefficient of the horizontal tail and wing, respectively, at incompressible flow conditions based on respective areas
C_{Lh}, C_{Lw}	lift coefficient of the horizontal tail and wing, respectively, based on the respective surface areas
$C_{Ln}, (C_L)_{Np}$	lift coefficient of the nacelles and normal forces of the propellers, respectively, based on wing area

$(C_{L\alpha})_{Np}$	lift-curve slope of the propeller normal force, based on the wing area, per deg
$(C_{L\alpha})_n, (C'_{L\alpha})_v$	lift-curve slope of the nacelles and effective lift-curve slope of the vertical tail, respectively, based on the wing area, per deg
$(C_{L\alpha})_{wC_L=0}, (C_{L\alpha})_{wC_L}$	lift-curve slope of the wing for propeller-off conditions at the wing zero-lift coefficient and wing lift coefficient, respectively, per deg
$(\Delta C_L)_{w(\Delta \bar{q})}, (\Delta C_L)_{w(\epsilon_p)}$	increment of the wing lift coefficient due to the power-induced change in the dynamic pressure and the change in downwash, respectively, acting on the portion of the wing immersed in the slipstream of one propeller
$(\Delta C_{L\alpha})_{w(\Delta \bar{q})} / \text{propeller}$	increment in the wing lift-curve slope due to the power-induced change in the dynamic pressure and the change in downwash, respectively, acting on the portion of the wing immersed in the slipstream of one propeller, per deg
$(\Delta C_{L\alpha})_{w(\epsilon_p)} / \text{propeller}$	increment in the wing lift-curve slope due to the power-induced change in the dynamic pressure and the change in downwash, respectively, acting on the portion of the wing immersed in the slipstream of one propeller, per deg
C_l	rolling-moment coefficient
C_{l_p}	damping-in-roll derivative, $\frac{\partial C_l}{\partial \frac{pb_w}{2V}}$, per rad
$(C_{l_p})_{hC_L=0}$	horizontal-tail contribution to C_{l_p} at the zero lift of the tail due to the lift characteristics of the tail at incompressible flow conditions with fuselage effects on the tail taken into account, based on the tail span and area, obtained from figure 6.1.1-2
$(C_{l_p})_{hf}$	net contribution of the horizontal tail to C_{l_p} , including the fuselage effect on the tail and the tail drag effects, based on the wing span and area
$(C_{l_p})_n$	contribution of the nacelles to C_{l_p} for propellers-off conditions, based on the wing span and area
$(C_{l_p})_v$	contribution of the vertical tail to C_{l_p} based on the wing span and area
$(C_{l_p})_{wC_L=0}$	propeller-off wing contribution to C_{l_p} at the zero lift of the wing due to the lift characteristics of the wing, at incompressible flow conditions, with the fuselage effects

on the wing taken into account, obtained from figure 6.1.1-2

$$(C_{l_p})_{wf}$$

net propeller-off wing contribution to C_{l_p} , including the fuselage effect on the wing, dihedral effects, and the wing drag effects

$$\frac{(C_{l_p})_\Gamma}{(C_{l_p})_{\Gamma=0}}$$

correction factor to be applied to $(C_{l_p})_{w_{C_L=0}}$ to account for the wing geometric dihedral, obtained from figure 6.1.1-3

$$(\Delta C_{l_p})_{h\text{ drag}}, (\Delta C_{l_p})_{w\text{ drag}}$$

increment of the horizontal-tail and wing contribution, respectively, to C_{l_p} due to the roll-induced drag of the surfaces under incompressible flow conditions and based on the respective surface span and area

$$(\Delta C_{l_p})_{N_p}$$

incremental contribution of the propeller normal force to C_{l_p}

$$(\Delta C_{l_p})_{n(\Delta \bar{q})}, (\Delta C_{l_p})_{n(\epsilon_p)}$$

increment of the nacelle contribution to C_{l_p} due to the power-induced change in the dynamic pressure and the change in downwash, respectively, acting on the nacelles

$$(\Delta C_{l_p})_{n(\Delta \bar{q} + \epsilon_p)} = (\Delta C_{l_p})_{n(\Delta \bar{q})} + (\Delta C_{l_p})_{n(\epsilon_p)}$$

$$(\Delta C_{l_p})_{\text{power}}$$

net contribution of the power effects to C_{l_p}

$$(\Delta C_{l_p})_{w(\Delta \bar{q})}, (\Delta C_{l_p})_{w(\epsilon_p)}$$

increment of the wing contribution to C_{l_p} due to the power-induced change in the dynamic pressure and the change in downwash, respectively, acting on the portions of the wing immersed in the propeller slip-streams

$$(\Delta C_{l_p})_{w(\Delta \bar{q} + \epsilon_p)} = (\Delta C_{l_p})_{w(\Delta \bar{q})} + (\Delta C_{l_p})_{w(\epsilon_p)}$$

d

width of the body at the lifting surface, in.

d_h, d_w

width of the fuselage at the horizontal tail and wing, respectively, in.

$$k = \left[\frac{\Delta \bar{q}}{\bar{q}_\infty} - \left(\frac{\frac{\partial \epsilon_p}{\partial \alpha_p}}{1 - \frac{\partial \epsilon_u}{\partial \alpha_w}} \right) \left(1 + \frac{\Delta \bar{q}}{\bar{q}_\infty} \right) \right]$$

l_h, l_v

distance parallel to the X-body axis from the center of gravity to the quarter chord of the horizontal- and vertical-tail mean aerodynamic chord, respectively, in.

M

Mach number

n

number of propellers

p

roll rate, rad/sec

q

pitch rate, rad/sec

\bar{q}_h

dynamic pressure at the horizontal tail, lb/sq ft

\bar{q}_v

dynamic pressure at the vertical tail, lb/sq ft

\bar{q}_∞

free-stream dynamic pressure, lb/sq ft

$\Delta \bar{q}$

power-induced change in the dynamic pressure in the propeller slipstream behind the propeller, lb/sq ft

S_h, S_w

area of the horizontal tail and wing, respectively, sq ft

T

thrust of the propellers, lb

T'_c

thrust coefficient of the propellers, $\frac{T}{\bar{q}_\infty S_w}$

V

free-stream velocity, ft/sec

y_T

distance from the XZ plane of symmetry to the thrust line of the propeller, in.

z_v

vertical distance parallel to Z-body axis from the center of gravity to the vertical-tail mean aerodynamic chord, positive down, in.

z'_w

vertical distance from the center of gravity to the quarter chord of the wing root chord, positive down, in.

α_b

airplane angle of attack relative to the X-body axis, deg

α_h

horizontal-tail angle of attack, $\alpha_b - \bar{\epsilon} + 57.3 \frac{ql_h}{V}$, deg

δ_e	elevator deflection, deg
$\bar{\epsilon}$	downwash at the horizontal tail, deg
ϵ_p	power-induced downwash behind the propeller in the propeller slipstream, deg
$\frac{\partial \epsilon_p}{\partial \alpha_p}$	rate of change of ϵ_p with the effective angle of attack of the propeller
$\frac{\partial \epsilon_u}{\partial \alpha_w}$	upwash gradient of the propeller; rate of change in the wing upwash at the propeller with wing angle of attack
Γ	wing geometric dihedral, deg
λ	taper ratio
λ_h, λ_w	taper ratio of the horizontal tail and wing, respectively
$\Lambda_{c/4}$	sweep of the quarter-chord line of the lifting surface, deg
$(\Lambda_{c/4})_h, (\Lambda_{c/4})_w$	sweep of the quarter-chord line of the horizontal tail and wing, respectively, deg
$\frac{\partial \sigma}{\partial \frac{pb_w}{2V}}$	rate of change of the sidewash on the vertical tail (induced by the wing rolling rate) with the rolling helix angle

TABLE 6.1, 1-1

WING-FUSELAGE CONTRIBUTION TO C_{l_p}

$$(C_{l_p})_{wf} = \frac{A_w + 4 \cos(\Lambda_c/4)_w}{A_w B_{2w} + 4 \cos(\Lambda_c/4)_w} \left[(C_{l_p})_{wC_L=0} \frac{(C_{L\alpha})_{wC_L}}{(C_{l_p})_{wC_L=0}} \frac{(C_{l_p})_\Gamma}{(C_{l_p})_{\Gamma=0}} + (\Delta C_{l_p})_{w\text{drag}} \right]$$

$$(\Delta C_{l_p})_{w\text{drag}} = -\frac{C_{Lw}^2}{8 \pi A_w \cos^2(\Lambda_c/4)_w} \left[1 + 2 \sin^2(\Lambda_c/4)_w \frac{A_w + 2 \cos(\Lambda_c/4)_w}{A_w + 4 \cos(\Lambda_c/4)_w} \right] - \frac{1}{8} (C_{D_0})_w$$

Symbol	Description	Reference	Magnitude
M	Mach number	Wind-tunnel test condition	0.083
B_{2w}	$\sqrt{1 - M^2 \cos^2 \Lambda_c/4}$	Equation (6.1.1-4)	.997
A_w	Wing aspect ratio	Figure 3.2-1	7.5
$(\Lambda_c/4)_w$	Wing sweep along quarter-chord line, deg	Figure 3.2-1	-2.5
λ_w	Wing taper ratio	Figure 3.2-1	.513
b_w	Wing span, in.	Figure 3.2-1	432.0
d_w	Width of fuselage at wing, in.	Figure 3.2-1	48.0
$\frac{d_w}{b_w}$	-----	-----	.11
$(C_{l_p})_{wC_L=0}$	Wing-fuselage C_{l_p} at $C_{Lw} = 0$ with $(C_{D_0})_w = 0$, rad	Figure 6.1.1-2	-.46
z'_w	Vertical distance from wind-tunnel center of gravity (waterline = -12 in.) to quarter chord of wing root chord (waterline = -16 in.), in.	Figure 3.2-2	4.0
$\frac{2z'_w}{b_w}$	-----	-----	.0185
Γ	Wing dihedral, deg	Figure 3.2-1	5.0
$\frac{(C_{l_p})_\Gamma}{(C_{l_p})_{\Gamma=0}}$	Factor to account for effect of dihedral on C_{l_p}	Figure 6.1.1-3	≈ 1.0
$(C_{L\alpha})_{wC_L=0}$	Wing lift-curve slope at $C_{Lw} = 0$, deg	Figure 4.1.1-1	0.0733
$(C_{L\alpha})_{wC_L}$	Wing lift-curve slope at C_{Lw} , deg	Figure 4.1.1-1	$f(\alpha_b)$
$(C_{D_0})_w$	Zero-lift drag of isolated wing	Table 4.12, 1-2 of reference 1	0.00993

$$(C_{l_p})_{wf} = -6.288 (C_{L\alpha})_{wC_L} - 0.00534 C_{Lw}^2 - 0.00124$$

(1)	(2)	(3)	(4)	(5)	(6)
Figure 4.1.1-1					
α_b , deg	$(C_{L\alpha})_{wC_L}$	C_{Lw}	$-6.288 (C_{L\alpha})_{wC_L} =$ $-6.288(2)$	$-0.00534(3)^2 - 0.00124$	$(C_{l_p})_{wf} =$ $(4) + (5)$
-4	0.0733	0	-0.46091	-0.00124	-0.46215
-2	.0733	.145	-.46091	-.00135	-.46226
0	0.0733	0.292	-0.46091	-0.00170	-0.46261
2	.0733	.437	-.46091	-.00226	-.46317
4	0.0733	0.584	-0.46091	-0.00306	-0.46397
6	.0733	.730	-.46091	-.00409	-.46500
8	0.0733	0.875	-0.46091	-0.00533	-0.46624
10	.0733	1.023	-.46091	-.00683	-.46774
Propeller-off characteristics in stall region with stall extended to power-on stall angles					

$T'_c = 0$	12	0.065	1.160	-0.40872	-0.00843	-0.41715
	13.8	0	1.240	0	-.00945	-.00945
$T'_c = 0.20$	12	0.068	1.170	-0.42444	-0.00855	-0.43299
	14.1	0	1.253	0	-.00962	-.00962
$T'_c = 0.44$	12	0.069	1.175	-0.43387	-0.00861	-0.44248
	14.4	0	1.272	0	-.00988	-.00988

TABLE 6.1, 2-1
HORIZONTAL-TAIL CONTRIBUTION TO C_{l_p}

$$\begin{aligned} (C_{l_p})_{hf} &= 0.5 \frac{S_h}{S_w} \left(\frac{b_h}{b_w} \right)^2 \left(\frac{\bar{q}_h}{\bar{q}_\infty} \right) \left[\frac{A_h + 4 \cos(\Lambda_c/4)_h}{A_h B_h + 4 \cos(\Lambda_c/4)_h} \right] \left[(C_{l_p})_{hC_L=0} + (\Delta C_{l_p})_{hdrag} \right] \\ (\Delta C_{l_p})_{hdrag} &= -\frac{1}{8} \left[\frac{C_{L_h}^2}{\pi A_h \cos(\Lambda_c/4)_h} \right] \left[1 + 2 \sin^2(\Lambda_c/4)_h \frac{A_h + 2 \cos(\Lambda_c/4)_h}{A_h + 4 \cos(\Lambda_c/4)_h} \right] - \frac{1}{8} (C_{D_0})_h \end{aligned}$$

Symbol	Description	Reference	Magnitude
M	Mach number	Wind-tunnel test condition	0.083
B_h	$\sqrt{1 - M^2 \cos^2(\Lambda_c/4)_h}$	Equation (6.1, 1-4)	.997
A_h	Horizontal-tail aspect ratio	Figure 3, 2-3	4.8
$(\Lambda_c/4)_h$	Horizontal-tail sweep along quarter-chord line, deg	Figure 3, 2-3	8
λ_h	Horizontal-tail taper ratio	Figure 3, 2-3	.515
b_h	Horizontal-tail span, in.	Figure 3, 2-3	150.0
d_h	Width of fuselage at horizontal tail, in.	Figure 3, 2-3	12.0
$\frac{d_h}{b_h}$	-----	-----	.08
$(C_{l_p})_{hC_L=0}$	Horizontal-tail C_{l_p} with $(C_{D_0})_h = 0$, rad	Figure 6.1, 1-2	-.34
S_h	Horizontal-tail area, sq ft	Figure 3, 2-2	32.5
S_w	Reference wing area, sq ft	Figure 3, 2-1	178.0
b_w	Wing span, ft	Figure 3, 2-1	36.0
$(C_{D_0})_h$	Zero-lift drag of horizontal tail referred to $S_h = 32.5$ sq ft	Table 4, 12, 1-2 of reference 1	0.00843
C_{L_h}	Horizontal-tail lift coefficient, referred to $S_h = 32.5$ sq ft at $\frac{\bar{q}_h}{\bar{q}_\infty} = 1.0$	Figure 4, 13, 3-1 of reference 1, function of δ_e and $\alpha_h = \alpha_b - \bar{\epsilon} + 57.3 \frac{q'_h}{V}$	
$\frac{\bar{q}_h}{\bar{q}_\infty}$	Dynamic-pressure ratio at horizontal tail	Table 5, 1, 2-1(b), column 11 (ref. 1)	$f(\alpha_b, T'_c)$
Summary: $(C_{l_p})_{hf} = -\left(0.00376 + 0.00009 C_{L_h}^2\right) \frac{\bar{q}_h}{\bar{q}_\infty} \approx -0.00376 \frac{\bar{q}_h}{\bar{q}_\infty}$			

(1)	(2)			(3)		
	$\frac{\bar{q}_h}{\bar{q}_\infty}$ from table 5, 1, 2-1(b) (ref. 1)			$(C_{l_p})_{hf} = -0.00376(2)$		
α_b , deg	T'_c			T'_c		
	0	0.20	0.44	0	0.20	0.44
-4	1.0	1.087	1.203	-0.00376	-0.00409	-0.00452
-2	1.0	1.103	1.211	-.00376	-.00415	-.00455
0	1.0	1.117	1.222	-0.00376	-0.00420	-0.00459
2	1.0	1.122	1.232	-.00376	-.00422	-.00463
4	1.0	1.133	1.243	-0.00376	-0.00426	-0.00467
6	1.0	1.139	1.254	-.00376	-.00428	-.00472
8	1.0	1.144	1.262	-0.00376	-0.00430	-0.00475
10	1.0	1.142	1.268	-.00376	-.00429	-.00477
12	1.0	1.136	1.276	-0.00376	-0.00427	-0.00480
13.8	1.0	1.128	1.281	-.00376	-.00424	-.00482
14.1	---	1.122	1.281	-----	-0.00422	-0.00482
14.4	---	1.122	1.278	-----	-----	-.00481

TABLE 6.1.3-1
VERTICAL-TAIL CONTRIBUTION TO C_{l_p}

$$(C_{l_p})_v = -57.3 \left(C'_{L\alpha} \right)_v \left(\frac{z_v \cos \alpha_b + l_v \sin \alpha_b}{b_w} \right) \left[\frac{2(z_v \cos \alpha_b + l_v \sin \alpha_b)}{b_w} + \frac{\frac{\partial \sigma}{\partial \frac{pb}{2V}}}{\frac{\partial \sigma}{\partial \frac{pb}{2V}}} \right] = ABC_1 + ABC_2$$

Symbol	Description	Reference	Magnitude
$(C'_{L\alpha})_v$	Effective lift-curve slope of vertical tail referenced to $S_w = 178$ sq ft, per deg	Table 4.5.1-1	0.00464
z_v	Vertical distance, parallel to Z-body axis, from center of gravity to tail mean aerodynamic chord (positive down), in.	Figure 3.2-4	-45.9
l_v	Distance, parallel to X-body axis, from center of gravity to quarter chord of vertical-tail mean aerodynamic chord (positive back), in.	Figure 3.2-4	164.9
b_w	Wing span, in.	Figure 3.2-1	432
$\frac{\partial \sigma}{\partial \frac{pb}{2V}}$	Sidewash factor to account for effect of rolling wing on tail	Reference 24	0.20
Summary: $(C_{l_p})_v = -0.5317(-0.10625 \cos \alpha_b + 0.3817 \sin \alpha_b)^2$ $-0.05317(-0.10625 \cos \alpha_b + 0.3817 \sin \alpha_b)$			

(1)	(2)	(3)	(4)	(5)	(6)	(7)	(8)	(9)	(10)
α_b , deg	$\cos(1)$	$\sin(1)$	-0.10625(2)	0.3817(3)	(4) + (5)	(6) ²	-0.5317(7)	-0.05317(6)	$(C_{l_p})_v = (8) + (9)$
-4	0.9976	-0.0698	-0.10600	-0.02664	-0.13264	0.01759	-0.00935	0.00705	-0.00230
-2	.9994	-.0349	-.10619	-.01332	-.11951	.01428	-.00759	.00635	-.00124
0	1.0000	0	-0.10625	0	-0.10625	0.01129	-0.00600	0.00565	-0.00035
2	.9994	.0349	-.10619	.01332	-.09287	.00862	-.00458	.00494	.00036
4	0.9976	0.0698	-0.10600	0.02664	-0.07936	0.00630	-0.00335	0.00422	0.00087
6	.9945	.1045	-.10567	.03989	-.06578	.00433	-.00230	.00350	.00120
8	0.9903	0.1392	-0.10522	0.05313	-0.05209	0.00271	-0.00144	0.00277	0.00133
10	.9848	.1736	-.10464	.06626	-.03838	.00147	-.00078	.00204	.00126
12	0.9782	0.2079	-0.10393	0.07936	-0.02457	0.00060	-0.00032	0.00131	0.00099
13.8	.9711	.2385	-.10318	.09104	-.01214	.00015	-.00008	.00065	.00057
14.1	0.9699	0.2436	-0.10305	0.09298	-0.01007	0.00010	-0.00005	0.00054	0.00049
14.4	.9686	.2487	-.10291	.09493	-.00798	.00006	-.00003	.00042	.00039

TABLE 6.1.4-1
CONTRIBUTION OF NACELLES TO PROPELLER-OFF C_{l_p}

$$(C_{l_p})_n = -114.6 (C_{L\alpha})_n \left(\frac{y_T}{b_w}\right)^2$$

Symbol	Description	Reference	Magnitude
y_T	Lateral distance from X-axis to thrust line, in.	Figure 3.2-1	69.44
b_w	Wing span, in.	Figure 3.2-1	432
$(C_{L\alpha})_n$	Lift-curve slope of two nacelles with propellers off, per deg	Figure 6.1.4-1	$f(\alpha_b)$

$$(C_{l_p})_n = -2.96 (C_{L\alpha})_n$$

(1)	(2)	(3)
----	Figure 6.1.4-1	-----
α_b , deg	$(C_{L\alpha})_n$	$(C_{l_p})_n = -2.96(2)$
-4	0.00160	-0.00474
-2	.00161	-.00477
0	0.00162	-0.00480
2	.00163	-.00482
4	0.00165	-0.00488
6	.00168	-.00497
8	0.00174	-0.00515
10	.00179	-.00530
Extended unpowered stall regions of wing for -	$T'_c = 0$	12 0.00184 -0.00545
		13.8 .00196 -.00580
	$T'_c = 0.20$	12 0.00184 -0.00545
		14.1 .00197 -.00583
	$T'_c = 0.44$	12 0.00184 -0.00545
		14.4 .00198 -.00586

TABLE 6.1.5-1
EFFECT OF POWER ON WING CONTRIBUTION TO C_{l_p}

$$\begin{aligned} (\Delta C_{l_p})_{w(\Delta \bar{q} + \epsilon_p)} &= (\Delta C_{l_p})_{w(\Delta \bar{q})} + (\Delta C_{l_p})_{w(\epsilon_p)} \\ &= -37.3(2n) \left[(\Delta C_{L_\alpha})_{w(\Delta \bar{q})}/\text{propeller} + (\Delta C_{L_\alpha})_{w(\epsilon_p)}/\text{propeller} \right] \left(\frac{y_T}{b_w} \right)^2 \end{aligned}$$

Symbol	Description	Reference	Magnitude
n	Number of propellers	-----	2
$(\Delta C_{L_\alpha})_{w(\Delta \bar{q})}/\text{propeller}$	Change in wing lift-curve slope due to power-induced increase in dynamic pressure on wing area immersed in slipstream of one propeller	Figure 6.1.5-1	$f(\alpha_b, T'_c)$
$(\Delta C_{L_\alpha})_{w(\epsilon_p)}/\text{propeller}$	Change in wing lift-curve slope due to power-induced downwash behind the propeller acting on immersed area	Figure 6.1.5-1	$f(\alpha_b, T'_c)$
y_T	Distance parallel to Y-axis from X-body axis to thrust centerline, in.	Figure 3.2-1	69.44
b_w	Wing span, in.	Figure 3.2-1	432
Summary: $(\Delta C_{l_p})_{w(\Delta \bar{q} + \epsilon_p)} = -5.92 \left[(\Delta C_{L_\alpha})_{w(\Delta \bar{q})}/\text{propeller} + (\Delta C_{L_\alpha})_{w(\epsilon_p)}/\text{propeller} \right]$			

(1)	(2)	(3)	(4)	(5)	(6)
----	Figure 6.1.5-1	Figure 6.1.5-1	Equation (6.1.5-1)	Equation (6.1.5-1)	Equation (6.1.5-1)
α_b , deg	$(\Delta C_{L_\alpha})_{w(\Delta \bar{q})}/\text{propeller}$	$(\Delta C_{L_\alpha})_{w(\epsilon_p)}/\text{propeller}$	$(\Delta C_{l_p})_{w(\Delta \bar{q})} = -5.92(2)$	$(\Delta C_{l_p})_{w(\epsilon_p)} = -5.92(3)$	$(\Delta C_{l_p})_{w(\Delta \bar{q} + \epsilon_p)} = (4) + (5)$
	T'_c	T'_c	T'_c	T'_c	T'_c
	0 0.10/ propeller	0.22/ propeller	0 0.20 0.44	0 0.20 0.44	0 0.20 0.44
-4	0 0.0077	0.0160	-0.0002 -0.0045 -0.0096	0 -0.04558 -0.09472 0.00118	0.02664 0.05683 0.00118 -0.01894 -0.03789
-2	0 .0076	.0145	-.0002 -.0043 -.0092	0 -.04499 -.08584 ,00118	,02546 ,05446 ,00118 ,01953 ,03138
0	0 0.0069	0.0137	-0.0002 -0.0041 -0.0089	0 -0.04085 -0.08110 0.00118	0.02427 0.05269 0.00118 -0.01658 -0.02841
2	0 .0065	.0133	-.0002 -.0039 -.0084	0 -.03848 -.07874 ,00118	,02309 ,04973 ,00118 ,01539 ,02901
4	0 0.0058	0.0122	-0.0002 -0.0037 -0.0080	0 -0.03434 -0.07222 0.00118	0.02190 0.04736 0.00118 -0.01244 -0.02486
6	0 .0050	.0109	-,0002 -,0033 -,0074	0 -,02960 -,06453 ,00118	,01954 ,04381 ,00118 ,01006 ,02072
8	0 0.0042	0.0094	-0.0002 -0.0029 -0.0065	0 -0.02486 -0.05565 0.00118	0.01717 0.03848 0.00118 -0.00769 -0.01717
10	0 .0028	.0072	≈ 0 -,0023 -,0056	0 -,01658 -,04262 ≈ 0	,01362 ,03815 ≈ 0 -,00296 -,00947
12	0 0.0006	0.0036	0.0002 -0.0014 -0.0044	0 -0.00355 -0.02131 -0.00118	0.00083 0.02605 -0.00118 -0.00272 0.00474
13.8	0 -,0024	-,0023	,0004 ≈ 0 -,0021	0 ,01421 ,01362 -,00237	,01243 ,00287 ,01421 ,02605
14.1	- -0.0061	-0.0067	-----	≈ 0 -0.0020 -	0.03611 0.03966 ≈ 0 0.01184 0.03611
14.4	-	-0.0117	-----	≈ 0 -0.0020 -	,06926 ----- ≈ 0 ,01184 ,08110

TABLE 6.1.5-2
CONTRIBUTION OF PROPELLER NORMAL FORCES TO C_{l_p}

$$(\Delta C_{l_p})_{N_p} = -114.6 (C_{L\alpha})_{N_p} \left(\frac{y_T}{b_w} \right)^2$$

Symbol	Description	Reference	Magnitude
y_T	Lateral distance from X-axis to thrust line, in.	Figure 3.2-1	69.44
b_w	Wing span, in.	Figure 3.2-1	432
$(C_{L\alpha})_{N_p}$	Lift-curve slope of normal forces of two propellers, deg	Figure 6.1.5-2	$f(\alpha_b)$

$$(\Delta C_{l_p})_{N_p} = -2.96 (C_{L\alpha})_{N_p}$$

(1)	(2)			(3)		
----	Figure 6.1.5-2			-----		
α_b , deg	$(C_{L\alpha})_{N_p}$, per deg			$(\Delta C_{l_p})_{N_p} = -2.96(2)$, per rad		
	T'_c			T'_c		
	0	0.20	0.44	0	0.20	0.44
-4	0.00063	0.00091	0.00111	-0.00186	-0.00269	-0.00329
-2	.00063	.00091	.00111	-.00186	-.00269	-.00329
0	0.00063	0.00091	0.00111	-0.00186	-0.00269	-0.00329
2	.00061	.00091	.00111	-.00181	-.00269	-.00329
4	0.00061	0.00087	0.00111	-0.00181	-0.00258	-0.00329
6	.00060	.00087	.00108	-.00178	-.00258	-.00320
8	0.00060	0.00087	0.00106	-0.00178	-0.00258	-0.00314
10	.00058	.00085	.00104	-.00172	-.00252	-.00308
12	0.00058	0.00084	0.00103	-0.00172	-0.00249	-0.00305
13.8	.00058	.00084	.00102	-.00172	-.00249	-.00302
14.1	-----	0.00084	0.00096	-----	-0.00249	-0.00284
14.4	-----	-----	.00096	-----	-----	-.00284

TABLE 6.1.5-3
POWER-INDUCED CHANGE IN NACELLE CONTRIBUTION TO C_{l_p}

$$(\Delta C_{l_p})_{n(\Delta \bar{q} + \epsilon_p)} \approx (C_{l_p})_n \left[\frac{\Delta \bar{q}}{\bar{q}_\infty} - \left(\frac{\frac{\partial \epsilon_p}{\partial \alpha_p}}{1 - \frac{\partial \epsilon_u}{\partial \alpha_w}} \right) \left(1 + \frac{\Delta \bar{q}}{\bar{q}_\infty} \right) \right]$$

(a)

Symbol	Description	Reference	Magnitude
$(C_{l_p})_n$	Contribution of two nacelles to C_{l_p} , propellers off	Table 6.1.4-1	$f(\alpha_b)$
$\frac{\Delta \bar{q}}{\bar{q}_\infty}$	Change in dynamic-pressure ratio behind propeller	Table 5.1.1-2(a)-2 (ref. 1)	$f(T'_c / \text{propeller})$
$\frac{\partial \epsilon_p}{\partial \alpha_p}$	Rate of change of propeller downwash with propeller angle of attack	Table 5.1.1-2(a)-2 (ref. 1)	$f(T'_c / \text{propeller})$
$\frac{\partial \epsilon_u}{\partial \alpha_w}$	Upwash gradient of propeller	Table 5.1.1-1(b) (ref. 1)	-0.195

①	②	③	④	⑤	⑥
T'_c	$T'_c / \text{propeller} = ①/2$	$\frac{\Delta \bar{q}}{\bar{q}_\infty}$	$\frac{\partial \epsilon_p}{\partial \alpha_p}$	$\frac{\partial \epsilon_u}{\partial \alpha_w}$	$\left[③ - \left(\frac{④}{1 - ⑤} \right) (1 + ③) \right] (C_{l_p})_n$
0	0	0	0.0234	-0.195	$(\Delta C_{l_p})_{n(\Delta \bar{q} + \epsilon_p)} = -0.0196 (C_{l_p})_n$
.20	.10	.6295	.1987	-.195	$(\Delta C_{l_p})_{n(\Delta \bar{q} + \epsilon_p)} = 0.3586 (C_{l_p})_n$
.44	.22	1.385	.2896	-.195	$(\Delta C_{l_p})_{n(\Delta \bar{q} + \epsilon_p)} = 0.8070 (C_{l_p})_n$

(b)

①	②	③
---	Table 6.1.4-1	⑥ of table 6.1.5-3(a)
α_b , deg	$(C_{l_p})_n$	$(\Delta C_{l_p})_{n(\Delta \bar{q} + \epsilon_p)} = k ②$
		T'_c
		0 0.20 0.44
		k
		-0.0196 0.3586 0.8070
-4	-0.00474	0.00009
-2	-.00477	.00009
0	-0.00480	0.00009
2	-.00482	.00009
4	-0.00488	0.00010
6	-.00497	.00010
8	-0.00515	0.00010
10	-.00530	.00010
12	-0.00545	0.00011
13.8	-.00580	.00011
14.1	-0.00583	-----
14.4	-.00586	-----

TABLE 6.1.6-1
SUMMARY OF CONTRIBUTIONS TO C_{l_p}

$$C_{l_p} = (C_{l_p})_{wf} + (C_{l_p})_{hf} + (C_{l_p})_v + (C_{l_p})_{n_{prop}} + (\Delta C_{l_p})_{w(\Delta \bar{q} + \epsilon_p)} + (\Delta C_{l_p})_{N_p} + (\Delta C_{l_p})_{n(\Delta \bar{q} + \epsilon_p)}$$

(1)	(2)	(3)			(4)	(5)	(6)				
---	Table 6.1.1-1 and figure 6.1.1-4	Table 6.1.2-1			Table 6.1.3-1	Table 6.1.4-1	Table 6.1.5-1				
α_b , deg	$(C_{l_p})_{wf}$			$(C_{l_p})_{hf}$			$(C_{l_p})_v$	$(\Delta C_{l_p})_{w(\Delta \bar{q} + \epsilon_p)}$			
				T'_c				T'_c			
	Propellers off			0	0.20	0.44		$\frac{\bar{q}_v}{\bar{q}_\infty} = 1.0$	0	0.20	0.44
-4	-0.4622	-0.0038	-0.0041	-0.0045	-0.00230	-0.0047	0.0012	-0.0189	-0.0379		
-2	-0.4623	-0.0038	-0.0042	-0.0046	-0.00124	-0.0048	.0012	-0.0195	-0.0314		
0	-0.4626	-0.0038	-0.0042	-0.0046	-0.00035	-0.0048	0.0012	-0.0166	-0.0284		
2	-0.4632	-0.0038	-0.0042	-0.0046	.00036	-0.0048	.0012	-0.0154	-0.0290		
4	-0.4640	-0.0038	-0.0043	-0.0047	0.00087	-0.0049	0.0012	-0.0124	-0.0249		
6	-0.4650	-0.0038	-0.0043	-0.0047	.00120	-0.0050	.0012	-0.0101	-0.0207		
8	-0.4662	-0.0038	-0.0043	-0.0048	0.00133	-0.0052	0.0012	-0.0077	-0.0172		
10	-0.4677	-0.0038	-0.0043	-0.0048	.00126	-0.0053	≈0	-0.0030	-0.0095		
	T'_c (a)										
	0	0.20	0.44								
12	-0.4172	-0.4330	-0.4425	-0.0038	-0.0043	-0.0048	0.00099	-0.0054	-0.0012	-0.0027	0.0047
b _{13.8}	-0.0094	-0.2300	-0.3230	-0.0038	-0.0042	-0.0048	.00057	-0.0058	-0.0024	.0142	.0261
c _{14.1}	-----	-0.0096	-0.2450	-----	-0.0042	-0.0048	0.00049	-0.0058	-----	0.0361	0.0515
d _{14.4}	-----	-----	-0.0099	-----	-----	-0.0048	.00039	-0.0059	-----	-----	.0811

(1)	(7)			(8)			(9)		
---	Table 6.1.5-2			Table 6.1.5-3			-----		
α_b , deg	$(\Delta C_{l_p})_{N_p}$			$(\Delta C_{l_p})_{n(\Delta \bar{q} + \epsilon_p)}$			$C_{l_p} = \sum (2) \text{ to } (8)$		
	T'_c			T'_c			T'_c		
	0	0.20	0.44	0	0.20	0.44	0	0.20	0.44
-4	-0.0019	-0.0027	-0.0053	0.0001	-0.0017	-0.0038	-0.4736	-0.4966	-0.5187
-2	-0.0019	-0.0027	-0.0033	.0001	-0.0017	-0.0038	-0.4724	-0.4964	-0.5114
0	-0.0019	-0.0027	-0.0033	0.0001	-0.0017	-0.0039	-0.4722	-0.4930	-0.5080
2	-0.0018	-0.0027	-0.0033	.0001	-0.0017	-0.0039	-0.4719	-0.4916	-0.5084
4	-0.0018	-0.0026	-0.0033	0.0001	-0.0018	-0.0039	-0.4723	-0.4895	-0.5048
6	-0.0018	-0.0026	-0.0032	.0001	-0.0018	-0.0040	-0.4731	-0.4876	-0.5014
8	-0.0018	-0.0026	-0.0031	0.0001	-0.0018	-0.0042	-0.4744	-0.4865	-0.4994
10	-0.0017	-0.0025	-0.0031	.0001	-0.0019	-0.0043	-0.4771	-0.4834	-0.4934
12	-0.0017	-0.0025	-0.0031	0.0001	-0.0020	-0.0044	-0.4282	-0.4489	-0.4545
b _{13.8}	-0.0017	-0.0025	-0.0030	.0001	-0.0021	-0.0047	-0.2224	-0.2298	-0.3146
c _{14.1}	-----	-0.0025	-0.0028	-----	-0.0021	-0.0047	-----	-0.0124	-0.2111
d _{14.4}	-----	-----	-0.0028	-----	-----	-0.0047	-----	-----	.0534

^aValues for propellers-off $(C_{l_p})_{wf}$ in stalling regions for the power conditions listed (obtained from fig. 6.1.1-4).

^{b,c,d}Stall angles for $T'_c = 0, 0.20$, and 0.44 , respectively.

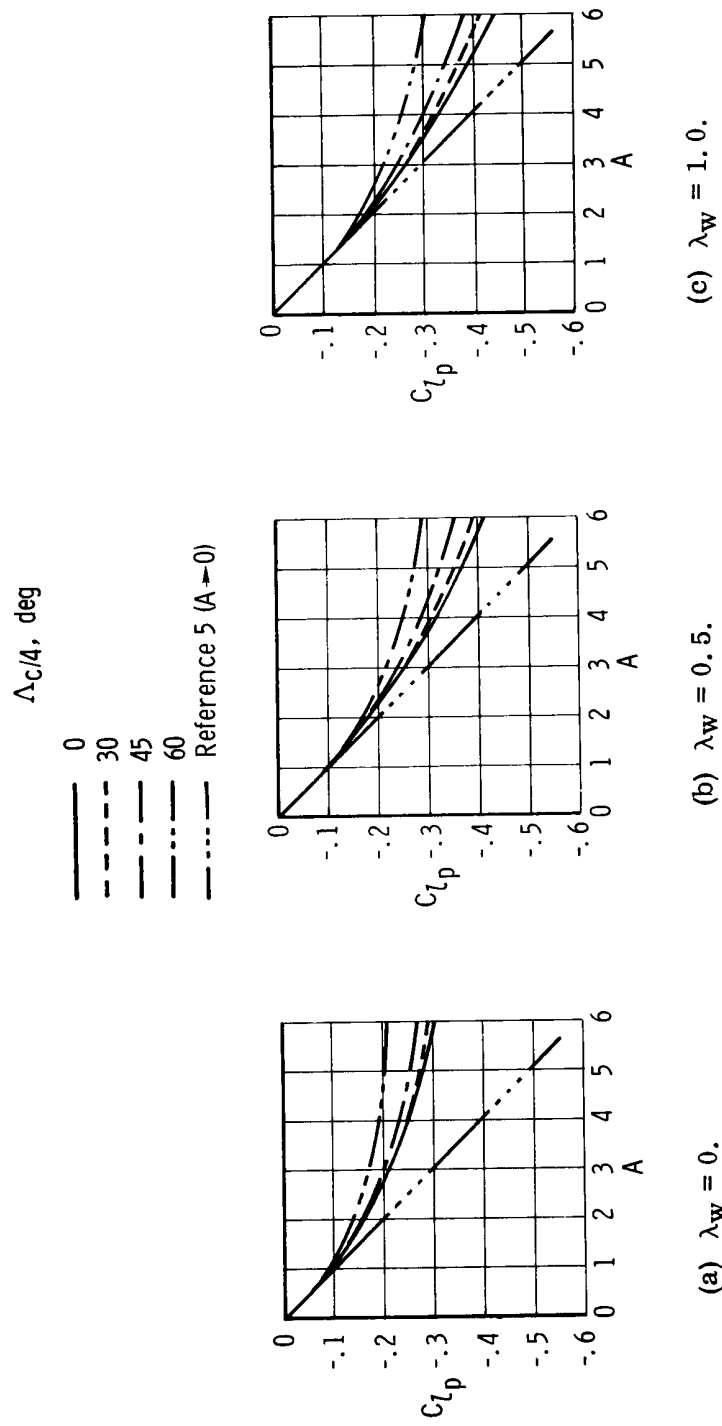


Figure 6.1.1-1. Values of C_{l_p} for wings of various taper ratios, sweeps, and aspect ratios as calculated by the seven-point method of Weissinger (ref. 12). $C_{LW} \approx 0; M < 0.2$; dihedral = 0.

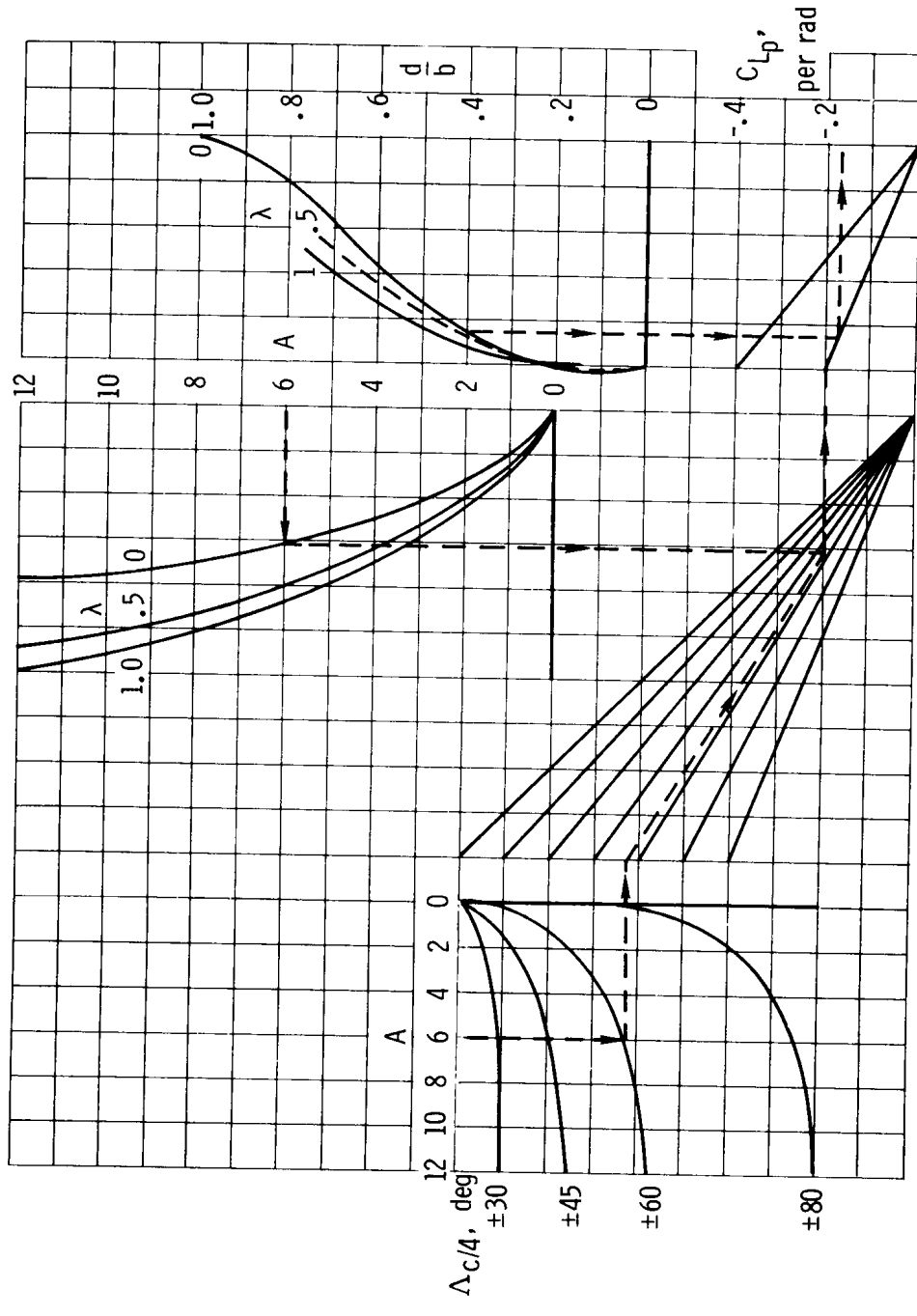


Figure 6. 1. 1-2. Nomograph for determining wing and horizontal-tail contributions to C_{l_p} , including fuselage effects at low speeds ($M < 0.2$) at $C_L = 0$ of the respective surfaces and excluding zero-lift drag effects (from ref. 3).

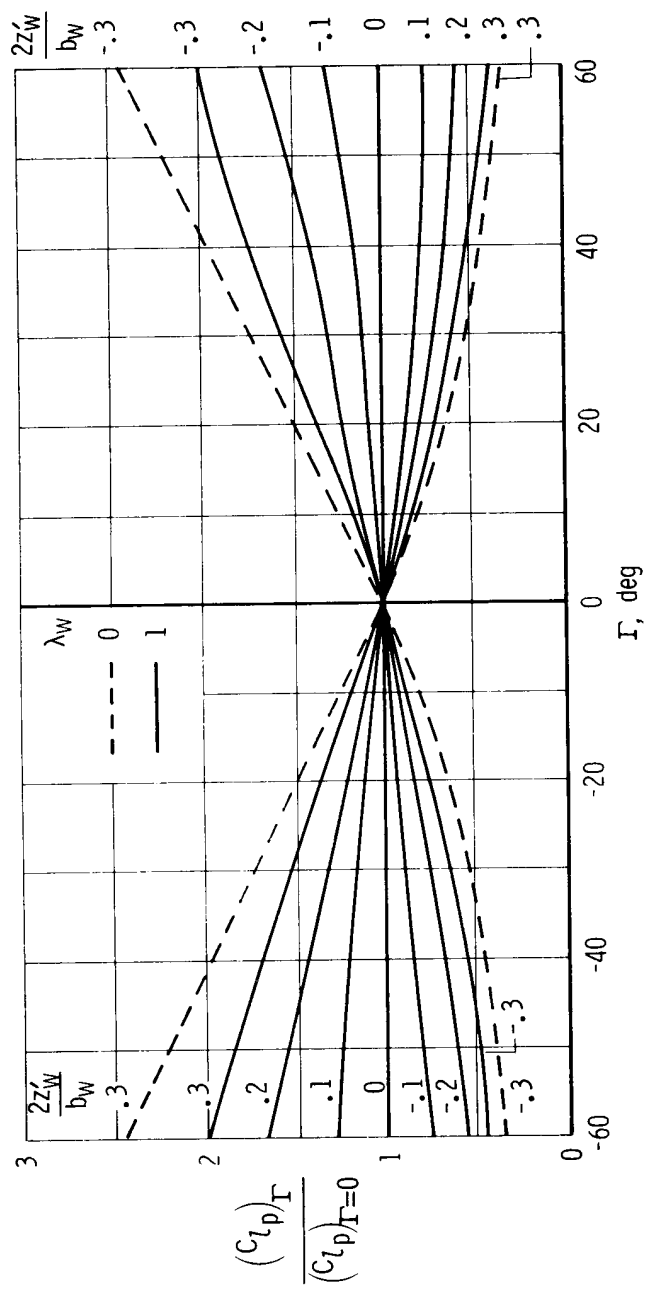


Figure 6.1.1-3. Effect of dihedral on wing-fuselage damping-in-roll derivative, C_{l_p} , at subsonic speeds (from ref. 21).

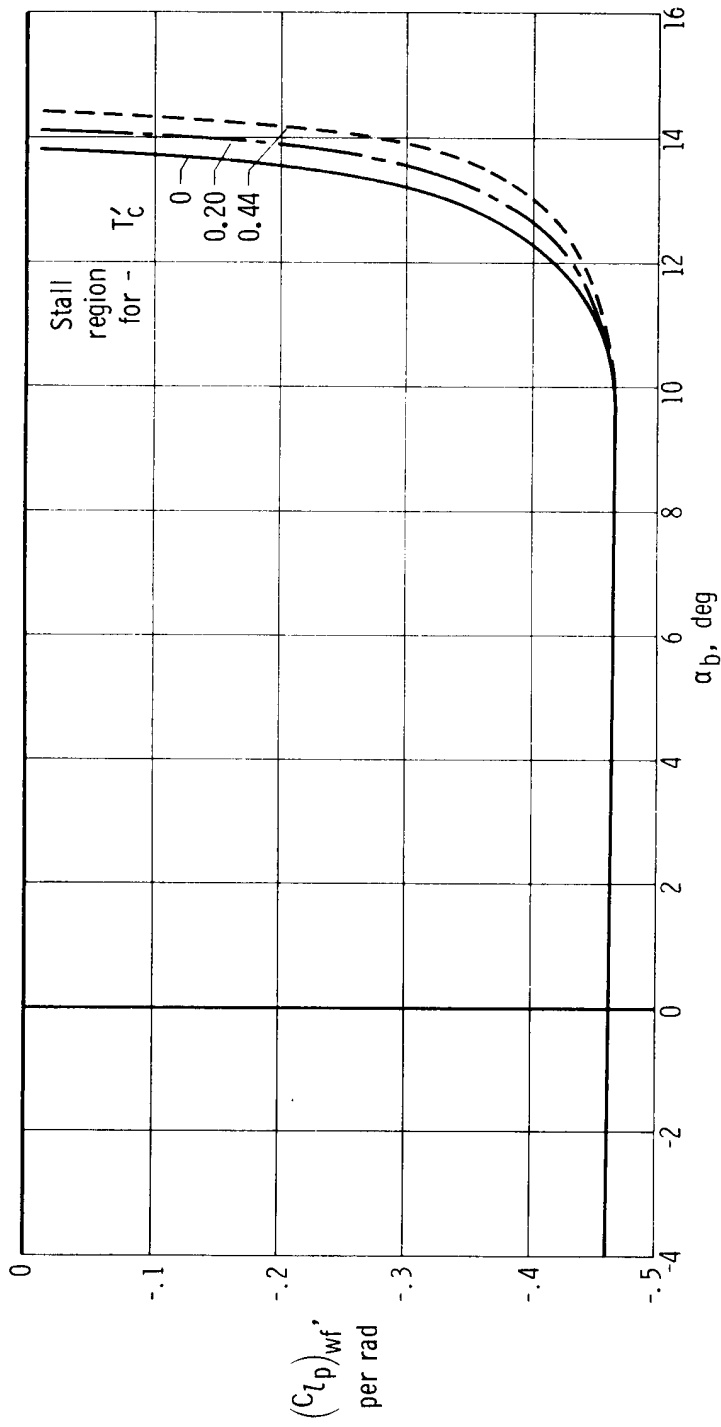


Figure 6.1.1-4. Calculated variation of damping-in-roll derivative of wing-body combination (propellers off) with angle of attack. Based on column 6 of table 6.1.1-1.

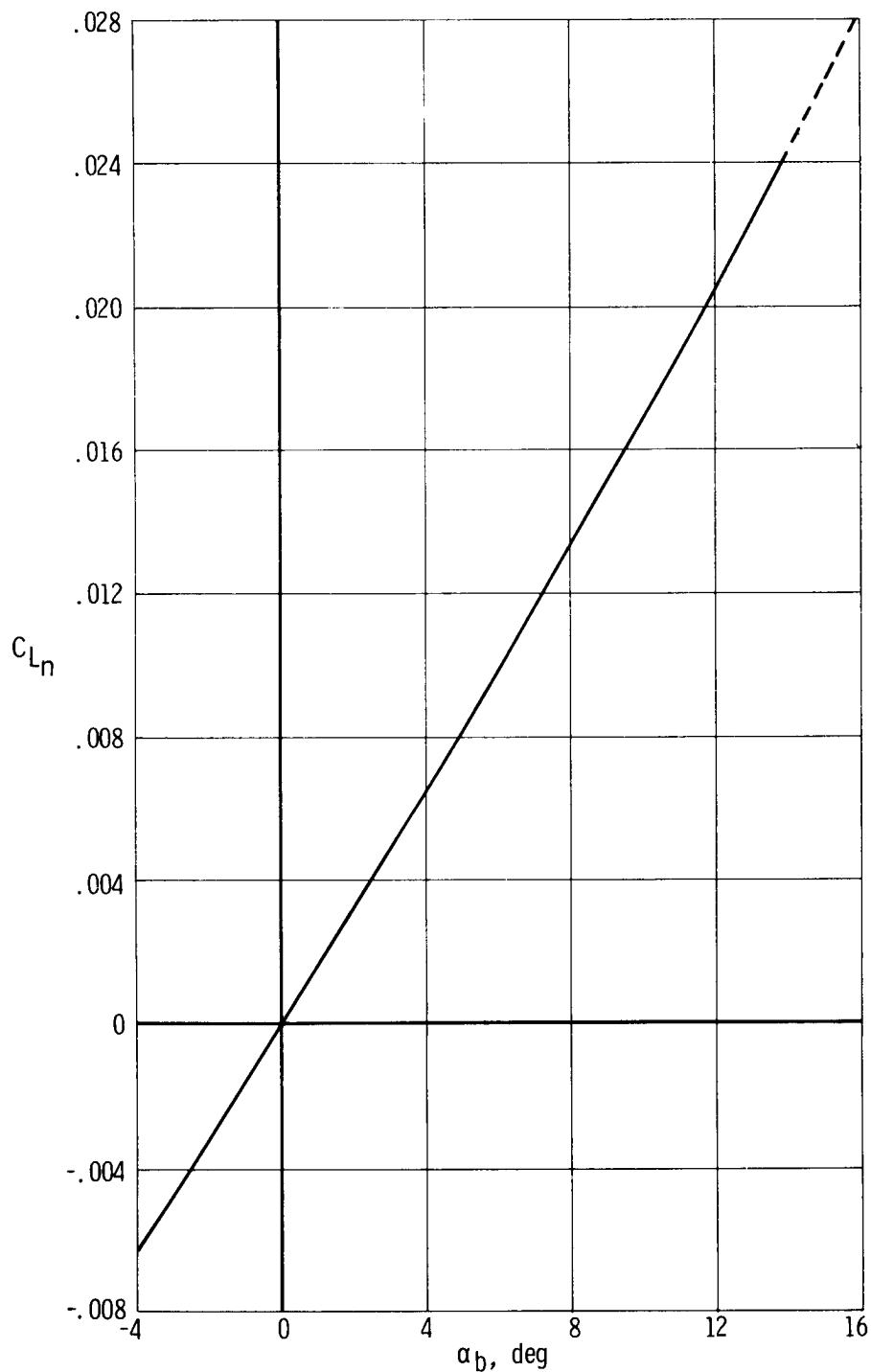


Figure 6.1.4-1. Variation in lift of two nacelles of subject airplane with angle of attack (from columns 5 and 6, table 4.4-1, ref. 1). Propellers off; referred to $S_W = 178$ sq ft.

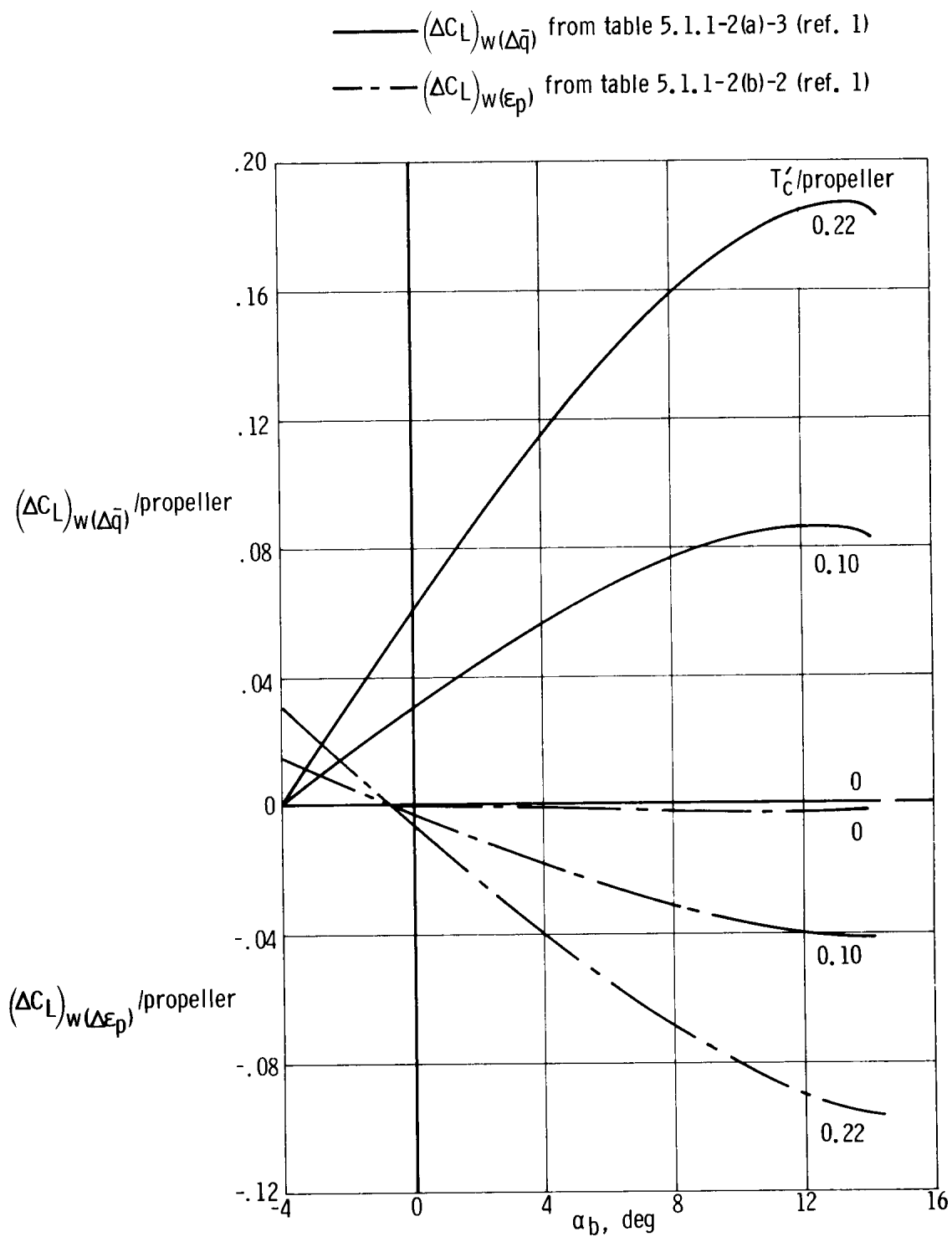


Figure 6.1.5-1. Variation in incremental lift per propeller due to power-induced increase in dynamic pressure and downwash behind propeller on portion of wing immersed in propeller slipstream (from ref. 1). Based on $S_w = 178 \text{ sq ft}$.

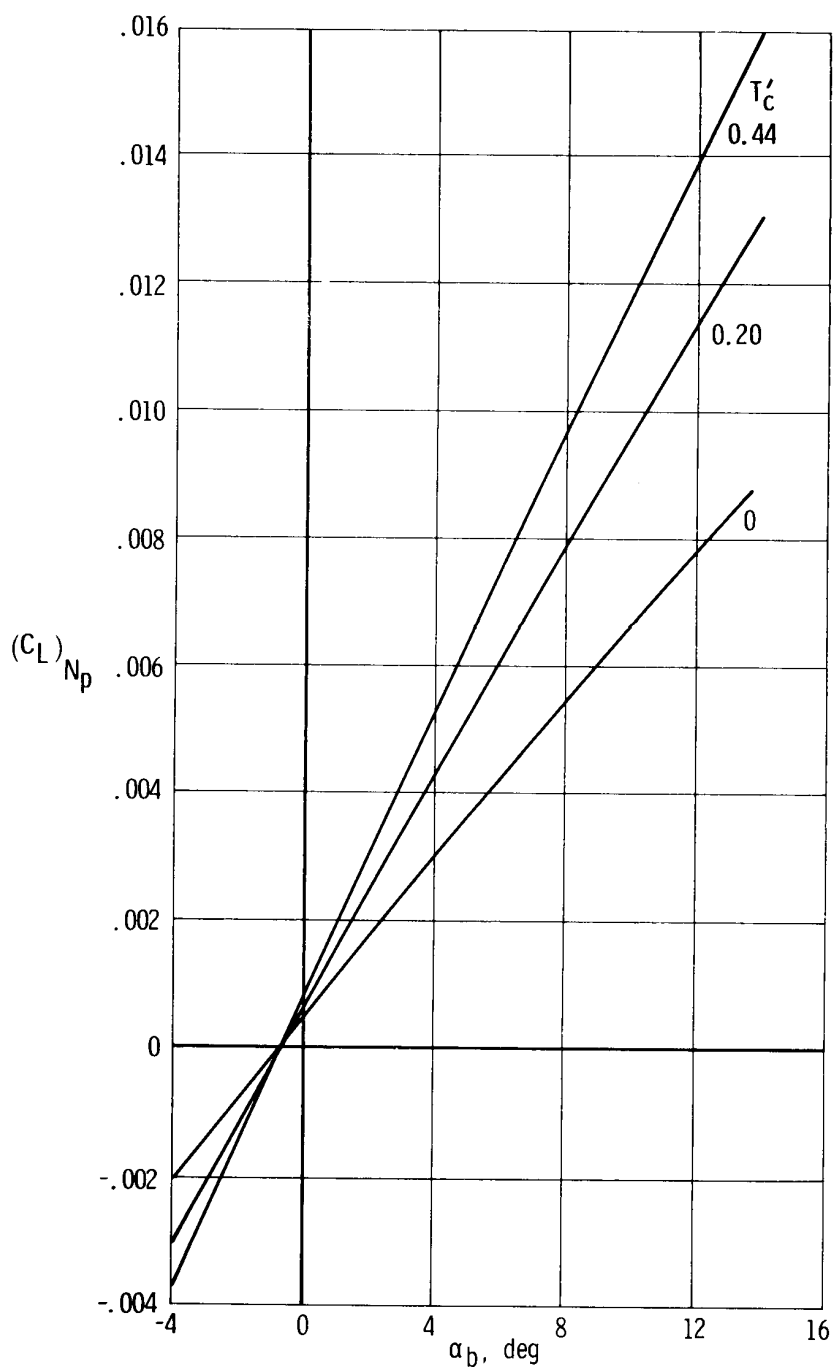


Figure 6.1.5-2. Variation in lift with angle of attack of propeller normal forces of subject airplane; for two propellers (from column 6, table 5.1.1-1(c), ref. 1). Referred to $S_w = 178$ sq ft.

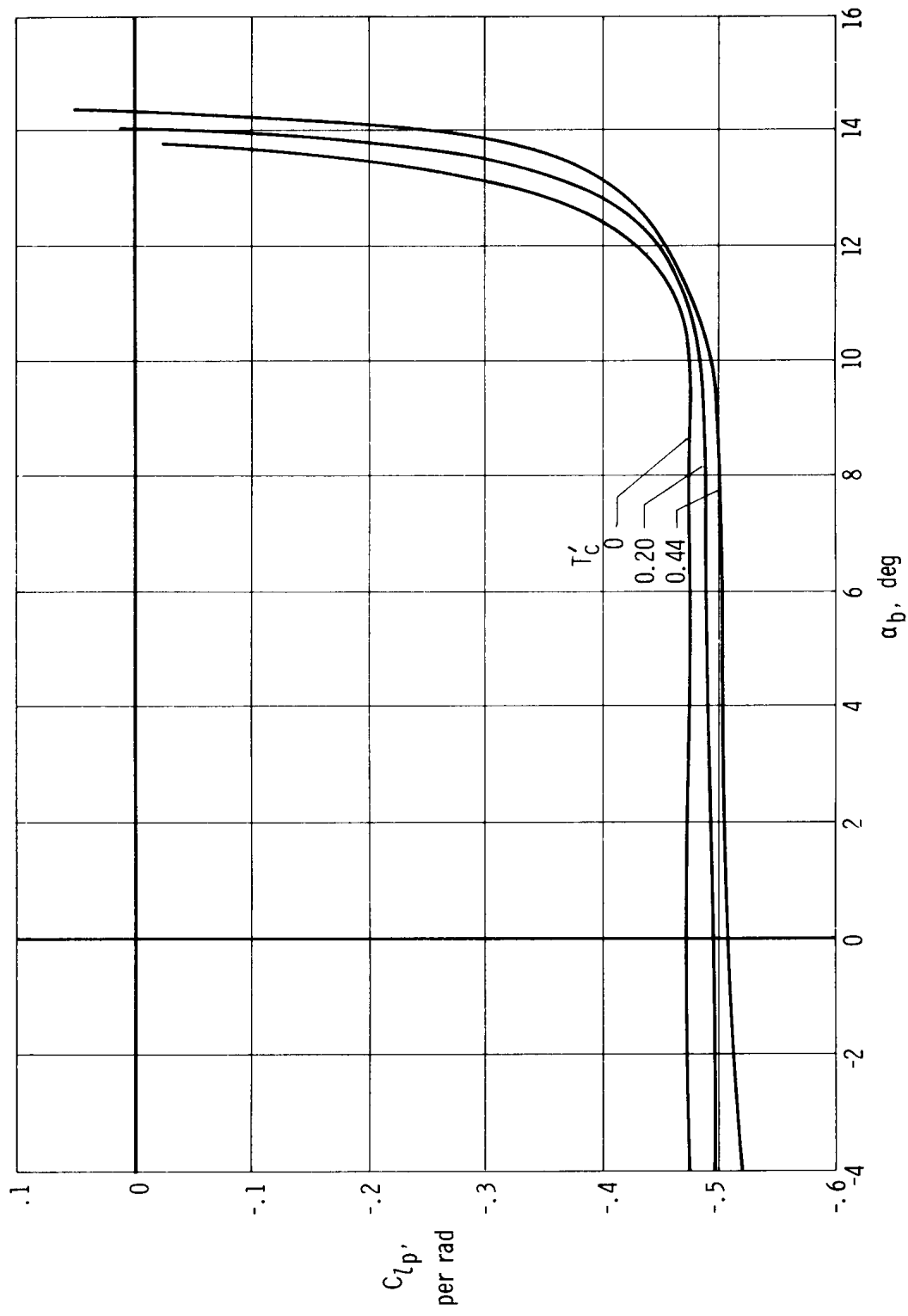


Figure 6.1.6-1. Variation of calculated damping-in-roll derivative of the subject airplane with angle of attack and power.

6.2 Damping-in-Yaw Derivative, C_{n_r}

The vertical tail is the prime contributor to the damping-in-yaw derivative, C_{n_r} . The wing contribution, although much smaller, is not necessarily negligible. The fuselage contribution is normally negligible for the wing-fuselage geometric proportions of general-aviation airplanes. However, the fuselage contribution could be important if the fuselage is large relative to the wing (ref. 15). The influence of power on C_{n_r} could be significant, but may be difficult to assess in the absence of general design procedure.

The following discussion considers the contributions of the wing, fuselage, vertical tail, and power effects on the damping-in-yaw derivative. On this basis, the damping-in-yaw derivative of the airplane is represented by

$$C_{n_r} = (C_{n_r})_w + (C_{n_r})_f + (C_{n_r})_v + (\Delta C_{n_r})_{\text{power}} \quad (6.2-1)$$

6.2.1 Wing Contribution to C_{n_r}

Wing contributions to C_{n_r} are due to asymmetric lift and drag distributions over the wing resulting from yawing velocity. Normally the calculations for C_{n_r} due to the wing are based on low-speed incompressible flow conditions. No comprehensive methods have been developed to account for compressibility effects in the subsonic and transonic regions. One procedure for obtaining the wing contribution to C_{n_r} is to use the following incompressible flow equation from reference 4, in which the profile-drag coefficient is evaluated for the desired Mach number:

$$(C_{n_r})_w = \left[\frac{(C_{n_r})_1}{C_{L_w}^2} \right] C_{L_w}^2 + \left[\frac{(\Delta C_{n_r})_2}{(C_{D_0})_w} \right] (C_{D_0})_w \quad (6.2.1-1)$$

In this equation the first term, $\frac{(C_{n_r})_1}{C_{L_w}^2}$, may be considered to be a result of the lift and induced forces resulting from the yawing of the isolated wing about its aerodynamic center plus an increment correction for displacement of the aerodynamic center from the yawing center (center of gravity) of the airplane. It does not include the effects of unsymmetrical spanwise distribution of profile drag, which is accounted for by the

$\frac{(\Delta C_{n_r})_2}{(C_{D_0})_w}$ term in the equation.

When the wing aerodynamic center and the airplane center of gravity coincide, the

first term, $\frac{(C_{n_r})_1}{C_{L_w}^2}$, is obtained from the following equation (from ref. 4):

$$\left[\frac{(C_{n_r})_1}{C_{L_w}^2} \right]_{\bar{x}=0} = \left[1 - \frac{3}{2} \left(\frac{4 \cos \Lambda_c/4}{A_w + 4 \cos \Lambda_c/4} + \frac{A_w}{2 \cos \Lambda_c/4} \right) \frac{\tan^2 \Lambda_c/4}{12} - \frac{9 \cos \Lambda_c/4}{A_w + 4 \cos \Lambda_c/4} \left(\frac{\tan^4 \Lambda_c/4}{12} \right) \right] \left[\frac{(C_{n_r})_1}{C_{L_w}^2} \right]_{\Lambda_c/4=0} \quad (6.2.1-2)$$

This equation is plotted as a function of wing aspect ratio, A_w , taper ratio, λ_w , and sweep angle of the quarter-chord line, $\Lambda_c/4$, in figure 6.2.1-1.

When the wing aerodynamic center and the airplane center of gravity do not coincide, the following increment should be added to equation (6.2.1-2):

$$\left[\frac{(\Delta C_{n_r})_1}{C_{L_w}^2} \right]_{\bar{x}} = - \left\{ \frac{3}{2} \left(\frac{4 \cos \Lambda_c/4}{A_w + 4 \cos \Lambda_c/4} + \frac{A_w}{2 \cos \Lambda_c/4} \right) \frac{\bar{x}}{\bar{c}_w} \frac{\tan \Lambda_c/4}{A_w} + \frac{9 \cos \Lambda_c/4}{A_w + 4 \cos \Lambda_c/4} \left[4 \left(\frac{\bar{x}}{\bar{c}_w} \right)^2 \frac{\tan^2 \Lambda_c/4}{A_w^2} \right] \right\} \left[\frac{(C_{n_r})_1}{C_{L_w}^2} \right]_{\Lambda_c/4=0} \quad (6.2.1-3)$$

where

\bar{x} is the distance parallel to the wing mean aerodynamic chord from the center of gravity to the wing aerodynamic center

\bar{c}_w is the wing mean aerodynamic chord

$\left[\frac{(C_{n_r})_1}{C_{L_w}^2} \right]_{\Lambda_c/4=0}$ is the wing damping-in-yaw parameter for zero sweep angle of the quarter-chord line, obtained from figure 6.2.1-1 as a function of the wing aspect ratio and taper ratio for $\Lambda_c/4 = 0$

The significance of $\left[\frac{(\Delta C_{n_r})_1}{C_{L_w}^2} \right]_{\bar{x}}$ increases with increasing distance and sweep angle.

It decreases with increasing aspect ratio. For the subject airplane, the term is insignificant, as will be shown.

The effect of unsymmetrical spanwise distribution of profile drag on yawing moment due to yaw, accounted for by the second term in equation (6.2.1-1), is approximated by assuming the profile drag to be constant over the wing surface. As a result of this

assumption, $\left[\frac{(\Delta C_{n_r})_2}{(C_{D0})_w} \right]$ becomes a function of wing geometry only, as shown in

figure 6.2.1-2, which is reproduced from reference 4. The profile drag of the wing itself, $(C_{D0})_w$, in equation (6.2.1-1) is obtained from section 4.12.1 of reference 1 or from table 6.1.1-1 of this report for the subject airplane.

The contribution of the wing can now be represented by

$$(C_{n_r})_w = C_{L_w}^2 \left\{ \left[\frac{(C_{n_r})_1}{C_{L_w}^2} \right]_{\bar{x}=0} + \left[\frac{(\Delta C_{n_r})_1}{C_{L_w}^2} \right]_{\bar{x}} \right\} + (C_{D0})_w \left[\frac{(\Delta C_{n_r})_2}{(C_{D0})_w} \right] \quad (6.2.1-4)$$

The degree of accuracy which can be expected from this equation can be inferred from figure 6.2.1-3 (from ref. 25) which compares calculated values of $(C_{n_r})_w$ with wind-tunnel data as functions of angle of attack for three aspect ratios and three sweep angles at a taper ratio of 1.0. At zero sweep, the correlation is good through the linear lift range. The lift range for good correlation decreases with increasing sweep.

The calculated C_{n_r} contribution of the subject airplane wing is given in table

6.2.1-1 as a function of angle of attack. The $\left[\frac{(\Delta C_{n_r})_1}{C_{L_w}^2} \right]_{\bar{x}}$ term is similar to zero in this instance.

6.2.2 Fuselage Contribution to C_{n_r}

As mentioned, the fuselage contribution to C_{n_r} could be important if the fuselage is large relative to the wing. Fuselages with flat sides or flattened cross sections with the major axis vertical may also make important contributions to C_{n_r} , especially at high angle of attack (ref. 15). On the other hand, fuselages with flattened cross sections with the major axis horizontal can have negative damping in yaw at moderate or high angles of attack. Systematic design data correlating the effects of fuselage and wing-fuselage geometry on C_{n_r} do not appear to be available.

For the subject airplane and on the basis of reference 26, which contains wind-tunnel data for a configuration which approximates the subject airplane (model 4 in the reference),

$$(C_{n_r})_f \approx -0.002 \text{ per rad}$$

6.2.3 Vertical-Tail Contribution to C_{n_r}

Because the vertical tail is the primary contributor to the damping-in-yaw derivative, C_{n_r} , particular attention should be given to the sidewash due to yaw rate,

$\frac{\partial \sigma}{\partial \frac{rb_w}{2V}}$, to which the vertical tail will be subjected. No general design procedures appear

to be available to obtain this sidewash factor as a function of wing-fuselage-tail geometry.

Reference 27 shows that on a midwing model tested at steady yaw-rate conditions with the wings off, the fuselage sidewash effects were the probable cause of a large increase in damping in yaw of the vertical tail with increase in angle of attack. Addition of a midwing resulted in little variation with angle of attack of the tail contribution to C_{n_r} , indicating a wing interference which approximately canceled the fuselage sidewash effects. This relative independence of the vertical tail of the midwing model from

apparent sidewash effects due to yaw rate, $\frac{\partial \sigma}{\partial \frac{rb_w}{2V}} \approx 0$, has been observed on a number

of other models.

On the assumption that wing effects approximately cancel the fuselage sidewash effects on the vertical tail, the following equation was used to obtain the vertical-tail contribution to C_{n_r} :

$$(C_{n_r})_v = -114.6 \left(C'_{L_\alpha} \right)_v \left(\frac{l_v \cos \alpha_b - z_v \sin \alpha_b}{b_w} \right) \quad (6.2.3-1)$$

where $(C'_{L_\alpha})_v$, l_v , and z_v are as defined in section 6.1.3.

The calculations for the vertical-tail contribution to C_{n_r} of the subject airplane are summarized in table 6.2.3-1.

6.2.4 Power Contributions to C_{n_r} and Summary

Systematic procedures to account for power effects on C_{n_r} are not available. Consequently, it is necessary to find C_{n_r} data for powered models similar to the airplane being analyzed. Such data are scarce.

Power effects on the C_{n_r} of the subject airplane were estimated by using data from reference 26 for a powered, two-engine model similar to the subject airplane. A geometric comparison of the reference model and the subject airplane is included in figure 6.2.4-1, which shows the variation of C_{n_r} of the reference model with

$T_c = \frac{\text{Thrust}}{\rho V^2 D_p^2}$ at $C_L = 0.7$. Superimposed on the plot are the subject airplane thrust coefficients, $T'_c = \frac{\text{Thrust}}{\bar{q}_\infty S_w}$, used in the analysis.

In using the reference model data to obtain an estimate of power effects on the C_{n_r} of the subject airplane, it was assumed for a first order of approximation that:

- (1) The variation of C_{n_r} of the reference model with power at $C_L = 0.7$ was representative of the variation at other lift coefficients in the linear lift range.
- (2) The C_{n_r} with the propeller off was similar to C_{n_r} at zero thrust.
- (3) The proportionality relationship in equation (6.2.4-1) between the reference twin-engine model and the subject airplane was qualitatively valid.

$$C_{n_r} = \left[\frac{(C_{n_r})_{T'_c}}{(C_{n_r})_{T'_c=0}} \right]_{\text{reference model}} (C_{n_r})_{\substack{\text{prop} \\ \text{off}}} \quad (6.2.4-1)$$

The estimated power effects on C_{n_r} of the subject airplane are summarized in table 6.2.4-1, which also summarizes the contributions of the wing, body, and vertical tail to the derivative. The results show the vertical tail to be the major contributor to C_{n_r} . The wing contribution is negligible at zero lift but not at high lift. The power effects are small in the normal operating range of the airplane ($T'_c < 0.1$) and moderate at the extreme thrust condition ($T'_c = 0.44$).

The calculated damping-in-yaw derivative, C_{n_r} , is plotted in figure 6.2.4-2 as a function of angle of attack and thrust coefficient. Lack of appropriate wind-tunnel data precludes comparison. Comparisons with flight data are made in section 6.5.

6.2.5 Symbols

A_w	wing aspect ratio
ac_w	aerodynamic center of the wing as a fraction of the wing mean aerodynamic chord
b_w	wing span, in.
$(C_{D_0})_w$	zero-lift drag coefficient of the wing
C_L	lift coefficient
C_{L_w}	wing-lift coefficient
$(C'_{L_\alpha})_v$	effective lift-curve slope of the vertical tail, based on the wing area, per deg

C_n	yawing-moment coefficient
C_{n_r}	damping-in-yaw derivative, $\frac{\partial C_n}{\partial \frac{rb_w}{2V}}$, per rad
$(C_{n_r})_f$	fuselage contribution to C_{n_r} for propeller-off conditions
$(C_{n_r})_{\text{prop off}}$	airplane C_{n_r} for propeller-off conditions
$(C_{n_r})_{T'_c=0}, (C_{n_r})_{T'_c}$	airplane C_{n_r} at zero and non-zero propeller-thrust conditions, respectively
$\left[\frac{(C_{n_r})_{T'_c}}{(C_{n_r})_{T'_c=0}} \right]_{\text{reference model}}$	correction factor for the propeller-off C_{n_r} to account for the power effects on C_{n_r} , based on wind-tunnel data for a powered model similar to the subject airplane
$(C_{n_r})_v$	vertical-tail contribution to C_{n_r} for propeller-off conditions
$(C_{n_r})_w$	wing contribution to C_{n_r} for propeller-off conditions
$\frac{(C_{n_r})_1}{C_{L_w}^2}$	contribution to C_{n_r} as a ratio of $C_{L_w}^2$, due to the lift and induced forces of the wing, resulting from the yawing of the wing about the airplane center of gravity (does not include the effects of the unsymmetrical spanwise distribution of the profile drag)
$\left[\frac{(C_{n_r})_1}{C_{L_w}^2} \right]_{\bar{x}=0}$	contribution to C_{n_r} as a ratio of $C_{L_w}^2$, due to the lift and induced forces of a wing, with sweep of the quarter-chord line, when the wing aerodynamic center and airplane center of gravity coincide longitudinally
$\left[\frac{(C_{n_r})_1}{C_{L_w}^2} \right]_{\Lambda_c/4=0}$	contribution to C_{n_r} as a ratio of $C_{L_w}^2$, due to the lift and induced forces of a wing with zero sweep of the quarter-chord line, when the wing aerodynamic center and airplane center of gravity coincide longitudinally

$$(\Delta C_{n_r})_{\text{power}}$$

contribution of power effects to C_{n_r}

$$\left[\frac{(\Delta C_{n_r})_1}{C_{L_w}^2} \right]_{\bar{x}}$$

increment correction for the displacement of the wing aerodynamic center from the center of gravity to be

$$\text{applied to } \left[\frac{(C_{n_r})_1}{C_{L_w}^2} \right]_{\bar{x}=0} \text{ to obtain } \frac{(C_{n_r})_1}{C_{L_w}^2}$$

$$\frac{(\Delta C_{n_r})_2}{(C_{D_0})_w}$$

contribution to C_{n_r} as a ratio of $(C_{D_0})_w$, due to the effects of the unsymmetrical spanwise distribution of the wing profile drag during yawing

$$\bar{c}_w$$

wing mean aerodynamic chord, in.

$$D_p$$

propeller diameter, ft

$$l_v$$

distance, parallel to the X-body axis, from the center of gravity to the quarter chord of the vertical-tail mean aerodynamic chord, in.

$$\bar{q}_{\infty}$$

free-stream dynamic pressure, lb/sq ft

$$r$$

yaw rate, rad/sec

$$S_w$$

wing area, sq ft

$$T$$

thrust of the propellers, lb

$$T_c = \frac{T}{\rho V^2 D_p^2}$$

$$T'_c = \frac{T}{\bar{q}_{\infty} S_w}$$

$$t$$

time, sec

$$V$$

airspeed, ft/sec

$$\bar{x}$$

distance parallel to the wing mean aerodynamic chord from the center of gravity to the wing aerodynamic center, in.

z_v	distance parallel to the Z-body axis from the center of gravity to the vertical-tail mean aerodynamic chord, in.
α_b	airplane angle of attack relative to the X-body axis, deg
$\Lambda_c/4$	sweep of the wing quarter-chord line, deg
λ_w	wing taper ratio
ρ	mass density of the air, slugs/cu ft
$\frac{\partial \sigma}{\partial \frac{rb_w}{2V}}$	rate of change of the sidewash on the vertical tail induced by the yaw rate, r , with $\frac{rb_w}{2V}$

TABLE 6.2, 1-1
WING CONTRIBUTION TO C_{n_r}

$$(C_{n_r})_w = \left\{ \left[\frac{(C_{n_r})_1}{C_{L_w}^2} \right]_{\bar{x}=0} + \left[\frac{(\Delta C_{n_r})_1}{C_{L_w}^2} \right]_{\bar{x}} \right\} C_{L_w}^2 + \left[\frac{(\Delta C_{n_r})_2}{(C_{D_0})_w} \right] (C_{D_0})_w$$

Symbol	Description	Reference	Magnitude
A_w	Wing aspect ratio	Figure 3.2-1	7.5
λ_w	Wing taper ratio	Figure 3.2-1	.513
$\Lambda_c/4$	Sweep of wing quarter-chord line, deg	Figure 3.2-1	-2.5
ac_w	Wing aerodynamic center	Figure 3.2-1	.25c
$\frac{\bar{x}}{c_w}$	ac_w - center of gravity	-----	.15
$\left[\frac{(C_{n_r})_1}{C_{L_w}^2} \right]_{\bar{x}=0}$	$f(A_w, \lambda_w, \Lambda_c/4)$	Figure 6.2.1-1 or equation (6.2.1-2)	-0.017
$\left[\frac{(C_{n_r})_1}{C_{L_w}^2} \right]_{\Lambda_c/4=0}$	$f(A_w, \lambda_w)$ with $\Lambda_c/4 = 0$	Figure 6.2.1-1	-0.017
$\left[\frac{(\Delta C_{n_r})_1}{C_{L_w}^2} \right]_{\bar{x}}$	$f(A_w, \lambda_w, \Lambda_c/4, \frac{\bar{x}}{c})$	Equation (6.2.1-3)	-0.0009
$\frac{(\Delta C_{n_r})_2}{(C_{D_0})_w}$	$f(A_w, \frac{\bar{x}}{c_w}, \Lambda_c/4)$	Figure 6.2.1-2	-0.30
C_{L_w}	Lift coefficient of wing referenced to $S_w = 178$ sq ft	Figure 4.1.1-1	$f(\alpha_b)$
$(C_{D_0})_w$	Profile drag coefficient of wing referenced to $S_w = 178$ sq ft	Table 6.1.1-1	0.0099
Summary: $(C_{n_r})_w = -0.017 C_{L_w}^2 - 0.0030$			

(1)	(2)	(3)	(4)	(5)
---	Figure 4.1.1-1	-----	-----	-----
α_b , deg	C_{L_w}	(2) ²	-0.017(3)	$(C_{n_r})_w =$ (4) - 0.0030
-4	0	0	0	-0.0030
-2	.145	.0210	-.0004	-.0034
0	0.292	0.0853	-0.0015	-0.0045
2	.437	.1910	-.0032	-.0062
4	0.584	0.3411	-0.0058	-0.0088
6	.730	.5329	-.0091	-.0121
8	0.875	0.7656	-0.0130	-0.0160
10	1.023	1.0465	-.0178	-.0208
12	1.160	1.3456	-0.0229	-0.0259

TABLE 6.2.3-1
VERTICAL-TAIL CONTRIBUTION TO C_{n_r}

$$(C_{n_r})_v = -114.6 (C'_{L_\alpha})_v \left(\frac{l_v \cos \alpha_b - z_v \sin \alpha_b}{b_w} \right)^2$$

Symbol	Description	Reference	Magnitude
$(C'_{L_\alpha})_v$	Effective lift-curve slope of vertical tail, referred to $S_w = 178$ sq ft, per deg	Table 4.5.1-1	0.00464
l_v	Distance, parallel to X-body axis from center of gravity to quarter chord of vertical-tail mean aerodynamic chord, positive back, in.	Figure 3.2-4	164.9
z_v	Vertical distance parallel to Z-body axis from center of gravity to tail mean aerodynamic chord, positive down, in.	Figure 3.2-4	-45.9
b_w	Wing span, in.	Figure 3.2-1	432
Summary: $(C_{n_r})_v = -0.5317 (0.382 \cos \alpha_b + 0.106 \sin \alpha_b)^2$			

(1)	(2)	(3)	(4)	(5)	(6)	(7)
α_b , deg	$\cos \alpha_b$	$\sin \alpha_b$	0.382(2)	0.106(3)	$(4) + (5)^2$	$(C_{n_r})_v =$ $-0.5317(6)$
-4	0.9976	-0.0698	0.3811	-0.0074	0.1396	-0.0742
-2	.9994	-.0349	.3818	-.0037	.1430	-.0760
0	1.000	0	0.3820	0	0.1459	-0.0776
2	.9994	.0349	.3818	.0037	.1486	-.0790
4	0.9976	0.0698	0.3811	0.0074	0.1509	-0.0802
6	.9945	.1045	.3799	.0111	.1529	-.0813
8	0.9903	0.1392	0.3783	0.0148	0.1545	-0.0822
10	.9848	.1736	.3762	.0184	.1557	-.0828
12	0.9782	0.2079	0.3737	0.0220	0.1566	-0.0833

TABLE 6.2.4-1
SUMMARY OF CONTRIBUTIONS TO C_{nr} INCLUDING POWER

$$(C_{nr})_{\text{prop}} = (C_{nr})_w + (C_{nr})_f + (C_{nr})_v$$

$$C_{nr} \approx \left[\frac{(C_{nr})_{T'_c}}{(C_{nr})_{T'_c=0}} \right]_{\text{reference model}} (C_{nr})_{\text{prop off}}$$

α_b , deg	$(C_{nr})_w$	$(C_{nr})_f$	$(C_{nr})_v$	$(C_{nr})_{\text{prop off}}$ $\stackrel{\text{②} + \text{③} + \text{④}}{=}$	$(C_{nr})_{T'_c}$ $\stackrel{\text{⑤}}{=}$ $\left[\frac{(C_{nr})_{T'_c}}{(C_{nr})_{T'_c=0}} \right]_{\text{reference model}}$	$(C_{nr})_{\text{prop off}}$ $\stackrel{\text{⑥}}{=}$ T'_c	T'_c $\stackrel{\text{⑦}}{=}$
4	-0.0030	-0.002	-0.0742	-0.0792	1.00	1.06	1.11
-2	-.0034	-.002	-.0760	-.0814	1.00	1.06	1.11
0	-0.0045	-0.002	-0.0776	-0.0841	1.00	1.06	1.11
2	-.0062	-.002	-.0790	-.0872	1.00	1.06	1.11
4	-0.0088	-0.002	-0.0802	-0.0910	1.00	1.06	1.11
6	-.0121	-.002	-.0813	-.0954	1.00	1.06	1.11
8	-0.0160	-0.002	-0.0822	-0.1002	1.00	1.06	1.11
10	-.0208	-.002	-.0828	-.1056	1.00	1.06	1.11
12	-0.0259	-0.002	-0.0833	-0.1112	1.00	1.06	1.11

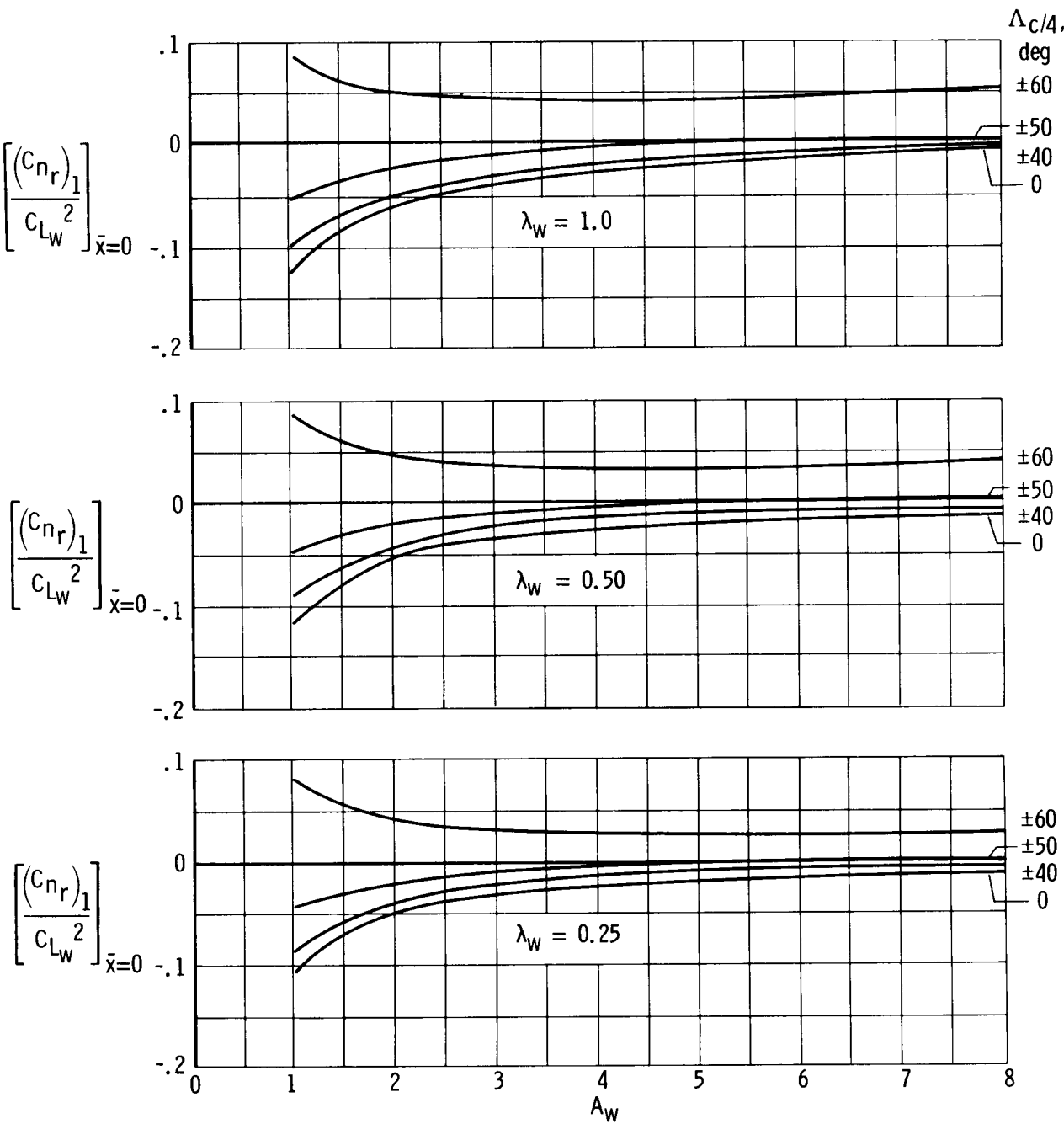


Figure 6.2.1-1. Chart (from ref. 15) for estimating the portion of the wing contribution to C_{n_r} due to the lift and induced forces resulting from yawing of the wing about its aerodynamic center ($\bar{x} = 0$) in subsonic incompressible flow on the basis of the method of reference 4.

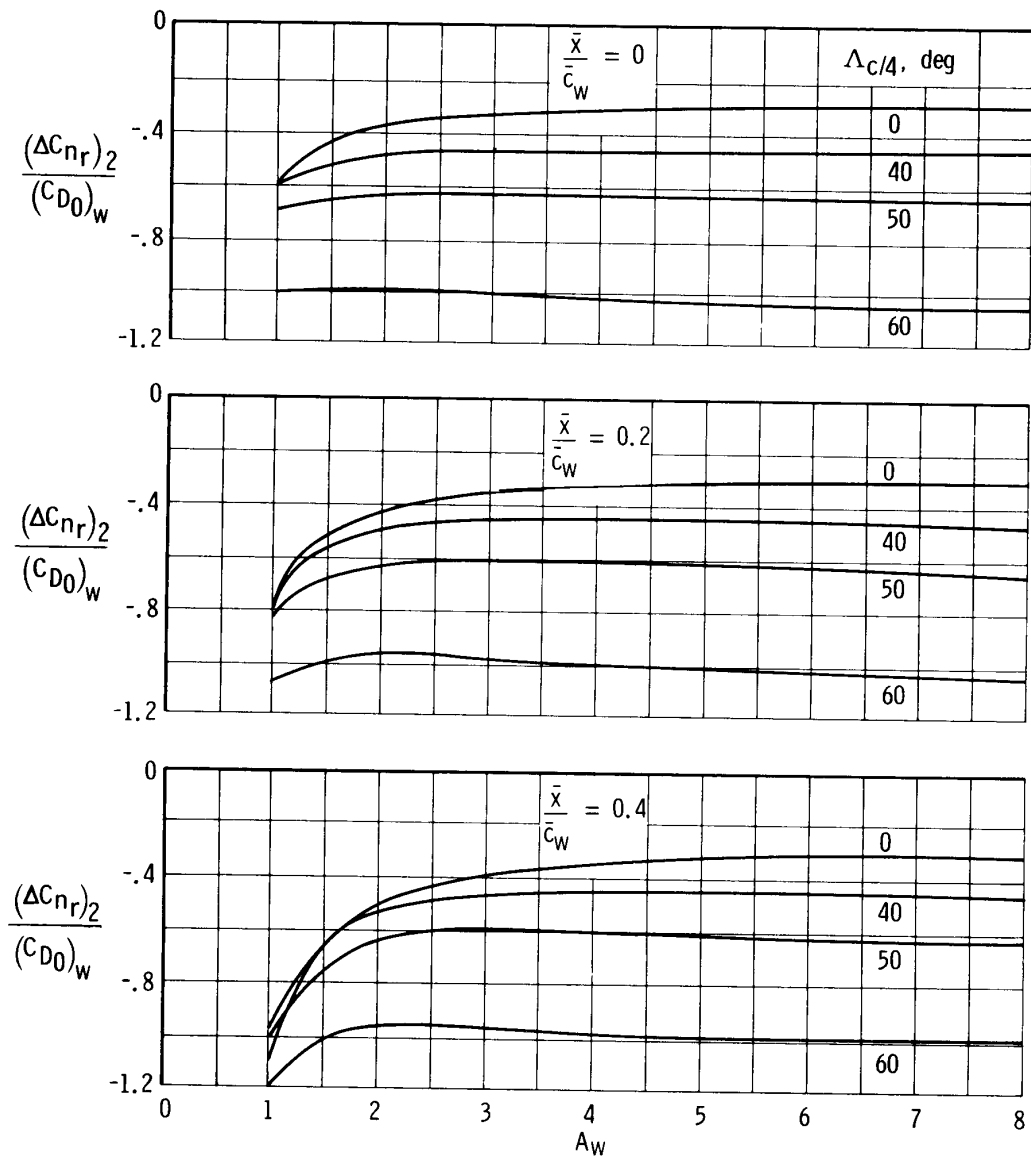


Figure 6.2.1-2. Chart for estimating approximate values of increment of yawing moment due to the yawing resulting from wing profile drag (from ref. 4). Taper ratios of 0.5 to 1.0.

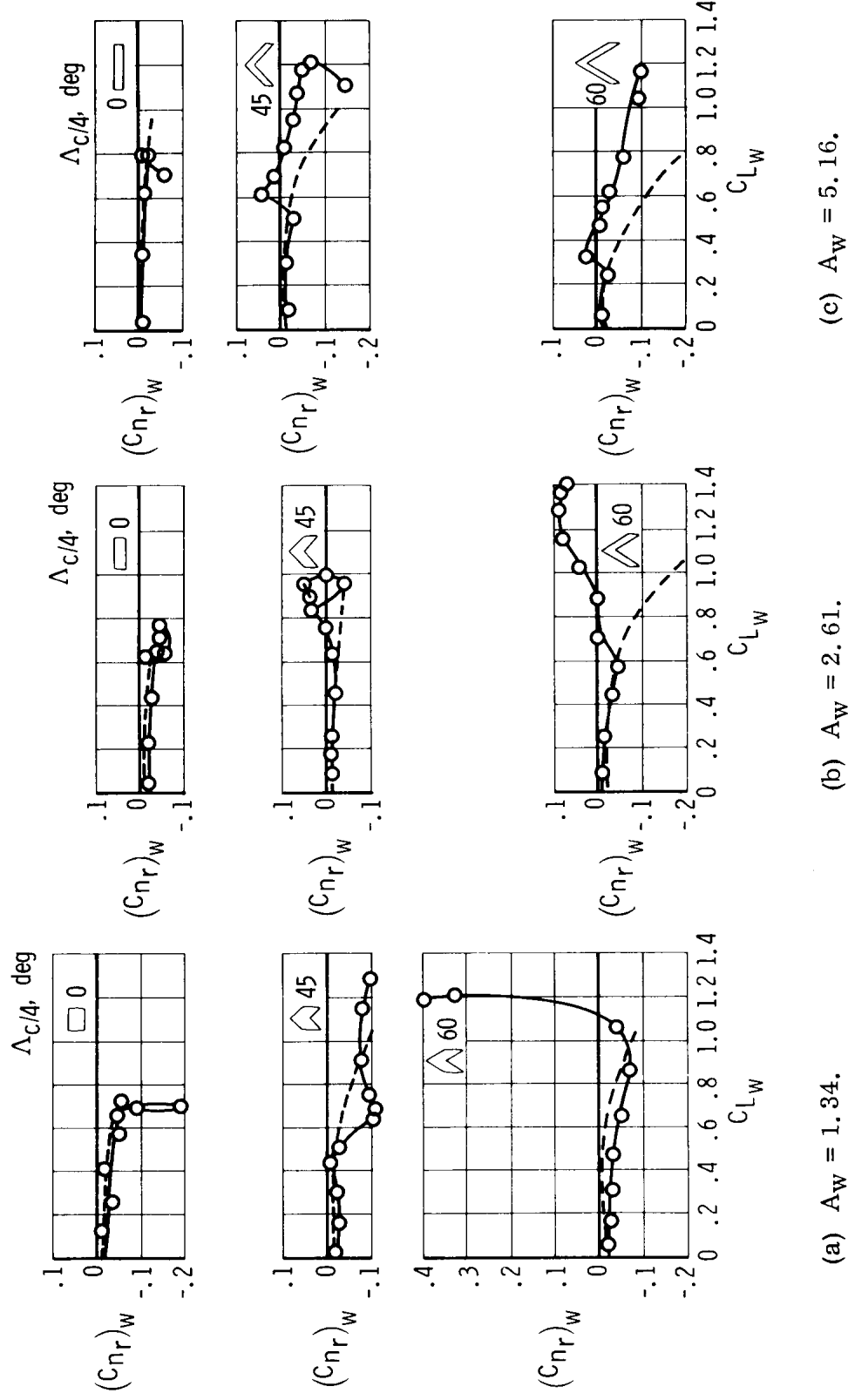


Figure 6.2, 1-3. Variation of experimental and theoretical values of $(C_{n_r})_W$ with lift coefficient and aspect ratio for a series of swept wings (from ref. 25). Taper ratio of 1.0.

	Wing aspect ratio	Vertical-tail area Wing area	Tail length Wing span	Propeller diameter Wing span	Lateral distance to thrust centerline Wing semispan
Reference model	7.8	0.111	0.39	0.138	0.31
Subject airplane	7.5	.0995	.38	.166	.324

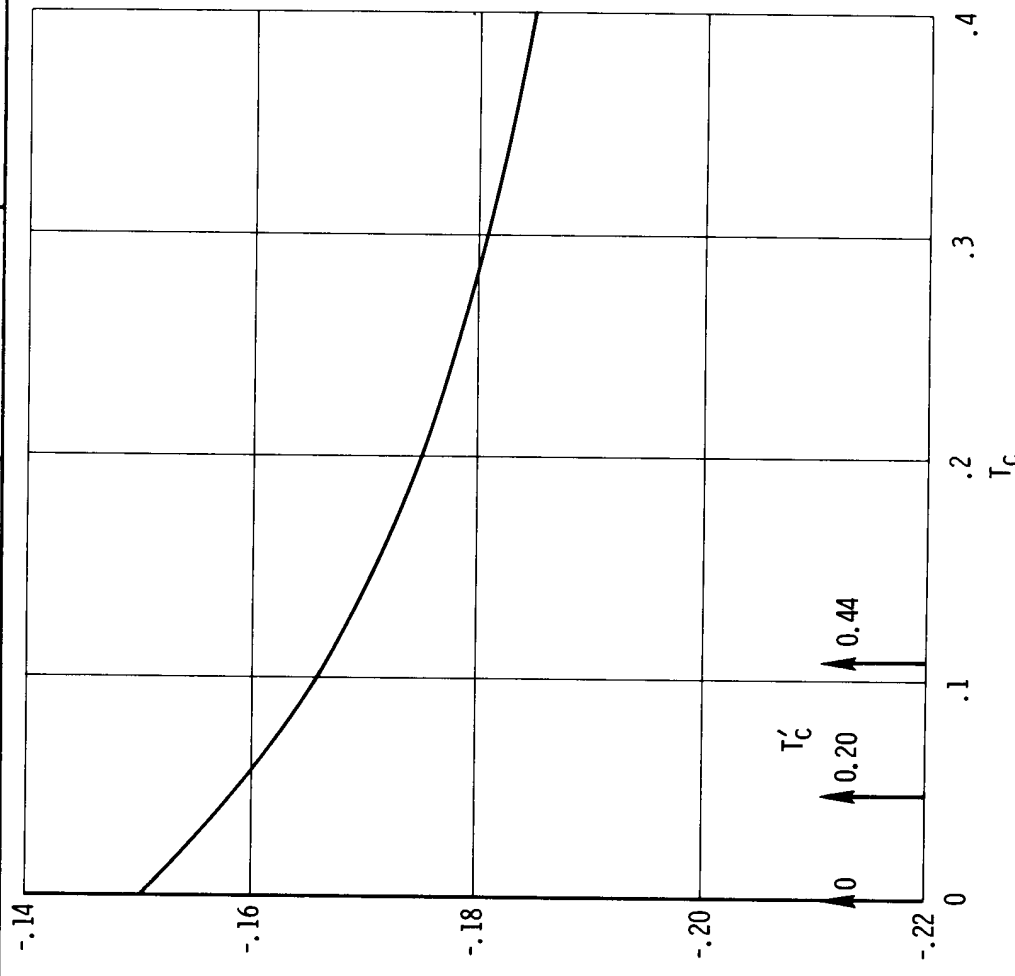


Figure 6.2.4-1. Variation of C_{n_r} with power of a twin-engine wind-tunnel model similar to the subject airplane. Model used to approximate the effects of power on the C_{n_r} of the subject airplane using equation (6.2.4-1); data reproduced from figure 5 of reference 26; $C_L = 0.7$.

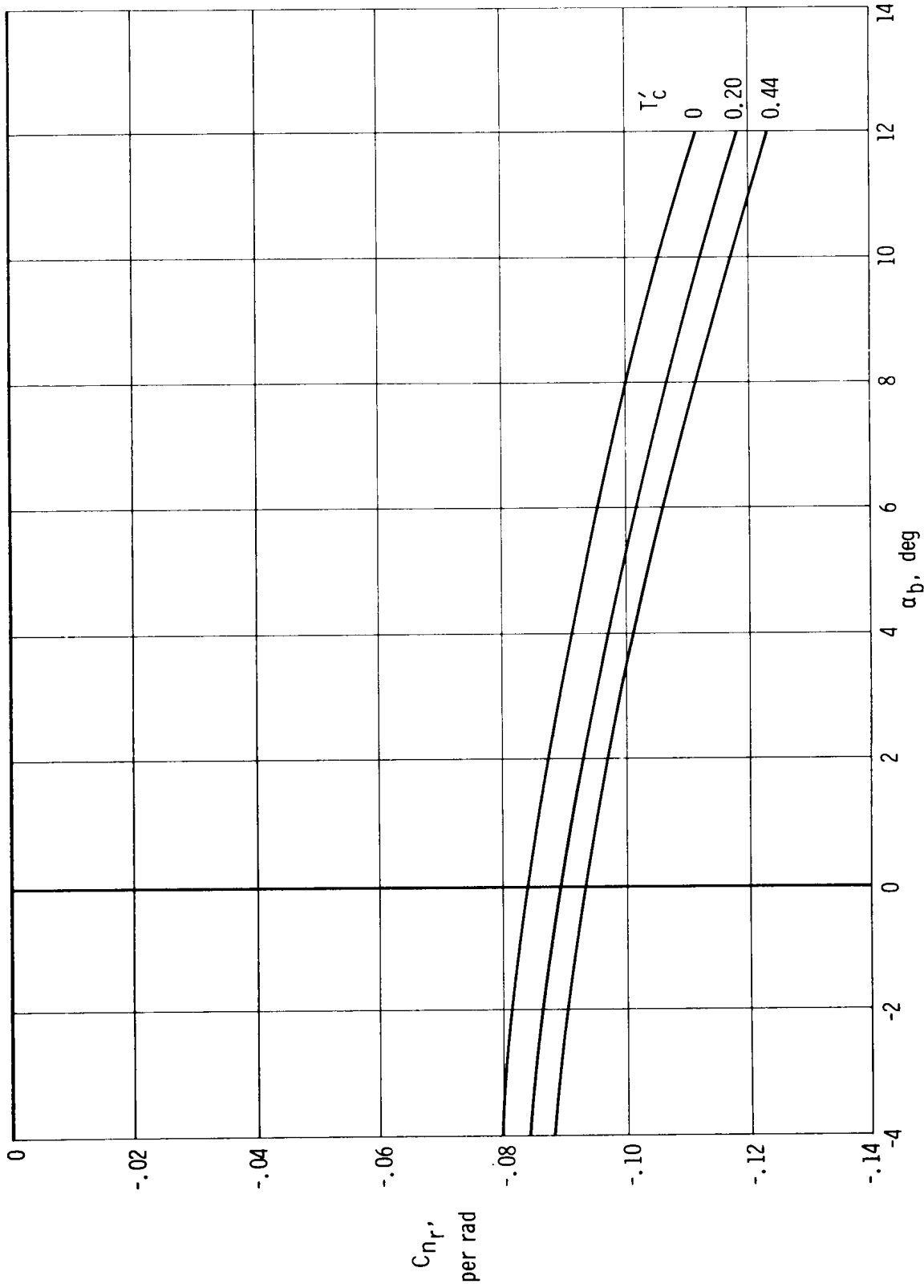


Figure 6.2.4-2. Variation of calculated damping-in-yaw derivative of complete airplane with power and angle of attack.

6.3 Roll-Due-to-Yawing Derivative, C_{l_r}

The wing and vertical tail are the only surface components that make significant contributions to the rolling-moment-due-to-yawing derivative, C_{l_r} , and thus are the only components considered in this section. An estimate of the effect of power on C_{l_r} is included. On this basis, the C_{l_r} of the airplane is represented by

$$C_{l_r} = \left(C_{l_r} \right)_w + \left(C_{l_r} \right)_v + \left(\Delta C_{l_r} \right)_{\text{power}} \quad (6.3-1)$$

6.3.1 Wing Contribution to C_{l_r}

For low speeds, the wing contribution to C_{l_r} may be approximated from

$$\left(C_{l_r} \right)_{w M=0} = \left(\frac{C_{l_r}}{C_{L_w}} \right)_{\Gamma=M=0} C_{L_w} + \left(\frac{\Delta C_{l_r}}{\Gamma} \right) \frac{\Gamma}{57.3} \quad (6.3.1-1)$$

where

$$\left(\frac{C_{l_r}}{C_{L_w}} \right)_{\Gamma=M=0} \quad \text{is the low-speed wing contribution to } C_{l_r} \text{ in the absence of the}$$

dihedral angle and when the center of gravity is at the same vertical height as the aerodynamic center of the wing mean aerodynamic chord

$\left(\frac{\Delta C_{l_r}}{\Gamma} \right)$ is the increment of C_{l_r} due to the dihedral angle

The first term of equation (6.3.1-1), $\left(\frac{C_{l_r}}{C_{L_w}} \right)_{\Gamma=M=0}$, has been particularly trouble-

some to determine. In reference 4 theoretical relations were developed which appear to work well for unswept wings with aspect ratios greater than approximately 3.0. As shown in reference 25, however, correlation deteriorates as the sweep angle of the quarter-chord line increases. In reference 3, on the basis of theoretical work by W. J. Pinsker of the Royal Aircraft Establishment and experimental data from references

25 and 28 a nomograph procedure for determining $\left(\frac{C_{l_r}}{C_{L_w}} \right)_{\Gamma=M=0}$ was developed.

Although the nomograph, shown in figure 6.3.1-1, provides good correlation with wind-tunnel data through the linear lift range when the sweep is zero, the lift range for

correlation decreases with increasing sweep in a manner similar to that shown for C_{n_r} in figure 6.2.1-3.

Compressibility effects on the low-speed values of $\left(\frac{C_l_r}{C_{L_w}}\right)_{\Gamma=0}$ are accounted for

by the following equation from reference 5:

$$\left(\frac{C_l_r}{C_{L_w}}\right)_{\Gamma=0} = \frac{1 + \frac{A_w(1 - B_2)^2}{2B_2(A_wB_2 + 2\cos\Lambda_c/4)} + \left(\frac{A_wB_2 + 2\cos\Lambda_c/4}{A_wB_2 + 4\cos\Lambda_c/4}\right)\left(\frac{\tan^2\Lambda_c/4}{8}\right)}{1 + \frac{A_w + 2\cos\Lambda_c/4}{A_w + 4\cos\Lambda_c/4}\left(\frac{\tan^2\Lambda_c/4}{8}\right)} \left(\frac{C_l_r}{C_{L_w}}\right)_{\Gamma=M=0} \quad (6.3.1-2)$$

where

$$B_2 = \sqrt{1 - M^2 \cos^2\Lambda_c/4}$$

$$\left(\frac{C_l_r}{C_{L_w}}\right)_{\Gamma=M=0} \text{ is obtained from figure 6.3.1-1}$$

The increment contribution to C_{l_r} due to wing dihedral is approximated by the following equation from reference 29:

$$\left(\Delta C_{l_r}\right)_\Gamma = \left(\frac{\Delta C_{l_r}}{\Gamma}\right) \frac{\Gamma}{57.3} = \frac{1}{12} \left(\frac{\pi A_w \sin\Lambda_c/4}{A_w + 4\cos\Lambda_c/4}\right) \frac{\Gamma}{57.3} \quad (6.3.1-3)$$

Two additional contributions to C_{l_r} , due to the wing, have not been accounted for because the basic effects of sweep on these contributions are not known to a reasonable degree of accuracy and because the contributions are generally small. The contributions consist of:

(1) The increment of C_{l_r} due to the fore and aft movement of the center of gravity relative to the aerodynamic center of the wing mean aerodynamic chord (for zero sweep the contribution is zero)

(2) The increment of C_{l_r} due to $(C_{Y_r})_w$ when the center of gravity is not at the same vertical height as the aerodynamic center of the wing mean aerodynamic chord (for zero sweep, the contribution is zero)

The contribution of the wing to the C_{l_r} of the subject airplane is summarized in table 6.3.1-1.

6.3.2 Vertical-Tail Contribution to C_{l_r}

In considering the contribution of the vertical tail to C_{n_r} in section 6.2.3, it was indicated that in the model data the effects of sidewash on the vertical tail due to yaw rate, $\frac{\partial \sigma}{\partial \frac{rb_w}{2V}}$, were negligible for common airplane configurations. If these sidewash

effects are excluded, the contribution of the vertical tail to C_{l_r} can be obtained from

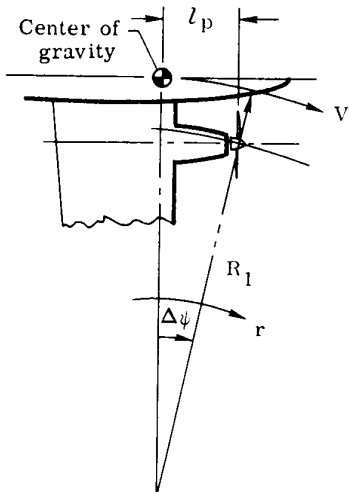
$$(C_{l_r})_v = -114.6 \left(C'_{L_\alpha} \right)_v \left(\frac{z_v \cos \alpha_b + l_v \sin \alpha_b}{b_w} \right) \left(\frac{l_v \cos \alpha_b - z_v \sin \alpha_b}{b_w} \right) \quad (6.3.2-1)$$

The calculations for the vertical-tail contribution to C_{l_r} of the subject airplane are summarized in table 6.3.2-1.

6.3.3 Power Contributions to C_{l_r}

Power effects on the C_{l_r} contribution of the single vertical tail of the twin-engine airplane are negligible and are not included in the calculations. The power effects on the contribution of the wing to C_{l_r} are also negligible, as is shown in the following discussion.

The propeller slipstream has some effect on the contribution of the wing to C_{l_r} as a result of the lateral displacement of this slipstream caused by yawing. The change in lift of the portion of the wing immersed in the propeller slipstream coupled with the lateral displacement of the immersed area due to yawing flight produces a yaw-induced roll. An equation that takes this effect into account can be developed as follows:



Consider the lift due to the increase in dynamic pressure and propeller-induced downwash on the immersed portion of the wing per propeller to be $(\Delta C_L)_{w(\Delta q)}$ /propeller and

$(\Delta C_L)_{w(\epsilon_p)}$ /propeller, respectively (obtained

from a figure like fig. 6.1.5-1). Assume the curvature of the propeller slipstream to be the same as the instantaneous radius of curvature of the yawing airplane flight path. (See sketch.) Also assume the lateral displacement of the propeller slipstream at the aerodynamic center of the mean aerodynamic chord of the immersed portion of the wing to

be similar to the displacement at the radial to the center of gravity.

From the preceding discussion and sketch, it is apparent that the increment of roll due to the two immersed wing areas is approximated by

$$\begin{aligned} (\Delta C_l)_{\text{power}} &\approx 2 \left[(\Delta C_L)_{w(\Delta \bar{q})}/\text{propeller} + (\Delta C_L)_{w(\epsilon_p)}/\text{propeller} \right] \frac{R_1 - R_1 \cos \Delta \psi}{b_w} \\ &= 2 \left[(\Delta C_L)_{w(\Delta \bar{q})}/\text{propeller} + (\Delta C_L)_{w(\epsilon_p)}/\text{propeller} \right] \left(\frac{R_1}{b_w} \right) (1 - \cos \Delta \psi) \end{aligned} \quad (6.3.3-1)$$

However, for small angles,

$$\cos \Delta \psi \approx 1 - \frac{(\Delta \psi)^2}{2} \quad (6.3.3-2)$$

Hence,

$$(\Delta C_l)_{\text{power}} \approx \left[(\Delta C_L)_{w(\Delta \bar{q})}/\text{propeller} + (\Delta C_L)_{w(\epsilon_p)}/\text{propeller} \right] \frac{R_1}{b_w} (\Delta \psi)^2 \quad (6.3.3-3)$$

Since

$$\Delta \psi \approx \frac{l_p}{R_1} \quad \text{and} \quad R_1 = \frac{V}{r}$$

then

$$(\Delta C_l)_{\text{power}} \approx 2 \left[(\Delta C_L)_{w(\Delta \bar{q})}/\text{propeller} + (\Delta C_L)_{w(\Delta \epsilon_p)}/\text{propeller} \right] \left(\frac{l_p}{b_w} \right)^2 \frac{rb_w}{2V} \quad (6.3.3-4)$$

from which

$$(\Delta C_{l_r})_{\text{power}} \approx 2 \left[(\Delta C_L)_{w(\Delta \bar{q})}/\text{propeller} + (\Delta C_L)_{w(\epsilon_p)}/\text{propeller} \right] \left(\frac{l_p}{b_w} \right)^2 \quad (6.3.3-5)$$

The calculations for the effects of power on the wing contribution to C_{l_r} of the subject airplane are summarized in table 6.3.3-1. Comparison with the propeller-off wing contribution (table 6.3.1-1) shows the power effects to be negligible.

6.3.4 Summary of Contributions to C_{l_r}

The contributions to C_{l_r} of the subject airplane are summarized in table 6.3.4-1.

The effect of power on the C_{l_r} of the subject airplane is negligible. The vertical tail contributes a significant percentage of the net C_{l_r} at low angles of attack. However, as the contribution of the wing increases with increasing angle of attack, the contribution of the tail becomes smaller. It should be noted that the contribution of the wing would increase with increase in sweepback angle, and the significance of the contribution of the tail would thus decrease.

The calculated roll-due-to-yawing derivative is plotted in figure 6.3.4-1 as a function of angle of attack and thrust coefficient. Lack of appropriate wind-tunnel data precluded comparison of calculated values with tunnel data, but it was possible to obtain flight values of the derivative. Calculated values of C_{l_r} are compared with flight data in section 6.6.2.

6.3.5 Symbols

A_w	wing aspect ratio
$B_2 = \left(1 - M^2 \cos^2 \Lambda_c / 4\right)^{1/2}$	
b_w	wing span, in.
C_{L_w}	wing-lift coefficient at propeller-off conditions
$(\Delta C_L)_{w(\Delta \bar{q})}/\text{propeller}$	change in the wing-lift coefficient due to the power-induced increase in dynamic pressure on the portion of the wing area immersed in the slipstream of one propeller
$(\Delta C_L)_{w(\epsilon_p)}/\text{propeller}$	change in the wing-lift coefficient due to the power-induced downwash behind the propeller acting on the wing area immersed in the slipstream of one propeller
$(C'_L)_v$	effective lift-curve slope of the vertical tail based on the wing area, per deg
C_l	rolling-moment coefficient
$C_{l_r} = \frac{\partial C_l}{\partial \left(\frac{rb_w}{2V} \right)}$, per rad	
$(C_{l_r})_v$	vertical-tail contribution to C_{l_r}

$(C_{l_r})_w$, $(C_{l_r})_{wM=0}$	propeller-off contribution of the wing to C_{l_r} at subsonic compressible and incompressible flow conditions, respectively
$\left(\frac{C_{l_r}}{C_{L_w}}\right)_{\Gamma=0}$	propeller-off contribution of the wing to C_{l_r} as a ratio of the wing-lift coefficient with wing dihedral effects unaccounted for
$\left(\frac{C_{l_r}}{C_{L_w}}\right)_{\Gamma=M=0}$	propeller-off contribution of the wing to C_{l_r} as a ratio of the wing-lift coefficient at zero dihedral and incompressible-flow conditions
$(\Delta C_{l_r})_{\text{power}}$	increment of C_{l_r} due to power effects
$(\Delta C_{l_r})_{\Gamma}$	increment of C_{l_r} due to the wing dihedral
$\frac{\Delta C_{l_r}}{\Gamma}$	increment of C_{l_r} due to the unit change in the wing dihedral, per rad
C_{n_r}	damping-in-yaw derivative, per rad
C_Y	side-force coefficient
$(C_{Y_r})_w$	nondimensional derivative, $\frac{\partial C_Y}{\partial \left(\frac{rb_w}{2V}\right)}$, defining the wing contribution to the side-force coefficient per unit change in the yaw rate, r , expressed as a nondimensional quantity, $\frac{rb_w}{2V}$, per rad
l_p	distance parallel to the X-body axis from the propeller plane to the center of gravity, in.
l_v	distance parallel to the X-body axis from the center of gravity to the quarter chord of the vertical-tail mean aerodynamic chord, in.
M	Mach number
\bar{q}_{∞}	dynamic pressure, lb/sq ft

R_1	instantaneous radius of curvature of the yawing flight path, in.
r	yaw rate, rad/sec
S_w	wing area, sq ft
T	propeller thrust, lb
$T'_c = \frac{T}{\bar{q}_\infty S_w}$	
V	true airspeed, ft/sec
z_v	vertical distance parallel to the Z-body axis from the center of gravity to the vertical-tail mean aerodynamic chord, in.
α_b	angle of attack relative to the X-body axis, deg
Γ	wing geometric dihedral, deg
$\Delta\psi$	incremental angular displacement of the airplane flight path in yaw, rad
$\Lambda_c/4$	sweep of the wing quarter-chord line, deg
λ_w	wing taper ratio
$\frac{\partial \sigma}{\partial \left(\frac{rb_w}{2V} \right)}$	rate of change of the sidewash on the vertical tail (induced by yaw rate, r) with $\frac{rb_w}{2V}$

TABLE 6.3.1-1

WING CONTRIBUTION TO C_{l_r}

$$(C_{l_r})_w = \left(\frac{C_{l_r}}{C_{L_w}} \right)_{\Gamma=0} C_{L_w} + \left(\frac{\Delta C_{l_r}}{\Gamma} \right) \frac{\Gamma}{57.3}$$

Symbol	Description	Reference	Magnitude
M	Mach number	As selected	0.083
A_w	Wing aspect ratio	Figure 3.2-1	7.5
λ_w	Wing taper ratio	Figure 3.2-1	.513
$\Lambda_c/4$	Wing sweep along quarter-chord line, deg	Figure 3.2-1	-2.5
Γ	Wing dihedral, deg	Figure 3.2-1	5
C_{L_w}	Wing lift coefficient referred to $S_w = 178$ sq ft	Figure 4.1.1-1	$f(\alpha_b)$
$\left(\frac{C_{l_r}}{C_{L_w}} \right)_{\Gamma=M=0}$	Wing contribution to C_{l_r} when dihedral is zero and $M \approx 0$	Figure 6.3.1-1	0.245
$\left(\frac{C_{l_r}}{C_{L_w}} \right)_{\Gamma=0}$	Wing contribution to C_{l_r} , when dihedral is zero, corrected for Mach effects	Equation (6.3.1-2)	$\approx .245$
$\left(\frac{\Delta C_{l_r}}{\Gamma} \right)$	Increment of C_{l_r} due to unit change in dihedral	Equation (6.3.1-3)	-0.00745 per rad
Summary: $(C_{l_r})_w = 0.245 C_{L_w} - 0.00065$			

(1)	(2)	(3)
---	Figure 4.1.1-1	-----
α_b , deg	C_{L_w}	$(C_{l_r})_w = 0.245(2) - 0.0006$
-4	0	0
-2	.145	.0349
0	0.292	0.0709
2	.437	.1065
4	0.584	0.1425
6	.730	.1782
8	0.875	0.2138
10	1.023	.2500
12	1.160	0.2836

TABLE 6.3.2-1
VERTICAL-TAIL CONTRIBUTION TO C_{l_r}

$$(C_{l_r})_v = -114.6 \left(C'_{L_\alpha} \right)_v \left(\frac{z_v \cos \alpha_b + l_v \sin \alpha_b}{b_w} \right) \left(\frac{l_v \cos \alpha_b - z_v \sin \alpha_b}{b_w} \right)$$

Symbol	Description	Reference	Magnitude
$(C'_{L_\alpha})_v$	Effective lift-curve slope of vertical tail referred to $S_w = 178$ sq ft, deg	Table 4.5.1-1	0.00464
z_v	Vertical distance parallel to Z-body axis from the center of gravity to the tail mean aerodynamic chord (positive down), in.	Figure 3.2-4	-45.9
l_v	Distance parallel to X-body axis from center of gravity to quarter chord of vertical-tail mean aerodynamic chord (positive back), in.	Figure 3.2-4	164.9
b_w	Wing span, in.	Figure 3.2-1	432
Summary: $(C_{l_r})_v = -0.5317 (-0.10625 \cos \alpha_b + 0.3817 \sin \alpha_b)$ $(0.3817 \cos \alpha_b + 0.10625 \sin \alpha_b)$			

(1)	(2)	(3)	(4)	(5)	(6)
α_b , deg	$\cos(1)$	$\sin(1)$	$-0.10625(2) + 0.3817(3)$	$0.3817(2) + 0.10625(3)$	$(C_{l_r})_v = -0.5317(4)(5)$
-4	0.9976	-0.0698	-0.13264	0.37337	0.0263
-2	.9994	-.0349	-.11951	.37776	.0240
0	1.000	0	-0.10625	0.38170	0.0216
2	.9994	.0349	-.09286	.38518	.0190
4	0.9976	0.0698	-0.07935	0.38820	0.0164
6	.9945	.1045	-.06578	.39070	.0137
8	0.9903	0.1392	-0.05209	0.39279	0.0109
10	.9848	.1736	-.03837	.39434	.0080
12	0.9782	0.2079	-0.02458	0.39547	0.0052

TABLE 6.3.3-1

EFFECT OF POWER ON WING CONTRIBUTION TO C_{l_r}

$$(\Delta C_{l_r})_{\text{power}} \approx 2 \left[(\Delta C_L)_{w(\Delta \bar{q})}/\text{propeller} + (\Delta C_L)_{w(\epsilon_p)}/\text{propeller} \right] \left(\frac{l_p}{b_w} \right)^2$$

Symbol	Description	Reference	Magnitude
$(\Delta C_L)_{w(\Delta \bar{q})}/\text{propeller}$	Change in lift coefficient due to power-induced increase in dynamic pressure on wing area immersed in slipstream of one propeller	Figure 6.1.5-1	$f(\alpha_b, T_c')$
$(\Delta C_L)_{w(\epsilon_p)}/\text{propeller}$	Change in lift coefficient due to power-induced downwash behind the propeller acting on the immersed area	Figure 6.1.5-1	$f(\alpha_b, T_c')$
l_p	Distance parallel to X-body axis from propeller plane to the center of gravity, in.	Figure 3.2-5	63.15
b_w	Wing span, in.	Figure 3.2-1	432
Summary: $(\Delta C_{l_r})_{\text{power}} = 0.0427 \left[(\Delta C_L)_{w(\Delta \bar{q})}/\text{propeller} + (\Delta C_L)_{w(\epsilon_p)}/\text{power} \right]$			

(1)	(2)	(3)	(4)
---	Figure 6.1.5-1	Figure 6.1.5-1	-----
α_b , deg	$(\Delta C_L)_{w(\Delta \bar{q})}/\text{propeller}$	$(\Delta C_L)_{w(\epsilon_p)}/\text{propeller}$	$(\Delta C_{l_r})_{\text{power}} = 0.0427 (2) + (3)$
	T_c'/propeller	T_c'/propeller	T_c'
	0 0.10 0.22	0 0.10 0.22	0 0.20 0.44
-4	0 0 0	0.001 0.014 0.031	≈ 0 0.0006 0.0013
-2	0 .015 .031	.001 .005 .013	≈ 0 .0009 .0019
0	0 0.030 0.061	0 -0.003 -0.006	0 0.0012 0.0023
2	0 .044 .088	0 -.011 -.023	0 .0014 .0028
4	0 0.056 0.115	-0.001 -0.018 -0.039	≈ 0 0.0016 0.0032
6	0 .067 .138	-.002 -.025 -.055	.0018 .0035
8	0 0.076 0.158	-0.002 -0.032 -0.069	0.0019 0.0038
10	0 .083 .174	-.002 -.036 -.081	.0020 .0040
12	0 0.086 0.184	-0.003 -0.040 -0.090	0.0020 0.0040

TABLE 6.3.4-1
SUMMARY OF CONTRIBUTIONS TO C_{l_r}

$$C_{l_r} = (C_{l_r})_w + (C_{l_r})_v + (\Delta C_{l_r})_{\text{power}}$$

α_b , deg	$(C_{l_r})_w$	$(C_{l_r})_v$	$C_{l_r} = \textcircled{2} + \textcircled{3}$	$\textcircled{4}$		$\textcircled{5}$		$\textcircled{6}$	
				$\textcircled{4}$		$\textcircled{5}$		$\textcircled{6}$	
---	Table 6.3.1-1	Table 6.3.2-1	-----	-----		Table 6.3.3-1		-----	
				$(\Delta C_{l_r})_{\text{power}}$		$(\Delta C_{l_r})_{\text{power}}$		Power on, $C_{l_r} = \textcircled{4} + \textcircled{5}$	
				Propeller off, $C_{l_r} = \textcircled{2} + \textcircled{3}$		T'_c		T'_c	
				0	0.20	0.44	0	0.20	0.44
-4	-0.0006	0.0263	0.0257	≈ 0	0.0006	0.0013	0.0257	0.0263	0.0270
-2	.0349	.0240	.0589	≈ 0	.0009	.0019	.0589	.0598	.0608
0	0.0709	0.0216	0.0925	0	0.0012	0.0023	0.0925	0.0937	0.0948
2	.1065	.0190	.1255	0	.0014	.0028	.1255	.1269	.1283
4	0.1425	0.0164	0.1589	≈ 0	0.0016	0.0032	0.1589	0.1605	0.1621
6	.1782	.0137	.1919	-.0001	.0018	.0035	.1918	.1937	.1954
8	0.2138	0.0109	0.2247	-0.0001	0.0019	0.0038	0.2246	0.2266	0.2285
10	.2500	.0080	.2580	-.0001	.0020	.0040	.2579	.2600	.2620
12	0.2836	0.0052	0.2888	-0.0001	0.0020	0.0040	0.2887	0.2908	0.2928

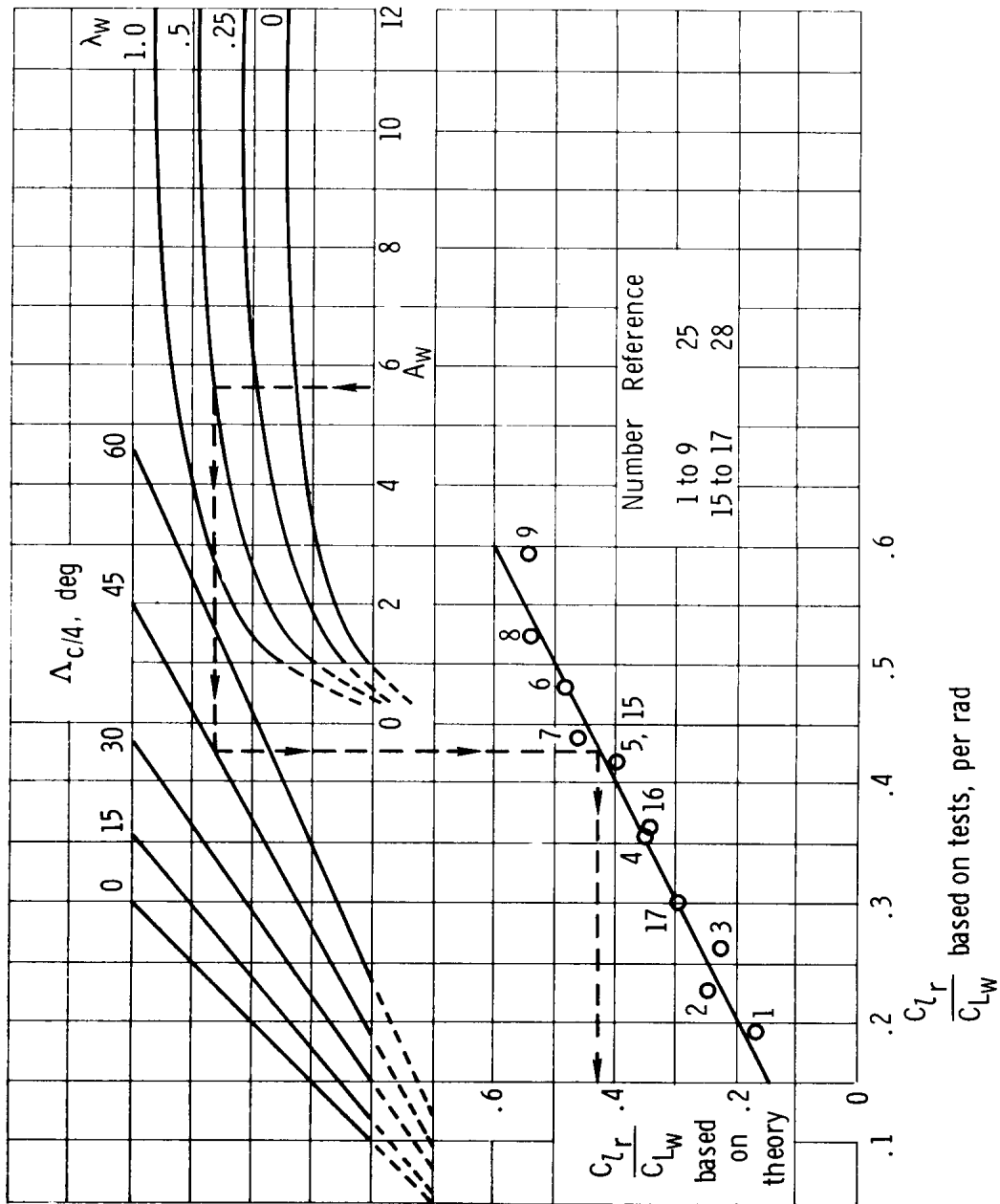


Figure 6.3.1-1. Wing yawing derivative, C_{l_r} , at incompressible speeds and zero dihedral (ref. 3).

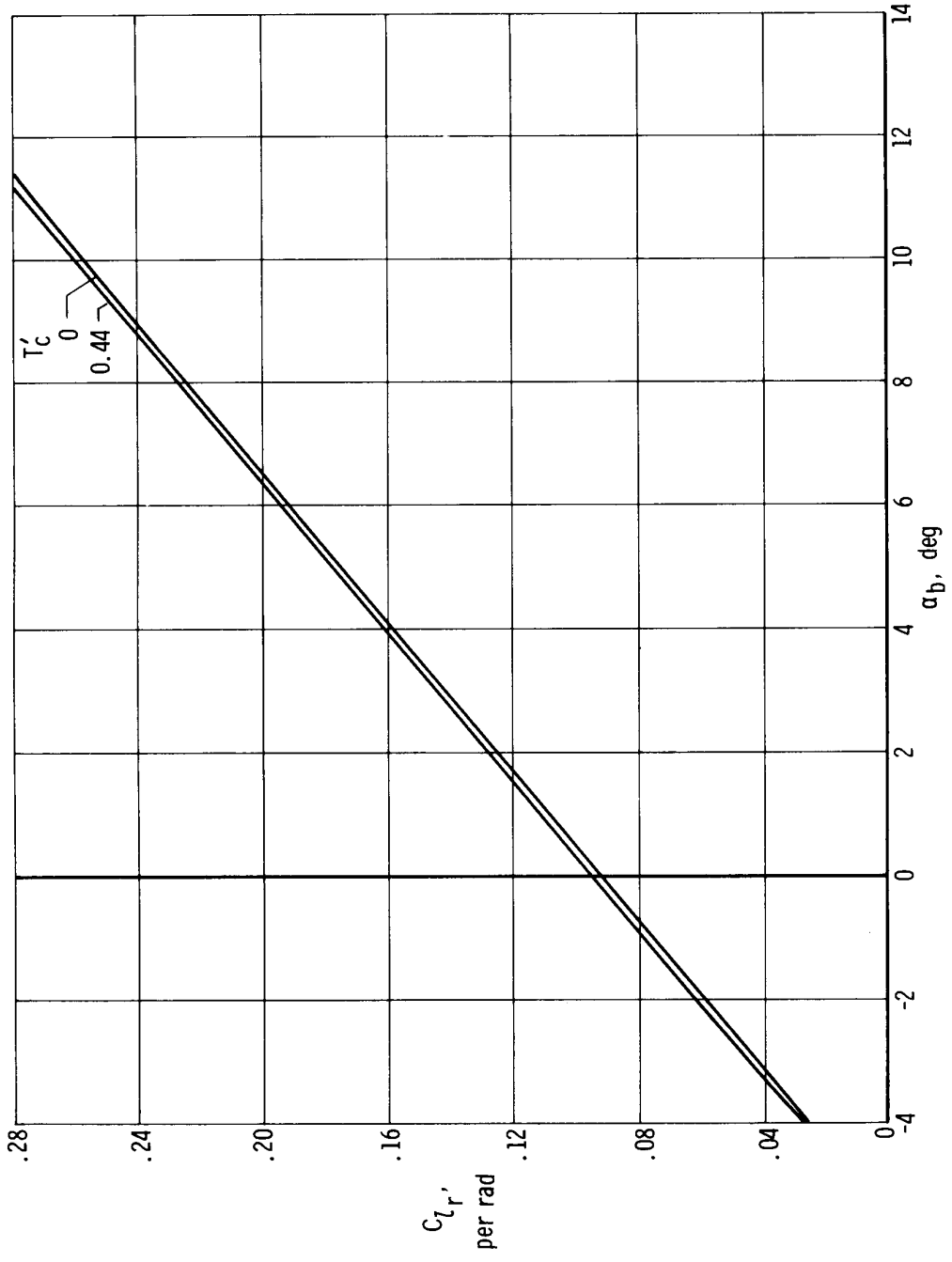


Figure 6.3.4-1. Variation of calculated C_{l_r}' derivative of the complete airplane with power and angle of attack.

6.4 Yaw-Due-to-Rolling Derivative, C_{np}

The wing and vertical tail are the only airplane surface components considered at this time since they are the only significant contributors to the derivative C_{np} . Power effects on C_{np} are not calculated because of the lack of suitable design information. On this basis,

$$C_{np} \approx (C_{np})_w + (C_{np})_v \quad (6.4-1)$$

6.4.1 Wing Contribution to C_{np}

The contributions of the wing to C_{np} are the result of antisymmetrical lift loading and induced drag due to rolling, and change in viscous drag due to roll-induced change in angle of attack. The contribution of antisymmetrical lift and induced drag is calculated by first considering the wing with zero dihedral and then adding the incremental effects of dihedral. The following equation summarizes the wing contribution to C_{np} :

$$(C_{np})_w = \left[\frac{(C_{np})_1}{C_{Lw}} \right]_{\Gamma=0} C_{Lw} + \left(\frac{\Delta C_{np}}{\Gamma} \right) \frac{\Gamma}{57.3} + \left(\frac{\Delta C_{np}}{\frac{\partial C_{D0}}{\partial \alpha}} \right) \frac{\partial C_{D0}}{\partial \alpha} \quad (6.4.1-1)$$

For low-speed and zero-dihedral conditions, the antisymmetrical lift and induced-drag contribution, $\left[\frac{(C_{np})_1}{C_{Lw}} \right]_{\Gamma=0}$, may be obtained from equation (6.4.1-2). The first

term in the equation was derived in reference 4. The second and third terms, which account for tip-suction effects, were derived in reference 30. The equation accounts for the longitudinal deviation of the airplane center of gravity from the aerodynamic center of the wing, \bar{x} (\bar{x} is positive when the aerodynamic center is aft of the center of gravity).

$$\left[\frac{(C_{np})_1}{C_{Lw}} \right]_{\Gamma=M=0} = \frac{A_w + 4}{A_w + 4 \cos \Lambda_c/4} \left[1 + 6 \left(1 + \frac{\cos \Lambda_c/4}{A_w} \right) \left(\frac{\bar{x}}{\bar{c}_w} - \frac{\tan \Lambda_c/4}{A_w} + \frac{\tan^2 \Lambda_c/4}{12} \right) \right] \left[\frac{(C_{np})_1}{C_{Lw}} \right]_{\Lambda_c/4=0} - \frac{1}{4A_w} \left(\tan \Lambda_c/4 + \frac{1}{A_w} \right) - \frac{1}{A_w^2} \frac{\bar{x}}{\bar{c}_w} \quad (6.4.1-2)$$

where $\left[\frac{(C_{np})_1}{C_{Lw}} \right]_{\Lambda_c/4=0}$ is obtained from figure 6.4.1-1.

Compressibility effects on the low-speed values of $\left[\frac{(C_{np})_1}{C_{Lw}} \right]_{\Gamma=0}$ are accounted for

by the following equation from reference 5:

$$\left[\frac{(C_{np})_1}{C_{Lw}} \right]_{\Gamma=0} = \left(\frac{A_w + 4 \cos \Lambda_c/4}{A_w B_2 + 4 \cos \Lambda_c/4} \right) \left[\frac{A_w B_2 + \frac{1}{2} (A_w B_2 + \cos \Lambda_c/4) \tan^2 \Lambda_c/4}{A_w + \frac{1}{2} (A_w + \cos \Lambda_c/4) \tan^2 \Lambda_c/4} \right] \left[\frac{(C_{np})_1}{C_{Lw}} \right]_{\Gamma=M=0} \quad (6.4.1-3)$$

where $B_2 = \sqrt{1 - M^2 \cos^2 \Lambda_c/4}$.

The incremental effect of dihedral angle, Γ , on C_{np} is accounted for by the following equation from reference 21:

$$\left(\frac{\Delta C_{np}}{\Gamma} \right) = - \left(\frac{\tan \Lambda_c/4}{4} + \frac{3}{A_w} \frac{\bar{x}}{\bar{c}_w} \right) (C_{l_p})_{\Gamma=0} \quad (6.4.1-4)$$

where $(C_{l_p})_{\Gamma=0}$ is obtained from section 6.1.1 with compressibility effects accounted for.

The incremental effect of viscous drag on C_{np} , the third term of equation (6.4.1-1), is approximately accounted for on a semiempirical basis by the following equation:

$$(\Delta C_{np})_{C'_{D0}} = \left(\frac{\Delta C_{np}}{\frac{\partial C'_{D0}}{\partial \alpha}} \right) \frac{\partial C'_{D0}}{\partial \alpha} \quad (6.4.1-5)$$

The parameter $\left(\frac{\Delta C_{np}}{\frac{\partial C'_{D0}}{\partial \alpha}} \right)$ is obtained from figure 6.4.1-2, which was empirically

determined from experimental model data in reference 30.

The rate of change of viscous drag with angle of attack, $\frac{\partial C'_{D0}}{\partial \alpha}$, may be obtained by calculating the viscous drag by the method given in section 4.12.4 of reference 1 as a function of angle of attack and obtaining the slopes from the plotted results. In reference 1 the viscous drag is represented by $k_3 \Delta_w$ instead of by the term C'_{D0} used herein.

The importance of including the incremental effect of viscous drag on the predicted wing contribution to C_{np} is shown in figure 6.4.1-3 (from ref. 30). The figure shows the correlation between calculated and wind-tunnel-determined C_{np} as a function of angle of attack for several wings of different aspect ratios and sweepback. Inclusion of

the viscous drag term improved the correlation significantly at higher angles of attack in practically all instances.

The calculated contributions of the subject airplane wing to C_{np} are summarized in tables 6.4.1-1(a) to 6.4.1-1(e) as a function of airplane angle of attack.

In table 6.4.1-1(c), the value of $(C_l p)_{\Gamma=0}$ used in determining the increment of C_{np} due to dihedral was obtained from column 6 of table 6.1.1-1. The results in this column were actually calculated with dihedral and body interference accounted for; however, the dihedral and body-interference effects were both negligible.

In table 6.4.1-1(d), the rate of change of viscous drag with angle of attack, $\frac{\partial C'_D}{\partial \alpha}$, was obtained by measuring the slope of the viscous drag curve in figure 6.4.1-4. The figure is based on columns 1 and 8 in table 4.12.4-1(b) of reference 1.

The summary of wing contributions to C_{np} in table 6.4.1-1(e) shows the contribution due to dihedral to be negligible. The viscous drag contribution, however, becomes more important with increasing angle of attack.

6.4.2 Vertical-Tail Contribution to C_{np}

The vertical-tail contribution to C_{np} is accounted for by the following equation, which takes into consideration the sidewash on the tail due to roll, $\frac{\partial \sigma}{\partial \frac{pb_w}{2V}}$:

$$(C_{np})_v = -57.3 (C'_{L\alpha})_v \left(\frac{l_v \cos \alpha_b - z_v \sin \alpha_b}{b_w} \right) \left[\frac{2(z_v \cos \alpha_b + l_v \sin \alpha_b)}{b_w} + \frac{\partial \sigma}{\partial \frac{pb_w}{2V}} \right] \quad (6.4.2-1)$$

The calculations for the vertical-tail contribution to C_{np} of the subject airplane are summarized in table 6.4.2-1.

6.4.3 Power Contributions to C_{np}

For a single-engine, propeller-driven airplane, the effects of power on the contribution of the vertical tail to C_{np} would be difficult to determine because of the lack of general design procedures accounting for this power effect and the scarcity of wind-tunnel data for similar geometric configurations. The effect of power on the wing contribution would be small.

For a twin-engine airplane like the subject airplane, the effect of power on the vertical-tail contribution is considered to be negligible. The effect of power on the

wing contribution is primarily the result of change in the induced drag of the portions of the wing immersed in the propeller slipstream due to roll-induced change in angle of attack. On the basis of section 5.3 of reference 1, it appears that the induced drag is affected by the proportions and location of the nacelles. Because of the uncertain magnitude of the changes in induced drag due to roll-induced change in angle of attack, no attempt is made to account for power effects on the wing contribution to C_{n_p} .

6.4.4 Summary of Contributions to C_{n_p}

The calculated net C_{n_p} of the subject airplane is listed in table 6.4.4-1 as a function of angle of attack on the basis of wing and vertical-tail contributions. The results are also plotted in figure 6.4.4-1. Although the wing is the major contributor to the derivative, the contribution of the vertical tail is appreciable.

Lack of appropriate wind-tunnel data precludes a comparison to assess the validity of the calculations.

6.4.5 Symbols

A_w	wing aspect ratio
ac_w	aerodynamic center of the wing as a fraction of the wing mean aerodynamic chord
$B_2 = (1 - M^2 \cos^2 \Lambda_c / 4)^{1/2}$	
b_w	wing span, in.
C'_D_0	viscous drag coefficient of the wing
$\frac{\partial C'_D_0}{\partial \alpha}$	variation of C'_D_0 with angle of attack, per deg
C_{L_w}	wing-lift coefficient for propeller-off conditions
$(C'_{L_\alpha})_v$	effective lift-curve slope of the vertical tail based on the wing area, per deg
C_l	rolling-moment coefficient
$C_{l_p} = \frac{\partial C_l}{\partial \frac{pb_w}{2V}}$	
$(C_{l_p})_{\Gamma=0}$	wing contribution to C_{l_p} at zero dihedral and propeller-off conditions

C_n

yawing-moment coefficient

$$C_{np} = \frac{\partial C_n}{\partial \left(\frac{pb_w}{2V} \right)}, \text{ per rad}$$

$(C_{np})_v$ vertical-tail contribution to C_{np}

$(C_{np})_w$ wing contribution to C_{np}

$(C_{np})_{1\Gamma=0}$ antisymmetric lift contribution of the wing, due to the roll rate, to $(C_{np})_w$ at zero dihedral and propeller-off conditions

$\left[\frac{(C_{np})_1}{C_{Lw}} \right]_{\Gamma=0}$ rate of change of $(C_{np})_{1\Gamma=0}$ with the wing C_{Lw}

$\left[\frac{(C_{np})_1}{C_{Lw}} \right]_{\Gamma=M=0}$ rate of change of $(C_{np})_{1\Gamma=0}$ with C_{Lw} at incompressible flow conditions ($M \approx 0$)

$\left[\frac{(C_{np})_1}{C_{Lw}} \right]_{\Lambda c/4=0}$ incompressible flow antisymmetric lift contribution of the wing, due to the roll rate, to $(C_{np})_w$ at zero sweep of the quarter-chord line, zero dihedral, and propeller-off conditions per unit change in C_{Lw}

$(\Delta C_{np})_{C'_D 0}$ increment of $(C_{np})_w$ due to $C'_D 0$

$(\Delta C_{np})_\Gamma$ increment of $(C_{np})_w$ due to the wing dihedral

$\frac{\Delta C_{np}}{\Gamma}$ rate of change of the increment of $(C_{np})_w$, due to the wing dihedral, with the wing dihedral angle, per rad

$\frac{\Delta C_{np}}{\left(\frac{\partial C'_D 0}{\partial \alpha} \right)}$ rate of change of the increment of $(C_{np})_w$, due to viscous drag, with $\frac{\partial C'_D 0}{\partial \alpha}$

\bar{c}_w	wing mean aerodynamic chord, in.
$k_3 \Delta_w = C'_D 0$	
l_v	distance parallel to the X-body axis from the center of gravity to the quarter chord of the vertical-tail mean aerodynamic chord, in.
M	Mach number
p	roll rate, rad/sec
S_w	wing area, sq ft
V	airspeed, ft/sec
\bar{x}	distance parallel to the wing mean aerodynamic chord from the center of gravity to the wing aerodynamic center, in.
z_v	vertical distance parallel to the Z-body axis from the center of gravity to the vertical-tail mean aerodynamic chord, positive down, in.
α_b	angle of attack relative to the X-body axis, deg
Γ	wing dihedral angle, deg
$\Lambda_c/4$	sweep of the wing quarter-chord line, deg
λ_w	wing taper ratio
$\frac{\partial \sigma}{\partial \left(\frac{pb_w}{2V} \right)}$	rate of change of the sidewash on the vertical tail (induced by the wing roll rate) with $\frac{pb_w}{2V}$

TABLE 6.4.1-1
WING CONTRIBUTIONS TO C_{n_p}

(a) Basic parameters

Symbol	Description	Reference	Magnitude
M	Mach number	As selected	0.083
B_2	$\sqrt{1 - M^2 \cos^2 \Lambda_c/4}$	-----	.997
A_w	Wing aspect ratio	Figure 3.2-1	7.5
λ_w	Wing taper ratio	Figure 3.2-1	.513
$\Lambda_c/4$	Sweep of wing quarter-chord line, deg	Figure 3.2-1	-2.5
b_w	Wing span, in.	Figure 3.2-1	432
\bar{c}_w	Wing mean aerodynamic chord, in.	Figure 3.2-1	59.5
\bar{x}	ac_w - center of gravity	Figure 3.2-1	$0.15\bar{c}_w$
$\left[\frac{(C_{n_p})_1}{C_{L_w}} \right]_{\Gamma=0}$	-----	Figure 6.4.1-1	-0.061
Γ	Wing dihedral, deg	Figure 3.2-1	5

(b) Antisymmetrical-lift and induced-drag contribution, $\Gamma = 0$

$$(C_{n_p})_{1\Gamma=0} = -0.06631 C_{L_w} \text{ (based on eqs. (6.4.1-2) and (6.4.1-3))}$$

(1)	(2)	(3)
---	Figure 4.1.1-1	-----
α_b , deg	C_{L_w}	$(C_{n_p})_{1\Gamma=0} = -0.06631(2)$
-4	0	0
-2	.145	-.0096
0	0.292	-.0194
2	.437	-.0289
4	0.584	-.0387
6	.730	-.0484
8	0.875	-.0580
10	1.023	-.0678
12	1.160	-.0769

TABLE 6.4.1-1 (Continued)

(c) Incremental effect of dihedral on C_{n_p}

$$\begin{aligned} (\Delta C_{n_p})_\Gamma &= \frac{\Gamma}{57.3} \left(\frac{\Delta C_{n_p}}{\Gamma} \right) = -\frac{\Gamma}{57.3} \left(\frac{\tan \Lambda_c/4}{4} + \frac{3}{A_w} \frac{\bar{x}}{\bar{c}_w} \right) (C_{l_p})_{\Gamma=0} \\ &= -0.00428 (C_{l_p})_{\Gamma=0} \end{aligned}$$

(1)	(2)	(3)
---	Table 6.1.1-1, column 6	-----
α_b , deg	$(C_{l_p})_{\Gamma=0}$	$(\Delta C_{n_p})_\Gamma = -0.00428(2)$
-4	-0.4622	0.00198
-2	-.4623	.00198
0	-0.4626	0.00198
2	-.4632	.00198
4	-0.4640	0.00199
6	-.4650	.00199
8	-0.4662	0.00200
10	-.4677	.00200
12	-0.4172	0.00179

(d) Incremental effect of viscous drag on C_{n_p}

$$(\Delta C_{n_p})_{C'_D} = \left(\frac{\Delta C_{n_p}}{\frac{\partial C'_D}{\partial \alpha}} \right) \frac{\partial C'_D}{\partial \alpha}$$

(1)	(2)	(3)	(4)
---	Figure 6.4.1-2	Figure 6.4.1-4	-----
α_b , deg	$\frac{\Delta C_{n_p}}{\frac{\partial C'_D}{\partial \alpha}}$	$\frac{\partial C'_D}{\partial \alpha}$	$(\Delta C_{n_p})_{C'_D} = (2)(3)$
-4	≈ 2.5	0	0
-2	≈ 2.5	0	0
0	≈ 2.5	0.00047	0.00118
2	≈ 2.5	.00160	.00400
4	≈ 2.5	0.00326	0.00815
6	≈ 2.5	.00445	.01112
8	≈ 2.5	0.00520	0.01300
10	≈ 2.5	.00800	.02000
12	≈ 2.5	0.00960	0.02400

TABLE 6.4.1-1 (Concluded)

(e) Summary of wing contributions to C_{np}

$$(C_{np})_w = (C_{np})_{1\Gamma=0} + (\Delta C_{np})_\Gamma + (\Delta C_{np})_{C'_{D0}}$$

①	②	③	④	⑤
---	Table 6.4.1-1(b)	Table 6.4.1-1(c)	Table 6.4.1-1(d)	---
α_b , deg	$(C_{np})_{1\Gamma=0}$	$(\Delta C_{np})_\Gamma$	$(\Delta C_{np})_{C'_{D0}}$	$(C_{np})_w = ② + ③ + ④$
-4	0	0.00198	0	0.0020
-2	-.0096	.00198	0	-.0076
0	-.0194	0.00198	0.00118	-.0162
2	-.0289	.00198	.00400	-.0229
4	-.0387	0.00199	0.00815	-.0286
6	-.0484	.00199	.01112	-.0353
8	-.0580	0.00200	0.01300	-.0430
10	-.0678	.00200	.02000	-.0458
12	-.0769	0.00179	0.02400	-.0511

TABLE 6.4.2-1
VERTICAL-TAIL CONTRIBUTION TO C_{n_p}

$$\left(C_{n_p}\right)_v = -57.3 \left(C'_{L_\alpha}\right)_v \left(\frac{l_v \cos \alpha_b - z_v \sin \alpha_b}{b_w} \right) \left[\frac{2(z_v \cos \alpha_b + l_v \sin \alpha_b)}{b_w} + \frac{\frac{\partial \sigma}{\partial \frac{pb_w}{2V}}}{\frac{pb_w}{2V}} \right]$$

Symbol	Description	Reference	Magnitude
$\left(C'_{L_\alpha}\right)_v$	Effective lift-curve slope of vertical tail referred to $S_w = 178$ sq ft, per deg	Table 4.5.1-1	0.00464
l_v	Distance parallel to X-body axis from center of gravity to quarter-chord line of vertical-tail mean aerodynamic chord (positive back), in.	Figure 3.2-4	164.9
z_v	Vertical distance parallel to Z-body axis from center of gravity to tail mean aerodynamic chord (positive down), in.	Figure 3.2-4	-45.9
b_w	Wing span, in.	Figure 3.2-1	432
$\frac{\partial \sigma}{\partial \frac{pb_w}{2V}}$	Sidewash factor to account for effect of rolling wing on tail	Reference 24	0.20
Summary: $\left(C_{n_p}\right)_v = -0.5317(0.3817 \cos \alpha_b + 0.10625 \sin \alpha_b)(-0.10625 \cos \alpha_b + 0.3817 \sin \alpha_b + 0.10)$			

(1)	(2)	(3)	(4)	(5)	(6)
α_b , deg	$\cos \alpha_b$	$\sin \alpha_b$	$0.3817(2) + 0.10625(3)$	$-0.10625(2) + 0.3817(3) + 0.10$	$\left(C_{n_p}\right)_v = -0.5317(4)(5)$
-4	0.9976	-0.0698	0.37337	-0.03264	0.00648
-2	.9994	-.0349	.37776	-.01951	.00392
0	1.0000	0	0.38170	-.00625	0.00127
2	.9994	.0349	.38518	.00714	-.00146
4	0.9976	0.0698	0.38820	0.02065	-0.00426
6	.9945	.1045	.39070	.03422	-.00711
8	0.9903	0.1392	0.39279	0.04791	-0.01001
10	.9848	.1736	.39434	.06163	-.01292
12	0.9782	0.2079	0.39547	0.07542	-0.01586

TABLE 6.4.4-1
SUMMARY OF CONTRIBUTIONS TO C_{np}

$$C_{np} = (C_{np})_w + (C_{np})_v$$

(1)	(2)	(3)	(4)
---	Table 6.4.1-1(e)	Table 6.4.2-1	-----
α_b , deg	$(C_{np})_w$	$(C_{np})_v$	$C_{np} = \textcircled{2} + \textcircled{3}$
-4	0.0020	0.00648	0.00848
-2	-.0076	.00392	-.00368
0	-0.0162	0.00127	-0.01493
2	-.0229	-.00146	-.02436
4	-0.0286	-0.00426	-0.03286
6	-.0353	-.00711	-.04241
8	-0.0430	-0.01001	-0.05301
10	-.0458	-.01292	-.05872
12	-0.0511	-0.01586	-0.06696

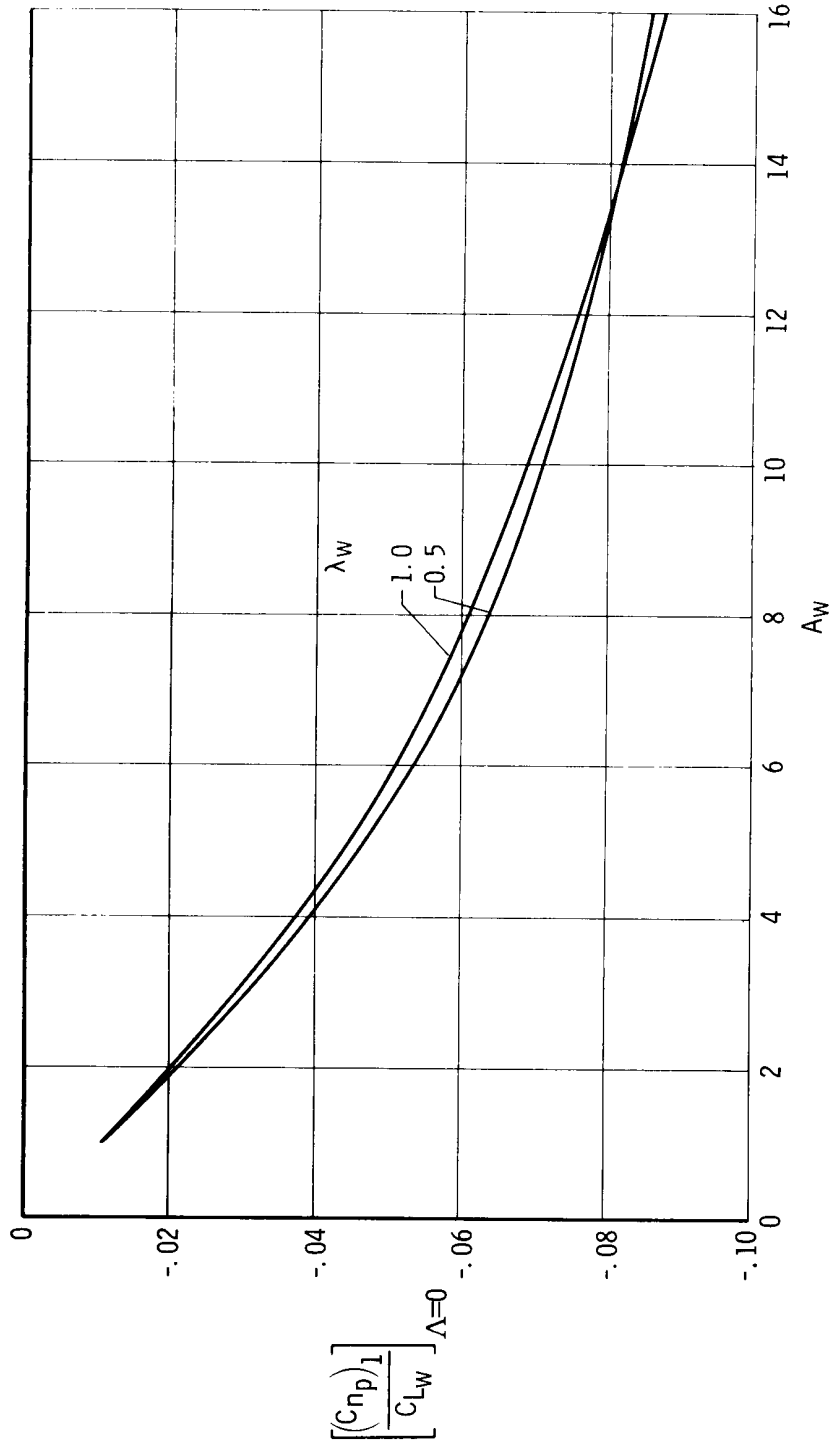


Figure 6.4. 1-1. Low-speed C_{np} of an unswept wing, as a ratio of C_{Lw} , due to antisymmetrical lift and induced drag with tip-suction effects not accounted for (from ref. 4).

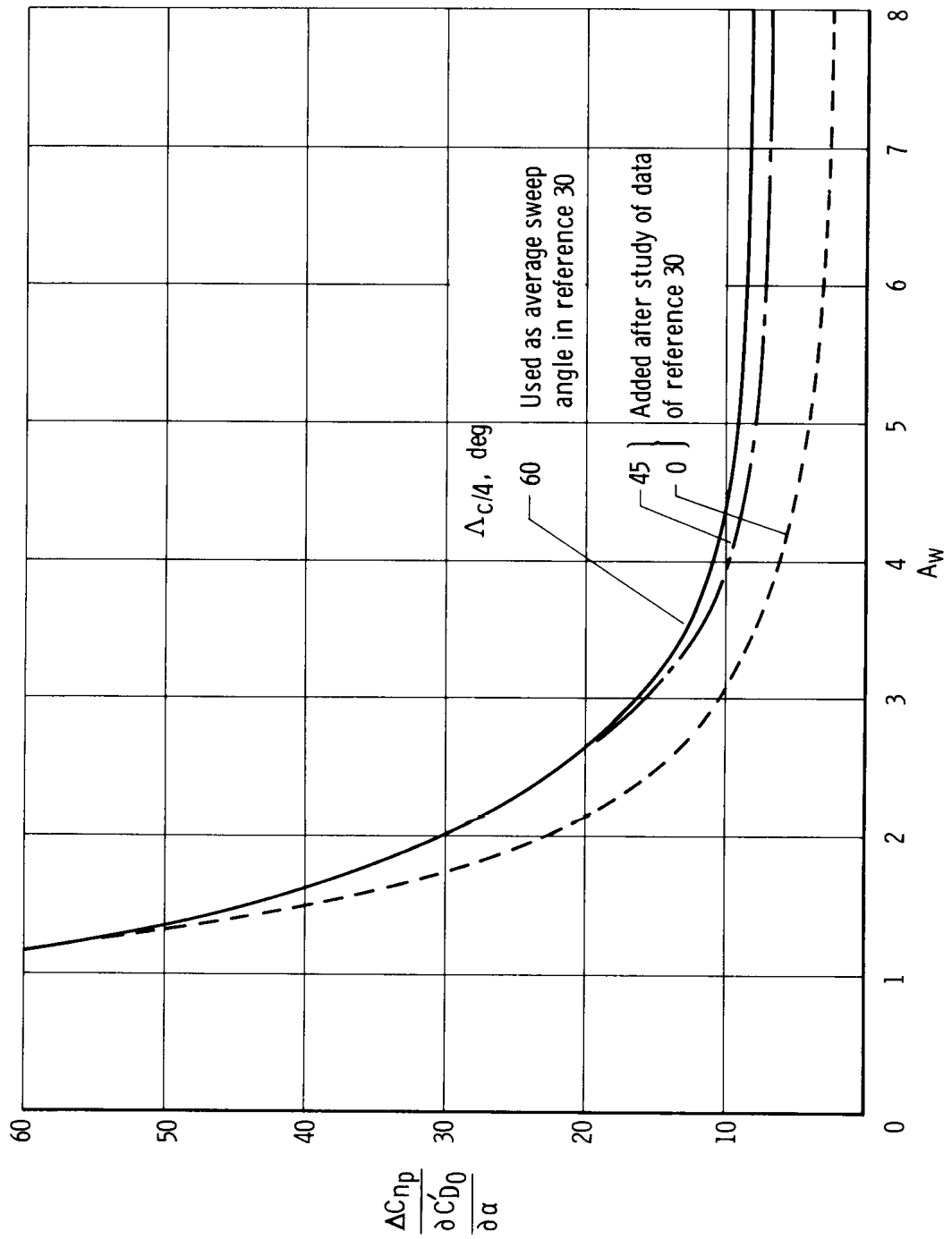


Figure 6.4.1-2. Variation of $\frac{\Delta C_{n_p}}{\partial C'_D \partial \alpha}$ with aspect ratio (from ref. 30).

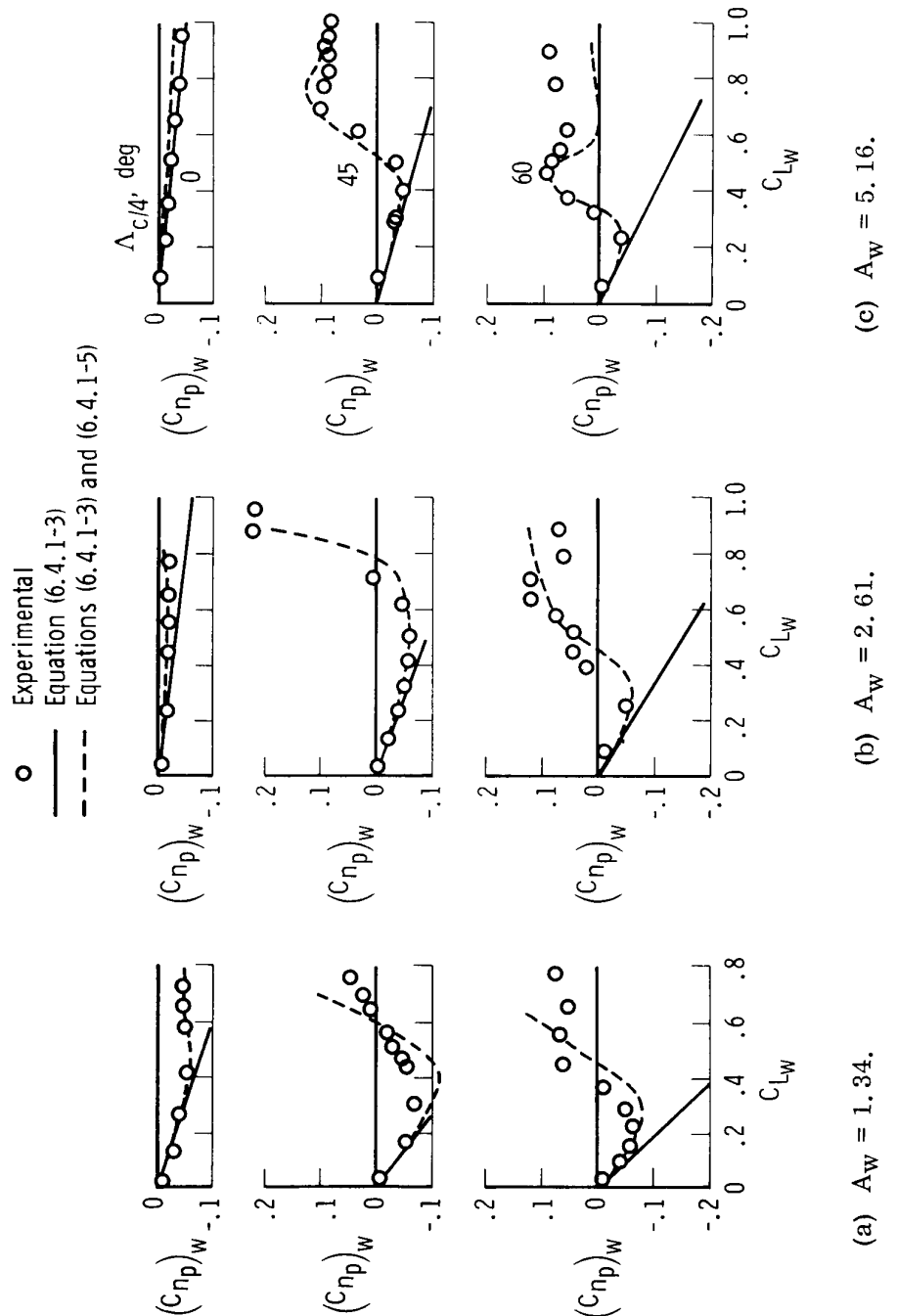


Figure 6.4.1-3. Variation of the experimental and calculated values of $(C_{np})_w$ with lift coefficient for a series of swept wings (from ref. 30).

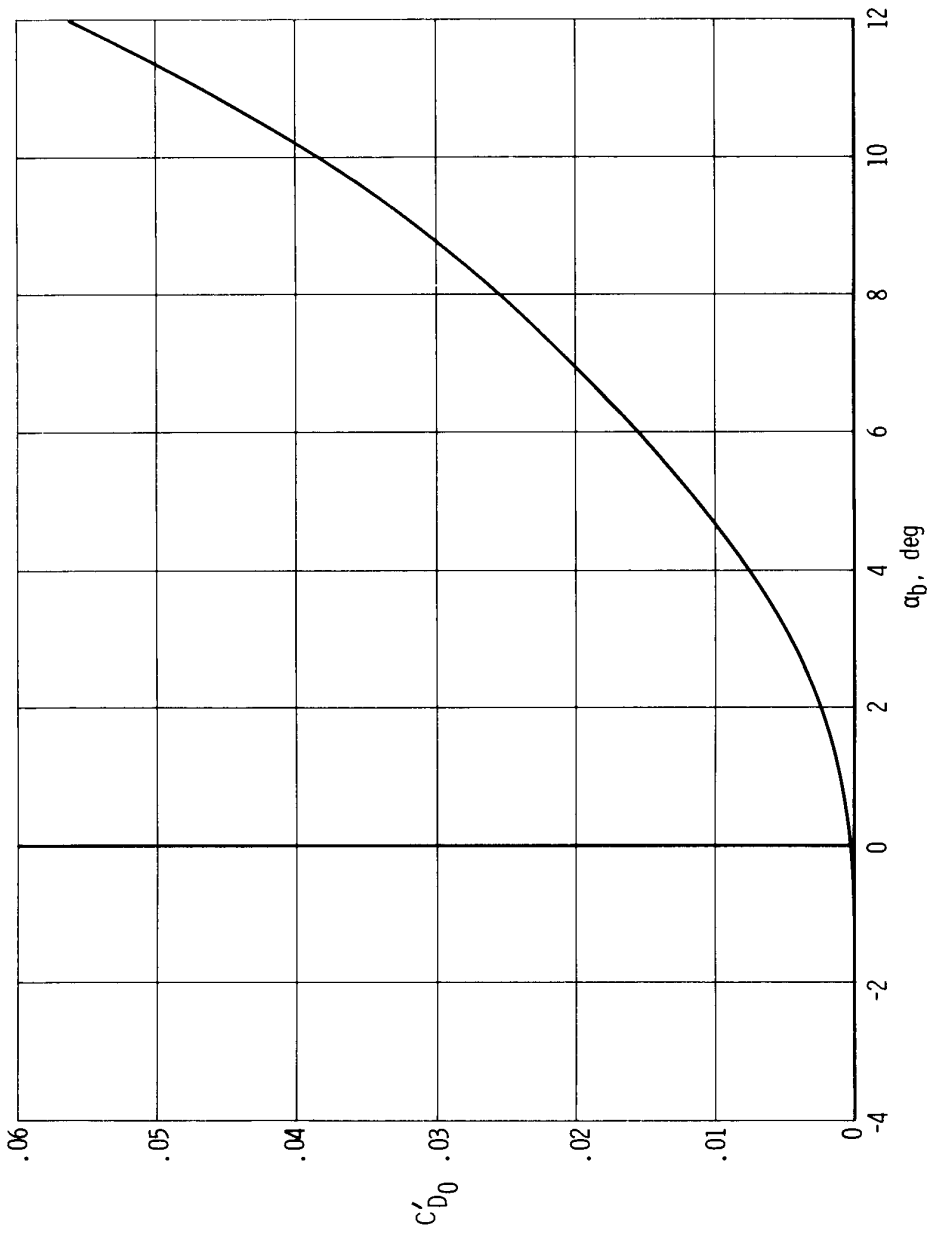


Figure 6.4.1-4. Calculated variation of viscous drag of subject airplane wing with angle of attack (from column 8 of table 4.12.4-1(b) of reference 1, with $S_W = 178$ sq ft).

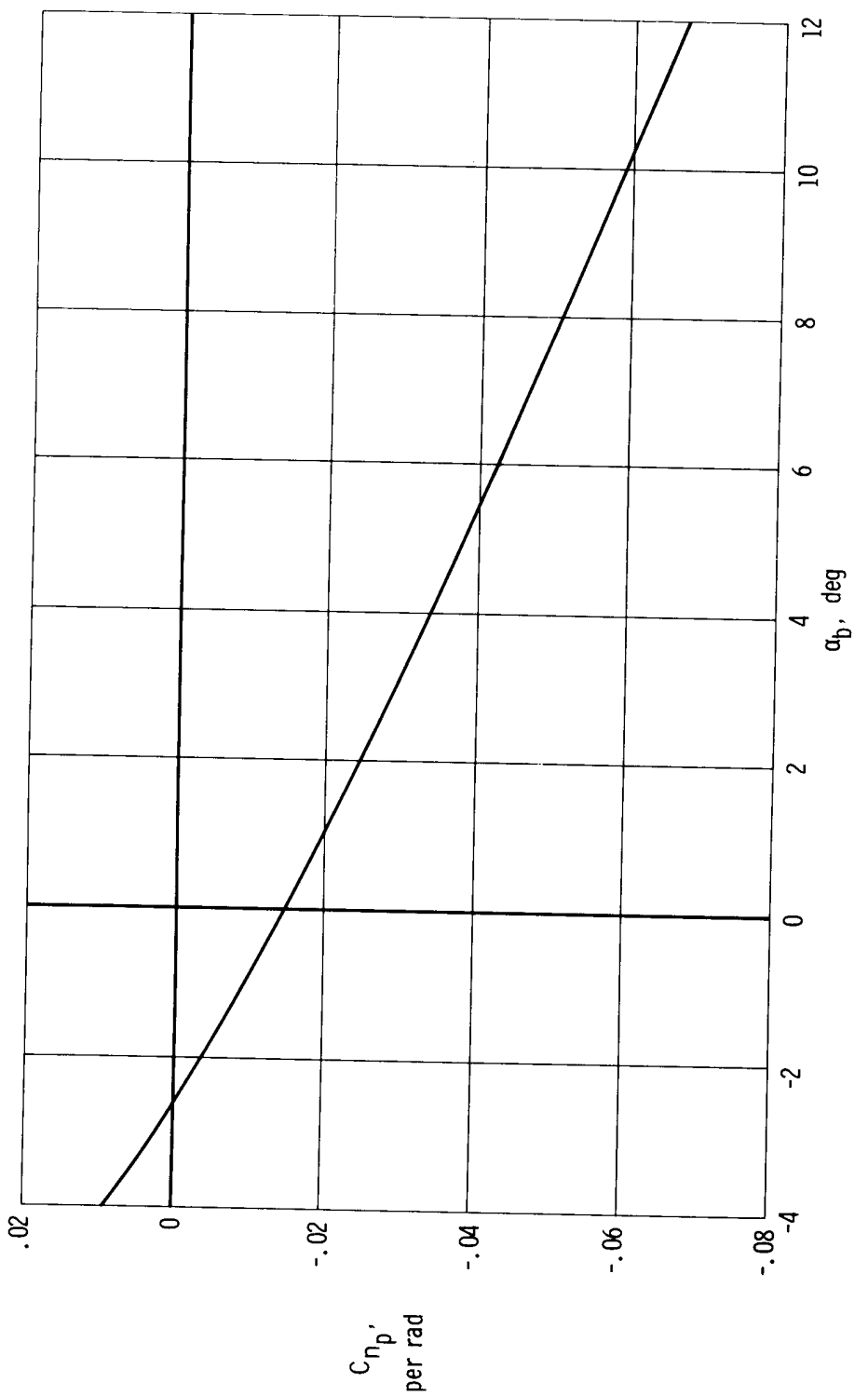


Figure 6.4.4-1. Calculated variation of C_{np} with angle of attack.

6.5 The Derivatives $C_{n\dot{\beta}}$ and $C_{l\dot{\beta}}$

The derivatives $C_{n\dot{\beta}}$ and $C_{l\dot{\beta}}$ are the result of lag in the sidewash effects that act on the vertical tail during the rate of change of sideslip with time.

If a pure sideslipping motion is considered, the effective angle of attack of the vertical tail is composed of a geometric sideslip angle, β , and an induced angle, σ . This effective angle of attack of the vertical tail during sideslip (involving time-varying sideslip) may be written as

$$\alpha_v = \beta + \frac{\partial \sigma}{\partial \beta} (\beta - \dot{\beta} \tau) \text{ in degrees} \quad (6.5-1)$$

The second term accounts for the effects of sidewash on the vertical tail with a time lag in change of sideslip at the vertical tail taken into account. The time lag, τ , is equal to $\frac{l_t}{V}$.

Regrouping equation (6.5-1) and substituting $\frac{l_t}{V}$ for τ ,

$$\alpha_v = \beta \left(1 + \frac{\partial \sigma}{\partial \beta} \right) + \dot{\beta} \left(-\frac{\partial \sigma}{\partial \beta} \frac{l_t}{V} \right) \text{ in degrees} \quad (6.5-2)$$

The first term is the effective angle of attack of the vertical tail as used in equation (4.1.4-5) to obtain the vertical-tail contribution to $C_{Y\beta}$; namely,

$$(C_{Y\beta})_v = -k'_1 (C_{L\alpha})_v \left(1 + \frac{\partial \sigma}{\partial \beta} \right) \frac{\bar{q}_v}{\bar{q}_\infty} \frac{S_v}{S_w} \text{ per degree} \quad (4.1.4-5)$$

Using the second term of equation (6.5-2), the derivative of C_Y with respect to $\dot{\beta} b_w / 2V$ can readily be shown to be

$$\begin{aligned} C_{Y\dot{\beta}} &= 114.6 k'_1 (C_{L\alpha})_v \frac{\partial \sigma}{\partial \beta} \frac{\bar{q}_v}{\bar{q}_\infty} \frac{S_v}{S_w} \left(\frac{l_v \cos \alpha_b - z_v \sin \alpha_b}{b_w} \right) \\ &= 114.6 \left(C'_{L\alpha} \right)_v \frac{\partial \sigma}{\partial \beta} \left(\frac{l_v \cos \alpha_b - z_v \sin \alpha_b}{b_w} \right) \text{ per radian} \end{aligned} \quad (6.5-3)$$

where

$$(C'_{L\alpha})_v = k'_1 (C_{L\alpha})_v \frac{\bar{q}_v}{\bar{q}_\infty} \frac{S_v}{S_w} \text{ per degree (eq. (4.5.1-2))}$$

k'_1 is a factor accounting for the body size relative to the vertical-tail size, obtained from figure 4.1, 4-1(d)

$(C_{L\alpha})_v'$ is the lift-curve slope of the vertical tail, per degree, based on the effective aspect ratio of the vertical tail, obtained from equation (4.1.4-2), referenced to the tail area, S_v , and a dynamic-pressure ratio of 1.0

$\frac{\bar{q}_v}{\bar{q}_\infty}$ is the dynamic-pressure ratio of the vertical tail (assumed to be 1.0 for twin-engine airplanes)

l_v, z_v are the distances from the center of gravity to the quarter chord of the vertical-tail mean aerodynamic chord parallel to the X-body axis and Z-body axis, respectively (z_v , positive down)

$\frac{\partial \sigma}{\partial \beta}$ is estimated from equation (4.1.4-6) assuming $\frac{\bar{q}_v}{\bar{q}_\infty} = 1.0$

On the basis of the expression for $C_{Y\beta}'$ given by equation (6.5-3), the following equations were obtained for $C_{n\beta}'$ and $C_{l\beta}'$:

$$C_{n\beta}' = -114.6 (C'_{L\alpha})_v \frac{\partial \sigma}{\partial \beta} \left(\frac{l_v \cos \alpha_b - z_v \sin \alpha_b}{b_w} \right)^2 \text{ per radian} \quad (6.5-4)$$

$$C_{l\beta}' = -114.6 (C'_{L\alpha})_v \frac{\partial \sigma}{\partial \beta} \left(\frac{l_v \cos \alpha_b - z_v \sin \alpha_b}{b_w} \right) \left(\frac{z_v \cos \alpha_b + l_v \sin \alpha_b}{b_w} \right) \text{ per radian} \quad (6.5-5)$$

The magnitude of these derivatives, and therefore their significance in the equations of motion, is reflected in the magnitude of the sidewash factor, $\frac{\partial \sigma}{\partial \beta}$. Equation (4.1.4-6) shows the sidewash factor to be primarily a function of the vertical position of the wing on the fuselage and of wing sweep. Because the equation is empirical and based on the sidewash at low angles of attack, it does not take into account the large changes in the sidewash factor which can take place at higher angles of attack. Such large changes are shown in figure 4.1.4-2.

The derivative $C_{n\beta}'$ is pertinent in the damping of the Dutch roll mode (lateral-directional transient oscillations). Normally, $\dot{\beta}$ is approximately 180° out of phase with yaw rate, r , in the Dutch roll mode. As a result, $C_{n\beta}'$ can be combined with C_{n_r} to provide an effective Dutch roll damping-in-yaw derivative, $\left(C_{n_r} - \frac{|\beta|}{|r|} C_{n\beta}' \right)$. This derivative is obtained from

$$C_{n_r} \frac{rb_w}{2V} + C_{n_{\dot{\beta}}} \frac{\dot{\beta}b_w}{2V} \approx \left(C_{n_r} - \frac{|\dot{\beta}|}{|r|} C_{n_{\dot{\beta}}} \right) \frac{rb_w}{2V} \quad (6.5-6)$$

When results of wind-tunnel investigations of damping in yaw are reported in the form $(C_{n_r} - C_{n_{\dot{\beta}}})$, it is implied that the tests were conducted about the stability axes, using oscillating model techniques in which $\psi = -\beta$ and in which the amplitude ratio, $\frac{|\dot{\beta}|}{|r|}$, is therefore equal to 1.0.

In flight-test investigations of the Dutch roll mode, in which the derivatives are commonly referred to the body system of axes, the amplitude ratio, $\frac{|\dot{\beta}|}{|r|}$, is similar to 1.0 at low angles of attack and decreases with increasing angle of attack. It is not practical to attempt to obtain flight-determined $C_{n_{\dot{\beta}}}$ by itself because of the approximate 180° phase relationship of $\dot{\beta}$ with r , so in reducing the flight data the combined effective derivative $(C_{n_r} - \frac{|\dot{\beta}|}{|r|} C_{n_{\dot{\beta}}})$ is used.

The preceding remarks about C_{n_r} and $C_{n_{\dot{\beta}}}$ are also pertinent to $(C_l_r$ and $C_{l_{\dot{\beta}}})$.

No attempt was made to calculate $C_{n_{\dot{\beta}}}$ and $C_{l_{\dot{\beta}}}$ for the subject airplane: for this airplane $\frac{\partial \sigma}{\partial \beta}$ is of the order of 0.02, which indicates that these derivations are negligible.

6.5.1 Symbols

b_w wing span, in. or ft

$(C_{L_{\alpha}})_v$ lift-curve slope of the vertical tail, based on the effective aspect ratio of the tail (obtained from eq. (4.1.4-2)), referenced to the tail area and a dynamic-pressure ratio of 1.0, per deg

$(C'_{L_{\alpha}})_v$ effective lift-curve slope of the vertical tail (obtained from eq. (4.5.1-2)), referenced to the wing area and the dynamic pressure at the tail, per deg

C_l rolling-moment coefficient

$$C_{l_r} = \frac{\partial C_l}{\partial \left(\frac{rb_w}{2V} \right)}, \text{ per rad}$$

$$C_{l_{\dot{\beta}}} = \frac{\partial C_l}{\partial \left(\frac{\dot{\beta}b_w}{2V} \right)}, \text{ per rad}$$

C_n	yawing-moment coefficient
$C_{n_r} = \frac{\partial C_n}{\partial \left(\frac{rb_w}{2V} \right)}$, per rad	
$C_{n_\beta} = \frac{\partial C_n}{\partial \left(\frac{\dot{\beta} b_w}{2V} \right)}$, per rad	
C_Y	side-force coefficient
$C_{Y_\beta} = \frac{\partial C_Y}{\partial \beta}$, per deg	
$(C_{Y_\beta})_v$	vertical-tail contribution to C_{Y_β} , per deg
$C_{Y_\dot{\beta}} = \frac{\partial C_Y}{\partial \left(\frac{\dot{\beta} b_w}{2V} \right)}$, per rad	
k'_1	factor accounting for the body size relative to the vertical-tail size, obtained from figure 4.1.4-1(d)
$l_t = l_v \cos \alpha_b - z_v \sin \alpha_b$, in. or ft	
l_v	distance parallel to the X-body axis from the center of gravity to the quarter chord of the vertical-tail mean aerodynamic chord, in. or ft
\bar{q}_v	dynamic pressure at the vertical tail, lb/sq ft
\bar{q}_∞	free-stream dynamic pressure, lb/sq ft
r	yaw rate, rad/sec
S_v, S_w	vertical-tail and wing area, respectively, sq ft
t	time, sec
V	free-stream velocity, ft/sec
z_v	distance parallel to the Z-body axis from the center of gravity to the vertical-tail mean aerodynamic chord, in.
α_b	angle of attack, deg

α_v	angle of attack of the vertical tail, deg
β	sideslip angle, deg or rad
$\dot{\beta} = \frac{\partial \beta}{\partial t}$, rad/sec	
$\frac{ \beta }{ r }, \frac{ \dot{\beta} }{ r }$	amplitude ratio of the sideslip vector and rate-of-sideslip vector to the yaw-rate vector, respectively, in the Dutch roll oscillation
σ	induced-sidewash angle at the vertical tail, deg
$\frac{\partial \sigma}{\partial \beta}$	rate of change of σ with β , deg/deg
τ	time lag, $\frac{l_t}{V}$, sec
$\psi = \int r dt$	

6.6 Comparison of Predicted Dynamic Derivatives With Flight Data

In the absence of dynamic wind-tunnel data, the calculated dynamic derivatives $C_{l_r} - \frac{|\dot{\beta}|}{|r|} C_{l\dot{\beta}}$ and $C_{n_r} - \frac{|\dot{\beta}|}{|r|} C_{n\dot{\beta}}$ are compared with flight data for validation. No attempt is made to compare calculated C_{l_p} and C_{n_p} with the flight data for reasons stated in section 6.6.1. The flight data were analyzed with techniques suitable for use at a desk.

Heretofore the calculated derivatives have been referenced to the stability system of axes. In comparing the predictions with flight results (referenced to the body system of axes), the predicted derivatives are referenced to the body system of axes to conform with the flight data. Table 5.3-1 lists a complete set of transformation equations to reorient the predicted characteristics from stability to body axes.

6.6.1 Analysis of Flight Data

The magnitude of C_{n_p} is generally small in comparison to the magnitudes of the other yawing-moment derivatives, so it is difficult to extract reasonably accurate values from flight data. As a result, no attempt was made to obtain flight values of C_{n_p} to validate the calculated values.

The derivatives $C_{l_r} - \frac{|\dot{\beta}|}{|r|} C_{l\dot{\beta}}$ and $C_{n_r} - \frac{|\dot{\beta}|}{|r|} C_{n\dot{\beta}}$ were obtained from graphical time-vector analysis of the flight data (ref. 18), from which the static derivatives $C_{l\dot{\beta}}$ and $C_{n\dot{\beta}}$ were obtained concurrently. As pointed out in section 5.3.2(c), C_{l_r} is not normally solved for as an unknown quantity when the time-vector technique is used because its time-vector representation is small compared to the other derivatives in the rolling-moment equation. However, as explained in section 5.3.2(c), for the subject airplane the magnitude of the C_{l_r} vector and its orientation with respect to the other vectors in the graphical representation of the rolling-moment equation permitted the solution of $C_{l_r} - \frac{|\dot{\beta}|}{|r|} C_{l\dot{\beta}}$, as well as of $C_{l\dot{\beta}}$, in lieu of C_{l_p} .

The derivative C_{l_p} could not be obtained from the graphical time-vector solution of the rolling-moment equation because the roll rate, p , was approximately 180° out of phase with the sideslip, β . This phase relationship, coupled with an experimental uncertainty of approximately $\pm 10^\circ$ in phase angle, necessitated the use of the calculated values of either C_{l_p} or $C_{l\dot{\beta}}$ in the rolling-moment equation. Since C_{l_p} can be calculated to within 5 percent, the calculated value of C_{l_p} was used and $C_{l\dot{\beta}}$ and $C_{l_r} - \frac{|\dot{\beta}|}{|r|} C_{l\dot{\beta}}$ were solved for.

Although some consideration was given to obtaining flight values of C_{l_p} from the

one-degree-of-freedom roll-mode equation (eq. (7.2.2-5)), the equation was considered to be too approximate for critical comparison of calculated and flight values of C_{l_p} .

6.6.2 Comparison of Predicted and Flight-Determined Dynamic Derivatives

Figure 6.6.2-1 shows the degree of correlation between flight-determined and calculated $C_{l_r} - \frac{|\dot{\beta}|}{|r|} C_{l\dot{\beta}}$ and $C_{n_r} - \frac{|\dot{\beta}|}{|r|} C_{n\dot{\beta}}$ as a function of angle of attack for level-flight conditions. The flight-determined derivative, $C_{l_r} - \frac{|\dot{\beta}|}{|r|} C_{l\dot{\beta}}$, shows unusually good

correlation with calculated values. Generally, the flight values are difficult to obtain to a reasonable degree of consistency and accuracy. However, the orientation and magnitude of the vectors in the graphical time-vector representation of the rolling-moment equation for the subject airplane were conducive to the accuracy with which

$C_{l_r} - \frac{|\dot{\beta}|}{|r|} C_{l\dot{\beta}}$ was obtained. (See section 5.3.2(c).)

In general, there is good correlation between flight and calculated values of $C_{n_r} - \frac{|\dot{\beta}|}{|r|} C_{n\dot{\beta}}$. The flight values were obtained from a graphical time-vector solution of the yawing-moment equation, from which the static derivative, $C_{n\dot{\beta}}$, was determined simultaneously. (See section 5.3.2(b).) Because the accuracy of the flight values of $C_{n_r} - \frac{|\dot{\beta}|}{|r|} C_{n\dot{\beta}}$ is dependent largely on the phase angle, $\Phi_{\beta r}$, which could be obtained within 1° , the flight values for the subject airplane are considered to be accurate to within 10 percent.

6.6.3 Symbols

b_w wing span, ft

C_l rolling-moment coefficient

$C_{l\beta} = \frac{\partial C_l}{\partial \beta}$, per deg

$C_{l\dot{\beta}} = \frac{\frac{\partial C_l}{\partial \dot{\beta}}}{\frac{\dot{\beta} b_w}{2V}}$, per rad

$C_{l_p} = \frac{\partial C_l}{\partial \left(\frac{pb_w}{2V} \right)}$, per rad

$$C_{l_r} = \frac{\partial C_l}{\partial \left(\frac{rb_w}{2V} \right)}, \text{ per rad}$$

C_n yawing-moment coefficient

$$C_{n_p} = \frac{\partial C_n}{\partial \left(\frac{pb_w}{2V} \right)}, \text{ per rad}$$

$$C_{n_r} = \frac{\partial C_n}{\partial \left(\frac{rb_w}{2V} \right)}, \text{ per rad}$$

$$\zeta_{n_\beta} = \frac{\partial C_n}{\partial \beta}, \text{ per deg}$$

$$C_{n\dot{\beta}} = \frac{\partial C_n}{\partial \left(\frac{\dot{\beta} b_w}{2V} \right)}, \text{ per rad}$$

p roll rate, rad/sec

\bar{q}_∞ free-stream dynamic pressure, lb/sq ft

r yaw rate, rad/sec

S_w wing area, sq ft

T thrust of the propellers, lb

$$T'_c = \frac{T}{\bar{q}_\infty S_w}$$

t time, sec

V airspeed, ft/sec

α_b airplane angle of attack relative to the X-body axis, deg

β sideslip angle, deg or rad

$$\dot{\beta} = \frac{\partial \beta}{\partial t}$$

$$\frac{|\dot{\beta}|}{|r|}$$

amplitude ratio of the rate-of-sideslip vector to the yaw-rate vector in the Dutch roll oscillation

$\Phi_{\beta r}$

phase angle of the β vector relative to the yaw-rate vector in the Dutch roll oscillation

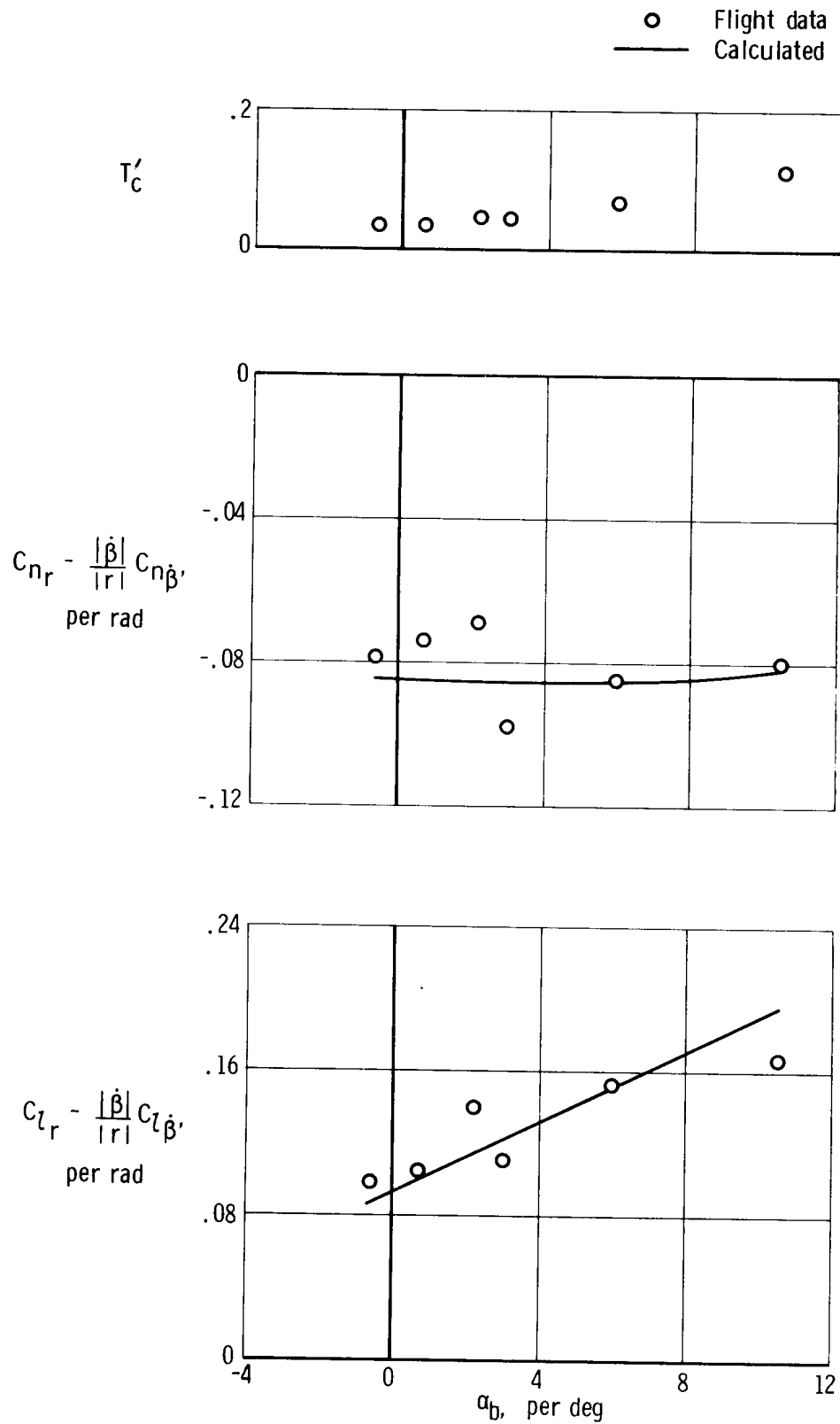


Figure 6.6.2-1. Comparison of flight-determined and calculated dynamic stability derivatives relative to the body axes as a function of angle of attack.

7.0 DYNAMIC STABILITY CHARACTERISTICS

In the following discussion of the dynamic stability characteristics, consideration is given first to the equations of motion that constitute the mathematical model of the airplane. This mathematical model is then manipulated to provide dynamic response expressions of various degrees of accuracy. Response characteristics accounted for include Dutch roll period and damping, roll subsidence, spiral divergence, roll-to-sideslip ratio, $\frac{|\varphi|}{|\beta|}$, maximum roll rate due to aileron input, and factors affecting roll performance. Calculated characteristics are compared with flight data whenever flight data are available.

7.1 Equations of Motion

Dynamic stability characteristics are normally based on the following linearized small-perturbation equations, which are referenced to the body-axes system (angles, rates, and accelerations are in radians):

$$mV(\Delta\dot{\beta} + \Delta r - \alpha_0\Delta p) - W(\sin\theta_0\Delta\psi' + \cos\theta_0\cos\varphi\Delta\varphi) = (C_{Y\beta}\Delta\beta + C_{Y\delta_r}\Delta\delta_r + C_{Y\delta_a}\Delta\delta_a)\bar{q}s \quad (7.1-1)$$

$$I_X\Delta\dot{p} - I_{XZ}\Delta\dot{r} = (C_{l_\beta}\Delta\beta + C_{l_p}\frac{b_w}{2V}\Delta p + C_{l_r}\frac{b_w}{2V}\Delta r + C_{l_{\delta_r}}\Delta\delta_r + C_{l_{\delta_a}}\Delta\delta_a)\bar{q}s b_w \quad (7.1-2)$$

$$I_Z\Delta\dot{r} - I_{XZ}\Delta\dot{p} = (C_{n_\beta}\Delta\beta + C_{n_p}\frac{b_w}{2V}\Delta p + C_{n_r}\frac{b_w}{2V}\Delta r + C_{n_{\delta_r}}\Delta\delta_r + C_{l_{\delta_a}}\Delta\delta_a)\bar{q}s b_w \quad (7.1-3)$$

where

$$\Delta\psi' = \int(\Delta r)dt \quad (7.1-4)$$

$$\Delta\varphi = \int(\Delta p)dt \quad (7.1-5)$$

The Laplace transform of equations (7.1-1) to (7.1-3) may be represented by the following matrix:

$$\begin{bmatrix} (s - \bar{Y}_\beta) & (s - g_1) & -[s(\sin\alpha_0) + g_2] \\ -\bar{L}_\beta & -(I'_X s^2 + \bar{L}_r s) & (s^2 - \bar{L}_p s) \\ -\bar{N}_\beta & (s^2 - \bar{N}_r s) & -(I'_Z s^2 + \bar{N}_p s) \end{bmatrix} \begin{bmatrix} \Delta\beta \\ \Delta\psi' \\ \Delta\varphi \end{bmatrix} = \begin{bmatrix} \bar{Y}_{\delta_r} & \bar{Y}_{\delta_a} \\ \bar{L}_{\delta_r} & \bar{L}_{\delta_a} \\ \bar{N}_{\delta_r} & \bar{N}_{\delta_a} \end{bmatrix} \begin{bmatrix} \Delta\delta_r \\ \Delta\delta_a \end{bmatrix} \quad (7.1-6)$$

where

$$g_1 = \frac{g}{V} \sin\theta_0 \quad g_2 = \frac{g}{V} \cos\theta_0 \cos\varphi \quad (7.1-7)$$

$$I'_X = \frac{I_{XZ}}{I_X} \quad I'_Z = \frac{I_{XZ}}{I_Z} \quad (7.1-8)$$

and

$$\left. \begin{array}{l}
 \bar{Y}_\beta = C_{Y_\beta} \frac{\bar{q}S}{mV} \quad \bar{N}_\beta = C_{n_\beta} \frac{\bar{q}Sb_w}{I_Z} \quad \bar{L}_\beta = C_{l_\beta} \frac{\bar{q}Sb_w}{I_X} \\
 \bar{N}_r = C_{n_r} \frac{\bar{q}Sb_w^2}{2VI_Z} \quad \bar{L}_r = C_{l_r} \frac{\bar{q}Sb_w^2}{2VI_X} \\
 \bar{N}_p = C_{n_p} \frac{\bar{q}Sb_w^2}{2VI_Z} \quad \bar{L}_p = C_{l_p} \frac{\bar{q}Sb_w^2}{2VI_X} \\
 \bar{Y}_{\delta_r} = C_{Y_{\delta_r}} \frac{\bar{q}S}{mV} \quad \bar{N}_{\delta_r} = C_{n_{\delta_r}} \frac{\bar{q}Sb_w}{I_Z} \quad \bar{L}_{\delta_r} = C_{l_{\delta_r}} \frac{\bar{q}Sb_w}{I_X} \\
 \bar{Y}_{\delta_a} = C_{Y_{\delta_a}} \frac{\bar{q}S}{mV} \quad \bar{N}_{\delta_a} = C_{n_{\delta_a}} \frac{\bar{q}Sb_w}{I_Z} \quad \bar{L}_{\delta_a} = C_{l_{\delta_a}} \frac{\bar{q}Sb_w}{I_X}
 \end{array} \right\} \quad (7.1-9)$$

The denominator determinant, represented by the first matrix on the left side of equation (7.1-6), constitutes the characteristic equation which may be arranged in the following general form to obtain its roots:

$$s(s^4 + bs^3 + cs^2 + ds + e) = 0 \quad (7.1-10)$$

where

$$\left. \begin{array}{l}
 b = -\bar{L}'_p - \bar{N}'_r - \bar{Y}_\beta \\
 c = -(\bar{N}'_p \bar{L}'_r - \bar{N}'_r \bar{L}'_p) + (\bar{L}'_p + \bar{N}'_r) \bar{Y}_\beta - \bar{L}'_\beta \sin \alpha_o + \bar{N}'_\beta \\
 d = -(\bar{N}'_\beta \bar{L}'_p - \bar{N}'_p \bar{L}'_\beta) - (\bar{N}'_r \bar{L}'_p - \bar{N}'_p \bar{L}'_r) \bar{Y}_\beta - g_1 \bar{N}'_\beta \\
 - g_2 \bar{L}'_\beta - (\bar{N}'_\beta \bar{L}'_r - \bar{N}'_r \bar{L}'_\beta) \sin \alpha_o \\
 e = -g_1 (\bar{L}'_\beta \bar{N}'_p - \bar{L}'_p \bar{N}'_\beta) - g_2 (\bar{N}'_\beta \bar{L}'_r - \bar{N}'_r \bar{L}'_\beta)
 \end{array} \right\} \quad (7.1-11)$$

and where the primed derivatives are equal to

$$\bar{N}'_{i=\beta, p, r, \delta_a, \delta_r} = \frac{\bar{N}_i + I'_Z \bar{L}_i}{1 - I'_X I'_Z} \text{ and } \bar{L}'_{i=\beta, p, r, \delta_a, \delta_r} = \frac{\bar{L}_i + I'_X \bar{N}_i}{1 - I'_X I'_Z} \quad (7.1-12)$$

For example,

$$\bar{N}'_{i=\beta} = \bar{N}'_\beta = \frac{\bar{N}_\beta + I'_Z \bar{L}_\beta}{1 - I'_X I'_Z}$$

The modes of the aircraft's motions are dependent upon the roots of the characteristic equation. The modes may be:

(1) Spiral divergence, roll subsidence, and Dutch roll oscillation, for which the characteristic equation is

$$\left(s + \frac{1}{T_S}\right)\left(s + \frac{1}{T_R}\right)\left(s^2 + 2\xi_{DR}\omega_{DR}s + \omega_{DR}^2\right) = 0 \quad (7.1-13)$$

(2) Coupled spiral and roll modes (lateral phugoid) and Dutch roll, for which the characteristic equation is

$$(s^2 + 2\xi_{ph}\omega_{ph}s + \omega_{ph}^2)(s^2 + 2\xi_{DR}\omega_{DR}s + \omega_{DR}^2) = 0 \quad (7.1-14)$$

The following criterion from reference 31, if satisfied, indicates the existence of the lateral phugoid and Dutch roll modes:

$$d^2 - 4ec < 0 \quad (7.1-15)$$

The criterion implies that the product ec is positive.

The spiral divergence, roll subsidence, and Dutch roll modes are considered in the following sections because of their more common occurrence. The lateral phugoid is considered in reference 31.

7.1.1 Symbols

a, b, c, d, e coefficients in a fifth-order characteristic equation
(eq. (7.1-10)) as defined in equations (7.1-11)

b_w wing span, ft

C_l rolling-moment coefficient

$$C_{l_p} = \frac{\partial C_l}{\partial \left(\frac{pb_w}{2V}\right)}, \text{ per rad}$$

$$C_{l_r} = \frac{\partial C_l}{\partial \left(\frac{rb_w}{2V}\right)}, \text{ per rad}$$

$$C_{l_\beta} = \frac{\partial C_L}{\partial \beta}, \text{ per rad}$$

$$C_{l_{\delta_a}} = \frac{\partial C_l}{\partial \delta_a}, \text{ per rad}$$

$$C_{l_{\delta_r}} = \frac{\partial C_l}{\partial \delta_r}, \text{ per rad}$$

C_n yawing-moment coefficient

$$C_{n_p} = \frac{\partial C_n}{\partial \left(\frac{pb_w}{2V} \right)}, \text{ per rad}$$

$$C_{n_r} = \frac{\partial C_n}{\partial \left(\frac{rb_w}{2V} \right)}, \text{ per rad}$$

$$C_{n_\beta} = \frac{\partial C_n}{\partial \beta}, \text{ per rad}$$

$$C_{n_{\delta_a}} = \frac{\partial C_n}{\partial \delta_a}, \text{ per rad}$$

$$C_{n_{\delta_r}} = \frac{\partial C_n}{\partial \delta_r}, \text{ per rad}$$

C_Y side-force coefficient

$$C_{Y_\beta} = \frac{\partial C_Y}{\partial \beta}, \text{ per rad}$$

$$C_{Y_{\delta_a}} = \frac{\partial C_Y}{\partial \delta_a}, \text{ per rad}$$

$$C_{Y_{\delta_r}} = \frac{\partial C_Y}{\partial \delta_r}, \text{ per rad}$$

g acceleration of gravity, ft/sec²

g_1, g_2 as defined in equations (7.1-7)

I_X, I_Z	mass moment of inertia of the airplane about the X- and Z-body axes, respectively, slug-ft ²
I_{XZ}	mass product of inertia, slug-ft ²
I'_X, I'_Z	as defined in equations (7.1-8)
$\bar{L}_p, \bar{L}_r, \bar{L}_\beta, \bar{L}_{\delta_a}, \bar{L}_{\delta_r}$	as defined in equations (7.1-9)
$\bar{L}'_p, \bar{L}'_r, \bar{L}'_\beta$	as defined in equations (7.1-12)
$m = W/g$, slugs	
$\bar{N}_p, \bar{N}_r, \bar{N}_\beta, \bar{N}_{\delta_a}, \bar{N}_{\delta_r}$	as defined in equations (7.1-9)
$\bar{N}'_p, \bar{N}'_r, \bar{N}'_\beta$	as defined in equations (7.1-12)
p, r	roll and yaw rate, respectively, rad/sec
\dot{p}, \dot{r}	roll and yaw acceleration, respectively, rad/sec ²
$\Delta p, \Delta r, \Delta \dot{p}, \Delta \dot{r}$	perturbed value of p , r , \dot{p} , and \dot{r} , respectively
\bar{q}	dynamic pressure, lb/sq ft
S	wing area, sq ft
s	Laplace transform variable
T_R, T_S	roll mode and spiral mode time constant, respectively, sec
t	time, sec
V	true airspeed, ft/sec
W	airplane weight, lb
$\bar{Y}_\beta, \bar{Y}_{\delta_a}, \bar{Y}_{\delta_r}$	as defined in equations (7.1-9)
α_0	airplane angle of attack relative to the X-body axis in a trimmed condition, rad
β	sideslip angle, rad
$\dot{\beta} = \frac{\partial \beta}{\partial t}$, rad/sec	

$\Delta\beta, \Delta\dot{\beta}$	perturbed value of β and $\dot{\beta}$, respectively
δ_a, δ_r	aileron and rudder position, respectively, rad
$\Delta\delta_a, \Delta\delta_r$	perturbed value of aileron and rudder deflection, respectively, rad
$\Delta\varphi = \mathcal{J}(\Delta p)dt$, rad	
$\Delta\psi' = \mathcal{J}(\Delta r)dt$, rad	
ξ_{DR}, ξ_{ph}	damping ratio of the Dutch roll and lateral-phugoid oscillation, respectively
θ_o	trimmed pitch attitude of the X-body axis, rad
φ	roll attitude about the X-body axis, $\mathcal{J}pd़t$, rad
$\frac{ \varphi }{ \beta }$	amplitude ratio of φ to β in the Dutch roll oscillation
ω_{DR}, ω_{ph}	undamped natural frequency of the Dutch roll and lateral-phugoid oscillation, respectively, rad/sec

7.2 Determination of Roots of Characteristic Equation When Spiral Divergence, Roll Subsidence, and Dutch Roll Modes Exist

When the spiral divergence, roll subsidence, and Dutch roll modes exist, the coefficients b , c , d , and e of the characteristic equation

$$s(s^4 + bs^3 + cs^2 + ds + e) = 0 \quad (7.1-10)$$

can be readily shown to be equal to:

$$\left. \begin{aligned} b &= 2\xi_{DR}\omega_{DR} + \frac{1}{T_R} + \frac{1}{T_S} \\ c &= \omega_{DR}^2 + 2\xi_{DR}\omega_{DR} \left(\frac{1}{T_R} + \frac{1}{T_S} \right) + \frac{1}{T_R T_S} \\ d &= \omega_{DR}^2 \left(\frac{1}{T_R} + \frac{1}{T_S} \right) + 2\xi_{DR}\omega_{DR} \frac{1}{T_R T_S} \\ e &= \omega_{DR}^2 \frac{1}{T_S T_R} \end{aligned} \right\} \quad (7.2-1)$$

In most instances, the spiral mode factor, $\frac{1}{T_S}$, is much smaller than the roll mode factor, $\frac{1}{T_R}$, and the coefficients are approximated by

$$\left. \begin{aligned} b &\approx 2\xi_{DR}\omega_{DR} + \frac{1}{T_R} \\ c &\approx \omega_{DR}^2 + 2\xi_{DR}\omega_{DR} \frac{1}{T_R} \\ d &\approx \omega_{DR}^2 \frac{1}{T_R} \end{aligned} \right\} \quad (7.2-2)$$

7.2.1 Spiral Divergence Root

Because the spiral divergence root is very small compared to the roots of the roll subsidence and Dutch roll modes, it may be estimated to a good degree of accuracy by considering only the last two terms of the characteristic equation (eq. (7.1-10)). This first approximation gives

$$\lambda_{sm} = -\frac{1}{T_S} = -\frac{e}{d} \quad (7.2.1-1)$$

By substituting the dimensional derivative equivalents of the coefficients d and e from equations (7.1-11) and simplifying by eliminating the minor quantities, the following approximation is obtained:

$$\lambda_{sm} \approx -\frac{-g_2 (\bar{N}'_{\beta} \bar{L}'_r - \bar{N}'_r \bar{L}'_{\beta})}{-(\bar{N}'_{\beta} \bar{L}'_p - \bar{N}'_p \bar{L}'_{\beta}) - g_2 \bar{L}'_{\beta}} \quad (7.2.1-2)$$

In terms of dimensionless derivatives,

$$\lambda_{sm} \approx -\frac{g}{V} \left[\frac{C_{n_r} C_{l_{\beta}} - C_{l_r} C_{n_{\beta}}}{\left(C_{n_p} - 2C_L \frac{I_Z}{mb_w} \right) C_{l_{\beta}} - \left(C_{l_p} + 2C_L \frac{I_{XZ}}{mb_w} \right) C_{n_{\beta}}} \right] \quad (7.2.1-3)$$

Equations (7.2.1-2) and (7.2.1-3) show that the spiral mode involves sideslip, β , yaw rate, r , and roll rate, p .

The criterion for stability is provided by the numerator of equation (7.2.1-3). Thus

$$C_{n_r} C_{l_{\beta}} - C_{l_r} C_{n_{\beta}} \begin{cases} > 0 & \text{Spirally convergent} \\ = 0 & \text{Neutral spiral stability} \\ < 0 & \text{Spirally divergent} \end{cases} \quad (7.2.1-4)$$

Because C_{n_r} and $C_{l_{\beta}}$ are both normally negative, the product $C_{n_r} C_{l_{\beta}}$ favors spiral stability. However, the product $C_{l_r} C_{n_{\beta}}$ is generally positive (since $C_{n_{\beta}}$ is positive for positive directional stability and C_{l_r} is normally positive) and tends to decrease spiral stability. The derivatives C_{l_r} and $C_{l_{\beta}}$ are primarily dependent upon the wing for their magnitudes. Because C_{l_r} is essentially a linear function of C_L (section 6.3), an increase in angle of attack is accompanied by a positive increase in C_{l_r} , which decreases spiral stability. To provide an acceptable degree of spiral stability at high angles of attack (the critical condition), sufficient geometric dihedral is incorporated to provide sufficient $C_{l_{\beta}}$ for stability.

Acceptable spiral stability is specified by reference 32 in terms of minimum time to double the spiral amplitude where

$$(T_2)_{sm} = -(ln 2) T_S = -0.693 T_S = \frac{0.693}{\lambda_{sm}} \quad (7.2.1-5)$$

For light aircraft, section 3.3.1-3 of reference 32 stipulates that $(T_2)_{sm}$ should not be less than 12 seconds for clearly adequate operation nor less than 4 seconds for minimum acceptable operation.

The predicted spiral stability characteristics of the subject airplane over its speed range at trimmed, level-flight power conditions (from fig. 5.2-8 of ref. 1) are summarized in figure 7.2.1-1 on the basis of the derivatives calculated in this report. Because the flight-determined values of $C_{l\beta}$ were markedly different from predicted (and wind-tunnel) values, the figure also includes predicted spiral stability characteristics in which flight values of $C_{l\beta}$ (fig. 5.3.3-1), obtained from oscillatory maneuvers, were used in place of calculated values.

7.2.2 Roll Subsidence Root

The roll subsidence root may be obtained from the following relation obtained from equations (7.2-2):

$$\lambda_{rm} = -\frac{1}{T_R} = \frac{d}{\omega_{DR}^2} \text{ per second} \quad (7.2.2-1)$$

Upon replacing the coefficient d by its dimensional derivative equivalent, and simplifying by eliminating the quantities which are minor for conventional aircraft configurations, the following approximation is obtained:

$$\begin{aligned} \lambda_{rm} &\approx \frac{(\bar{N}'\bar{L}'_p - \bar{N}'\bar{L}'_\beta) + g_2 \bar{L}'_\beta}{\omega_{DR}^2} \\ &= \frac{\bar{N}'\bar{L}'_p - \bar{L}'_\beta (\bar{N}'_p - \frac{g}{V})}{\omega_{DR}^2} \end{aligned} \quad (7.2.2-2)$$

In terms of nondimensional derivatives and with ω_{DR}^2 replaced by its approximate derivative equivalent as obtained in section 7.2.3,

$$\lambda_{rm} \approx \frac{\left[C_{n\beta} \left(C_{l_p} + 2C_L \frac{I_{XZ}}{mb_w^2} \right) - C_{l\beta} \left(C_{n_p} - 2C_L \frac{I_Z}{mb_w^2} \right) \right] \frac{\bar{q}Sb_w^2}{2VI_X}}{C_{n\beta} - C_{l\beta} \left(\frac{I_Z}{I_X} \sin \alpha - \frac{I_{XZ}}{I_X} \right) + \left(C_{nr} C_{l_p} + \frac{I_{XZ}}{I_X} C_{l_r} C_{l_p} \right) \left(\frac{b_w}{2V} \right)^2 \left(\frac{\bar{q}Sb_w}{I_X} \right) + C_{l_p} C_{Y\beta} \frac{I_Z}{I_X} \frac{g}{V} \frac{b_w}{2V} \frac{1}{C_L}} \quad (7.2.2-3)$$

In accordance with reference 31, equation (7.2.2-3) is valid if $\bar{Y}_\beta \bar{L}'_r \ll \bar{L}'_\beta$ and if the Dutch roll damping ratio is of the order of 0.2 or less. If $\bar{L}'_p(\bar{Y}_\beta + \bar{N}'_r) \ll \bar{N}'_\beta$, the dynamic derivatives in the denominator can be disregarded and the equation becomes

$$\lambda_{rm} \approx \frac{C_{n\beta} \left(C_{l_p} + 2C_L \frac{I_{XZ}}{mb_w^2} \right) - C_{l\beta} \left(C_{n_p} - 2C_L \frac{I_Z}{mb_w^2} \right)}{C_{n\beta} - C_{l\beta} \left(\frac{I_Z}{I_X} \sin \alpha - \frac{I_{XZ}}{I_X} \right)} \frac{\bar{q} S b_w^2}{2 V I_X} \quad (7.2.2-4)$$

For a first approximation,

$$\lambda_{rm} = C_{l_p} \frac{\bar{q} S b_w^2}{2 V I_X} \quad (7.2.2-5)$$

The predicted roll subsidence characteristics of the subject airplane over its speed range at trimmed, level-flight conditions are summarized in figure 7.2.2-1 on the basis of equation (7.2.2-3). This equation was used rather than equation (7.2.2-4) because its denominator, ω_{DR}^2 , was significantly affected by the dynamic terms. (See section 7.2.3.) Included in the figure for comparison are roll-mode characteristics calculated by using flight values of $C_{l\beta}$, which did not affect the results significantly. Also included are the predicted roll-mode characteristics based on the single-degree-of-freedom equation (eq. (7.2.2-5)). The results indicate that the roll subsidence mode is primarily a single-degree-of-freedom rotation about the X-axis and is heavily dependent on C_{l_p} . Because C_{l_p} is essentially determined by the wing, heavy damping of the roll mode can be expected for light aircraft configurations. Also, because C_{l_p} is a function of the wing lift-curve slope, which is not significantly affected by compressibility up to a Mach number of approximately 0.6, the roll subsidence will decrease with increase in pressure altitude for constant-dynamic-pressure flight as a result of the decrease in $\frac{\bar{q}}{V}$.

Acceptable roll-mode characteristics are specified by reference 32 in terms of the roll mode time constant, $T_R = -\frac{1}{\lambda_{rm}}$, which reflects roll damping. For light aircraft, section 3.3.1.2 of reference 32 stipulates that T_R should not be greater than 1.4 seconds for clearly adequate operation nor greater than 10 seconds for minimum acceptable operation.

The roll mode time constant is discussed further in section 7.4.3 in relation to the influence of the convergent spiral mode on the apparent flight value of T_R .

7.2.3 Roots of the Dutch Roll Mode

The oscillatory frequency of the Dutch roll mode is obtained to a good degree of accuracy from the following relation (from eqs. (7.2-2) and (7.1-11)), if the damping ratio is of the order of 0.2 or less:

$$\begin{aligned} \omega_{DR}^2 &\approx c \\ &\approx \bar{N}'_\beta - \bar{L}'_\beta \sin \alpha + \bar{N}'_r \bar{L}'_p + \bar{L}'_p \bar{Y}_\beta \end{aligned} \quad (7.2.3-1)$$

In terms of nondimensional derivatives,

$$\begin{aligned}\omega_{DR}^2 \approx & \left[C_{n\beta} - C_{l\beta} \left(\frac{I_Z}{I_X} \sin \alpha - \frac{I_{XZ}}{I_X} \right) + \left(C_{nr} C_{lp} + \frac{I_{XZ}}{I_X} C_{lr} C_{lp} \right) \left(\frac{b_w}{2V} \right)^2 \frac{\bar{q}Sb_w}{I_X} \right. \\ & \left. + C_{lp} C_{Y\beta} \frac{I_Z}{I_X} \frac{g}{V} \frac{b_w}{2V} \frac{1}{C_L} \right] \frac{\bar{q}Sb_w}{I_Z} \quad (7.2.3-2)\end{aligned}$$

For the more normal situations where $\bar{L}'_p(\bar{Y}_\beta + \bar{N}'_r) \ll \bar{N}'_\beta$, equation (7.2.3-2) can be reduced to the following more commonly used format:

$$\omega_{DR}^2 = \left[C_{n\beta} - C_{l\beta} \left(\frac{I_Z}{I_X} \sin \alpha - \frac{I_{XZ}}{I_X} \right) \right] \frac{\bar{q}Sb_w}{I_Z} \quad (7.2.3-3)$$

Equation (7.2.3-3) was not applicable to the subject airplane, because the dynamic derivative terms in equation (7.2.3-2) had a significant effect on the frequency, as shown in figure 7.2.3-1.

The Dutch roll damping constant, $\zeta_{DR} \omega_{DR}$, and damping ratio, ζ_{DR} , have not been estimated satisfactorily by the greatly simplified expressions which have appeared in the literature. The utility of these expressions is restricted to very small angles of attack. A fairly accurate estimate of the damping constant may be obtained from the following equation, derived from equations (7.2-2):

$$\zeta_{DR} \omega_{DR} \approx \frac{1}{2} \frac{c(bc - d)}{c^2 + bd} \quad (7.2.3-4)$$

where

$$\begin{aligned}b &= -(\bar{L}'_p + \bar{N}'_r + \bar{Y}_\beta) \\ &\approx - \left(C_{nr} + C_{lp} \frac{I_Z}{I_X} \right) \frac{\bar{q}Sb_w}{2VI_Z} - C_{Y\beta} \frac{g}{V} \frac{1}{C_L} \\ c &\approx \omega_{DR}^2 \\ d &\approx -\bar{N}'_\beta \bar{L}'_p + \bar{N}'_p \bar{L}'_\beta - g_2 \bar{L}'_\beta \\ &\approx \left[-C_{n\beta} \left(C_{lp} + 2C_L \frac{I_{XZ}}{mb_w^2} \right) + C_{l\beta} \left(C_{np} - 2C_L \frac{I_Z}{mb_w^2} \right) \right] \left(\frac{b_w}{2V} \right)^2 \frac{(\bar{q}Sb_w)^2}{I_X I_Z} \quad \left. \right\} (7.2.3-5)\end{aligned}$$

The period, P_{DR} , of the Dutch roll oscillations and the time, $(T_{1/2})_{DR}$, for the oscillations to damp to half amplitude are obtained from:

$$(T_{1/2})_{DR} = \frac{\ln 2}{\zeta_{DR} \omega_{DR}} = \frac{0.693}{\zeta_{DR} \omega_{DR}} \quad (7.2.3-6)$$

$$P_{DR} = \frac{2\pi}{\omega_{DR} (1 - \zeta_{DR}^2)^{1/2}} \quad (7.2.3-7)$$

For normal cruise and approach configurations, minimum adequate Dutch roll frequency and damping requirements for light aircraft are specified by section 3.3.1.1 of reference 32 to be:

$$\begin{aligned} \text{Minimum } \omega_{DR} &= 0.4 \text{ rad/sec (cruise)} \\ &= 1.0 \text{ rad/sec (approach)} \end{aligned}$$

$$\text{Minimum } \zeta_{DR} = 0.08$$

$$\text{Minimum } \zeta_{DR} \omega_{DR} = 0.15$$

In the damping requirements, indicated by ζ_{DR} and $\zeta_{DR} \omega_{DR}$, the governing requirement is the one that yields the larger value of ζ_{DR} .

Additional insight into more desirable Dutch roll characteristics for small general aviation airplanes is provided in reference 33. On the basis of a flight test investigation of Dutch roll mode frequency and damping in which a variable-stability airplane was used, the reference concluded that for a small airplane with good roll mode and near-neutral spiral characteristics flown on an ILS approach:

- (1) The best level of Dutch roll frequency is between 1.8 and 2.3 radians per second. This represents a compromise in which the level of directional stability is large enough to provide good dynamics, but not large enough to cause excessive yawing in turbulence.
- (2) Dutch roll frequencies near 3 radians per second lead to excessive yaw in turbulence. Frequencies lower than 1.4 radians per second are undesirable because they require the pilot to compensate for poor heading control, large sideslip excursions, and difficulty in trimming the airplane in roll and yaw.
- (3) The instrument approach task becomes rapidly more difficult with Dutch roll damping ratios less than 0.10. However, relatively little is gained by increasing the damping ratio beyond this value, at least for Dutch roll excitation in roll response. In some instances of high Dutch roll excitation, higher damping would undoubtedly be desirable.

(4) The best range of dihedral effect is $\bar{L}_\beta = \frac{C_l \bar{q} S b_w}{I_X} = -8$ to -16 radians per second² per radian, but there is little penalty for lower values (such as -6 or -4). Large dihedral effect ($\bar{L}_\beta = -20$ or more negative) is undesirable because it produces excessive rolling due to turbulence.

Predicted Dutch roll characteristics of the subject airplane were based on the preceding derived relations (eqs. (7.2.3-2) and (7.2.3-4) to (7.2.3-7)) and on calculated derivatives. Predictions were obtained for P_{DR} , $(T_{1/2})_{DR}$, and ξ_{DR} for typical flight conditions at 6000 feet pressure altitude as a function of velocity. The results are compared with predicted characteristics based on wind-tunnel data and with flight data in figure 7.2.3-2.

The predicted period characteristics are slightly lower than flight values. Substitution of flight values of C_{l_β} (which were approximately 40 percent lower than predicted) into the equations had a negligible effect on the predicted period.

The predicted time to damp to half amplitude, $(T_{1/2})_{DR}$, is slightly longer in the low-speed region than indicated by the flight data. Substitution of flight values of C_{l_β} into the equations resulted in improved correlation of predicted $(T_{1/2})_{DR}$ with flight data in the low-speed region.

7.2.4 Symbols

b, c, d, e coefficients in a fifth-order characteristic equation (eq. (7.1-10)) as defined in equations (7.1-11) and (7.2-1)

b_w wing span, ft

C_L airplane lift coefficient

C_l rolling-moment coefficient

$$C_{l_p} = \frac{\partial C_l}{\partial \left(\frac{pb_w}{2V} \right)}, \text{ per rad}$$

$$C_{l_r} = \frac{\partial C_l}{\partial \left(\frac{rb_w}{2V} \right)}, \text{ per rad}$$

$$C_{l_\beta} = \frac{\partial C_l}{\partial \beta}, \text{ per rad}$$

C_n	yawing-moment coefficient
$C_{n_p} = \frac{\partial C_n}{\partial \left(\frac{pb_w}{2V} \right)}$, per rad	
$C_{n_r} = \frac{\partial C_n}{\partial \left(\frac{rb_w}{2V} \right)}$, per rad	
$C_{n_\beta} = \frac{\partial C_n}{\partial \beta}$, per rad	
C_Y	side-force coefficient
$C_{Y_\beta} = \frac{\partial C_Y}{\partial \beta}$, per rad	
g	acceleration of gravity, ft/sec ²
$g_2 = \frac{g}{V} \cos \theta_o \cos \varphi$	
I_X, I_Z	mass moment of inertia of the airplane about the X- and Z-body axis, respectively, slug-ft ²
I_{XZ}	mass product of inertia, slug-ft ²
$\bar{L}'_p, \bar{L}'_r, \bar{L}'_\beta$	as defined in equations (7.1-12)
$m = \frac{W}{g}$, slugs	
$\bar{N}'_p, \bar{N}'_r, \bar{N}'_\beta$	as defined in equations (7.1-12)
P_{DR}	period of the Dutch roll oscillation, sec
p, r	roll and yaw rate, respectively, rad/sec
\bar{q}	dynamic pressure, lb/sq ft
S	wing area, sq ft
s	Laplace transform variable
T	thrust of the propellers, lb

$T'_c = \frac{T}{\bar{q}S}$	
T_R, T_S	roll mode and spiral mode time constant, respectively, sec
$(T_{1/2})_{DR}$	time required to decrease the Dutch roll oscillation to half amplitude, sec
$(T_2)_{sm}$	time required for the spiral mode to double its amplitude, sec
V	true airspeed, ft/sec
V_c	calibrated airspeed, knots
W	airplane weight, lb
$\bar{Y}_\beta = C_{Y_\beta} \left(\frac{\bar{q}S}{mV} \right)$, per rad/sec	
α	airplane angle of attack relative to the X-body axis, rad (unless noted otherwise)
β	angle of sideslip, rad
ζ_{DR}	damping ratio of the Dutch roll oscillation
θ_o	trimmed pitch attitude of the X-body axis, rad
λ_{rm}	roll subsidence root, equal to $-\frac{1}{T_R}$
λ_{sm}	spiral divergence root, equal to $-\frac{1}{T_S}$
φ	roll attitude about the X-body axis, rad
ω_{DR}	undamped natural frequency of the Dutch roll oscillation, rad/sec

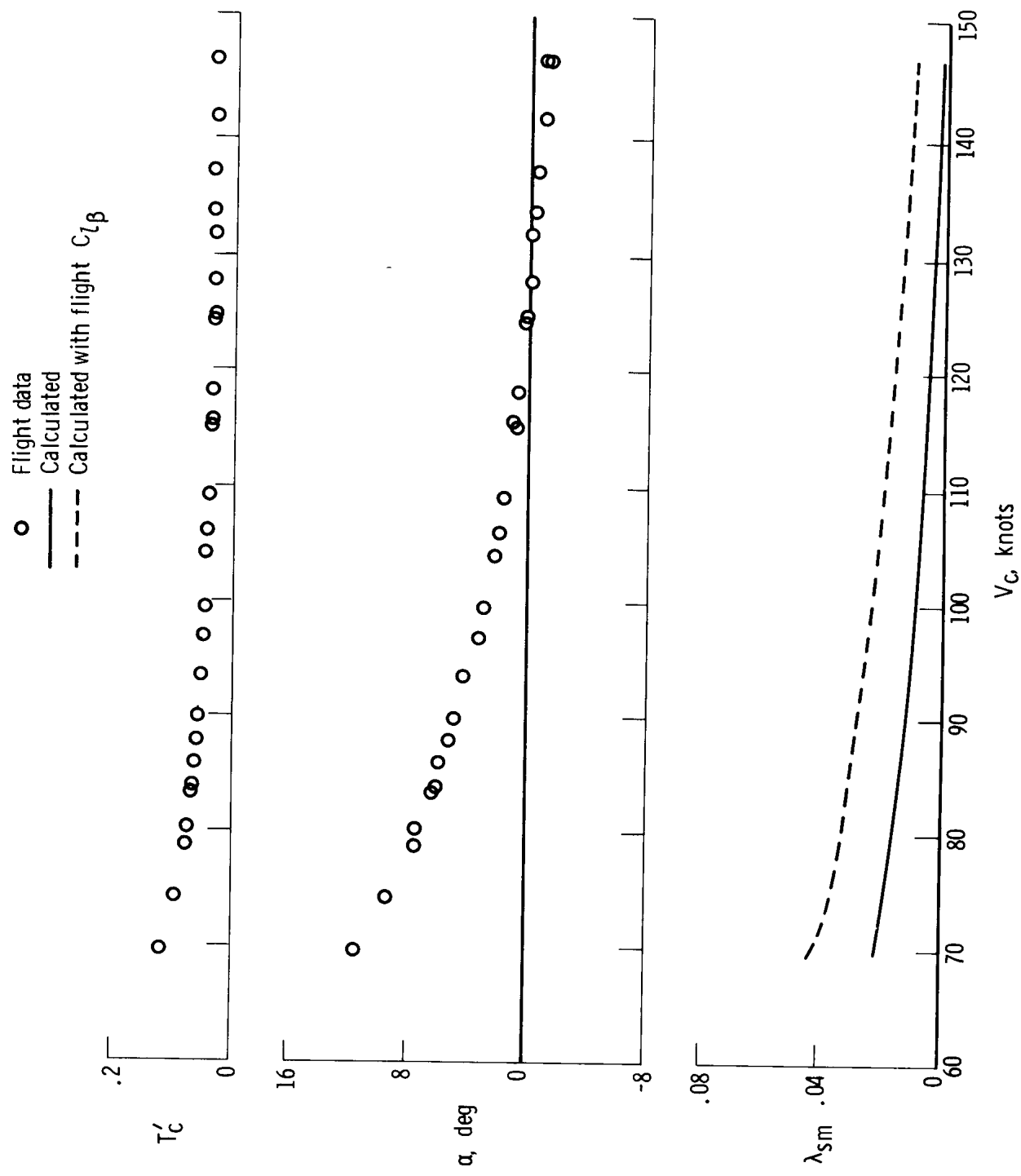


Figure 7.2.1-1. Predicted spiral stability characteristics of the subject airplane over its speed range at trimmed, level-flight power conditions.

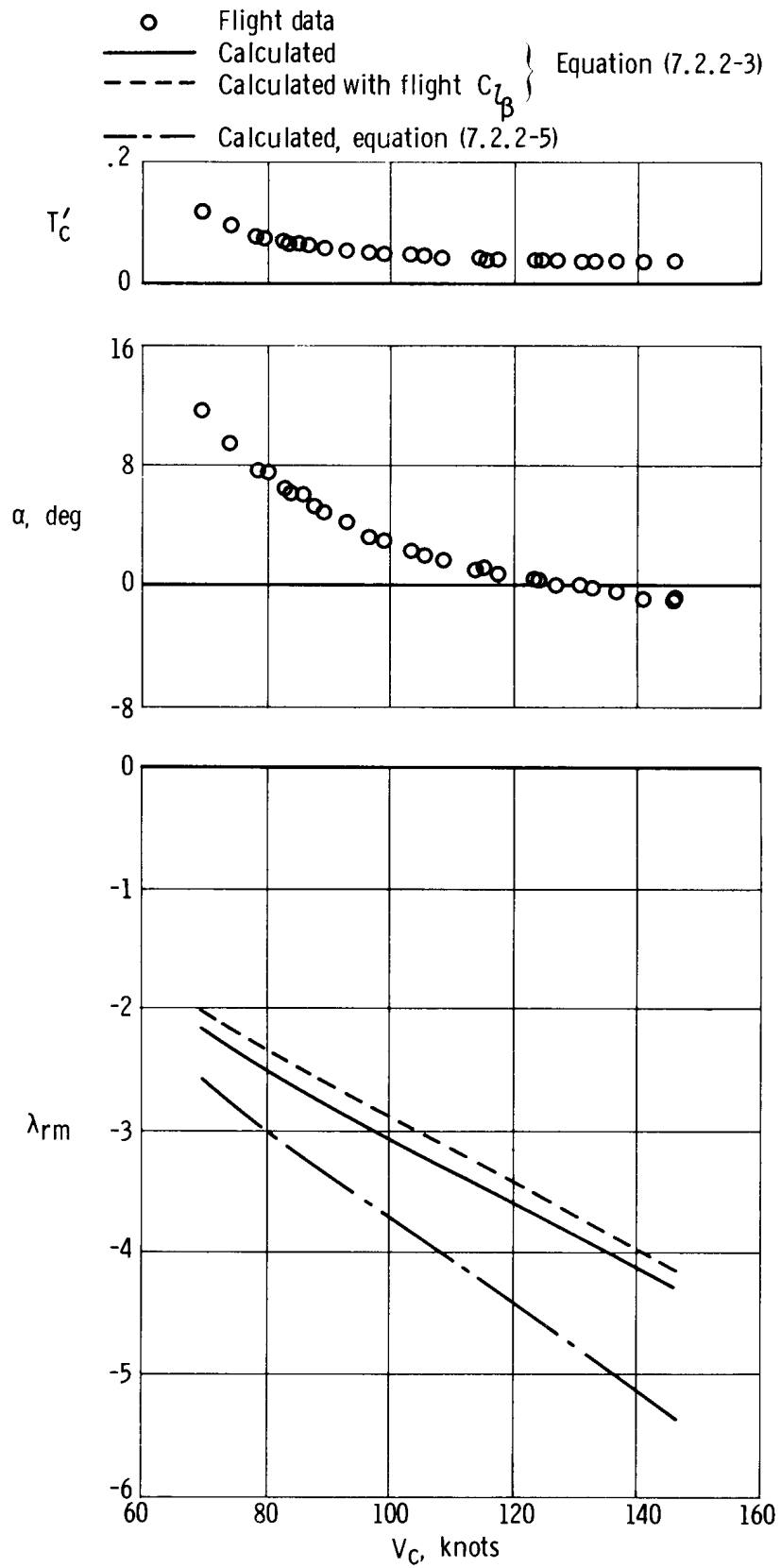


Figure 7.2.2-1. Predicted roll mode stability characteristics of the subject airplane over the speed range of the airplane at trimmed level-flight powered conditions.

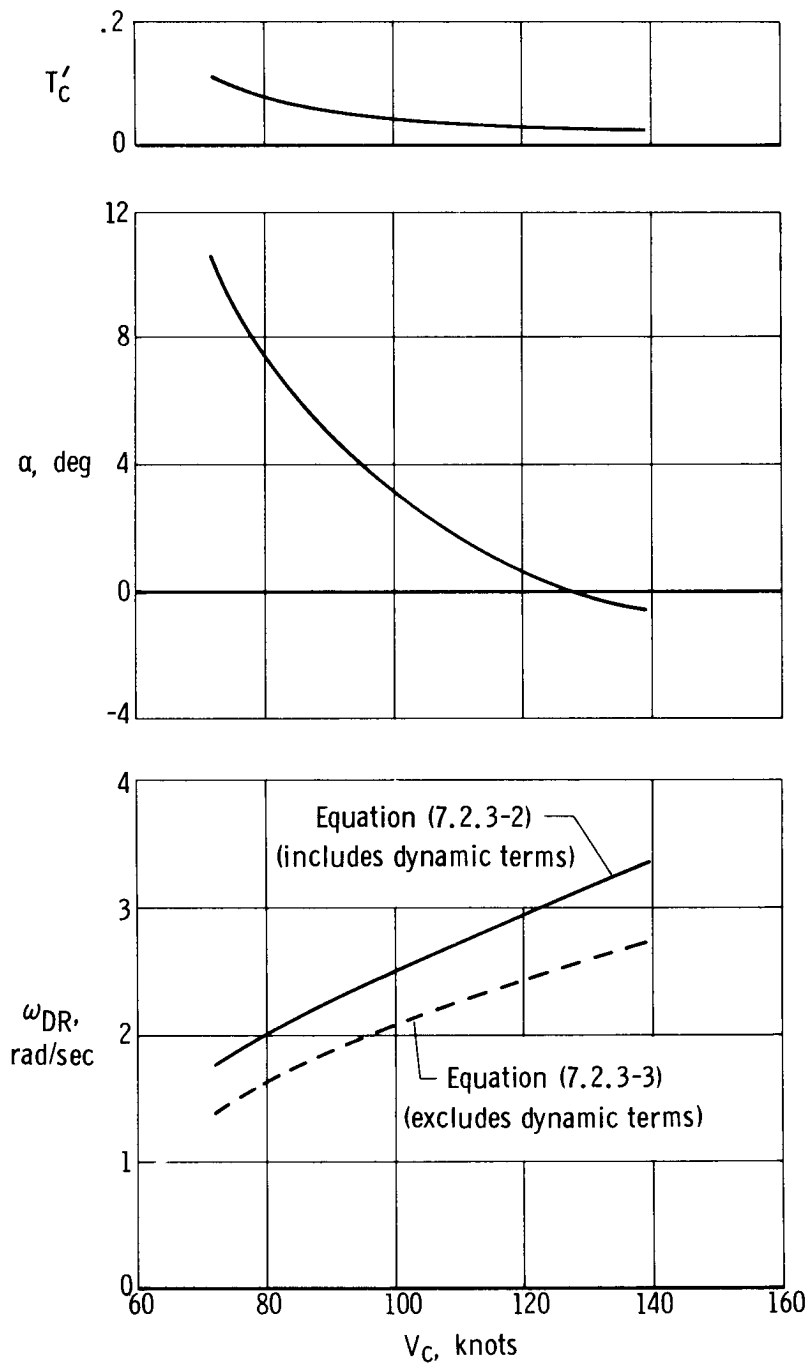


Figure 7.2.3-1. Effect of exclusion of dynamic derivative terms from Dutch roll frequency equation on predicted frequency characteristics of the subject airplane.

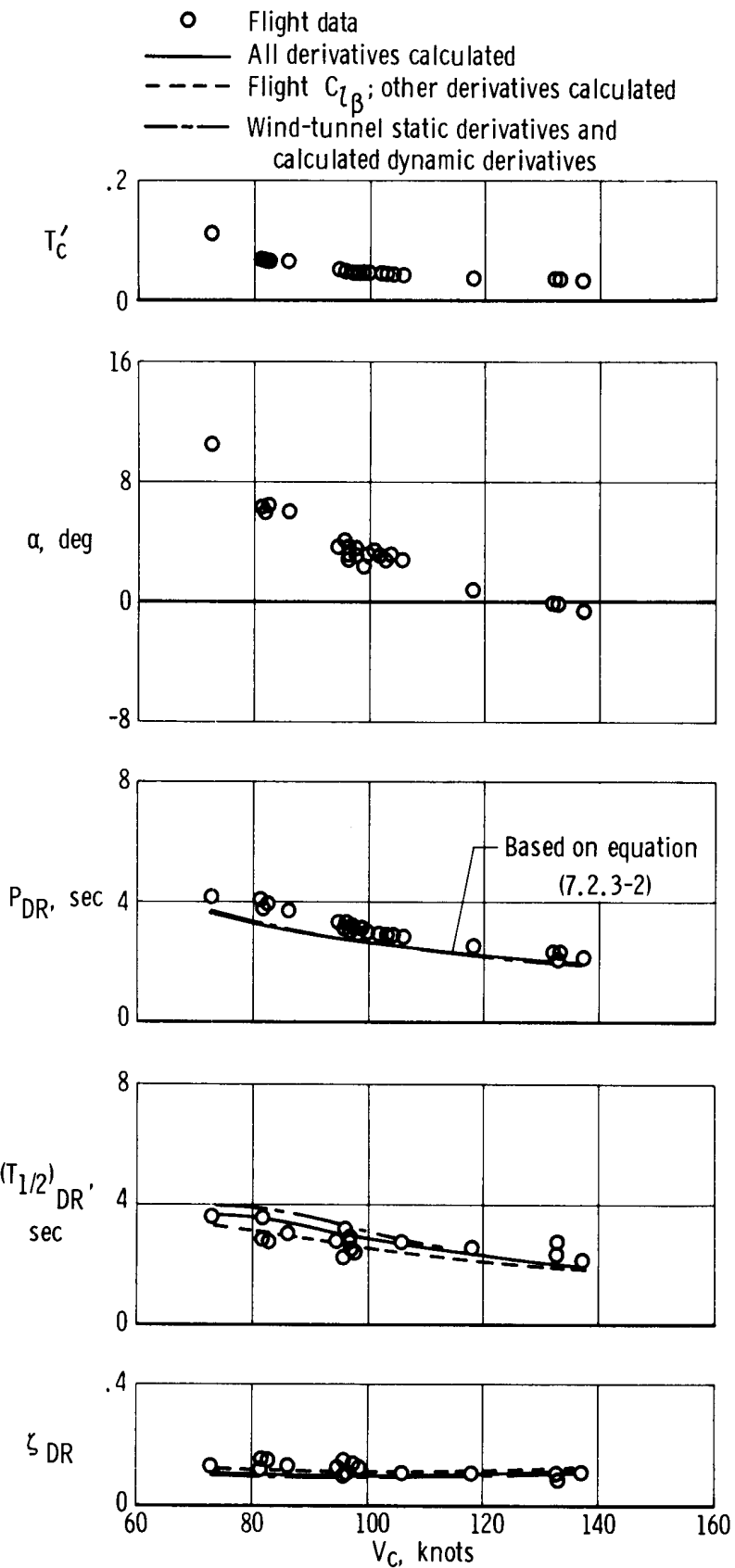


Figure 7.2.3-2. Predicted period and damping characteristics of the subject airplane compared with flight data.

7.3 Ratio of Roll to Sideslip in the Dutch Roll Mode

Experience has shown that the pilot may be sensitive to the roll-to-sideslip response ratio as well as to the damping and frequency of the Dutch roll mode. As a result, the roll-to-sideslip ratio, $\frac{|\varphi|}{|\beta|}$, and the phase angle, $\Phi_{\varphi\beta}$, are factors that should be taken into account when considering dynamic stability characteristics.

7.3.1 Roll-To-Sideslip Ratio

With low roll-to-sideslip ratios, sideslip is the disturbing factor to the pilot. If roll rate or aileron control excite the sideslip, oscillations of the nose on the horizon during a turn or a lag in yaw rate during entry into a turn may make it difficult for the pilot to quickly or precisely track a new heading. Also, rudder inputs may be required to damp the oscillations.

With large ratios, it is difficult to control roll rate or bank angle precisely. With very large ratios, the sensitivity of roll to rudder movements or lateral gusts makes it difficult to control the airplane.

From the equations of motion (eq. (7.1-6)), with control inputs set at zero, several different equations may be arrived at for the Laplace transform of the roll-to-sideslip ratio, depending upon which two of the three equations are considered. The following transfer function is obtained from a simultaneous solution of the rolling- and yawing-moment equations:

$$\frac{\varphi(s)}{\beta(s)} = \frac{\bar{L}'_B s + (\bar{L}'_r \bar{N}'_\beta - \bar{L}'_\beta \bar{N}'_r)}{s[s^2 - (\bar{L}'_p + \bar{N}'_r)s + (\bar{L}'_p \bar{N}'_r - \bar{L}'_r \bar{N}'_p)]} \quad (7.3.1-1)$$

In terms of nondimensional derivatives,

$$\frac{\varphi(s)}{\beta(s)} = \frac{a_1 s + a_2}{s(b_1 s^2 + b_2 s + b_3)} \quad (7.3.1-2)$$

where

$$\left. \begin{aligned} a_1 &= \frac{I_Z}{\bar{q}Sb_w} C_l_\beta + \frac{I_{XZ}}{\bar{q}Sb_w} C_{n_\beta} \\ a_2 &= \left(C_l_r C_{n_\beta} - C_{l_\beta} C_{n_r} \right) \frac{b_w}{2V} \end{aligned} \right\} \quad \text{(Equation continued on next page)}$$

$$\left. \begin{aligned}
 b_1 &= \frac{I_X I_Z}{(\bar{q} Sb_w)^2} - \left(\frac{I_{XZ}}{\bar{q} Sb_w} \right)^2 \\
 b_2 &= \left[-\frac{I_X}{\bar{q} Sb_w} C_{n_r} - \frac{I_Z}{\bar{q} Sb_w} C_{l_p} - \frac{I_{XZ}}{\bar{q} Sb_w} (C_{n_p} + C_{l_r}) \right] \frac{b_w}{2V} \\
 b_3 &= \left(C_{n_r} C_{l_p} - C_{n_p} C_{l_r} \right) \left(\frac{b_w}{2V} \right)^2
 \end{aligned} \right\} (7.3.1-3)$$

The amplitude ratio may be obtained by substituting the following complex Dutch roll root of the characteristic equation for s in equation (7.3.1-1) or (7.3.1-2):

$$\begin{aligned}
 s &= -\zeta_{DR} \omega_{DR} + i \omega_{DR} \sqrt{1 - \zeta_{DR}^2} \\
 &\approx -\zeta_{DR} \omega_{DR} + i \omega_{DR} \text{ for } \zeta_{DR} < 0.2
 \end{aligned} \tag{7.3.1-4}$$

When R_N and I_N , and R_D and I_D indicate the real and imaginary parts of the numerator and denominator, respectively, the amplitude ratio and phase angle are found from

$$\frac{|\varphi|}{|\beta|} = \sqrt{\frac{R_N^2 + I_N^2}{R_D^2 + I_D^2}} \tag{7.3.1-5}$$

and

$$\tan \Phi_{\varphi\beta} = \left(\frac{\frac{I_N}{R_N} - \frac{I_D}{R_D}}{1 + \frac{I_N I_D}{R_N R_D}} \right) \tag{7.3.1-6}$$

A qualitative insight into the effects of the major parameters on $\frac{|\varphi|}{|\beta|}$ is obtained from the following approximate equation:

$$\frac{|\varphi|}{|\beta|} \approx \left[\frac{(\bar{L}'_\beta)^2 + \bar{N}'_\beta (\bar{L}'_r)^2}{(\bar{N}'_\beta)^2 + \bar{N}'_\beta (\bar{L}'_p)^2} \right]^{1/2} \tag{7.3.1-7}$$

This equation shows that a decrease in effective dihedral, an increase in directional

stability, an increase in C_{l_p} , or a decrease in $\frac{I_Z}{I_X}$ will decrease the roll-to-sideslip ratio and tend to result in a predominantly yawing motion. A reverse trend in these parameters will tend toward large rolling motions. Since the pilot controls turning by gaging the bank angle, it may be desirable to minimize the amount of roll per unit of sideslip of the Dutch roll mode.

For typical light airplanes the roll-to-sideslip ratio is of the order of 1 or less; for high-performance fighter airplanes the ratio may be of the order of 10. For the subject airplane, the ratio is of the order of 0.5.

7.3.2 Roll-To-Sideslip Phase Angle

The effect of the phase angle, $\Phi_{\varphi\beta}$, on the pilot's coordination of control inputs is often neglected. For the subject airplane, $\Phi_{\varphi\beta}$ is of the order of 80° . This means that the maximum amplitude of bank angle in the Dutch roll mode leads the maximum amplitude of sideslip by 80° (or $\frac{80}{360} P_{DR}$ seconds of the Dutch roll period, P_{DR}). In a typical high-performance fighter aircraft, $\Phi_{\varphi\beta}$ is of the order of 45° .

The phase angle, $\Phi_{\varphi\beta}$, is primarily affected by the parameters \bar{L}'_p and \bar{L}'_β . If \bar{L}'_p is large at positive dihedral conditions, the phase angle will move toward 90° . If \bar{L}'_p is small, the phase angle will tend toward 0° . Figure 7.3.2-1 (based on ref. 34) shows the qualitative effects of \bar{L}'_p on the phase angle for both positive and negative dihedral conditions.

7.3.3 Comparison of Predicted Characteristics With Flight Data

The predicted roll-to-sideslip ratio and phase angle of the subject airplane are presented in figure 7.3.3-1 for trimmed, level-flight power conditions as a function of calibrated airspeed. Included for comparison are several flight-determined values. The correlations are relatively poor when the predicted characteristics are based entirely on calculated derivatives. However, when flight-determined values of C_{l_β} are substituted for the calculated values in the prediction equation, good correlations are obtained. Although very good correlations of calculated and wind-tunnel values of C_{l_β} had been obtained (section 4.3.4), flight values of C_{l_β} were approximately 40 to 50 percent lower than predicted. This discrepancy is discussed in section 5.3.4.

7.3.4 Symbols

a_1, a_2

coefficients of a first-order differential equation in the numerator of equation (7.3.1-2) as defined in equations (7.3.1-3)

b_1, b_2, b_3	coefficients of a second-order differential equation in the denominator of equation (7.3.1-2) as defined in equations (7.3.1-3)
b_w	wing span, ft
C_l	rolling-moment coefficient
$C_{l_p} = \frac{\partial C_l}{\partial \left(\frac{pb_w}{2V} \right)}$, per rad	
$C_{l_r} = \frac{\partial C_l}{\partial \left(\frac{rb_w}{2V} \right)}$, per rad	
$C_{l_\beta} = \frac{\partial C_l}{\partial \beta}$, per rad	
C_n	yawing-moment coefficient
$C_{n_p} = \frac{\partial C_n}{\partial \left(\frac{pb_w}{2V} \right)}$, per rad	
$C_{n_r} = \frac{\partial C_n}{\partial \left(\frac{rb_w}{2V} \right)}$, per rad	
$C_{n_\beta} = \frac{\partial C_n}{\partial \beta}$, per rad	
I_N, I_D	net value of the imaginary parts of the numerator and denominator, respectively, of equation (7.3.1-5)
I_X, I_Z	mass moment of inertia of the airplane about the X- and Z-body axes, respectively, slug-ft ²
I_{XZ}	mass product of inertia, slug-ft ²
i	imaginary
$\bar{L}'_p, \bar{L}'_r, \bar{L}'_\beta$	as defined in equations (7.1-12)

$\bar{N}'_p, \bar{N}'_r, \bar{N}'_\beta$	as defined in equations (7.1-12)
P_{DR}	period of the Dutch roll oscillation, sec
p, r	roll and yaw rate, respectively, rad/sec
\bar{q}	dynamic pressure, lb/sq ft
R_N, R_D	net value of the real parts of the numerator and denominator, respectively, of equation (7.3.1-5)
S	wing area, sq ft
s	Laplace transform variable
T	thrust of the propellers, lb
$T'_c = \frac{T}{\bar{q}S}$	
V	true airspeed, ft/sec
V_c	calibrated airspeed, knots
α	airplane angle of attack relative to the X-body axis, deg
β	sideslip angle, rad
ξ_{DR}	damping ratio of the Dutch roll oscillation
φ	roll attitude about the X-body axis, rad
$\frac{ \varphi }{ \beta }$	amplitude ratio of φ to β in the Dutch roll oscillation
$\frac{\varphi(s)}{\beta(s)}$	Laplace transform of the equation for $\frac{ \varphi }{ \beta }$
Φ_d	Dutch roll mode damping angle, deg
$\Phi_{p\beta}$	phase angle of the p-vector relative to the β -vector in the Dutch roll oscillation
$\Phi_{\varphi\beta} = \Phi_{p\beta} - (90 + \Phi_d)$, deg	
ω_{DR}	undamped natural frequency of the Dutch roll oscillation, rad/sec

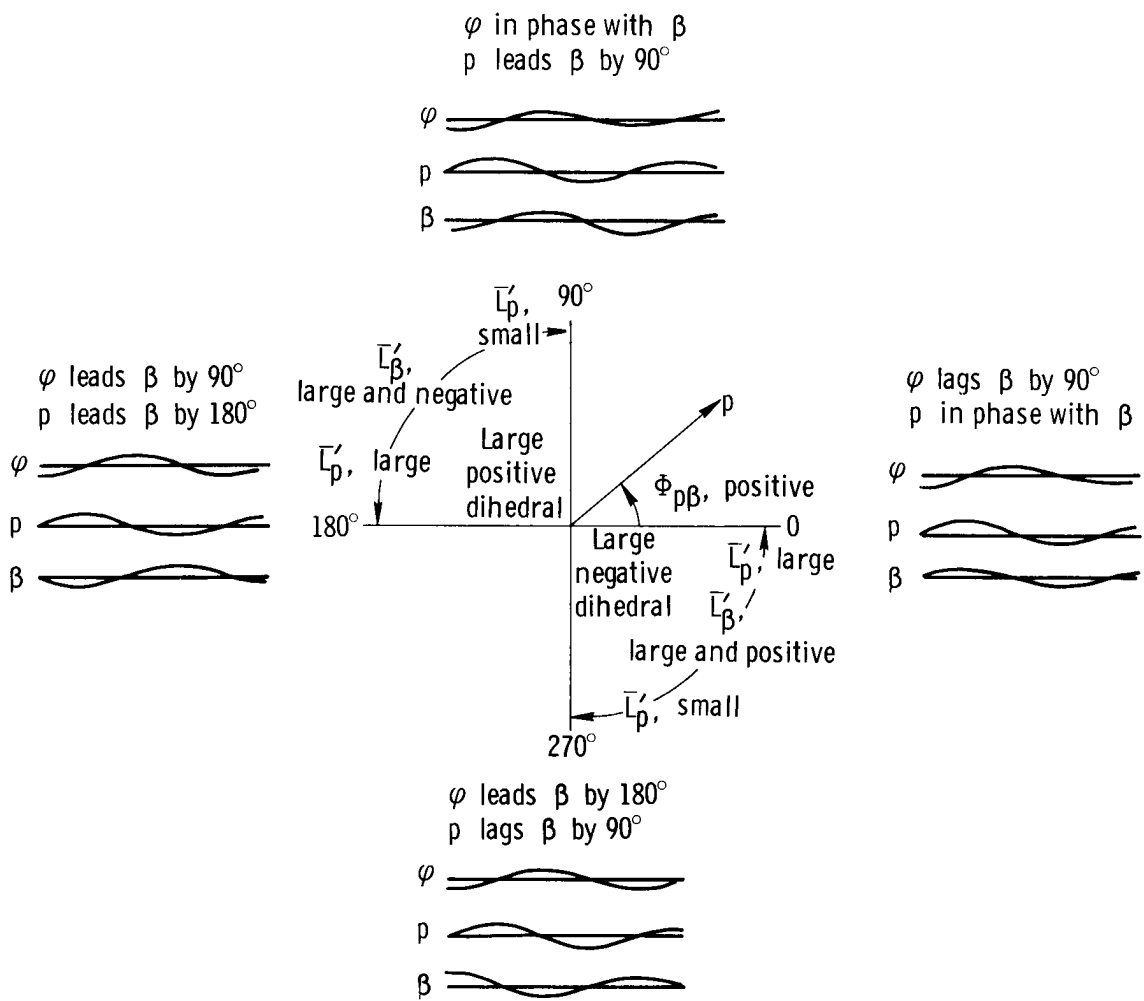


Figure 7.3.2-1. Effect of effective dihedral and roll damping on roll-sideslip phasing in the Dutch roll mode (based on ref. 34).

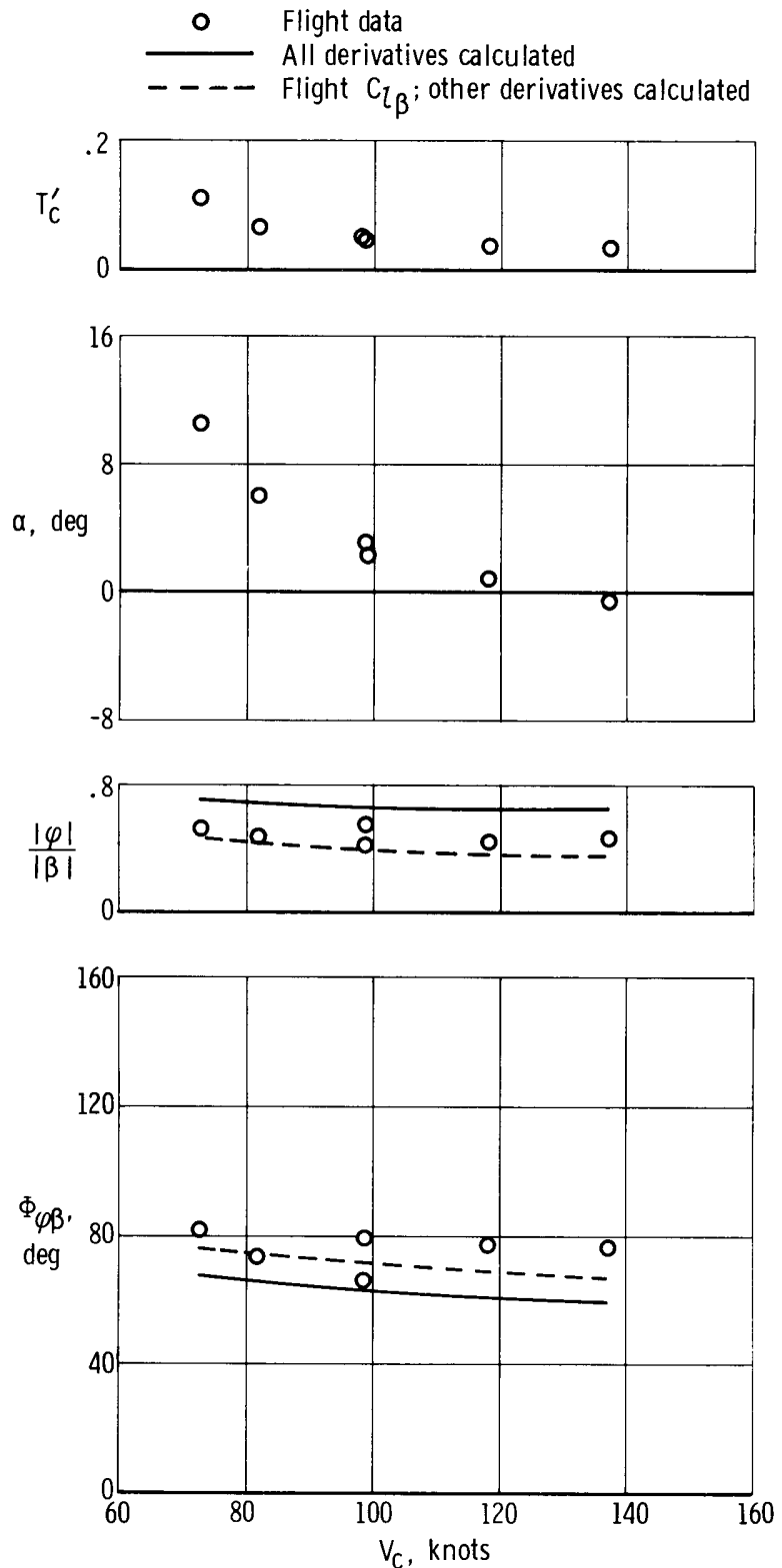


Figure 7.3.3-1. Predicted amplitude ratio and phase angle characteristics of the subject airplane for trimmed, level-flight conditions compared with several flight-determined values.

7.4 Roll Performance

The manner in which the airplane responds to the application of aileron is a primary factor in the consideration of the stability characteristics of the airplane. The following roll performance parameters have been proposed and used:

- (1) Steady-state roll rate, p_{ss} , per unit of aileron deflection
- (2) Steady-state wing-tip helix angle, $\frac{p_{ss} b_w}{2V}$, per unit of step input of aileron or per maximum deflection (step input) of aileron
- (3) The time required for the roll rate to attain 63.2 percent of its steady-state value, expressed as a roll mode time constant, T_R
- (4) The amount of Dutch roll excited due to an aileron step input.

Because roll performance characteristics are a function of many interrelated factors, a roll equation is derived to illustrate the complexity of the factors involved and for use as the basis for detailed considerations of the factors affecting rolling performance.

7.4.1 Derivation of the Roll Equation

The first step in deriving the roll performance equation is to obtain the following Laplace transform from the lateral-directional equations of motion (eq. (7.1-6)) and the characteristic equation (eq. (7.1-10)):

$$\frac{p(s)}{\delta_a(s)} = s \left(\frac{\varphi(s)}{\delta_a(s)} \right) = s \frac{\begin{vmatrix} (s - \bar{Y}_\beta) & (s - g_1) & \bar{Y}_{\delta_a} \\ -\bar{L}_\beta & -(I_X s^2 + \bar{L}_R s) & \bar{L}_{\delta_a} \\ -\bar{N}_\beta & (s^2 - \bar{N}_R s) & \bar{N}_{\delta_a} \end{vmatrix}}{s \left(s + \frac{1}{T_S} \right) \left(s + \frac{1}{T_R} \right) \left(s^2 + 2\xi_{DR} \omega_{DR} s + \omega_{DR}^2 \right)} \quad (7.4.1-1)$$

$$= \frac{(A_\varphi s^3 + B_\varphi s^2 + C_\varphi s + D_\varphi)}{\left(s + \frac{1}{T_S} \right) \left(s + \frac{1}{T_R} \right) \left(s^2 + 2\xi_{DR} \omega_{DR} s + \omega_{DR}^2 \right)} \quad (7.4.1-2a)$$

$$\approx \frac{s(A_\varphi s^2 + B_\varphi s + C_\varphi)}{\left(s + \frac{1}{T_S} \right) \left(s + \frac{1}{T_R} \right) \left(s^2 + 2\xi_{DR} \omega_{DR} s + \omega_{DR}^2 \right)} \quad (7.4.1-2b)$$

$$= \frac{\bar{L}'_{\delta_a} [s(s^2 + 2\xi_\varphi \omega_\varphi s + \omega_\varphi^2)]}{\left(s + \frac{1}{T_S} \right) \left(s + \frac{1}{T_R} \right) \left(s^2 + 2\xi_{DR} \omega_{DR} s + \omega_{DR}^2 \right)} \quad (7.4.1-2c)$$

where, with \bar{Y}_{δ_a} considered negligible, and in terms of primed derivatives defined by equations (7.1-12),

$$\left. \begin{aligned} A_\varphi &= \bar{L}'_{\delta_a} \\ B_\varphi &= -\bar{L}'_{\delta_a} \bar{Y}_\beta - \left(\bar{N}'_r \bar{L}'_{\delta_a} - \bar{L}'_r \bar{N}'_{\delta_a} \right) \\ C_\varphi &= -\left(\bar{L}'_\beta \bar{N}'_{\delta_a} - \bar{N}'_\beta \bar{L}'_{\delta_a} \right) - \left(\bar{L}'_r \bar{N}'_{\delta_a} - \bar{N}'_r \bar{L}'_{\delta_a} \right) \bar{Y}_\beta \\ D_\varphi &= -\left(\bar{N}'_\beta \bar{L}'_{\delta_a} - \bar{L}'_\beta \bar{N}'_{\delta_a} \right) g_1 \text{ (considered negligible)} \end{aligned} \right\} \quad (7.4.1-3)$$

and where

$$2\xi_\varphi \omega_\varphi = \frac{B_\varphi}{A_\varphi} = -\left(\bar{Y}_\beta + \bar{N}'_r \right) + \bar{L}'_r \frac{\bar{N}'_{\delta_a}}{\bar{L}'_{\delta_a}} \quad (7.4.1-4)$$

$$\omega_\varphi^2 = \frac{C_\varphi}{A_\varphi} = \bar{N}'_\beta - \bar{L}'_\beta \frac{\bar{N}'_{\delta_a}}{\bar{L}'_{\delta_a}} - \left(\bar{L}'_r \frac{\bar{N}'_{\delta_a}}{\bar{L}'_{\delta_a}} - \bar{N}'_r \right) \bar{Y}_\beta \quad (7.4.1-5a)$$

$$\approx \bar{N}'_\beta - \bar{L}'_\beta \frac{\bar{N}'_{\delta_a}}{\bar{L}'_{\delta_a}} \quad (7.4.1-5b)$$

For an aileron step input, $\delta_a(s)$ in equation (7.4.1-2c) is replaced by $\frac{\delta_a}{s}$. By factoring the resulting equation and performing the inverse Laplace transformation, the following approximate real-time equation (from ref. 35), in which ξ_φ is considered to be negligible and ξ_{DR} is considered to be small, can be obtained for roll rate, p:

$$\left. \begin{aligned} \frac{p}{\bar{L}'_{\delta_a}} &\approx T_R \left(\frac{\omega_\varphi}{\omega_{DR}} \right)^2 \left(e^{-t/T_S} - 1 \right) + T_R \frac{1 + \omega_\varphi^2 T_R^2}{1 + \omega_{DR}^2 T_R^2} \left(1 - e^{-t/T_R} \right) \\ &+ T_R \frac{\left(\frac{\omega_\varphi}{\omega_{DR}} \right)^2 - 1}{\sqrt{1 + \omega_{DR}^2 T_R^2}} \left[e^{-\xi_{DR} \omega_{DR} t} \sin \left(\omega_{DR} t - \sin^{-1} \frac{1}{\sqrt{1 + \omega_{DR}^2 T_R^2}} \right) + \frac{1}{\sqrt{1 + \omega_{DR}^2 T_R^2}} \right] \end{aligned} \right\} \quad (7.4.1-6a)$$

$$\left. \begin{aligned} \frac{P}{L' \delta_a} &= T_R \left(\frac{\omega_\varphi}{\omega_{DR}} \right)^2 e^{-t/T_S} - T_R \left(\frac{1 + \omega_\varphi^2 T_R^2}{1 + \omega_{DR}^2 T_R^2} \right) e^{-t/T_R} \\ &+ T_R \frac{\left(\frac{\omega_\varphi}{\omega_{DR}} \right)^2 - 1}{\sqrt{1 + \omega_{DR}^2 T_R^2}} e^{-\zeta_{DR} \omega_{DR} t} \sin \left(\omega_{DR} t - \sin^{-1} \frac{1}{\sqrt{1 + \omega_{DR}^2 T_R^2}} \right) \end{aligned} \right\} \quad (7.4.1-6b)$$

where T_S and T_R are spiral and roll mode time constants, respectively, obtained from equations (7.2.1-3) and (7.2.2-2) on the basis that

$$T_S = -\frac{1}{\lambda_{sm}} \quad \text{and} \quad T_R = -\frac{1}{\lambda_{rm}}$$

The three terms in equations (7.4.1-6a) and (7.4.1-6b) identify the rolling motions attributed to the spiral, roll subsidence, and Dutch roll modes, respectively.

7.4.2 Steady-State Roll Rate

One means of assessing rolling performance has been to determine the roll response to an aileron step input in the form of steady-state wing-tip helix angle, $\frac{p_{ss} b_w}{2V}$. This steady-state helix angle is not always attainable realistically. In the following consideration of $\frac{p_{ss} b_w}{2V}$, it is assumed that positive Dutch roll damping ($\zeta_{DR} > 0$) and roll subsidence conditions prevail.

For convergent spiral conditions, equations (7.4.1-6a) and (7.4.1-6b) indicate that the rolling velocity approaches zero as $t \rightarrow \infty$. In effect, there is no rolling velocity which can be considered to be steady state for large values of $\frac{1}{T_S}$. For small values of $\frac{1}{T_S}$, an effective $\frac{p_{ss} b_w}{2V}$ may be approached; however, it occurs at large bank angles (1000° , for example) and is not practical.

For divergent spiral conditions, large values of $\frac{1}{T_S}$ do not permit a well-defined steady-state roll rate. For small values of $\frac{1}{T_S}$, the small rate of divergence allows an effective $\frac{p_{ss} b_w}{2V}$ to be defined, because the steady-state roll rate is reached before the spiral motion has progressed to any significant degree. Thus, for conventional steady-state roll rate consideration, since $\frac{1}{T_S} \ll \frac{1}{T_R}$, the spiral parameter $\frac{1}{T_S}$ can be considered to be equal to zero.

With the motions due to the spiral mode equal to zero ($\frac{1}{T_S} = 0$), equation (7.4.1-6a)

may be reduced to the following steady-state roll rate expression:

$$\frac{p_{ss}}{\delta_a} \approx \frac{\bar{L}'_{\delta_a} \omega_\varphi^2}{\frac{1}{T_R} \omega_{DR}^2} \quad (7.4.2-1)$$

Substituting for ω_φ^2 (eq. (7.4.1-5b)) and $\frac{1}{T_R}$ (using eq. (7.2.2-2)),

$$\frac{p_{ss}}{\delta_a} \approx \frac{\bar{N}'_{\beta} \bar{L}'_{\delta_a} - \bar{L}'_{\beta} \bar{N}'_{\delta_a}}{\bar{L}'_{\beta} \left(\bar{N}'_p - \frac{g}{V} \right) - \bar{L}'_p \bar{N}'_{\beta}} \quad (7.4.2-2)$$

In terms of nondimensional derivatives, and with higher order terms eliminated, equation (7.4.2-2) takes the following form:

$$\frac{p_{ss} b_w}{2V} \approx \frac{C_{n\beta} C_{l\delta_a} - C_{l\beta} C_{n\delta_a}}{\left(C_{n_p} - 2C_L \frac{I_z}{mb_w^2} \right) C_{l\beta} - \left(C_{l_p} + 2C_L \frac{I_{xz}}{mb_w^2} \right) C_{n\beta}} \quad (7.4.2-3)$$

A study of equation (7.4.2-3) indicates roll power per unit input to be primarily a function of C_{l_p} and $C_{l\delta_a}$. Effective dihedral, however, tends to decrease the roll power to some extent with increasing angle of attack. These observations show that for

geometrically similar airplanes and lateral control arrangements, $\frac{p_{ss} b_w}{2V}$ tends to be of similar magnitude. The roll power, $\frac{p_{ss} b_w}{2V}$, that can be produced by full aileron step input is a measure of the relative control power available. Minimum acceptable roll control power for light aircraft calls for sufficient maximum deflection to be available to produce $\frac{p_{ss} b_w}{2V} = 0.09$ radian (ref. 35).

Recent investigations have shown the wing-tip helix angle to be deficient as a design criterion. Current roll-control-effectiveness requirements are based on the time interval between an initial step input and the attainment of a specific roll displacement. Section 3.3.4 of reference 32 stipulates that for light aircraft under cruise conditions or in a climb, clearly adequate roll control effectiveness is demonstrated if 60° of bank is attained in 1.7 seconds; minimum adequate roll control effectiveness is defined as attaining 60° of bank in 3.4 seconds. Corresponding criteria for takeoff and approach conditions are 30° of bank in 1.3 seconds and 30° of bank in 2.6 seconds, respectively.

Figure 7.4.2-1(a) shows the aileron step input roll rate response flight time histories of the subject airplane obtained at 84 and 134 knots calibrated airspeed. The results of

the analysis of the flight data in the form of $\frac{p_{ss}b_w}{2V}$ as a function of δ_a and a comparison of these results with corresponding predicted characteristics are shown in figure 7.4.2-1(b). As shown, reasonably good correlation was obtained when the predicted characteristics were based on calculated derivatives. Substitution of flight values of $C_l\beta$ for the calculated values in the response equation resulted in improved correlation.

The discrepancy between flight and predicted values of $C_l\beta$ is discussed in section 5.3.4.

7.4.3 Apparent Roll Mode Time Constant

Although roll response characteristics are influenced by the spiral and Dutch roll modes, the primary response to an aileron input is provided by the roll mode. This response can be reduced significantly by a stable spiral mode ($-\frac{1}{T_s} < 0$) even though the spiral root may be much smaller than the roll root ($-\frac{1}{T_R}$). The effect of the stable spiral mode is of interest for two reasons. First, the roll mode time constant, T_R , is an important parameter which has been used, as illustrated by figure 7.4.3-1 from reference 36, to assess the degree of acceptability of the airplane's initial rates of response to aileron step inputs. For a given aileron step input, the second term of equation (7.4.1-6a) indicates that a very large value of T_R will result in a sluggish initial roll-rate response; a very small value of T_R indicates a trend toward excessive initial roll rate response. Both extremes are objectionable to a pilot. Second, the roll mode time constant, T_R , has usually been estimated from flight records of the roll rate response to aileron step inputs on the assumption that only the single-degree-of-freedom roll mode is excited during the initial response. Thus, the roll mode time constant obtained from analysis of the flight data may differ considerably from the true constant.

For a single-degree-of-freedom roll mode response to an aileron step input, the roll mode time constant can be considered to be the length of time after the step input is initiated that would be required for the roll rate to attain 63.2 percent of its steady-state value (fig. 7.4.3-2(a)). This percentage is arrived at by reducing equation (7.4.1-6a) to the single-degree-of-freedom roll mode (retaining only the second term). The ratio of roll rate, p , at time, t , to steady-state roll rate, p_{ss} , at $t = \infty$ is readily determined to be

$$\frac{p}{p_{ss}} = 1 - e^{-t\left(\frac{1}{T_R}\right)} \quad (7.4.3-1)$$

At $t = T_R$

$$\frac{p}{p_{ss}} = 1 - e^{-1} = 0.632$$

or

$$p = 0.632 p_{ss} \quad (7.4.3-2)$$

The significance of the roll mode time constant, T_R , is placed in another perspective if it is defined as the time that would be required to obtain steady-state conditions, p_{ss} , after a step input if the single-degree-of-freedom roll rate response changed at a constant rate equal to the actual initial rate of change (fig. 7.4.3-2(a)).

When the spiral mode is not equal to zero and is convergent ($\frac{1}{T_S}$ is positive), the presence of the convergent spiral mode reduces the roll response. The degree of degradation depends upon the magnitude of $\frac{1}{T_S}$. Attempts to use the single-degree-of-freedom roll mode procedure of equation (7.4.3-2) to obtain the roll mode constant, T_R , from flight records involving convergent spiral modes resulted in an apparent value of the roll time constant, T_A , which was smaller than the actual T_R . This apparent roll time constant, T_A , is defined in figure 7.4.3-2(b), which also shows the resulting apparent p_{ss} in relation to the p_{ss} for $\frac{1}{T_S} = 0$.

The apparent roll time constant, T_A , and apparent p_{ss} as ratios of T_R and p_{ss} , respectively, were obtained from the following equation (from ref. 37) as a function of T_R and T_S :

$$\frac{T_A}{T_R} = \frac{(p_{ss})_{app}}{(p_{ss})_1} = \left(\frac{T_R}{T_S} \right) \frac{\frac{T_R}{T_S} \left(1 - \frac{T_R}{T_S} \right)}{\frac{1}{T_S} = 0} \quad (7.4.3-3)$$

Figure 7.4.3-3 shows that the presence of a converging spiral mode, $\frac{1}{T_S} > 0$, makes the apparent roll time constant, T_A , smaller than the actual roll time constant, T_R , because of the reduction in maximum roll rate caused by $\frac{1}{T_S} > 0$. The sensitivity of maximum roll rate to $\frac{1}{T_S}$ is clearly indicated by the figure. For $\frac{1}{T_S} = \frac{1}{20} \left(\frac{1}{T_R} \right)$, the roll rate is reduced 15 percent. It appears, therefore, that a criterion such as that in figure 7.4.3-1 should take the spiral mode into account as a third dimension.

7.4.4 Roll and Dutch Roll Mode Coupling

In considering the roll response of an airplane to an aileron step input, the general

lateral-directional response characteristics are of concern to the pilot. These characteristics are dependent upon T_R , $\zeta_{DR}\omega_{DR}$, and $\left(\frac{\omega_\varphi}{\omega_{DR}}\right)^2$ as well as T_S . The parameter, $\left(\frac{\omega_\varphi}{\omega_{DR}}\right)^2$, which, together with T_R , greatly influenced steady-state roll rate, p_{SS} (eq. (7.4.2-1)), is also a major contributing factor to the amount of Dutch roll in roll rate response. This is reflected in the third term of equation (7.4.1-6b). This parameter may be approximated by the following expression on the basis of equations (7.2.3-1) and (7.4.1-5b), if the dynamic derivative and angle-of-attack terms are assumed to be negligible:

$$\left(\frac{\omega_\varphi}{\omega_{DR}}\right)^2 = 1 - \left(\frac{\bar{L}' \bar{N}'_{\delta_a}}{\bar{N}'_{\beta} \bar{L}'_{\delta_a}} \right) \quad (7.4.4-1)$$

Although $\left(\frac{\omega_\varphi}{\omega_{DR}}\right)^2$ must always be positive (greater than zero) to obtain roll velocity in the correct direction, roll reversal is possible within certain bounds of the parameter as a result of the Dutch roll term in equation (7.4.1-6b). In addition, the signs of \bar{L}'_{β} and \bar{N}'_{δ_a} , which appear in the expression for $\left(\frac{\omega_\varphi}{\omega_{DR}}\right)^2$, and the sign of $(\bar{N}'_p - \frac{g}{V})$, which appears in the equations for Dutch roll damping (eq. (7.2.3-4)), roll subsidence (eq. (7.2.2-2)), and sideslip response to aileron input all have important bearing on the airplane's response to an aileron step input and the pilot's acceptance of that response.

The effect of $\left(\frac{\omega_\varphi}{\omega_{DR}}\right)^2$ on the roll rate, sideslip, and yaw rate of an airplane is shown in figure 7.4.4-1 (from ref. 38). For a value of unity, the Dutch roll mode is zero. Sideslip, however, is present. The response in sideslip is due primarily to the lateral gravity component resulting from bank angle. For values greater than unity, the sideslip response due to gravity is reduced, initially causing the aircraft to slip out of the turn while yawing into it. For values less than unity, the amount of sideslip increases with decreasing values of $\left(\frac{\omega_\varphi}{\omega_{DR}}\right)^2$, with consequent roll reversal (due to \bar{L}'_{β}) when the ratio decreases below a value which is dependent upon the Dutch roll damping ratio, ζ_{DR} .

Roll reversal is discussed in reference 35. As indicated by the reference, if $\frac{1}{T_S}$ is assumed to be zero, it is possible to compute the value of $\left(\frac{\omega_\varphi}{\omega_{DR}}\right)^2$ by using equation (7.4.1-6b), which corresponds to incipient rolling velocity reversal (change in roll rate sign) as sketched in figure 7.4.4-2(a) (from ref. 35). Incipient roll reversal is a function of T_R , ω_{DR} , and ζ_{DR} . For zero Dutch roll damping, ζ_{DR} , figure

7.4.4-2(b) (from ref. 35) shows that $\left(\frac{\omega_\varphi}{\omega_{DR}}\right)^2$ should be greater than 0.5. As the Dutch roll damping increases, the value of $\left(\frac{\omega_\varphi}{\omega_{DR}}\right)^2$ at which roll reversal will occur decreases.

The sign of \bar{N}'_{δ_a} , which appears in the equation for $\left(\frac{\omega_\varphi}{\omega_{DR}}\right)^2$, affects not only the roll power but also the phasing and magnitude of the sideslip-in-roll response to aileron inputs and the ability of the pilot to make aileron-only turns. The effects of \bar{N}'_{δ_a} on roll rate and sideslip responses to a step aileron input are shown by the sketches in figures 7.4.4-3(a) and 7.4.4-3(b) (from ref. 34).

The aerodynamic parameter $\bar{N}'_p - \frac{g}{V}$ also affects the phasing and magnitude of the sideslip-in-roll response and the ability of the pilot to make aileron-only turns. It also influences roll power. This is shown by the sketches in figures 7.4.4-4(a) and 7.4.4-4(b) (from ref. 34).

The pilot's acceptance of the roll performance of an airplane appears to be related to $\left(\frac{\omega_\varphi}{\omega_{DR}}\right)^2$ and the task to be performed. Several interdependent parameters are involved. These include Dutch roll characteristics such as damping, frequency, and roll-to-sideslip ratio, as well as roll power and \bar{N}'_{δ_a} and $\bar{N}'_p - \frac{g}{V}$. Improper combinations of basic parameters can result in decreasing the effective roll power and thus increasing the tendency toward pilot-induced oscillations (PIO) and the associated decrease in the effective damping with the pilot in the loop. Reference 39 discusses the

interrelated effects of $\frac{\omega_\varphi}{\omega_{DR}}$, $\frac{|\varphi|}{|\beta|}$, and the Dutch roll damping ratio on handling qualities in terms of pilot ratings. The parameter $\frac{\omega_\varphi}{\omega_{DR}}$ measures effects that are sensitive to

a number of the parameters and responses, although it does not account for the interrelated effects of damping. This is illustrated to some extent by figure 7.4.4-5. The figure includes flight data for the subject airplane. On the basis of the plotted points, an increase in angle of attack from -0.65° to 10.5° results in a decrease in

$\frac{\omega_\varphi}{\omega_{DR}}$ from 0.990 to 0.967 and some decrease in roll power, as well as an increase in

$\frac{|\varphi|}{|\beta|}$ and some increase in adverse yaw due to aileron.

The pilot's opinion of roll performance improves when $\frac{\omega_\varphi}{\omega_{DR}}$, for low positive damping, is equal to or slightly less than 1.0. Under these conditions the Dutch roll mode, which is troublesome in turns, is effectively eliminated.

7.4.5 Symbols

$A_\varphi, B_\varphi, C_\varphi, D_\varphi$

coefficients of a third-order differential equation
in the numerator of equations (7.4.1-2a) and
(7.4.1-2b), as defined in equations (7.4.1-3)

b_w

wing span, ft

$$C_L = \frac{W}{\bar{q}S}$$

C_l

rolling-moment coefficient

$$C_{l_p} = \frac{\partial C_l}{\partial \left(\frac{pb_w}{2V} \right)}, \text{ per rad}$$

$$C_{l_\beta} = \frac{\partial C_l}{\partial \beta}, \text{ per rad}$$

$$C_{l_{\delta_a}} = \frac{\partial C_l}{\partial \delta_a}, \text{ per rad}$$

C_n

yawing-moment coefficient

$$C_{n_p} = \frac{\partial C_n}{\partial \left(\frac{pb_w}{2V} \right)}, \text{ per rad}$$

$$C_{n_\beta} = \frac{\partial C_n}{\partial \beta}, \text{ per rad}$$

$$C_{n_{\delta_a}} = \frac{\partial C_n}{\partial \delta_a}, \text{ per rad}$$

g

acceleration of gravity, ft/sec²

$$g_1 = \left(\frac{g}{V} \right) \sin \theta_o$$

I_X, I_Z

mass moment of inertia of the airplane about the
X- and Z-body axis, respectively, slug-ft²

I_{XZ}

mass product of inertia, slug-ft²

$$L_{\delta_a} = \frac{(C_l \delta_a \bar{q} Sb_w)}{I_X}$$

$\bar{L}_r, \bar{L}_\beta, \bar{L}_{\delta_a}$ as defined in equations (7.1-9)

$\bar{L}'_p, \bar{L}'_r, \bar{L}'_\beta, \bar{L}'_{\delta_a}$ as defined in equations (7.1-12)

$$m = \frac{W}{g}, \text{ slugs}$$

$\bar{N}_r, \bar{N}_\beta, \bar{N}_{\delta_a}$ as defined in equations (7.1-9)

$\bar{N}'_p, \bar{N}'_r, \bar{N}'_\beta, \bar{N}'_{\delta_a}$ as defined in equations (7.1-12)

p, r roll and yaw rate, respectively, rad/sec

p_{max} maximum roll rate, rad/sec

$(p_{max}) \frac{1}{T_S} = 0$ maximum roll rate in the absence of the spiral mode

p_{ss} steady-state roll rate, rad/sec

$(p_{ss})_{app}$ apparent steady-state roll rate

$(p_{ss}) \frac{1}{T_S} = 0$ steady-state roll rate in the absence of the spiral mode

$\frac{p(s)}{\delta_a(s)}$ Laplace transform of the roll rate response to an aileron input

\bar{q} dynamic pressure, lb/sq ft

S wing area, sq ft

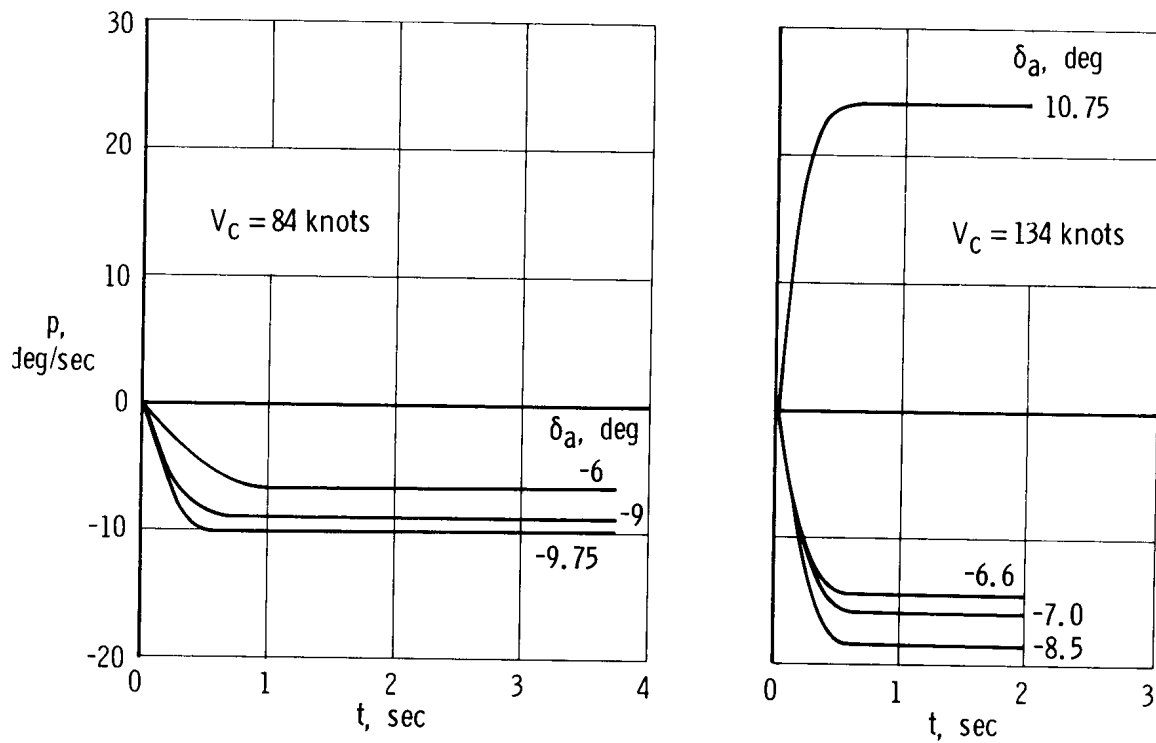
s Laplace transform variable

T_A apparent roll mode time constant, sec

T_R, T_S roll mode and spiral mode time constant, respectively, sec

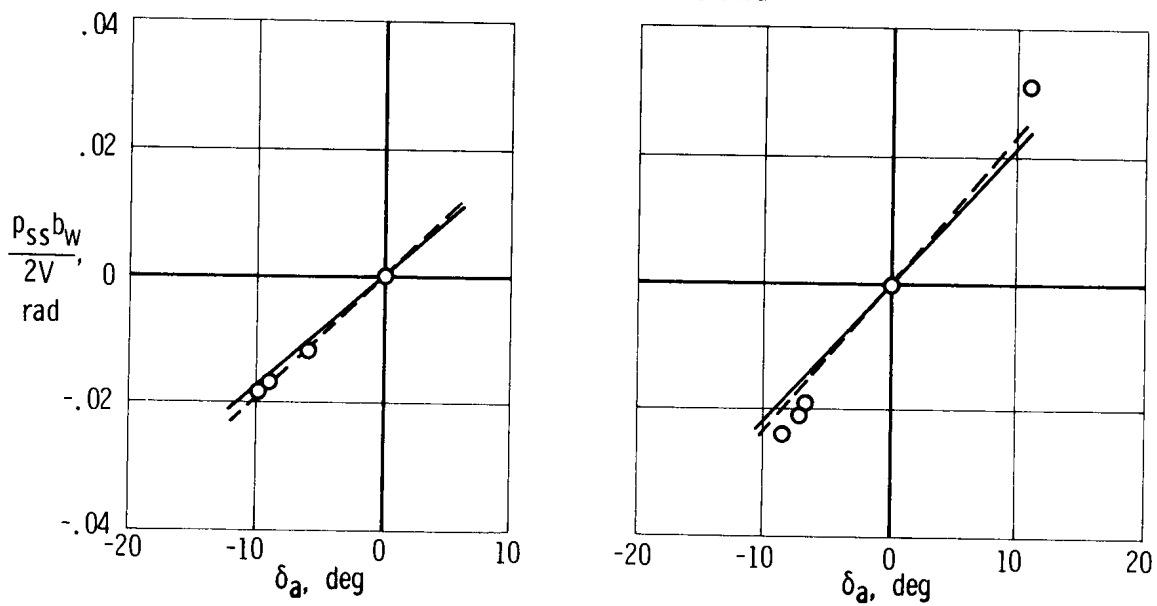
t time, sec

V	true airspeed, ft/sec
V_c	calibrated airspeed, knots
W	airplane weight, lb
$\bar{Y}_\beta, \bar{Y}_{\delta_a}$	as defined in equations (7.1-9)
α	angle of attack, deg
β	sideslip angle, rad
δ_a	differential aileron deflection, rad
$\delta_{a_{max}}$	maximum aileron deflection, rad
$\delta_a(s)$	Laplace transform of an aileron input
ζ_{DR}	damping ratio of the Dutch roll mode
ζ_φ	damping ratio of the second-order differential equation in the numerator of equation (7.4.1-2c)
θ_o	trimmed pitch attitude of the X-body axis, rad
λ_{rm}	roll mode root, $-\frac{1}{T_R}$
λ_{sm}	spiral mode root, $-\frac{1}{T_S}$
φ	roll attitude about the X-body axis, rad
$\varphi(s)$	Laplace transform of the roll attitude
$\left \frac{\varphi}{\beta} \right $	amplitude ratio of φ to β in the Dutch roll oscillation
$\frac{\varphi(s)}{\beta(s)}$	Laplace transform of the equation for $\left \frac{\varphi}{\beta} \right $
ω_{DR}	undamped natural frequency of the Dutch roll oscillation, rad/sec
ω_φ	undamped natural frequency of the second-order differential equation in the numerator of equation (7.4.1-2c)



(a) Time histories of roll rate.

- Flight data
- All derivatives calculated
- - - Flight $C_{l\beta}$; other derivatives calculated



(b) Wing-tip helix angle.

Figure 7.4.2-1. Time histories of roll rate response to aileron input and the wing-tip helix angle, $\frac{P_{ss} b_w}{2V}$, shown as a function of δ_a .

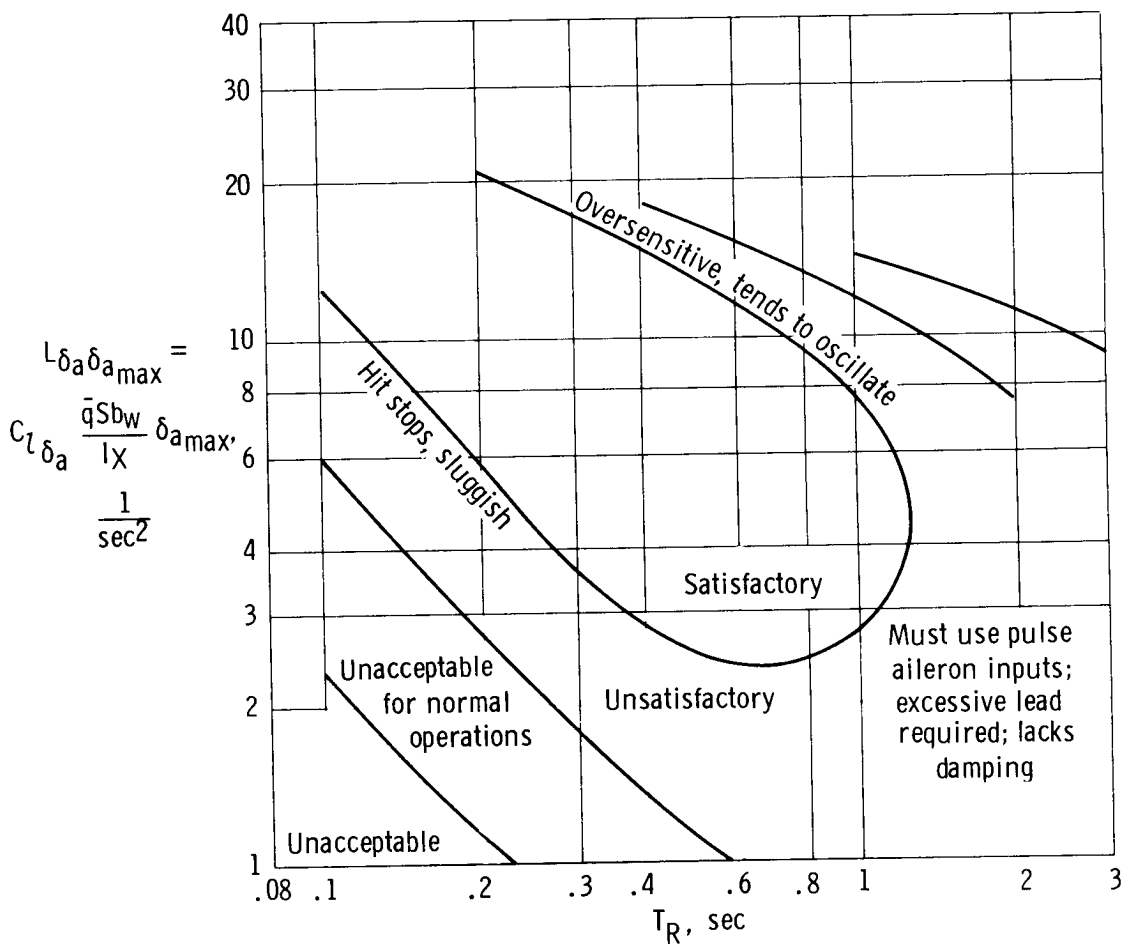
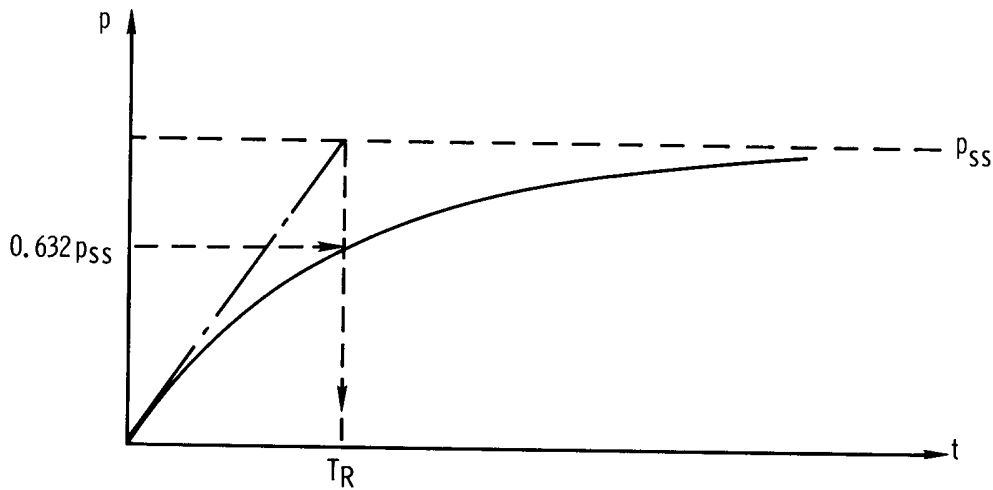
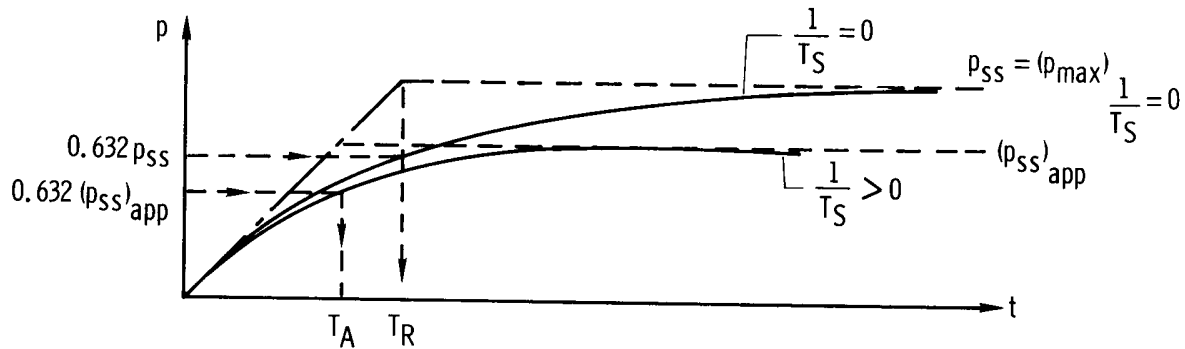


Figure 7.4.3-1. Proposed roll criterion for fighter aircraft, including pilot comments (from ref. 36).



(a) Single-degree-of-freedom roll mode response to aileron step input. Relationship of steady-state roll rate, p_{ss} , to true roll mode time constant, T_R .



(b) Relationship of two-degree-of-freedom (convergent spiral mode and roll mode) response and single-degree-of-freedom (roll mode) response to an aileron step input (from ref. 37). (The two-degree-of-freedom data analyzed on a single-degree-of-freedom basis result in an apparent roll mode time constant, T_A .)

Figure 7.4.3-2. Definitions of true and apparent roll mode time constants.

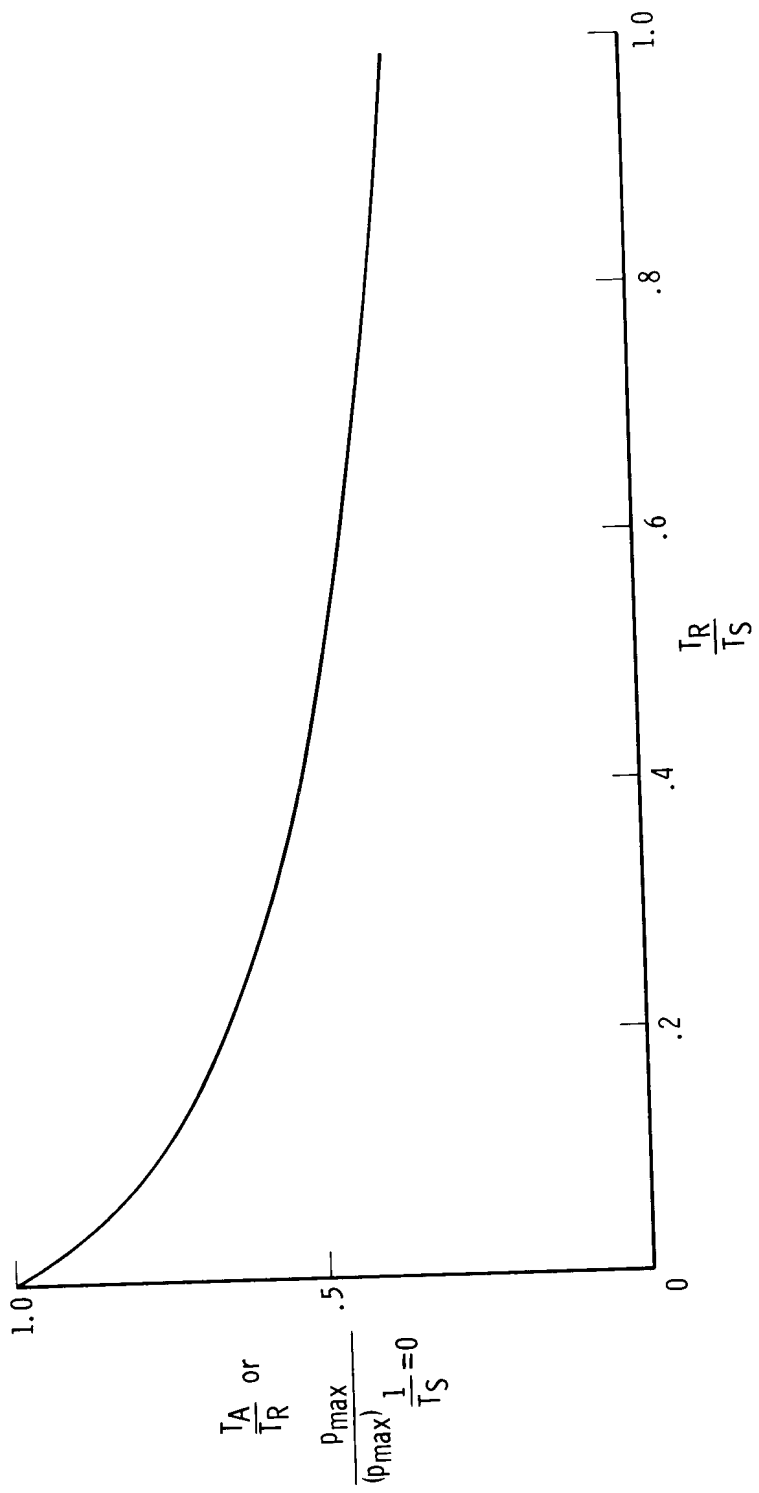


Figure 7.4.3-3. Apparent roll mode time constant (from ref. 37).

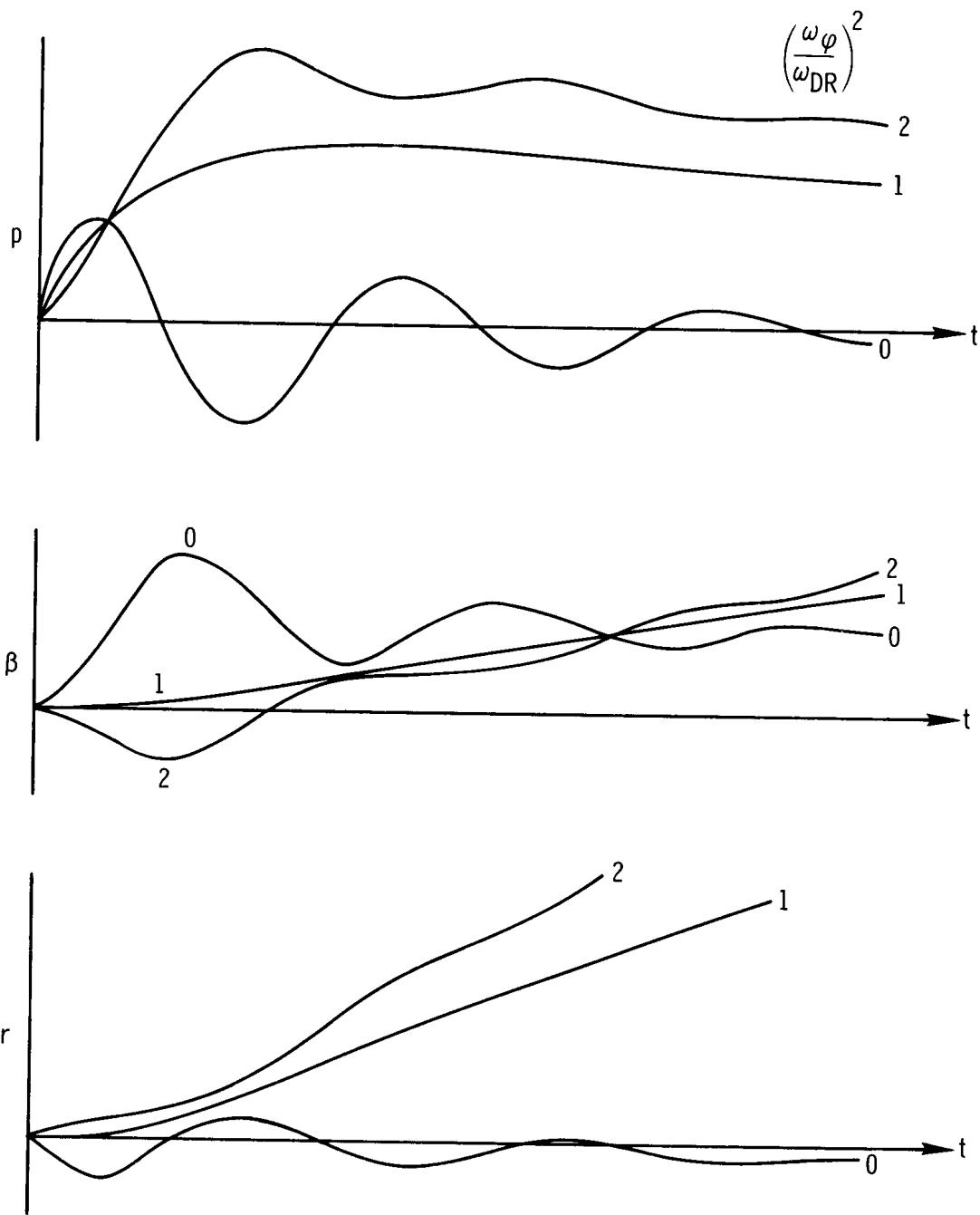
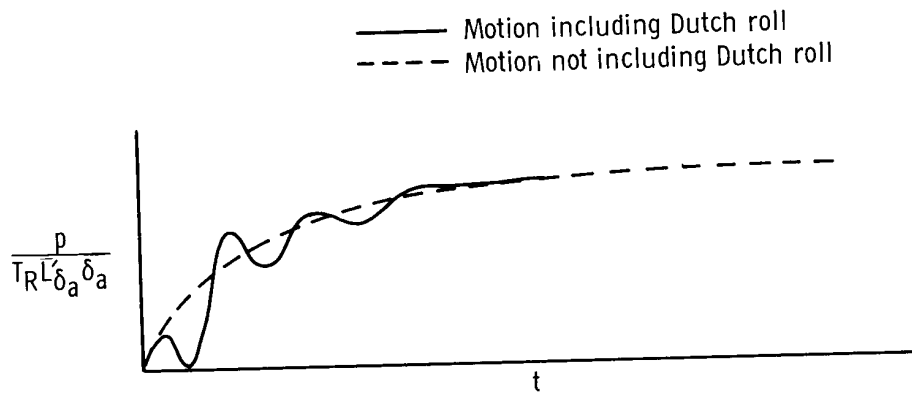
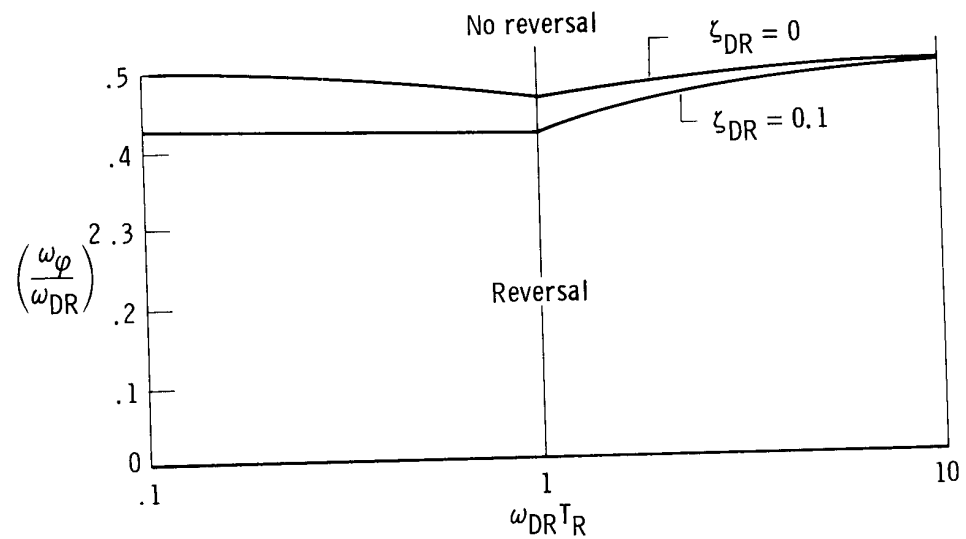


Figure 7.4.4-1. Effect of $\left(\frac{\omega_\varphi}{\omega_{DR}}\right)^2$ on response to aileron step input (from ref. 38).
 High C_{l_β} ; low C_{n_β} ; high α ; $\zeta_{DR} = 0.16$; $\omega_{DR} = 1.16$ rad/sec.

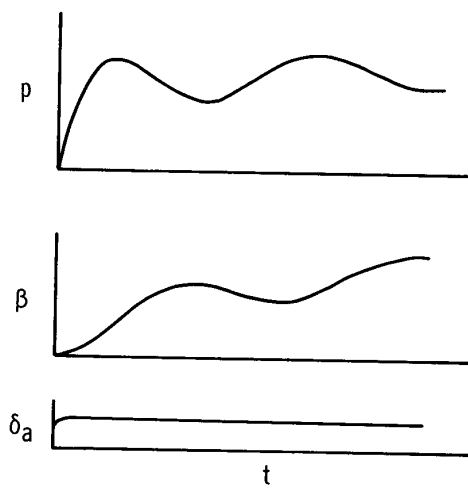


(a) Incipient roll reversal.

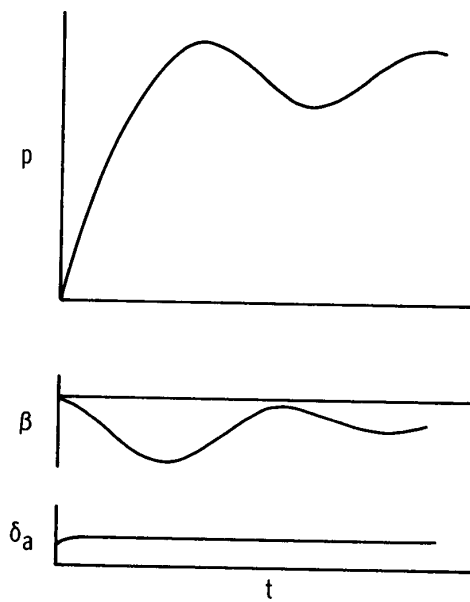


(b) Conditions for incipient rolling velocity reversal.

Figure 7.4.4-2. Roll reversal (from ref. 35).

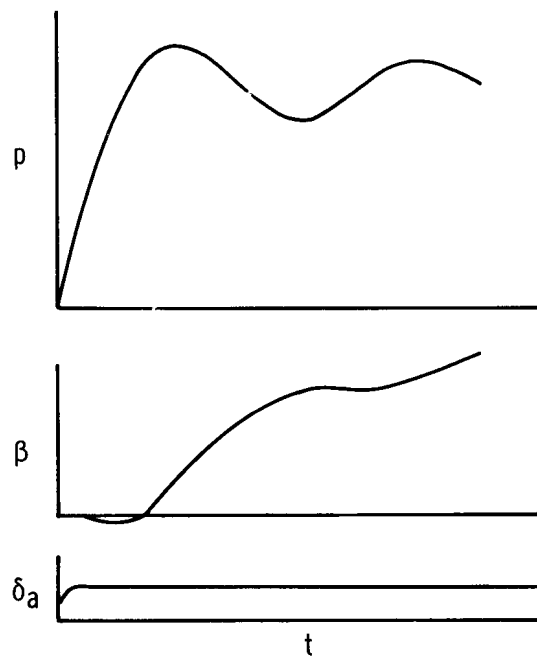


(a) Adverse \bar{N}'_{δ_a} ; \bar{L}'_β is negative.

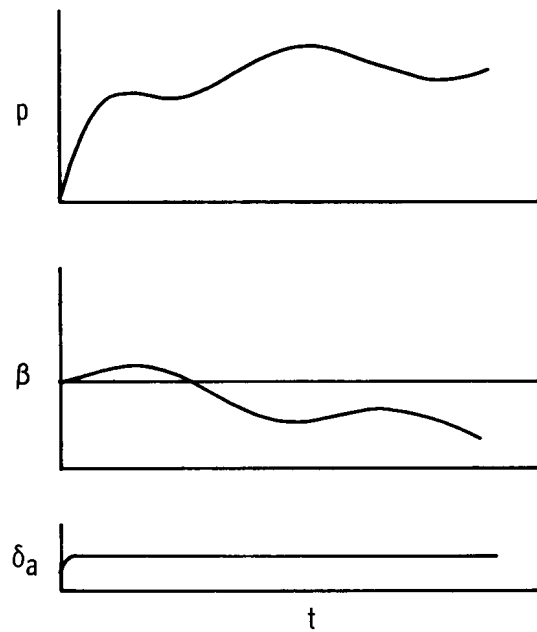


(b) Proverse \bar{N}'_{δ_a} (positive); \bar{L}'_β is negative.

Figure 7.4.4-3. Effect of \bar{N}'_{δ_a} on time history responses of roll rate and sideslip for an aileron step input (from ref. 34).



(a) Adverse $\bar{N}_p' - \frac{g}{V}$ is negative; \bar{L}_β' is negative.



(b) Proverse $\bar{N}_p' - \frac{g}{V}$ is positive; \bar{L}_β' is negative.

Figure 7.4.4-4. Effect of $\bar{N}_p' - \frac{g}{V}$ on time history responses of roll rate and sideslip for an aileron step input (from ref. 34).

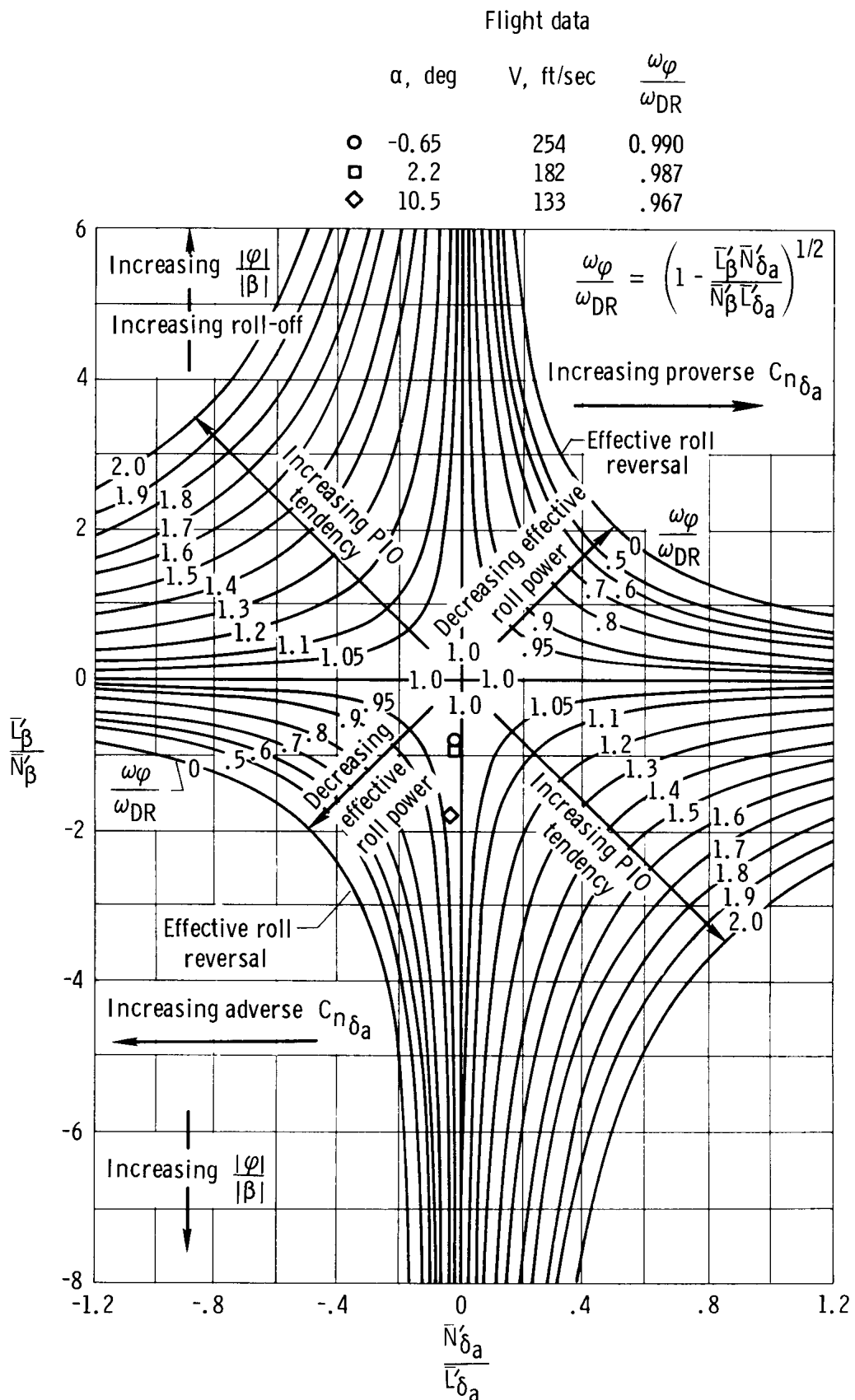


Figure 7.4.4-5. Factors affecting roll performance.

8.0 REFERENCES

1. Wolowicz, Chester H.; and Yancey, Roxanah B.: Longitudinal Aerodynamic Characteristics of Light, Twin-Engine, Propeller-Driven Airplanes. NASA TN D-6800, 1972.
2. Fink, Marvin P.; and Freeman, Delma C., Jr.: Full-Scale Wind-Tunnel Investigation of Static Longitudinal and Lateral Characteristics of a Light Twin-Engine Airplane. NASA TN D-4983, 1969.
3. Anon.: USAF Stability and Control Datcom. Air Force Flight Dynamics Lab., Wright-Patterson Air Force Base, Oct. 1960 (rev. Aug. 1968).
4. Toll, Thomas A.; and Queijo, M. J.: Approximate Relations and Charts for Low-Speed Stability Derivatives of Swept Wings. NACA TN 1581, 1948.
5. Fisher, Lewis R.: Approximate Corrections for the Effects of Compressibility on the Subsonic Stability Derivatives of Swept Wings. NACA TN 1854, 1949.
6. Hopkins, Edward J.: A Semiempirical Method for Calculating the Pitching Moment of Bodies of Revolution at Low Mach Numbers. NACA RM A51C14, 1951.
7. Goodman, Alex: Effects of Wing Position and Horizontal-Tail Position on the Static Stability Characteristics of Models With Unswept and 45° Sweptback Surfaces With Some Reference to Mutual Interference. NACA TN 2504, 1951.
8. Anon.: USAF Stability and Control Handbook. Flight Control Lab., Wright Air Development Center, U. S. Air Force, Aug. 1956.
9. Fink, Marvin P.; Freeman, Delma C., Jr.; and Greer, H. Douglas: Full-Scale Wind-Tunnel Investigation of the Static Longitudinal and Lateral Characteristics of a Light Single-Engine Airplane. NASA TN D-5700, 1970.
10. Queijo, M. J.: Theory for Computing Span Loads and Stability Derivatives Due to Sideslip, Yawing, and Rolling for Wings in Subsonic Compressible Flow. NASA TN D-4929, 1968.
11. Polhamus, E.; and Sleeman, W., Jr.: The Rolling Moment Due to Sideslip of Swept Wings at Subsonic and Transonic Speeds. NASA TN D-209, 1960.
12. Bird, John D.: Some Theoretical Low-Speed Span Loading Characteristics of Swept Wings in Roll and Sideslip. NACA TR 969, 1950.
13. De Young, John: Theoretical Antisymmetric Span Loading for Wings of Arbitrary Plan Form at Subsonic Speeds. NASA TR 1056, 1951.
14. Multhopp, H.: Aerodynamics of the Fuselage. NACA TM 1036, 1942.
15. Campbell, John P.; and McKinney, Marion O.: Summary of Methods for Calculating Dynamic Lateral Stability and Response and for Estimating Lateral Stability Derivatives. NACA Rep. 1098, 1952.

16. Lowry, John G.; and Polhamus, Edward C.: A Method for Predicting Lift Increments Due to Flap Deflection at Low Angles of Attack in Incompressible Flow. NACA TN 3911, 1957.
17. Ribner, Herbert S.: Notes on the Propeller and Slip-stream in Relation to Stability. NACA WR L-25, 1944. (Formerly NACA ARR L4I12a.)
18. Wolowicz, Chester H.: Considerations in the Determination of Stability and Control Derivatives and Dynamic Characteristics From Flight Data. AGARD Rep. 549-Part 1, 1966.
19. Seckel, E.; and Morris, J. J.: The Stability Derivatives of the Navion Aircraft Estimated by Various Methods and Derived From Flight Test Data. Princeton University Report No. 923, July 1970.
20. Swanson, Robert S.; and Priddy, E. LaVerne: Lifting-Surface-Theory Values of the Damping in Roll and of the Parameter Used in Estimating Aileron Stick Forces. NACA WR L-53, 1945. (Formerly NACA ARR L5F23.)
21. Queijo, M. J.; and Jaquet, Byron M.: Calculated Effects of Geometric Dihedral on the Low-Speed Rolling Derivatives of Swept Wings. NACA TN 1732, 1948.
22. Goodman, Alex; and Adair, Glenn H.: Estimation of the Damping in Roll of Wings Through the Normal Flight Range of Lift Coefficient. NACA TN 1924, 1949.
23. Letko, William; and Riley, Donald R.: Effect of an Unswept Wing on the Contribution of Unswept-Tail Configurations to the Low-Speed Static- and Rolling-Stability Derivatives of a Midwing Airplane Model. NACA TN 2175, 1950.
24. Michael, William H., Jr.: Analysis of the Effects of Wing Interference on the Tail Contributions to the Rolling Derivatives. NACA Rep. 1086, 1952.
25. Goodman, Alex; and Brewer, Jack D.: Investigation at Low Speeds of the Effect of Aspect Ratio and Sweep on Static and Yawing Stability Derivatives of Untapered Wings. NACA TN 1669, 1948.
26. Cotter, William E., Jr.: Summary and Analysis of Data on Damping in Yaw and Pitch for a Number of Airplane Models. NACA TN 1080, 1946.
27. Letko, William: Effect of Vertical-Tail Area and Length on the Yawing Stability Characteristics of a Model Having a 45° Sweptback Wing. NACA TN 2358, 1951.
28. Letko, William; and Cowan, John W.: Effect of Taper Ratio on Low-Speed Static and Yawing Stability Derivatives of 45° Sweptback Wings With Aspect Ratio of 2.61. NACA TN 1671, 1948.
29. Queijo, M. J.; and Jaquet, Byron M.: Investigation of Effects of Geometric Dihedral on Low-Speed Static Stability and Yawing Characteristics of an Untapered 45° Sweptback-Wing Model of Aspect Ratio 2.61. NACA TN 1668, 1948.

30. Goodman, Alex; and Fisher, Lewis R.: Investigation at Low Speeds of the Effect of Aspect Ratio and Sweep on Rolling Stability Derivatives of Untapered Wings. NACA Rep. 968, 1950.
31. Ashkenas, Irving L.; and McRuer, Duane T.: Approximate Airframe Transfer Functions and Application to Single Sensor Control Systems. Tech. Rep. 58-82. (ASTIA No. AD 151025), Wright Air Dev. Center, U. S. Air Force, June 1958.
32. Anon.: Flying Qualities of Piloted Airplanes. Military Specification MIL-F-8785B (ASG). Aug. 7, 1969.
33. Ellis, David R.; and Seckel, Edward: Flying Qualities of Small General Aviation Airplanes. Part 1: The Influence of Dutch-Roll Frequency, Dutch-Roll Damping, and Dihedral Effect. Rep. No. DS-69-8, FAA, June 1969.
34. Chalk, C. R.; Neal, T. P.; Harris, T. M.; Pritchard, F. E.; and Woodcock, R. J.: Background Information and User Guide for MIL-F-8785(ASG), "Military Specification - Flying Qualities of Piloted Airplanes." Tech. Rep. AFFDL-TR-69-72, Air Force Flight Dynamics Lab., Wright-Patterson Air Force Base, Aug. 1969.
35. Ashkenas, Irving L.; and McRuer, Duane T.: The Determination of Lateral Handling Quality Requirements From Airframe-Human Pilot System Studies. WADC Tech. Rep. 59-135 Wright Air Dev. Center, U. S. Air Force, June 1959. (Available from ASTIA as AD 212152.)
36. Creer, Brent Y.; Stewart, John D.; Merrick, Robert B.; and Drinkwater, Fred J. III: A Pilot Opinion Study of Lateral Control Requirements for Fighter-Type Aircraft. NASA Memo 1-29-59A, 1959.
37. Anon.: Analysis of Several Handling Quality Topics Pertinent to Advanced Manned Aircraft. Tech. Rep. AFFDL-TR-67-2, Air Force Flight Dynamics Lab., Wright-Patterson Air Force Base, June 1967.
38. Leyman, C.; and Nuttall, E. R.: A Survey of Aircraft Handling Criteria. C. P. No. 833, British A. R. C., 1966.
39. Ashkenas, I. L.: Some Open- and Closed-Loop Aspects of Airplane Lateral-Directional Handling Qualities. AGARD Rep. 533, May 1966.